Ion gel gating of perovskite cobaltite thin films: Understanding mechanisms and control of magnetism

A DISSERTATION
SUBMITTED TO THE FACULTY OF THE
UNIVERSITY OF MINNESOTA
BY

Jeff Walter

IN PARTIAL FULFILLMENT OF THE REQUIREMENTS
FOR THE DEGREE OF
DOCTOR OF PHILOSOPHY

Advisors: Chris Leighton
C. Daniel Frisbie

May, 2018

Acknowledgements

The most important section of this thesis comes first. I was only able to reach this point due to the help of many people and I could not be more thankful for their support. I will also start with the most important thanks, which goes to my primary advisor, Chris Leighton. His work ethic, and the manner in which he applies it to everything he does, is something I continually try to emulate, but always fall short. Chris's commitment not only to producing the best research possible, but also to mentoring and providing opportunities for us graduate students is remarkable. He constantly challenges us to develop our scientific skills, with my critical thinking and presentation skills greatly benefitting from his tutelage. Further, Chris made possible opportunities such as conferences (including one in Hawaii!!!), workshops, neutron scattering schools, *etc*. where I could develop those skills as well as collaborations (where I met many of the people acknowledged below). I particularly appreciated the challenges on the golf course and pool table, though I think I may have ended with the upper hand on those battlefields.

I would also like to thank my co-advisor, Dan Frisbie. I really enjoyed designing homework and exam problems with Dan during two stints as his teaching assistant for Structures. While not my advisor on paper, Eray Aydil played a crucial role in my PhD career with weekly advisement in our sulfide meetings. Unfortunately, my work on FeS_2 will not make it into this thesis, but I really enjoyed being part of the sulfide group and want to thank Eray for his guidance. I also cannot forget to thank my undergraduate physics advisor, Bruce Bolon. Not only did he first introduce me to Chris, making all of this possible, but he also is a blast to be around, with many past (and hopefully, future) occurrences of playing cards, Mahjong, or simply having a beer. I have also had the privilege of working with some excellent collaborators. Turan Birol, Rafael Fernandes, Boris Shklovskii, and Peter Orth have always been there to help us with theoretical guidance. Martin Greven and his students Biqiong Yu and Guichuan Yu played a critical role in developing synchrotron X-ray techniques we used. I received fantastic help in this work from beamline scientists, including John Freeland, Tim Charlton, Haile Ambaye, Mike Fitzsimmons, Alex Grutter, Brian Kirby, and Julie Borchers. I want to make special

mention of the folks from NIST; Alex, Brian, and Julie treated me wonderfully during my beam times as well as during the summer school I attended. Further, Alex designed a brilliant sample holder specifically for my experiments and both Brian and Julie went out of their way to provide both research and professional advice.

I have been really lucky in the network of support my Leighton lab coworkers have provided. When I first joined the group there were some truly incredible people to teach me the inner workings of the lab and my project. Shun Wang and Wei Xie (Frisbie group) got me started with electrolyte gating, Liam O'Brien and Danny Phelan provided excellent mentorship on measurement systems and physics concepts, and Shameek Bose was a *huge* help in teaching me the growth of cobaltite films. Mike Manno is the definition of a mentor; I learned so much from him and did my best to pursue his accomplishments as a Leighton group member. I thank all the folks above for their patience, as I am sure my learning curve was slow. I would also like to thank other graduate students and post-docs I have had the privilege to work with: Xin Zhang, Koustav Ganguly, Palak Ambwani, Helin Wang, Bryan Voigt, Vipul Chaturvedi, Will Postiglione, John Dewey, Linmin Wang, Eric McCalla, and Joe Batley. Special thanks go to Bryan, who agreed to proofread this. Everything I have done in the Leighton group, Bryan seems to be doing better; his future is bright. Finally, I would like to thank some incredible undergraduates that have worked with me: Michael Braun, Ryan Hool, Kyle Wagner, and Joey Gotchnik, all of whom have done countless measurements for me. I really cannot thank all of these coworkers enough.

I have many friends that deserve recognition. My nerdiness can be traced all the way back to high school, where my good friend Jeff Rossow and I would continually challenge each other in the classroom. Myles Peterson (nearest friends for life) and Will Brown encouraged me to foster this nerdiness during and after our time at Hamline. Mark Sullivan and Boo Schliep made graduate school a blast and are incredible scientists themselves. Boo and his wife, Sara, even introduced me to my girlfriend, Crystal Jones, who has made the last couple of years the best of my life. Crystal's support truly cannot be valued. I look forward to every day with her. Finally, I have to thank my family. My

mother, Susan Walter, made my education possible through her hard work as an employee at Gustavus. My father, Mike Walter, is where I get my competitive attitude from. Without this attitude, I would not have strived to be the best scientist I could be, and much of this would not have happened. Lastly, there is no one throughout my life that has supported me more than my sister, Erica Walter. For her support, as well as all the support from everybody above, I say THANK YOU!

Abstract

Recently, electrolyte gating techniques using ionic liquids and gels have proven highly effective in tuning large carrier densities at material surfaces. These electrolytes enable electric double layer transistor operation, the large capacitances (10's of $\mu F/cm^2$) generating electron/hole densities up to 10^{15} cm^{-2}, *i.e.*, significant fractions of an electron per unit cell in most materials. Uncertainties remain, however, including the true doping mechanism (*i.e.*, electrostatic *vs*. electrochemical), the challenge of *in operando* characterization, and the need to understand the full potential and universality. In regard to universality, superconductivity and insulator-metal transitions have been extensively studied with electrolyte gating, but this promising technique has been less applied to controlling *magnetism*. Electrical control of magnetism is a long-standing goal in physics and technology, electrolyte gating techniques providing a promising route to realization.

Employing electric double layer transistors based on ultrathin epitaxial $La_{1-x}Sr_xCoO_3$ as a model system, our findings first address the true doping mechanism, clarifying charge carrier *vs*. oxygen defect creation. Transport measurements reveal dramatic asymmetry with respect to bias polarity. Negative gate biases lead to reversible behavior (*i.e.*, predominantly electrostatic operation) up to some threshold, whereas positive bias immediately induces irreversibility. Experiments in inert/O_2 atmospheres directly implicate oxygen vacancies in this irreversibility, supported by atomic force microscopy and X-ray photoelectron spectroscopy. We then demonstrate the use of synchrotron hard X-ray diffraction and polarized neutron reflectometry as *in operando* probes to further investigate the gating mechanism. An asymmetric gate bias response is confirmed to derive from electrostatic hole accumulation at negative bias *vs*. oxygen vacancy formation at positive bias. The latter is detected *via* a large gate-induced lattice expansion (up to 1 %), complementary bulk measurements and density functional calculations enabling *quantification* of the bias-dependent oxygen vacancy density. Remarkably, the gate-induced oxygen vacancies proliferate through the entire thickness of 30-40-unit-cell-thick films, quantitatively accounting for changes in the magnetization depth profile and demonstrating electrochemical control of magnetism. This is interpreted in a simple

picture where electrostatic *vs*. electrochemical response is dictated by the low formation enthalpy and high diffusivity of oxygen vacancies in $La_{1-x}Sr_xCoO_3$. These results, therefore, directly elucidate the issue of electrostatic *vs*. redox-based response in electrolyte-gated oxides, also demonstrating powerful new approaches to their *in operando* investigation. Control of ferromagnetism is then demonstrated in electrostatic mode by working at negative bias. Guided by theory, we demonstrate reversible electrical control of Curie temperature over a 150 K window. This is achieved *via* gate-induced cluster percolation, leading to optimized control of ferromagnetism, directly verified by magnetoresistance, anomalous Hall effect, and PNR measurements.

Table of Contents

List of tables

List of figures

Chapter 1

Chapter 2

Chapter 3

Chapter 4

Chapter 5

Chapter 6

Chapter 7

List of symbols

Bolded symbols represent a vector object

Symbols listed in order of appearance

Γ	Goldschmidt tolerance factor
r_i	Ionic radius of ion "i"
x	Perovskite A-site substitution fraction in $A_{1-x}A'_xBO_3$
y	Perovskite B-site substitution fraction in $AB_{1-y}B'_yO_3$
δ	Oxygen non-stoichiometry in perovskite $ABO_{3-\delta}$
Δ_{CF}	Crystal field energy
J_H	Hund's coupling energy
P	Double exchange transfer probablility
θ	Generic angle
T	Temperature
T_C	Curie temperature
V_g	Gate voltage
n_{2D}	Sheet charge density
λ_D	Debye length
R_s	Sheet resistance
n_{3D}	3D electron density
T_{MI}	Metal-insulator transition temperature
a	Cubic lattice parameter
a_R	Rhombohedral edge length
α_R	Rhombohedral angle
a_c	Pseudocubic lattice parameter
S	Spin quantum number
$x_{c,LSCO}$	Critical doping level for percolation in LSCO (0.18)
ρ	Resistivity
MR	Magnetoresistance value
M	Magnetization

M_s	Saturation magnetization
x_{eff}	Effective doping level
t	Thickness
q	Modulation vector of oxygen vacancy ordering
P_O	O_2 partial pressure
T_{sub}	Substrate temperature
λ	Wavelength
ω	Angle between incident probe beam and sample plane
2θ	Scattering angle
$\boldsymbol{Q}$	Scattering vector
$2\theta_{002}$	(002) peak position
c_{op}	Out-of-plane lattice parameter
t_S	Scherrer length
t_f	Film thickness calculated from Laue fringes
θ_{nL}	n_Lth order Laue fringe position
n_L	Laue fringe number
$Q_{//,\perp}$	In-plane, out-of-plane scattering vector component
$d_{010,001}$	(010), (001) interplanar spacing
ρ_{xray}	X-ray scattering length density
ρ_m	Mass density
N_a	Avogadro's number
b_i	Scattering length from atom "i"
m_i	Atomic mass of atom "i"
r_{el}	Classical electron radius
f_i	Real part of the atomic scattering factor for atom "i"
θ_c	Critical angle
θ_{nK}	n_Kth order Kiessig fringe position
n_K	Kiessig fringe number
ρ_{el}	Electron density
Z	Target-to-substrate distance

B	Magnetic flux density
H	Magnetic field
B_c, H_c	Coercive flux density, magnetic fields
R	Resistance
f	van-der-Pauw anisotropy factor
RRR	Residual resistivity ratio
ρ_n	Neutron scattering length density
ρ_m	Magnetic scattering length density
C	Constant to convert ρ_m to M
$M_{//,\perp}$	Magnetization parallel, perpendicular to neutron polarization axis
$R^{++,--}$	Non-spin-flip neutron reflectivity channels
$R^{+-,-+}$	Spin-flip neutron reflectivity channels
c_t	Counting time
τ	Time
A	Resistance drift rate
I_g	Gate current
$I_{g,\tau\to\infty}$	Long time limit of gate current
A_c	Channel area
p	Surface hole density
ΔR_{gate}	Gate induced resistance change
ΔR_{irrev}	Irreversible resistance change
σ_{AH}	Anomalous Hall conductivity
ρ_{xy}	Transverse resistivity
μ_0	Permeability of free space
R_O	Ordinary Hall coefficient
R_{AH}	Anomalous Hall coefficient
σ_{xy}	Transverse conductivity
$\rho_{xx,0}$	Zero field resitivity
L	Scattering vector in reciprocal lattice units
ΔV	Unit cell volume change

U	DFT correction parameter
a_1	Expansion rate of LSCO upon introducing δ from DFT
σ_{ij}	Stress tensor
C_{ijkl}	Stiffness tensor
ε_{kl}	Strain tensor
E	Young's modulus
ν	Poisson ratio
a_2	Expansion rate of LSCO upon introducing electrons from DFT
SA	Spin asymmetry
x_c	Bulk percolation threshold
s	Surface doping level
Δs_c	Induced surface charge density to reach percolation
$x_{c,3D}$	3D site percolation threshold
l	In-plane size of theoretical sample
ξ	Cluster size
b,c_i	Percolation constants
ν	Correlation length exponent
N	Number of sites
N_c	Number of sites of largest cluster per surface area
$t_{th,exp}$	Theoretical, experimental thickness (only differentiated in Ch. 6)
$\Delta s_{c,th}$	Theoretical Δs_c for LSCO
Δs_{exp}	Experimentally induced surface charge
$R_{g,ug}$	Resistances of gated, ungated layers
$\rho_{g,ug}$	Resistivity of gated, ungated layers
M_R	Remnant magnetization
H_s	Saturation magnetic field
K	Magnetic anisotropy energy
α_i	Cosines of angle between M and principal axis "i"
H_a	Anisotropy magnetic field
AMR	Anisotropy of MR

List of acronyms

Acronyms listed in order of appearance

LS	Low spin
IS	Intermediate spin
HS	High spin
STO	$SrTiO_3$
2DEG	Two-dimensional electron gas
LAO	$LaAlO_3$
GMR	Giant magnetoresistance
CMR	Colossal magnetoresistance
MEPS	Magneto-electronic phase separation
MOSFET	Metal-oxide-semiconductor field effect transistor
EDLT	Electric double layer transistor
IL	Ionic liquid
RT	Room temperature
EMI:TFSI	1-ethyl-3-methylimidazolium bis(trifluoromethylsulfonyl)imide
P(VDF-HFP)	poly(vinylidene fluoride-*co*-hexafluoropropylene)
V_O	Oxygen vacancy
SXRD	Synchrotron X-ray diffraction
LSCO	$La_{1-x}Sr_xCoO_{3-\delta}$
LCO	$LaCoO_3$
SST	Spin state transition
FM	Ferromagnetic
FMM	Ferromagnetic and metallic
AF	Antiferromagnetic
MR	Magnetoresistance
IGMR	Intercluster giant magnetoresistance
AMR	Anisotropic magnetoresistance
HRTEM	High resolution transmission electron microscopy

OVO	Oxygen vacancy ordering
EELS	Electron energy loss spectroscopy
SANS	Small angle neutron scattering
PNR	Polarized neutron reflectometry
LSAT	$(La_{0.18}Sr_{0.82})(Al_{0.59}Ta_{0.41})O_3$
SLAO	$SrLaAlO_4$
HRXRD	High resolution X-ray diffraction
WAXRD	Wide angle X-ray diffraction
RC	Rocking curve
RSM	Reciprocal space mapping
GIXR	Grazing incidence X-ray reflectometry
SLD	Scattering length density
AFM	Atomic force microscopy
RMS	Root mean square
SQUID	Superconducting quantum interference device
MPMS	Magnetic Property Measuring System
XPS	X-ray photoelectron spectroscopy
BE	Binding energy
AHE	Anomalous Hall effect
PXRD	Powder X-ray diffraction
TGA	Thermo-gravimetric analysis
DFT	Density functional theory
XMCD	X-ray magnetic circular dichroism
MOKE	Magneto-optical Kerr effect
IMT	Insulator-metal transition
PMA	Perpendicular magnetic anisotropy
IP	In-plane
OoP	Out-of-plane
FCC	Face-centered-cubic
LSMO	$La_{1-x}Sr_xMnO_3$

List of publications

J. Walter, H. Wang, B. Luo, C. D. Frisbie, C. Leighton. "Electrostatic *versus* electrochemical doping and control of ferromagnetism in ion-gel-gated ultrathin $La_{0.5}Sr_{0.5}CoO_{3-\delta}$." *ACS Nano* 10, 7799-7810 (2016).

E. McCalla, **J. Walter**, C. Leighton. "A unified view of the substitution-dependent antiferrodistortive phase transition in $SrTiO_3$." *Chem. Mater.* 28, 7973-7981 (2016).

P. Orth, R. Fernandes, **J. Walter**, C. Leighton, B. Shklovskii. "Percolation via combined electrostatic and chemical doping in complex oxide films." *Phys. Rev. Lett.* 118, 106801 (2017).

X. Ren, E. Schmidt, **J. Walter**, K. Ganguly, C. Leighton, C. D. Frisbie. "Rubrene Single Crystal Transistors with Perfluoropolyether (PFPE) Liquid Dielectric: Exploiting Free Dipoles to Induce Charge Carriers at Organic Surfaces." *J. Phys. Chem. C*. 121, 6540-6545 (2017).

X. Zhang, M. Li, **J. Walter**, L. O'Brien, M. Manno, B. Voigt, F. Mork, S. V. Baryshev, J. Kakalios, E. Aydil, C. Leighton. "Potential resolution to the 'doping puzzle' in iron pyrite: carrier type determination by Hall effect and thermopower." *Phys. Rev. Mater.* 1, 015402 (2017).

X. Wu, **J. Walter**, T. Feng, J. Zhu, X. Ruan, C. Leighton, X. Wang. "Glass-like through-plane thermal conductivity induced by oxygen vacancies in nanoscale epitaxial $La_{0.5}Sr_{0.5}CoO_{3-\delta}$." *Adv. Funct. Mater.* 27, 1704233 (2017).

J. Walter, X. Zhang, B. Voigt, F. Mork, R. Hool, M. Manno, E. Aydil, C. Leighton. "Surface conduction in *n*-type FeS_2 single crystals." *Phys. Rev. Mater.* 1, 065403 (2017).

J. Walter, G. Yu, B. Yu, A. Grutter, B. Kirby, J. Borchers, Z. Zhang, H. Zhou, T. Birol, M. Greven, C. Leighton. "Ion-gel-gating-induced oxygen vacancy formation in epitaxial $La_{0.5}Sr_{0.5}CoO_{3-\delta}$ films from *in operando* X-ray and neutron scattering." *Phys. Rev. Mater.* 1, 071403(R) (2017).

J. Walter, T. Charlton, H. Ambaye, M. Fitzsimmons, P. P. Orth, R. Fernandes, B. Shklovskii, C. Leighton, "Giant electrostatic modification of magnetism *via* electrolyte-

gate-induced cluster percolation in $La_{1-x}Sr_xCoO_{3-\delta}$." *Phys. Rev. Lett*., under review, (2018).

B. Voigt, W. Moore, M. Manno, **J. Walter**, J. D. Jeremiason, E. S. Aydil, C. Leighton, "Transport evidence for sulfur vacancies as the origin of *n*-type doping in pyrite FeS_2." *Phys. Rev. Mater*., in preparation.

H. Wang, **J. Walter**, K. Ganguly, C. Leighton, "Wide voltage window control of electronic transport in epitaxial $BaSnO_3$ via ion gel gating." *Phys. Rev. Mater*., in preparation.

J. Walter, M. C. Piris, G. Yu, Z. Zhang, M. Greven, M. Varela, C. Leighton, "Strain controlled magnetic anisotropy in $La_{1-x}Sr_xCoO_{3-\delta}$ Films." *Phys. Rev. Mater*., in preparation.

Chapter 1: Introduction

Exponential growth of electronic technology in the last 50 years has driven transformational societal changes. Conventional electrical technologies, however, are reaching fundamental physical limits in both size and speed, suggesting the exponential improvement currently realized could soon come to an end. The search for next-generation device concepts, many of which rely on the development of tunable quantum materials, thus provides a grand challenge for today's researchers. In this chapter I will introduce a promising class of such quantum materials, the "perovskite oxides." Included are brief discussions on the underlying chemistry and physics giving rise to the multitude of phenomena in these oxides, the attractive aspects of using the perovskite building block in heterostructures, and the potential for external control of their electronic and magnetic properties in a device. I will then introduce "electrolyte gating", a particularly attractive technique used to control material properties with electric fields. Focus will be placed on current shortcomings of electrolyte gating studies on oxides, including poorly differentiated electrostatic *vs.* electrochemical gating mechanisms, the dearth of experimental probes beyond electrical transport measurements, and its limited application to the control of magnetic properties. Finally, I will provide background on the material of focus for this work, the perovskite cobaltite $La_{1-x}Sr_xCoO_{3-\delta}$, with emphasis on how electrolyte gating studies on this material could address the shortcomings of electrolyte gating of oxides.

1.1 Perovskite oxides

"Abundant" is a great word to describe solid oxides, as the majority of Earth's crust is made up of oxides; they are used in a huge variety of applications, and are the focus of prolific fundamental research studies. These materials, as the name implies, are made up of oxygen and at least one other element serving as the cation in these primarily ionic materials. Many gemstones, for example, are single crystalline oxides with properties such as shape and color determined by the identity of the cation(s) and the crystal structure they form with oxygen anions. One particularly interesting class of oxides is the perovskites, their defining feature being the prototypical chemical formula of ABO_3 and base crystal structure shown in Fig. 1.1(a). The perovskite oxides exhibit a vast range of electronic and

magnetic properties, tuned by the choice of A- and B-site cations, leading to a wealth of research interest and commercially available products. To name a few electronic applications, perovskites are found in solid oxide fuel cells [1], piezoelectric transducers [2], and ferroelectric non-volatile memory [3]. At least three primary attributes make perovskite oxides an ideal playground for a material scientist: (1) the chemical flexibility of the perovskite structure, leading to diverse functionality, (2) the ability to tune, combine, and discover diverse properties in perovskite heterostructures, and (3) the potential for external control of these properties in devices employing excitations such as electric fields.

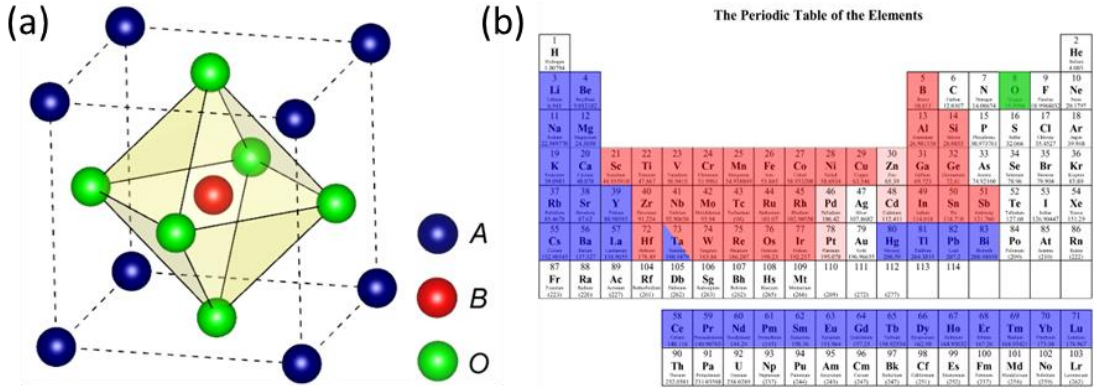

Fig. 1.1. (a) The cubic ABO_3 perovskite unit cell showing the A-site (blue), B-site (red), and oxygen (green) sites, as well as highlighting the BO_6 octahedron in light yellow. (b) The periodic table of the elements highlighting the sites each element can take with the same color scheme.

1.1.1 *Basic chemistry and physics*

Critical to the vast interest in perovskites is the chemical flexibility of the prototypical perovskite structure shown in Fig. 1.1(a). The majority of elements can occupy either the A- or B-site, as shown in Fig. 1.1(b). A key feature of this chemical flexibility is the ability of the simple cubic structure shown in Fig. 1.1(a) to distort. A common parameter used to predict the distortions for a given combination of A- and B-site cations is the Goldschmidt tolerance factor (Γ) which is defined as

$$\Gamma = \frac{r_A + r_O}{\sqrt{2}(r_B + r_O)}, \qquad 1.1$$

where r_A, r_B, and r_O are the ionic radii of A, B, and O, respectively. For the ideal cubic structure shown in Fig. 1.1(a), which has a space group of $Pm\bar{3}m$, Γ = 1. Typically, the

cubic $Pm\bar{3}m$ structure is observed for $0.9 < \Gamma < 1$. For $0.71 < \Gamma < 0.9$, the structure accommodates the small A-site ions by rotating the BO_6 octahedra and lowering the symmetry to either orthorhombic or rhombohedral symmetries. Cation displacements leading to non-centrosymmetric tetragonal structures are typically observed for $\Gamma > 1$. With access to such a variety of different elements and crystal symmetries, perovskite oxides exhibit a multitude of physical phenomena, including high-temperature superconductivity in the cuprates [4], colossal magnetoresistance and ferromagnetism in the manganites [5], ferroelectricity in the titanates [6], mixed ionic conductivity in the cobaltites [7], and many more. Further, these different functionalities can often be tuned by chemical substitution. A more general form of a chemically substituted perovskite is $A_{1-x}A'_xB_{1-y}B'_yO_{3-\delta}$, where x, y, and δ represent substitution on the A-site, B-site, and oxygen non-stoichiometry, respectively. Such chemical substitution can significantly influence important factors in the electronic and magnetic properties, such as bond lengths, bond angles, and electron or hole densities.

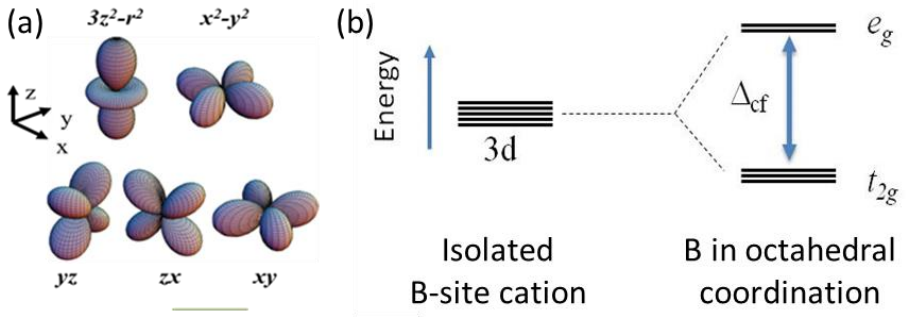

Fig. 1.2. (a) The 3*d* orbitals of a transition metal B-site cation [8]. (b) Diagram showing the breaking of degeneracy of 3*d* orbitals when placed in an octahedral bonding environment.

The B-site cation (typically a transition metal) at the center of the unit cell, shown in Fig. 1.1(a), is also the centerpiece in describing the underlying physics responsible for the phenomena observed in perovskite oxides. The electronic and magnetic properties of most perovskite oxides are primarily a result of the *d* shell electrons of the transition metal B-site cation and their hybridization with neighboring oxygen 2*p* orbitals. The effects of the A-site cation have important influences on properties of perovskites, but typically only through indirect effects on the B-site *d* orbitals. The scaffold of the *d* orbital energies is determined by the crystal field splitting experienced by the B-site cation. In an isolated

transition metal cation, the five *d*-orbitals (x^2-y^2, $3z^2$-r^2, *xy*, *yz*, *zx*) shown in Fig. 1.2(a) are degenerate. When the cation is placed in a perovskite structure, however, the octahedral crystal field of the O^{2-} ligands lifts the degeneracy, raising the x^2-y^2 and $3z^2$-r^2 orbital energies and lowering the *xy*, *zx* and *yz* energies, as shown in Fig. 1.2(b). The two orbitals that point toward the O^{2-} ligands (x^2-y^2 and $3z^2$-r^2, the so-called "e_g" orbitals) experience enhanced Coulombic repulsion between occupying electrons and the negatively charged O^{2-} ligands, and thus have higher energy compared to the other three "t_{2g}" orbitals. The magnitude of the energy difference between the e_g and t_{2g} orbitals (typically of order 1 eV for perovskite oxides) is termed the crystal field energy (Δ_{CF}).

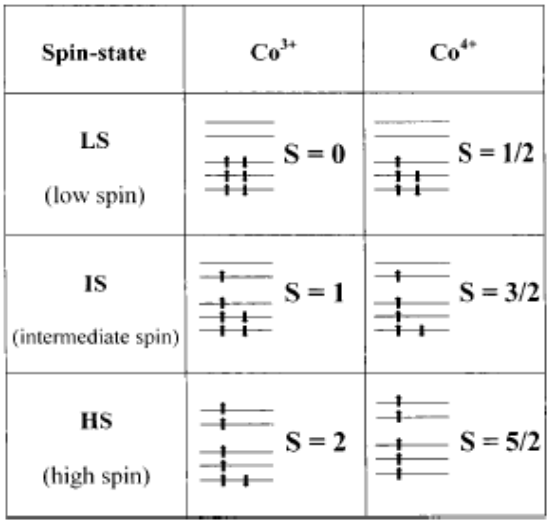

Fig. 1.3. The possible electron occupation and spin states in the 3*d* orbitals of Co^{3+} and Co^{4+} cations in an octahedral crystal field [9].

The electron occupation of these non-degenerate *d*-orbitals is often non-trivial and a primary source of the diverse functionality in perovskite oxides. The first consideration in this regard is simply the number of electrons occupying the *d*-orbital manifold, which is determined by the identity and valence state of the transition metal B-site cation. Considering the electron configuration of Co ($[Ar]4s^2 3d^7$), for example, Co^{3+} will have six electrons occupying the *d*-orbitals, whereas Co^{4+} will have five. The next consideration comes in determining which *d*-orbitals will be occupied. Occupation of the lower t_{2g} orbitals is favored by Δ_{CF} while Hund's coupling energy (J_H, a direct result of electron-electron repulsion and the Pauli Exclusion Principle) tends to maximize the total spin by singly occupying each orbital. The occupation state of the *d*-electrons will thus depend on the balance between these two energies along with other external factors such as

temperature, pressure, strain, *etc*. An example of non-trivial occupation scenarios for Co^{3+} and Co^{4+}, where Δ_{CF} is comparable to J_H, is shown in Fig. 1.3 [9]. The low spin (LS) states will be favored if $\Delta_{CF} > J_H$ whereas the high spin (HS) or intermediate spin (IS) states will be favored if $\Delta_{CF} < J_H$. Clearly, the competition between crystal field and Hund's coupling energies will have significant consequences on the magnetic properties in this case, which will be discussed in more detail in Section 1.3.1. Finally, distorting the BO_6 octahedron can affect the crystal field splitting and lead to lower overall energy in many systems. A common distortion that occurs in systems with 1 or 3 e_g electrons is the Jahn-Teller effect, shown schematically in Fig. 1.4. Essentially, the elongation or compression of the octahedron in one direction breaks the degeneracy of the e_g and t_{2g} orbitals (on energy scales of order 0.1 eV in the manganites [5], for example), resulting in a lower overall energy. Such distortions play a significant role in determining the final electronic/magnetic state of a system and can often lead to localization of e_g electrons.

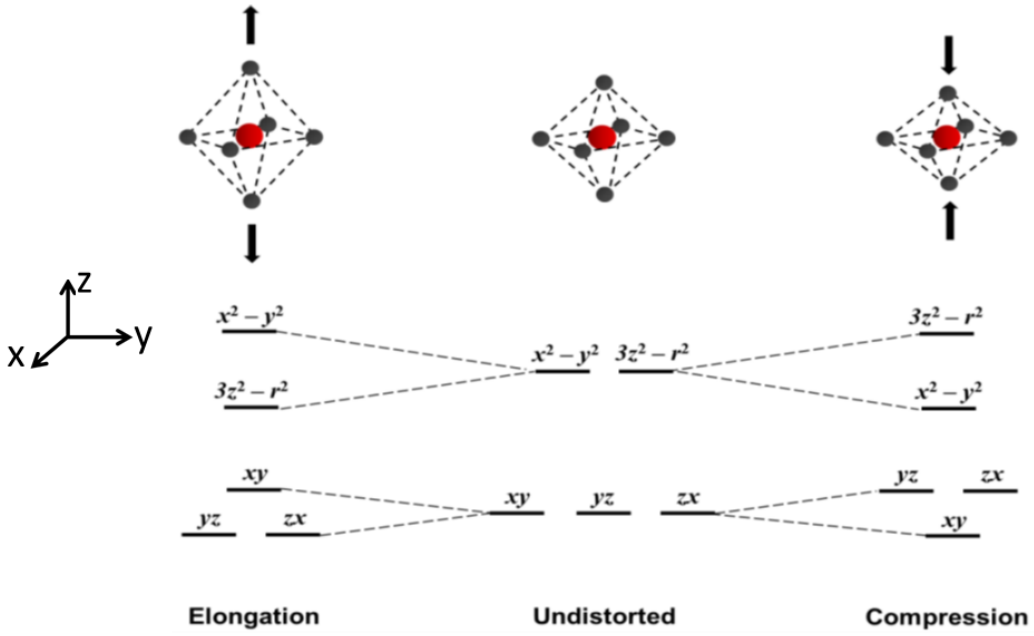

Fig. 1.4. A schematic showing how Jahn-Teller distortions to the BO_6 octahedra change the crystal field environment for a transition metal B-site cation in perovskite oxides [10].

Once the local occupation/spin state of the transition metal cation is determined, magnetic exchange interactions must be considered to determine the final magnetic ground state (*i.e.*, will the spin states of neighboring cations "talk" to one another to form a long range ferro- or antiferromagnetic state). As opposed to pure transition metal materials, where magnetic exchange interactions are dominated by direct exchange between

neighboring atoms, indirect exchange interactions of B-site cations through the bridging oxygen anions typically dominate in perovskites. Two exchange interactions of interest here are "superexchange" and "double exchange" [11]. The superexchange interaction in transition metal oxides has been treated extensively [12–14], resulting in the so-called "Goodenough-Kanamori-Anderson rules" for predicting the ferromagnetic and antiferromagnetic states of such oxides. Important considerations in determining the favored magnetic state include the octahedral rotation angle, the *d* orbital orthogonality, and the occupancy of the *d* orbital manifold.

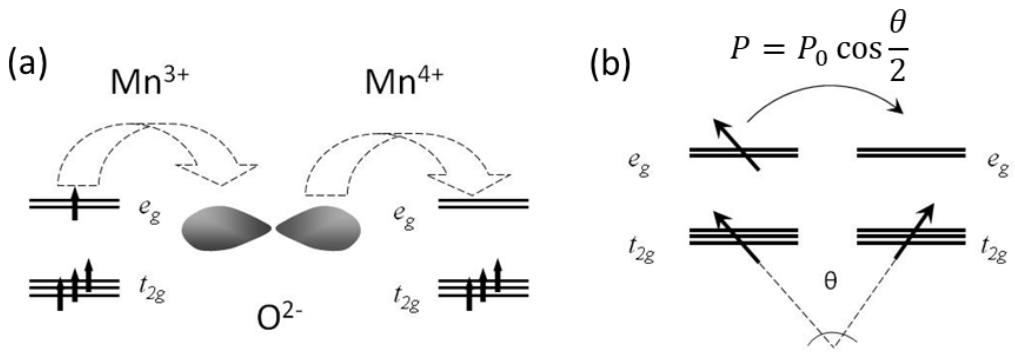

Fig. 1.5. (a) Schematic of electron transfer in a double exchange system. (b) Diagram the core spin alignment dependent probability, *P*, of an electron transfer [10]. The transfer probability is maximized when the core spins are aligned (θ = 0°) and is zero for antiparallel alignment (θ = 180°).

The double exchange interaction applies for exchange between B-site cations of different nominal valence, and describes the stabilization of ferromagnetism through the interaction of localized spin and delocalized electrons. The theory for double exchange was developed to describe the correlation of ferromagnetism and metallicity in the mixed valence manganites [15], shown schematically in Fig. 1.5. In the manganites, $\Delta_{CF} < J_H$, resulting in the high spin states for Mn^{3+} and Mn^{4+} shown in Fig. 1.5(a). Electron transport in this case occurs *via* the simultaneous transfer of the e_g electron from the Mn^{3+} to the O^{2-} and from the O^{2-} to the empty e_g state of the Mn^{4+} (Fig. 1.5(a)). The strong Hund's coupling in this system favors the alignment of the e_g electron's spin with that of the t_{2g} electrons in the same Mn^{3+} atom; therefore, parallel spin moments on neighboring Mn ions facilitates delocalization of the e_g electron, where the transfer probability (P) in some models goes as $P_0\cos(\theta/2)$, where θ is the angle between neighboring Mn ion spins (Fig. 1.5(b)) [15]. This creates a fundamental link between ferromagnetism and the conductivity in these materials,

in that ferromagnetic ordering suppresses spin fluctuations, thereby increasing transfer probability and enhancing conductivity. In a similar vein, conductivity enhancement can also be seen by applying a magnetic field, which suppresses spin fluctuations. As will be returned to later, the magnetic-field-induced conductivity enhancement possible through double exchange alone is only 50 %, however, and cannot explain the observation of colossal magnetoresistance.

As mentioned above, the choice of A-site cation can affect the underlying physics at work in the B-site *d* orbitals. Perhaps the simplest example of this comes in aliovalent substitution on the A-site. This is the strategy used to form the multivalent manganites shown in the double exchange discussion. To balance charge in $LaMnO_3$, for example, the Mn ion is in the 3+ state because of the essentially fixed oxidation states of 3+ and 2- for La and O, respectively. In contrast, the 2+ oxidation state of Sr in $SrMnO_3$ results in a Mn ion in the 4+ state. Subsequently, an alloy with 1/3 of the sites occupied by Sr (*i.e.*, $La_{2/3}Sr_{1/3}MnO_3$) would be expected to have 1/3 of the Mn ions in the 4+ state. In an ideal case, such doping would only affect the B-site valence and leave the band structure unaltered. However, the alloying element (Sr in this case) and host (La) ionic radii will undoubtedly be different, which can cause changes in B-O-B bond lengths and angles (through octahedral rotations). These structural changes lead to changes in the bandwidth which can in turn have significant influence on electronic properties such as carrier mobility and even change the electronic or magnetic ground state. In fact, isovalent A-site substitution with cations of different radii is a commonly used strategy to tune the properties of perovskites in and of itself. Similarly, oxygen non-stoichiometry (*i.e.*, the δ in $ABO_{3-\delta}$) can significantly influence the properties of perovskites by changing the electron count on the B-site cation. Oxygen vacancies, for example, are positively charged and donate two electrons to the lattice, thus decreasing the nominal B-site valence. Finally, ordered defects in the basic perovskite structure lead to entirely new perovskite-derived crystal structures. One example is the high-temperature superconducting system $La_{2-x}Sr_xCuO_{4-\delta}$, which clearly has a different stoichiometry from the prototypical ABO_3 perovskite. As shown in Fig. 1.6, this material adds an extra layer of (La,Sr)O compared to the usual perovskite structure, resulting in the so-called $n = 1$ Ruddlesden-Popper crystal structure.

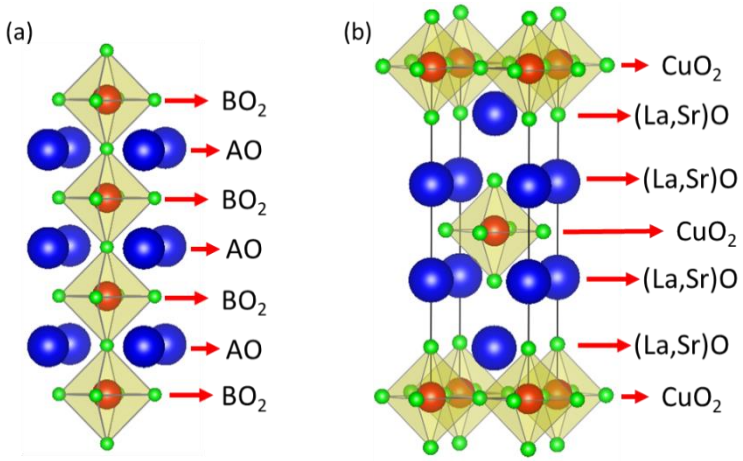

Fig. 1.6. Schematic showing the layer by layer stacking in (a) a prototypical ABO_3 perovskite and (b) in a so-called n = 1 Ruddlesden-Popper crystal structure observed in $La_{2-x}Sr_xCuO_{4-\delta}$.

1.1.2 *Thin films and heterostructures*

The chemical doping strategies of bulk perovskites highlighted in the previous section result in an essentially endless parameter space for rational materials design. Incredibly, the possibilities are expanded exponentially in perovskite oxide thin films and heterostructures. Key in this regard is the ability to control such a vast set of properties in the single perovskite building block, which allows for the growth of epitaxial films and heterostructures of an infinite variety (shown schematically in Fig. 1.7). The ability to integrate different perovskites in thin films and heterostructures adds powerful new "knobs" for controlling electronic and magnetic properties. The first of these new control strategies is the use of lattice mismatch, with lattice parameters (*i.e.*, the edge length of the cubic unit cell in Fig. 1.1(a)) of perovskites varying from 3.7 to 4.2 Å. Accommodation of the lattice mismatch in an epitaxial perovskite film grown on a single crystalline substrate can happen in a variety of ways, but perhaps the simplest is a resultant strain in the film (*i.e.*, the film stretches or compresses from its bulk equilibrium structure to match the substrate lattice). Importantly, strains up to a few percent can be achieved in thin films, which is at least an order of magnitude larger than that achievable in bulk perovskite samples. Strain can thus be used to significantly modify, or even lead to bulk-inaccessible, ground states in perovskite thin films. A powerful demonstration comes in tensile-strained-$SrTiO_3$ (STO) films, in which a ferroelectric ground state not observable in the bulk can be stabilized up to room temperature [16].

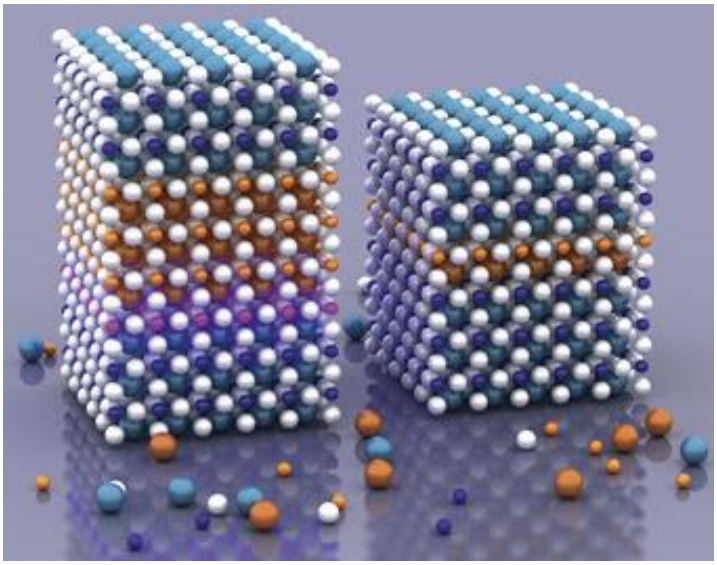

Fig. 1.7. Schematic [17] showing how the single perovskite building block allows for different perovskite oxides (represented by cations of different colored balls and oxygen anions as white balls) can be seamlessly integrated in thin films and heterostructures. The stack on the left represents an interfacial state (*e.g.*, the two-dimensional electron gas at the $LaAlO_3/SrTiO_3$ interface) by highlighting the B-site cations in pink.

The second control strategy provided by heterostructuring of perovskite oxides is simply the ability to integrate two materials with different functionalities with atomic precision. This allows for the exciting prospect of rationally engineered multifunctionality within a single heterostructure sample. For example, the growth of a ferromagnetic film on a ferroelectric substrate (or underlayer) could artificially create a multiferroic sample, of which there are few examples in bulk materials alone [3]. Beyond combining two different bulk-like functionalities, the *discovery* of novel electronic and magnetic states at the interface between two perovskites has been an extremely prolific area of research. The premier example in this case is the two-dimensional electron gas (2DEG) formed at the interface between the two band insulators, $LaAlO_3$ (LAO) and STO [18], where the polar nature of LAO causes electron transfer to the STO lattice across the interface. The resulting 2DEG, which is shown schematically in Fig. 1.7, has interesting superconducting and magnetic properties that have been studied extensively since its discovery in 2004 [18,19]. These rational design strategies in perovskite oxide heterostructures not only open up novel electronic device concepts, but also make powerful fundamental research opportunities possible.

1.1.3 External control

The final attribute making perovskite oxides an attractive materials class (at least of those I will discuss here) is the ability to control their properties with external fields. Perhaps the most extensively researched area in this regard is the colossal magnetoresistance (CMR) effect observed in the manganites [5], so-named to differentiate it from the Nobel-Prize-winning giant magnetoresistance (GMR) effect. While research on the manganites started in the 1950s [20], efforts surged in the 1990s after it was discovered that magnetic fields could induce changes in the resistivity of these materials by factors up to 10^8 [5]. Basically, the application of magnetic field causes large decreases in resistivity, and can even induce an insulator to metal transition in manganites of the right composition [5]. While the double exchange mechanism discussed previously is consistent with decreased resistivity of mixed-valence manganites in magnetic fields, it cannot exceed 50 % MR values and thus cannot account for the "colossal" magnitude of CMR.

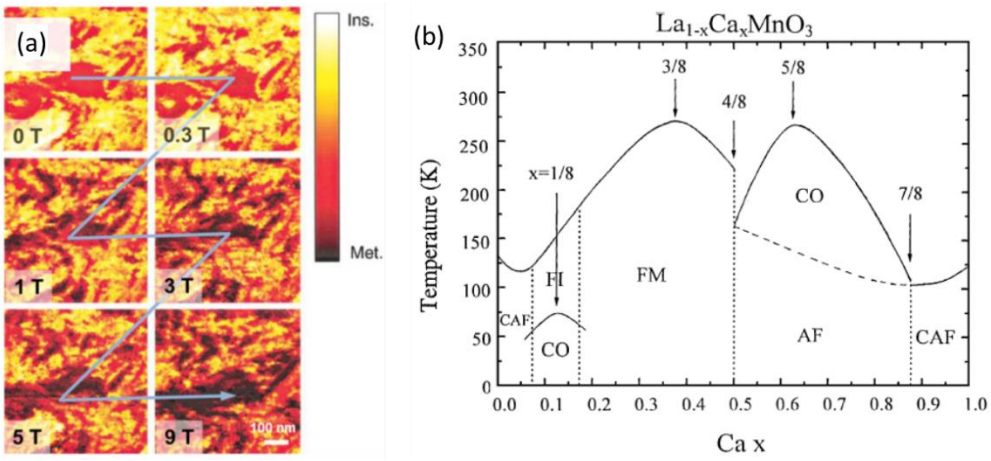

Fig. 1.8. (a) Differential conductance map [21] of a $La_{0.73}Ca_{0.27}MnO_3$ thin film showing magnetoelectronic phase separation with spatial coexistence of insulating (bright) and metallic (dark) regions just below the Curie temperature, as well as its suppression under large magnetic fields. (b) Phase diagram of $La_{1-x}Ca_xMnO_3$ [5]. FM: ferromagnetic metal, FI: ferromagnetic insulator, AF: antiferromagnetic, CAF: canted AF, and CO: Charge/orbital ordering.

Critical in regard to explaining this large magnitude is the existence of inhomogeneous magnetic and electronic states in these manganites, despite being chemically homogeneous, which is a phenomenon called "magneto-electronic phase separation" (MEPS). Competition between two phases close in energy, such as the ferromagnetic and paramagnetic phases near the Curie temperature (T_C) in $La_{0.73}Ca_{0.27}MnO_3$ shown in Fig.

1.8(a) [21], results in a spatial coexistence of both phases. Application of a magnetic field favors the ferromagnetic metallic phase (also shown in Fig. 1.8(a)), which can lead to the percolation of previously isolated metallic clusters, and a subsequent decrease in resistivity [5]. The MEPS shown in Fig. 1.8(a) exists on *nanometer* length scales, which can lead to a factor of 10 decrease in resistivity. At higher doping values in typical manganites (typically ~0.5 as shown in Fig. 1.8(b) [5]), competition between a ferromagnetic phase and an antiferromagnetic or charge/orbital-ordered phase with MEPS on *micron* length scales leads to the many orders-of-magnitude decrease in resistivity with applied fields (*i.e.*, the "colossal" magnitude of CMR). The discovery of the CMR effect immediately attracted attention for potential applications as sensors in magnetic recording; unfortunately, however, relatively large fields (> 1 T) are required to observe such dramatic effects, ruling the manganites impractical for use in magnetic recording. Regardless of the practicality in eventual applications, the CMR effect demonstrates nicely how the subtle phase competition common in perovskite oxides can be susceptible to minor external perturbations, leading to strong resultant changes in properties.

While external control of bulk perovskite properties through CMR-like effects can be powerful, the use of multifunctional heterostructures opens the door to many new strategies. The development of artificial multiferroic devices, for example, has been heavily pursued [3]. The general strategy in such multiferroic heterostructures has been the combination of ferromagnetic perovskites with piezo- or ferroelectric perovskites. Applying voltages to the piezoelectric or ferroelectric components causes changes in their lattice parameter or electric polarization, respectively, which can significantly affect the magnetic properties of the ferromagnetic layer. In fact, the general research area of such "voltage-controlled magnetism" is being heavily pursued in many different materials with a host of strategies, as it could prove crucial in the development of ultra-low power spintronic technologies. Successes outside the world of perovskite oxides include voltage-assisted switching in spin orbit torque devices [22] and magnetoionic control of the perpendicular magnetic anisotropy of ultrathin Co films [23]. Successes within the perovskite community include voltage-controlled: (a) exchange bias in $BiFeO_3$ (an antiferromagnetic ferroelectric)/$La_{0.7}Sr_{0.3}MnO_3$ heterostructures [24], (b) spin polarization in Co/$PbZr_{0.2}Ti_{0.8}O_3$/ $La_{0.7}Sr_{0.3}MnO_3$ magnetic tunnel junctions [25], and (c) T_C in

$PbZr_{0.2}Ti_{0.8}O_3/La_{0.8}Sr_{0.2}MnO_3$ field effect transistors [26–28]. These examples utilize the switchable polarization of the ferroelectric layer to change the electric field applied to the $La_{1-x}Sr_xMnO_3$ layer, affecting the ferromagnetic properties.

1.2 Electrolyte gating

Another appealing approach to controlling the magnetic properties of a material with a voltage is the use of more standard field-effect structures, such as metal-oxide-semiconductor field-effect transistors (MOSFETs). A MOS junction under different applied gate voltages (V_g) is shown in Fig. 1.9; applied between the metal gate electrode and the semiconductor, V_g can tune the carrier density and type in the semiconductor *via* the electric field it induces across the oxide. The ability of the oxide to act as an insulating dielectric, therefore sustaining the electric field without allowing current to leak through it, is the key to achieving charge density control in the semiconductor. Typical oxide dielectrics, such as SiO_2, can induce interfacial charge densities in the semiconductor up to 10^{13} cm^{-2}, and are limited from reaching higher values by dielectric breakdown [26,29,30]. In semiconductors such as Si, changes in charge density of 10^{13} cm^{-2} leads to many orders of magnitude change in conductivity, thus making MOSFETs extremely relevant in data processing and storage technologies (we all currently carry ~1 billion MOSFETs in our cell phones).

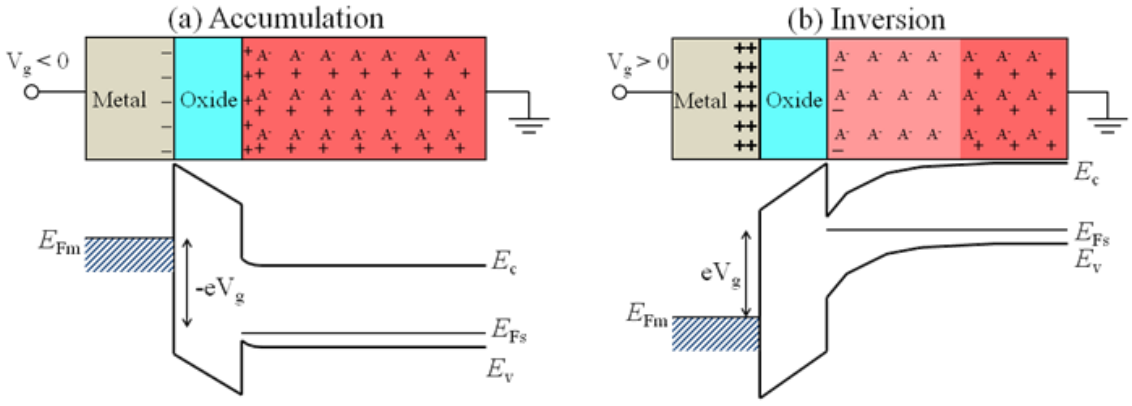

Fig. 1.9. (a) Accumulation regime of a MOS capacitor showing hole accumulation at the *p*-type semiconductor interface. (b) Inversion regime showing electron accumulation. Delocalized holes and electrons are signified using +/- symbols respectively. A^- symbols represent acceptor ions in the *p*-type semiconductor. E_{Fm} and E_{Fs} mark the Fermi levels of the metal and semiconductor respectively. E_c and E_v mark the conduction and valence band edges respectively.

While controlling the conductivity in semiconductors in MOSFETs has proven powerful, controlling the electronic and magnetic phases of materials such as perovskite oxides then becomes an appealing idea, perhaps leading to next-generation electrical device concepts [26,29,30]. Such electronic/magnetic phase control, however, cannot be achieved using standard MOSFET structures with oxide channels (Fig. 1.10(a) [26,29,30]). As shown in Fig. 1.10(b), the characteristic charge densities required to significantly affect the magnetic properties of perovskites like the manganites are in the $10^{14} - 10^{15}$ cm^{-2} regime (*i.e.*, at the level of significant fractions of an electron per unit cell, as demonstrated by phase diagrams such as Fig. 1.8(b) [26,29,30]). The charge accumulation below 10^{13} cm^{-2} in conventional MOSFETs thus falls short of the levels required to significantly affect the properties of perovskites. This is why the use of ferroelectric gate-dielectrics, which are capable of reaching the 10^{14} cm^{-2} level in field-effect structures, was crucial to the successful demonstration of electric-field-controlled magnetic properties in the studies above (Sec. 1.1.3). Recently, an appealing and potentially more versatile alternative for the controlled induction of very high surface electron/hole densities has gained momentum based on the use of *electrolyte* gate-dielectrics.

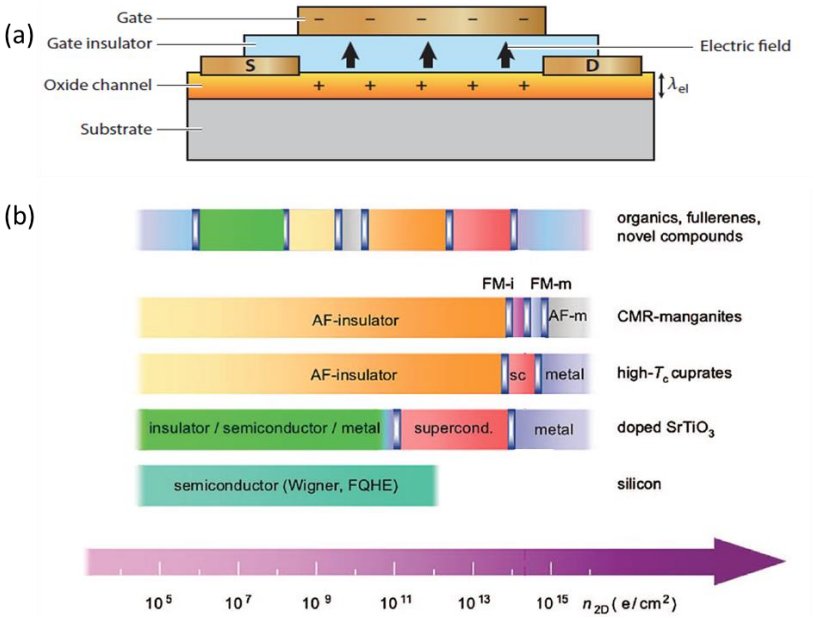

Fig. 1.10. (a) Geometry of electric-field-effect devices for electrostatically doping oxide-based channel materials, where S and D denote the source and drain electrodes, respectively [30]. (b) Illustration of the zero temperature behavior of various correlated materials as a function of sheet charge density (n_{2D}). AF, FM, I, M, SC, FQHE, and Wigner stand for antiferromagnetic, ferromagnetic, insulator, metal, superconductor, fractional quantum Hall effect, and Wigner crystal, respectively [29].

1.2.1 *Electric double layer transistor operation and successes*

The use of an electrolyte, a material made up of mobile ions typically in a solvent, as the gate-dielectric, is the key feature of this new gating technique. The relevant device is referred to as an electric double layer transistor (EDLT, Fig. 1.11(a)) [31,32,41–50,33,51–54,34–40], where V_g is applied between the electrolyte and the conductor of interest. The mobile ions of the electrolyte move under V_g, but typically cannot permeate the sample, and therefore accumulate at the electrolyte/sample interface. An equal charge density of electrons or holes (dependent on the V_g polarity) is thus induced on the sample side of the interface, completing what is known as an electric double layer, or EDL. The result is essentially a capacitor with an electrode separation of one Debye length ($\lambda_D \sim 1$ nm), resulting in giant specific capacitances (up to 10's of μFcm^{-2}), and thus very large induced charge densities [54–56]. The latter can exceed 10^{14} cm^{-2}, or even 10^{15} cm^{-2}, with electrolytes called "ionic liquids" (ILs) [57–59]. ILs are a special class of electrolytes that are *solvent-free*. Classical electrolytes consist of a salt (*i.e.*, a solid material made up of cations and anions) dissolved in a molecular solvent (*e.g.*, NaCl dissolved in H_2O). ILs, however, are salts with melting temperatures near or below room temperature (RT), such that at RT the constituent ions are mobile, even without dissolution in a solvent. Typically, ILs are made up of large, unsymmetrical organic ions, such as 1-ethyl-3-methylimidazolium bis(trifluoromethylsulfonyl)imide (EMI:TFSI) shown in Fig. 1.11(b). The odd shape of these ions makes packing into a solid salt structure difficult, thus driving the melting temperature to near or below RT.

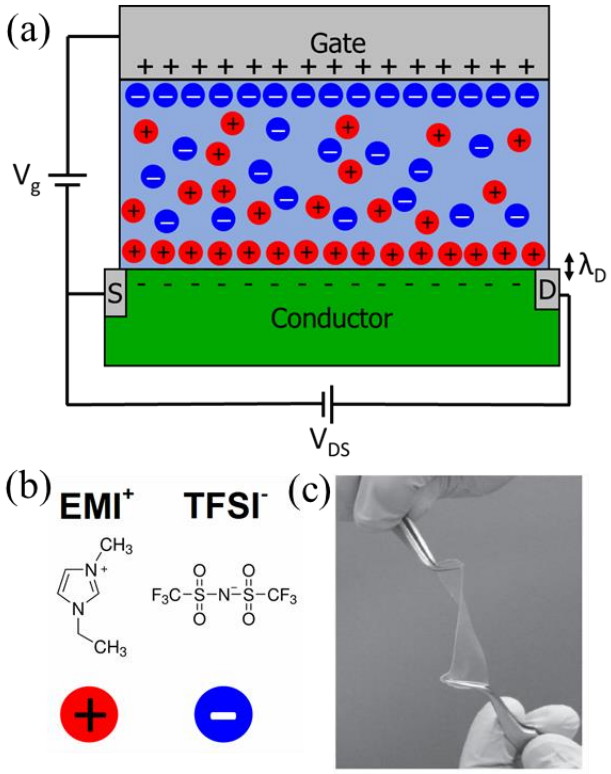

Fig. 1.11. (a) Schematic of an electric double layer transistor (EDLT). The blue area is the ionic liquid or gel, with its constituent cations/anions represented by the red/blue charges, respectively. S and D denote the source and drain electrodes, respectively. The schematic is showing a positive gate bias (V_g) and the resultant EDL formation at the gate/electrolyte and electrolyte/conductor interfaces. The characteristic Debye length (λ_D) is shown as well. (b) Molecular structures of the cation and anion of a typical ionic liquid, EMI:TFSI. (c) Optical image [55] of a "cut and stick" ion gel based on 80 wt% EMI:TFSI and 20 wt% of the polymer P(VDF-HFP).

Many attractive features make ILs a natural choice for electrolyte gating, the first being high ionic conductivity. In order for an EDLT to operate and do so quickly, ionic conductivities must be high so that EDL formation is fast. Ionic conductivities of ~10 mS/cm are typically observed in ILs, which is comparable to Li-ion conductivity in Li-ion batteries, and ~100 times larger than $LiClO_4$/poly(ethylene oxide) [57]. This high ionic conductivity makes transistor operation at frequencies as high as 10 kHz possible [43]. The second attractive feature of ILs for electrolyte gating is their wide electrochemical stability windows, with typical values near ~5 V (depends on the working electrode used; this typical value is for Pt) [57]. This means voltages up to ~5 V can be applied in EDLTs without causing electrochemical degradation of the IL ions (though, as will be returned to later, the materials being gated can be susceptible to electrochemical effects even at low

V_g). The chemical flexibility and low vapor pressure ($<10^{-12}$ Torr) make ILs practical for EDLT studies of a wide range of materials, including those that need to be studied at low temperature in evacuated environments.

Further, the recent development of so-called "ion gels" (Fig. 1.11(c)) [55,59], which move IL electrolytes to the solid state, make IL-based EDLTs even more practical. These ion gels consist of IL with a small amount of dissolved polymer (< 20 wt. %), resulting in a rubbery solid that is easy to handle and maintains high ionic conductivity and capacitance. The choice of polymer is crucial in the design of these ion gels, both in achieving the desired structural integrity (Fig. 1.11(c) demonstrates how these gels can be manipulated with tweezers) and maintaining the high ionic conductivity needed for EDLT operation. Typically, copolymers are used, with one of the copolymer substituents (or "blocks" in block-copolymers, discussed below) being soluble in the IL and the other being insoluble. For example, the polymer in the "cut-and-stick" ion gel shown in Fig. 1.11(c) is the random copolymer poly(vinylidene fluoride-*co*-hexafluoropropylene), P(VDF-HFP). The IL (EMI:TFSI) is insoluble in P(VDF), but soluble in P(HFP), thus the P(VDF) portions of P(VDF-HFP) give the ion gel structural integrity and the P(HFP) portions allow for dissolution in the IL. A particularly exciting area of research, in fact, is utilizing the nanostructuring of block-copolymers to further tune ion gels for a variety of applications, including EDLTs [59].

Based on the above, IL and ion gel gating has grown rapidly, and has been applied to a variety of materials with noteworthy results. The materials studied include molecular crystals [46,47,60], polymer semiconductors [43,53,61,62], binary oxides [31,38,41,42,50,54,56], perovskites [32–34,36,44], a variety of other complex oxides [35,37], and 2D materials from several classes [39,40,45], to name a few. These studies have demonstrated not only reversible electrical tuning of quantum and thermodynamic electronic phase transitions (*e.g.*, metal-insulator transitions [34,42,45,49,50,56] and superconductor-insulator transitions [32,35,37]), but have also enabled the discovery of interesting phenomena, such as a superconducting ground state in $KTaO_3$ (Figs. 1.12(a,b)) [36], and electric field-controlled superconductivity in MoS_2 (Fig. 1.12(c)) [39]. There is thus indication of a realm, beyond

perturbative doping, in which electrostatic manipulation of carrier densities at significant fractions of an electron/hole per unit cell induces dramatic property modification.

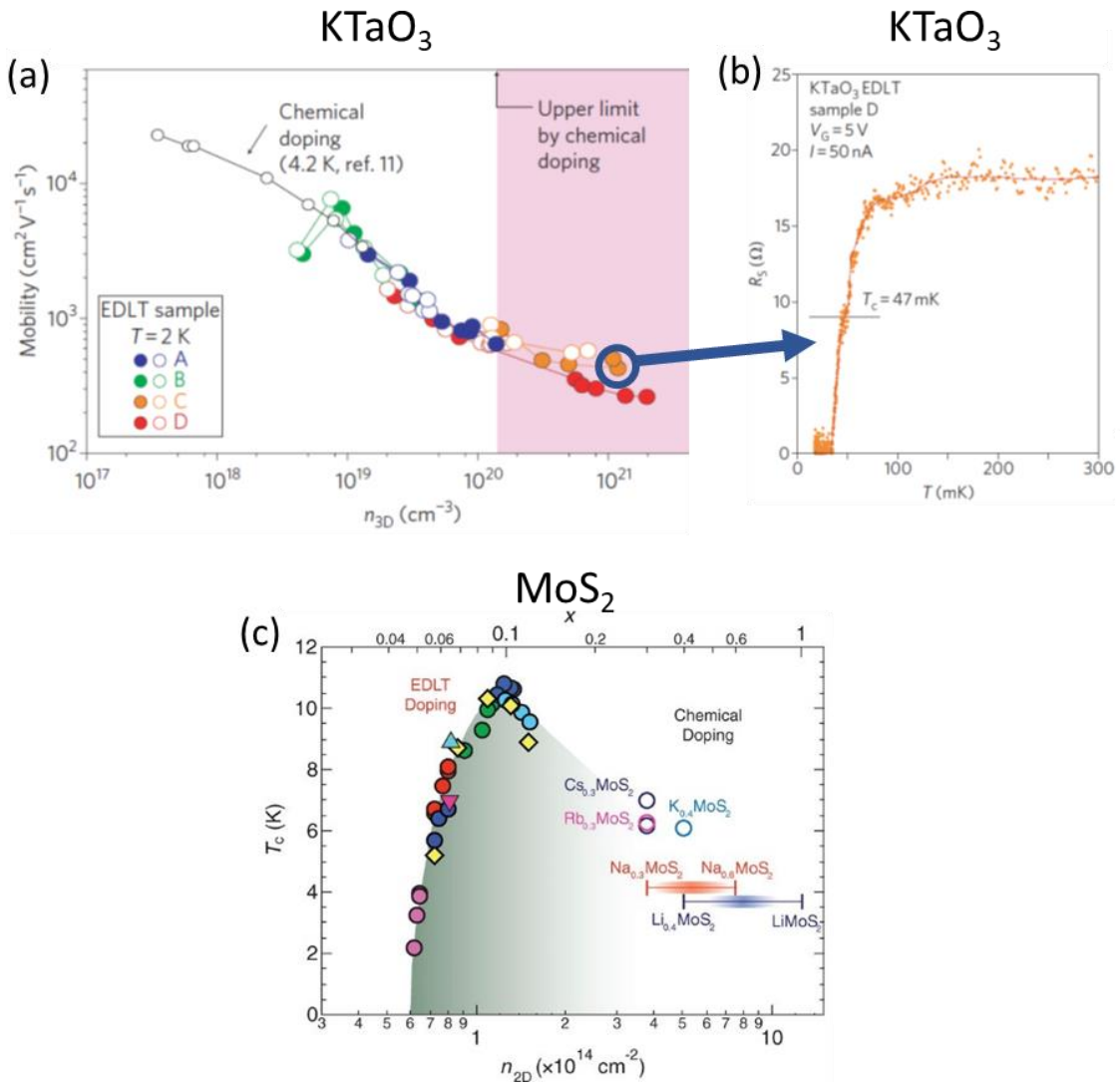

Fig. 1.12. (a) Electron mobility *vs*. three-dimensional electron density (n_{3D}) observed with the pink shading representing the region accessible only with electrolyte gating in Ref. [36]. The blue arrow points to (b) the sheet resistance (R_s) *vs*. temperature (T), which shows the superconducting state achieved with electrolyte gating that was unobtainable with chemical doping. (c) The superconducting transition temperature (T_c) *vs* two-dimensional n (n_{2D}) dome observed with electrolyte gating in MoS_2 [39] that could not be investigated with chemical doping due to issues with control at low doping levels (limited to $n_{2D} > 3 \times 10^{14}$ cm^{-2}).

1.2.2 *Open questions*

There are, of course, open questions that remain to be addressed with this promising technique. A particularly pressing area in this regard is the poor understanding of the doping mechanism active in electrolyte gating of different materials. The simple electrostatic charge accumulation in the EDLs discussed above, in fact, has been called into question in many systems where evidence for *electrochemical* doping is strong. For example, in the field of organic conductors, it is now generally accepted that electrolyte-gated devices operate predominantly electrostatically for some materials (*e.g.*, single crystals of small molecule semiconductors) [46,47], but electrochemically for others (*e.g.*, semi-crystalline thin film polymer semiconductors) [53]. Due to the tight molecular packing in single crystal organic semiconductors (*e.g.*, rubrene [46,47]), they are impermeable to the IL ions, resulting in the simple electrostatic EDL picture shown in Fig. 1.11(a). The relatively open structure of semi-crystalline polymers (*e.g.*, P3HT [53]), in contrast, allow for permeation of the ions, resulting in a more 3D "electrochemical" doping compared to the 2D electrostatic doping observed in the single crystalline organics. Identifying differences in doping mechanisms is crucial to understanding gating effects and their tunability, reversibility, and reproducibility, and most material systems are far behind the understanding established in electrolyte-gated organics.

Differentiating electrostatic *vs.* electrochemical operation in oxide EDLTs [44,48–52,63–66], which are the focus of the current work, are one such example of poor understanding. While single crystalline oxides (or epitaxial oxide films) are generally accepted to be impermeable to ionic liquid ions, thus ruling out the electrochemical doping method active in semi-crystalline polymer EDLTs, other electrochemical doping effects have been suggested. A particularly high-profile example illustrates this poor understanding, and the urgency for an answer, in electrolyte-gating studies of VO_2. In 2012, Nakano *et al*. reported impressive control of the metal-insulator transition in VO_2 films, including control of the transition temperature from 0 to 330 K, as shown in Fig. 1.13 [42]. Importantly, Hall effect measurements in EDLTs with different VO_2 film thickness suggested that the electrostatic accumulation of electrons on the surface was driving delocalization of carriers in the *bulk* of the film (shown schematically in Fig. 1.13(b) [42]).

The authors proposed that they had achieved the long sought after "Mott transistor," in which electrostatic accumulation of a small number of carriers in a strongly correlated material (such as VO_2) could drive pre-existing localized carriers to be mobile [42].

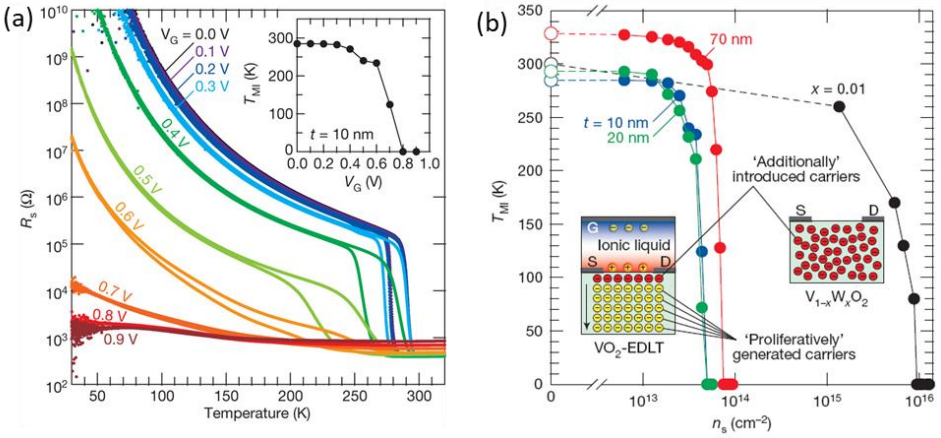

Fig. 1.13. (a) Temperature dependence of the sheet resistance (R_s) for a 10-nm strained VO_2 film with different gate biases in different colors [42]. The inset shows the transition temperature (T_{MI}), which is the average of the two inflection points for cooling and warming in plots of d[ln(R_s)]/d(1/T) *vs.* T. (b) T_{MI} plotted against sheet charge density (n_{2D}) for both VO_2 EDLTs and 40-nm $V_{1-x}W_xO_2$ films [42]. The insets schematically illustrate the nature of the metallic state in each case, with red and yellow dots representing 'additionally' introduced carriers (that is, n_s) and 'proliferatively' generated carriers, respectively.

However, work by Jeong *et al*. the following year brought this gating mechanism into question [50]. The authors demonstrated similarly powerful control over the metal-insulator transition, but also showed that the positive-V_g-induced metallic state could be suppressed when the device was operated in high ambient O_2 pressures (shown in Fig. 1.14(a)) [50]. Further, using V_g cycling experiments in the presence of heavy $^{18}O_2$ in tandem with secondary ion mass spectrometry measurements, they demonstrated uptake of ^{18}O into the VO_2 films (shown in Fig. 1.14(b)) [50]. All of this evidence pointed to electron doping *via* oxygen vacancy (V_O) formation (as opposed to simple electrostatic electron accumulation) under positive V_g, which could be suppressed in O-rich atmospheres (possibly due to the saturation of the ionic liquid with O_2) and, because the effect was reversible, eventually lead to the uptake of ^{18}O upon cycling V_g. Essentially, under positive V_g, the electric field is oriented in the correct direction for O^{2-} removal from the film and, due to its large magnitude (10s of MV/cm), O^{2-} removal is quite reasonable. Importantly, this V_O formation could be occurring deep in the film as the length scale involved is no longer the electronic screening length, but rather V_O diffusion length. Importantly, V_O

diffusion can be significant in oxides such as VO_2 and, therefore, be responsible for the bulk doping observed by Nakano *et al.*, nullifying the proposed achievement of a Mott transistor.

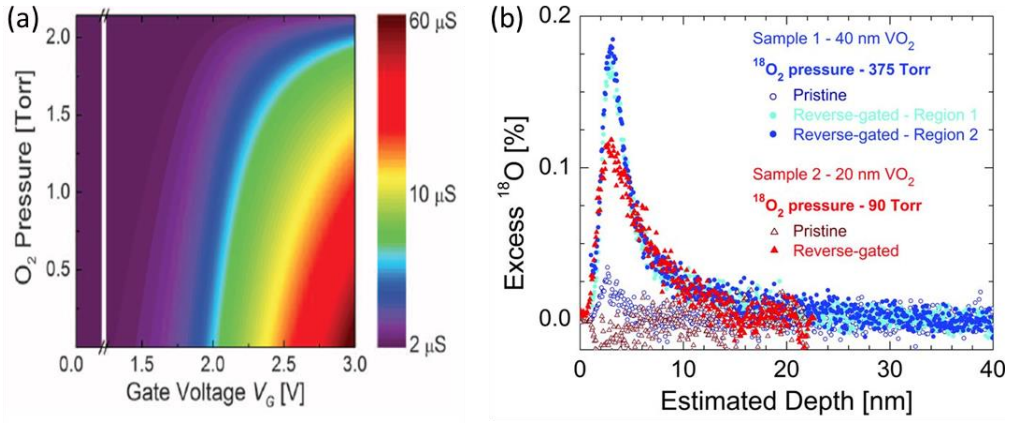

Fig. 1.14. (a) Sheet conductance (color scale) as a function of gate voltage (V_G) and O_2 pressure for an electrolyte gating device using a 20-nm-thick VO_2 film on $Al_2O_3(10\bar{1}0)$ and operated at 300 K [50]. (b) Excess ^{18}O concentration above the natural abundance (~0.2 atomic %) *vs*. depth determined by secondary ion mass spectrometry for two electrolyte-gated VO_2 films (20 and 40 nm thick) on $Al_2O_3(10\bar{1}0)$ [50]. The devices were gated to the metallic state in vacuum and reverse-gated in $^{18}O_2$ to recover the insulating state. Data are compared to pristine channels on the same wafer that were not gated but were subjected to the same dosage of $^{18}O_2$.

The generality of electrostatic *vs.* electrochemical operation in oxide EDLTs, therefore, is an important question to address. Similar suppression of gating effects in high O_2 ambient environments for other *n*-type oxides (*e.g.*, STO [51] and TiO_2 [52]) have been reported. Further, other electrochemical effects, such as V_g-induced cation diffusion (including H^+ [63,66] and the constituent cations of the host channel [67]), have also been reported in oxide EDLTs. One impediment to improved understanding of electrolyte gating mechanisms is the dearth of available probes beyond electronic transport. Electronic transport is dominant in the field, with other more direct probes, such as spectroscopy and scattering, being challenging to implement in EDLTs. Difficulties include the small volume of gated material, and the thick overlying ion gel or ionic liquid, which induce absorption and scattering. Few demonstrations of *in operando* scattering or spectroscopy of electrolyte-gated oxides have thus appeared, although this now appears to be changing. Synchrotron X-ray diffraction (SXRD) results on ionic-liquid-gated VO_2 [68], $La_{2-x}Sr_xCuO_4$ [69], $SrCoO_{2.5}$ [63], WO_3 [66], and $NdNiO_3$ [64] have recently appeared, along with X-ray absorption on $YBa_2Cu_3O_{7-x}$ [65] and $NdNiO_3$ [64]. Noteworthy findings

emerge from these studies, including giant V_g-induced lattice expansion in VO_2 [68], deoxygenation of $YBa_2Cu_3O_{7-x}$ under positive V_g [65], three-phase switching of (H)$SrCoO_{3-\delta}$ [63], and gate bias polarity asymmetry in $NdNiO_3$ [64]. *In operando* probes have thus yielded substantial insight, and additional work is clearly desirable, particularly with techniques capable of detecting V_O formation quantitatively, with spatial resolution.

A final point, which applies to oxides but also more generally in electrolyte gating, is that while phenomena such as insulator-metal transitions and superconductivity have attracted much attention in EDLTs, the potential of this approach for the understanding and manipulation of *magnetic* order and properties is not so well understood. Work in this regard is starting to gather steam, with results reported on electrolyte-gate-control of magnetic properties in manganites [33,70], cobaltites [63], $SrRuO_3$ [44], and $Ti_{1-x}Co_xO_2$ [38]. However, it remains unclear what magnitude of gate-induced effect can be generally expected in quantities such as the T_C, magnetization, coercivity, anisotropy, *etc*. Further, strategies to optimize such gate-induced changes are completely absent. Additionally, how electrolyte gating performs in comparison to other emerging approaches to electric field control of magnetism is also not well understood, examples being electric field control of magnetic anisotropy and switching in tunnel junctions [22], or ultrathin film perpendicular magnetic anisotropy heterostructures [23].

In summary, there are three open issues on electrolyte gating which will be the focus of this thesis work:

1. Poorly understood electrostatic *vs.* electrochemical gating mechanisms, particularly with respect to oxygen vacancy formation in oxide EDLTs.
2. A general lack of *in operando* probes.
3. The universality of the approach with respect to control of magnetic material properties.

Note that there are other unknowns to be addressed in the electrolyte gating technique, including the differences between conventional 3D chemical and 2D electrostatic doping, the location of the induced charges (with respect to interface proximity, energy, and orbital occupation), and the potential role of EDL-induced electrostatic disorder. While addressing these unknowns will be important, they are not directly addressed in this work.

1.3 $La_{1-x}Sr_xCoO_{3-\delta}$ background

In this thesis, EDLTs based on epitaxial thin films of $La_{1-x}Sr_xCoO_{3-\delta}$ (LSCO) will be used to address the open questions on electrolyte gating summarized in the previous section. In order to appreciate the reasons why LSCO is an ideal material system to explore these questions, some background on LSCO is warranted. In this section I will review the basic chemistry and physics of both the bulk and thin film forms of LSCO, with particular emphasis on how its properties make it well-suited for EDLT studies.

1.3.1 *Bulk*

The $x = 0$ parent compound of the LSCO system, $LaCoO_3$ (LCO), has a $\Gamma \approx 0.88$ (the ionic radius of Co^{3+} depends on the spin state, which is complicated and discussed below), leading to distortions of the CoO_6 octahedra. Rhombohedral symmetry ($R\bar{3}c$) is observed at room temperature, a result of cooperative rotation and compression of the CoO_6 octahedra along the pseudocubic <111> axis [71]. The rhombohedral unit cell is shown in Fig. 1.15, including its defining lattice parameters, the edge length (a_R) and the rhombohedral angle (α_R). Also shown in Fig. 1.15 is the pseudocubic lattice parameter (a_c), which is related to a_R by $a_R = a_c\sqrt{2}$ ($\alpha_R = 60°$ for a cubic lattice). The values of these rhombohedral lattice parameters at 300 K for LCO ($a_R = 5.37$ Å, $\alpha_R = 60.8°$) result in a O-Co-O bond angle of 163.7° [71].

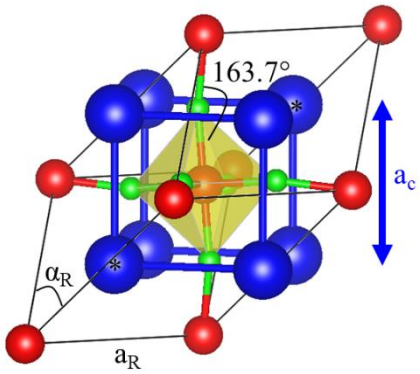

Fig. 1.15. The rhombohedral ($R\bar{3}c$) unit cell of $LaCoO_3$, where the blue/red/green spheres represent La/Co/O ions, respectively. The rhombohedral unit cell is outlined with a black line, with the rhombohedral lattice parameter ($a_R = 5.37$ Å) and angle ($\alpha_R = 60.8°$) shown. The Co-O-Co bond angle of 163.7° is shown. The pseudocubic unit cell and its lattice parameter ($a_c = 3.805$ Å) are also shown (blue lines) and, because α_R isn't far from the 60° required for the cubic structure, it remains pretty recognizable. Note that only the La ions labelled with the * are inside the rhombohedral unit cell, the others are outside, but were included so the pseudocubic unit cell could be visualized.

The valence state of Co in LCO is 3+, resulting in six electrons occupying the Co *d* orbitals. Interestingly, the crystal field and Hund's energies in these cobaltites are quite similar, making the *d* orbital occupation of these six electrons non-trivial and leading to so-called spin state transitions (SSTs). In LCO the crystal field splitting is slightly larger than Hund's coupling, quantified by the so-called "spin gap" of ~10 meV [72]. Therefore, LCO is in the LS state with all six *d* electrons filling the t_{2g} states at 0 K (as shown in Fig. 1.3) and is a diamagnetic insulator. The thermal energy provided by warming above ~30 K, however, leads to the promotion of some t_{2g} electrons to e_g states and results in finite spin (*i.e.*, the "SST"), as shown in Fig. 1.3. This SST persists up to ~100 K and LCO remains insulating, until an insulator-metal transition is traversed at ~500 K [73,74]. Despite extensive research, the exact spin state evolution between 30-500 K remains unclear, with researchers disagreeing on whether the Co^{3+} ions are in the IS or HS states [71,72,81,73–80]. In fact, the strong hybridization of Co – O bonds may even cause these simple atomic spin state models to be invalid. Regardless of these subtle details, the Co ions in LCO have finite spin above ~30 K. Importantly, no long-range ordering of these finite spins is observed, resulting in paramagnetic behavior.

Substitution of Sr for La leads to modifications of the rhombohedral crystal structure and electronic/magnetic ground states observed in LCO. Beginning with structure, the introduction of Sr gradually increases the lattice parameter and reduces α_R, the latter eventually reaching the cubic value of 60° at $x \approx 0.5$. Therefore, the crystal symmetry of LSCO is $R\bar{3}c$ for $x \lesssim 0.5$, and $Pm\bar{3}m$ for $x \gtrsim 0.5$ [82]. These changes are driven by the slightly larger ionic radius of Sr^{2+} compared to La^{3+}. Electronically, Sr doping increases the nominal valence of Co to the formal 4+ state (*i.e.*, hole dopes the system). Importantly, with one less *d* electron, Co^{4+} has finite spin even in its LS state (spin quantum number, $S = 1/2$), leading to drastic changes in magnetic properties. At low doping levels ($x < 0.05$) the Sr dopants are isolated, as are the corresponding Co^{4+} ions. These isolated Co^{4+} ions interact with their six Co^{3+} neighbors, however, inducing finite spin states in these Co^{3+} ions and lead to the so-called "seven-site magnetic polarons" shown in Fig. 1.16 [72,83–86]. The spin quantum number for these magnetic polarons are quite large, with *S* values between 10 and 16 reported [72].

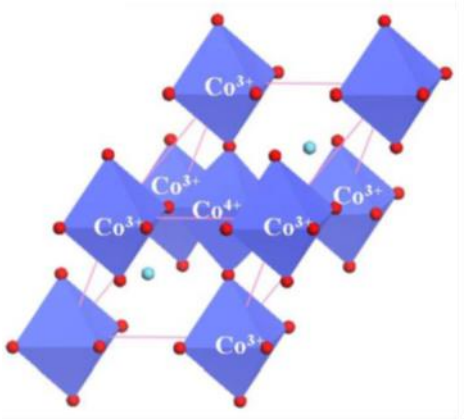

Fig. 1.16. Schematic of the seven-site magnetic polaron found in $La_{1-x}Sr_xCoO_3$ at low x [84].

Simple percolation arguments suggest these magnetic polarons should percolate at $x \sim 0.05$, resulting in interacting polarons and a transition to long-range ferromagnetic (FM) behavior for $x > 0.05$ [87]. While short-range order is observed in hole-rich FM metallic (FMM) clusters (~6-8 Å in size [88]) at $x = 0.05$, the transition to long-range FM order is delayed to much higher x. This discrepancy has been attributed to magnetic frustration between these polarons, a consequence of competing antiferromagnetic (AF) superexchange interactions between Co^{3+}-Co^{3+} and the FM double exchange interactions between Co^{4+}-Co^{3+} [87]. Above $x = 0.05$ LSCO thus exhibits MEPS, with the coexistence of FMM clusters in an insulating non-FM matrix as shown in Fig. 1.17, similar to the manganites at certain doping levels as discussed in Section 1.1.3. This MEPS persists to $x_{c,LSCO} = 0.18$, where the clusters have grown in size (~20-25 Å [88]) and density to the point where they percolate (also shown in Fig. 1.17). Above this critical threshold LSCO thus exhibits long-range FMM behavior. Note that the presence of insulating non-FM regions persists up to $x = 0.22$, above which LSCO becomes a uniform (non-phase separated) FMM, as shown in Fig. 1.17.

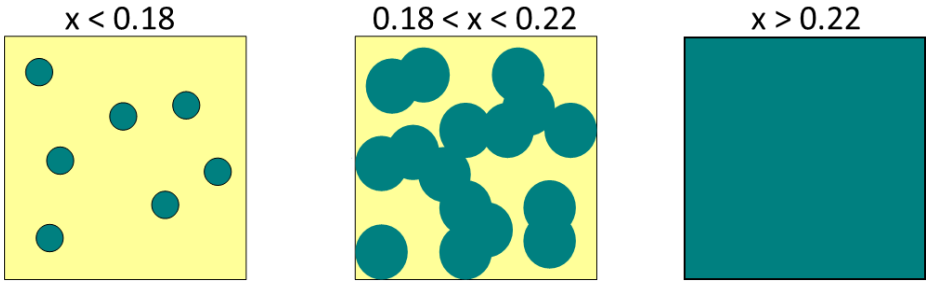

Fig. 1.17. Schematic of the magnetoelectronic phase separation observed in $La_{1-x}Sr_xCoO_3$ in different x ranges, where the lighter color represents an insulating non-ferromagnetic region and the darker color represents a ferromagnetic, metallic region.

A variety of experimental techniques were used to verify the MEPS and percolation transitions in LSCO discussed above, including small angle neutron scattering [88,89], nuclear magnetic resonance [90,91], inelastic neutron scattering [84,92], electron spin resonance [85], heat capacity [93], and magnetometry [9,89]. Important signatures in electrical transport measurements also arise, however, and will be particularly relevant to this thesis work. In the sub-percolated regime ($0.05 < x < 0.18$) the primary transport signatures are insulating behavior ($d\rho/dT < 0$, where ρ is the resistivity, shown in Fig. 1.18(a)) and the isotropic intercluster giant magnetoresistance effect (IGMR), a consequence of spin-dependent transport between isolated FM clusters [89]. The characteristic magnetic field dependence of IGMR is shown in Fig. 1.18(b) [89], with large negative *MR* persisting to high fields, which is hysteretic with the same coercivity observed in magnetometry and yields different results in virgin curves compared to subsequent field sweeps. This magnetic field dependence is described by increased alignment of neighboring clusters leading to increased transport probability, which scales with the square of the reduced magnetization [89]. The IGMR is enhanced at low temperatures, a consequence of the Coulomb energy penalty associated with individual electron-charging events, leading to a distinct form of hopping conduction [89].

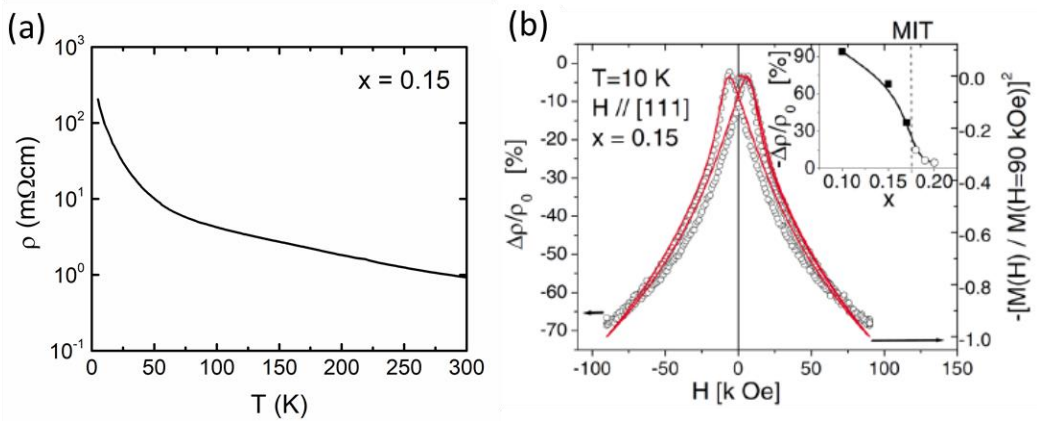

Fig. 1.18. [89] (a) Temperature (T) dependence of resistivity (ρ) for an $x = 0.15$ $La_{1-x}Sr_xCoO_3$ (LSCO) single crystal. (b) 10 K magnetoresistance ($\Delta\rho/\rho_0$, open symbols, left axis) of an $x = 0.15$ LSCO single crystal *vs*. magnetic field (H) applied along the [111] crystal direction and perpendicular to the sample plane. Also shown by the red line is the square of the reduced magnetization, $-[M(H)/M(H = 90\ \text{kOe})]^2$ (right axis). The inset shows the evolution of the magnetoresistance with x.

The primary transport signatures in the uniform FM doping regime ($x > 0.22$) are shown in Fig. 1.19(e) and (j) [94]. As expected, metallic behavior ($d\rho/dT > 0$) is observed, as shown in Fig. 1.19(e), with an inflection point near the FM $T_C \approx 230$ K. Again, the *MR* is negative and hysteretic at low temperatures (below T_C), but this *MR* is *anisotropic*. Negative *MR* is observed when the current is flowing perpendicular to the magnetic field, whereas positive *MR* is observed when the current is parallel to the magnetic field [95]. This is described by the conventional anisotropic magnetoresistance (AMR) effect, which is observed in all FMs, and is a consequence of spin orbit coupling [96]. The AMR effect scales with the magnetization and consequently decreases as temperature increases, disappearing above T_C. The second transport signature in the uniform FM region is the peak in $-MR(T)$ observed in large fields near T_C, as shown in Fig. 1.19(j) [94]. This effect is described by field suppression of spin disorder scattering in the FM metal near T_C, is isotropic, and similar to the CMR effect observed in the manganites, but is far smaller in magnitude. It turns out these cobaltites lack a key requirement to make this MR effect "colossal," which is a strongly insulating phase in competition with the FMM phase, such as the AF, charge, or orbital ordered phases observed in the manganites [5]. Finally, in the percolated yet phase separated regime ($0.18 < x < 0.22$) metallic conduction is observed below T_C, weakly insulating is observed above T_C, and all three of the MR mechanisms are active. Both IGMR and AMR are observed at low temperature, as is the CMR-like negative MR near the T_C for the percolated FMM pathway.

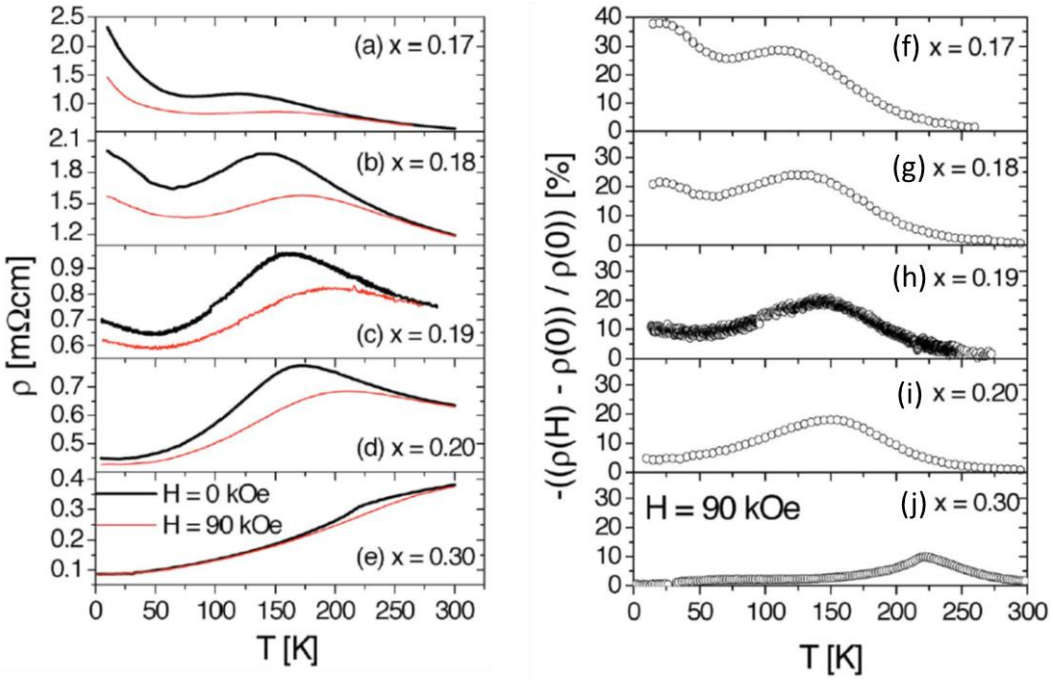

Fig. 1.19. [94] Temperature (*T*) dependence of (a-e) the resistivity (ρ) and (f-j) the negative magnetoresistance ($-\Delta\rho/\rho_0$) in a 9 T magnetic field (*H*) for $La_{1-x}Sr_xCoO_3$ single crystals with x = 0.17, 0.18, 0.19, 0.20, and 0.30, respectively.

The last item regarding bulk LSCO that will be important in this thesis is the stability of Co^{4+}. The effects of Sr doping to this point have been described by an increase in valence of a commensurate number of Co^{3+} to Co^{4+}. While this simple presentation is useful for understanding the basic physics at work in both the SST in LCO and the percolation transition in LSCO, it neglects two key details. The first of these has to do with the strong hybridization of Co 3*d* and O 2*p* orbitals in LSCO. Strong evidence has been compiled that a negative charge transfer gap exists, suggesting the Sr-doping-induced holes may actually reside in O 2*p* states (*i.e.*, ligand holes) rather than on the Co (which is supposed to be what drives the valence from 3+ to 4+) [97]. For the majority of the above discussion and the rest of the thesis, this subtle difference is slightly semantic as all of the arguments hold if one simply replaces "Co^{4+}" with "Co^{3+} and O-2*p*-hole". The second detail concerning Co^{4+}, which is much more important in regard to this thesis work, is its general instability in the octahedral environment in LSCO. The instability of Co^{4+} was demonstrated as early as 1953 by Jonker and van Santen [98], as shown in Fig. 1.20. Upon Sr doping at low levels the nominal Co valence increases commensurately, as expected, but deviates from the 1:1 line above $x \approx 0.5$ at 1200° C synthesis temperatures. At these high Sr concentrations,

LSCO spontaneously forms V_Os that compensate the hole doping by donating two electrons back to the lattice, resulting in an effective doping level of $x_{eff} = x - 2\delta$, where δ represents the oxygen deficiency in the chemical formula $La_{1-x}Sr_xCoO_{3-\delta}$. In fact, the first $SrCoO_3$ single crystal was only just synthesized in 2011 and required extremely high oxygen pressures (65,000 atm) and the presence of the oxidizing agent $KClO_4$ [99]. Therefore, formation of V_Os in LSCO is quite facile, particularly at high x.

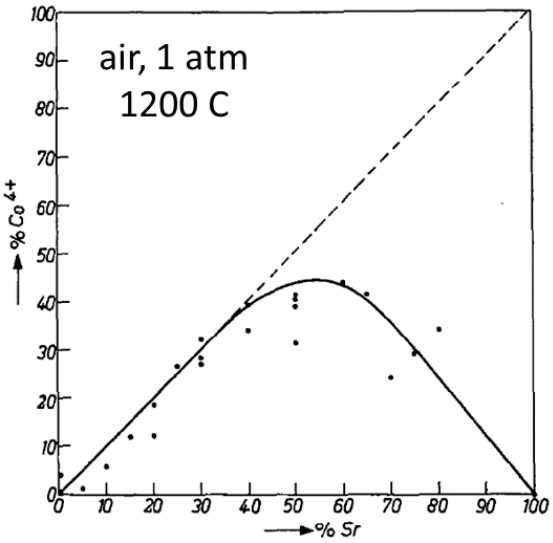

Fig. 1.20. The amount of Co^{4+} observed in $La_{1-x}Sr_xCoO_{3-\delta}$ synthesized in air at 1200°C as a function of Sr content [98].

1.3.2 *Films*

As discussed in Section 1.1.2, a lot of interesting physics and engineering science becomes accessible in perovskite oxide films and heterostructures, and the cobaltites are no exception. A great example lies in epitaxial films of LCO. Despite being non-FM in the bulk, epitaxial LCO films grown under tensile lattice mismatch (*i.e.*, the single crystalline substrate lattice parameter is larger than LCO) exhibit FM order with $T_C \approx 80$ K [100–104]. A variety of explanations for this mismatch-stabilized FM state in LCO have been put forth, including simple strain-stabilization of finite spin states with superexchange-induced FM coupling [104] and ideas reliant on the presence of defects such as cation non-stoichiometry [100] and/or oxygen vacancies (that are possibly ordered, which is discussed in detail below) [101–103]. No consensus has been reached, however, and much research on LCO films is ongoing.

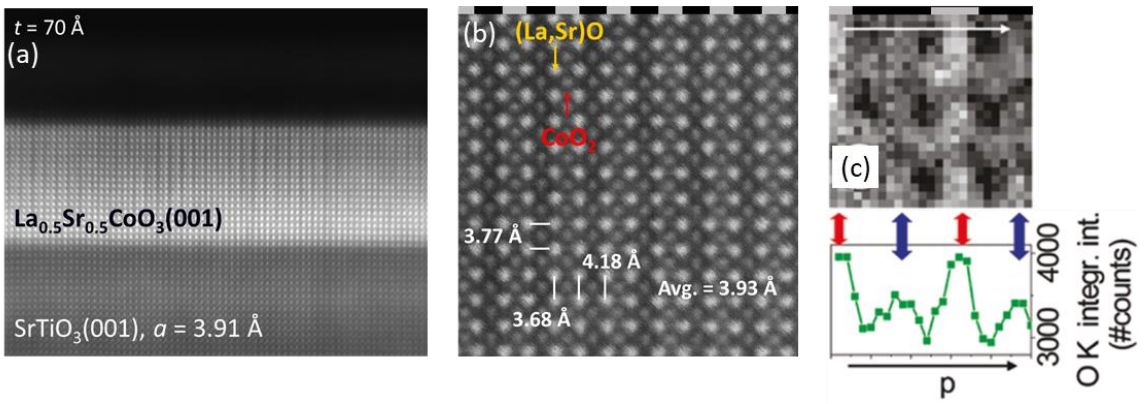

Fig. 1.21. High resolution Z-contrast scanning transmission electron microscopy images of $x = 0.5$ $La_{1-x}Sr_xCoO_{3-\delta}$ (LSCO) films grown on $SrTiO_3(001)$ [105], the whole 70 Å-thick film shown in (a) and a zoomed in image of just the LSCO shown in (b). The (La,Sr)O and CoO_2 planes are labelled, as are the various interplanar spacings (averaged over the entire image). The black and gray bars at the top of the image are guides to the eye for identifying the dark and bright planes, respectively. (c) shows an O elemental map corresponding to the O K-edge, with the line trace beneath showing the averaged O K image intensity along the direction of the white arrow. The red/blue arrows and the gray/black bars highlight the oxygen sufficient and deficient planes, respectively.

Another interesting phenomenon observed in epitaxial LSCO films, which will be extremely important in this thesis work, is the manner in which they accommodate lattice mismatch. Most perovskite oxides accommodate lattice mismatch by straining the film to the underlying substrate lattice parameter. As the films grow thicker, however, misfit dislocations form and lead to relaxation of the film lattice parameter to the bulk value. Simple estimates for the characteristic length by which strain relaxation is expected to occur in a given system can be calculated using the Mathews-Blakeslee equation [106]. LSCO films, however, do not form misfit dislocations, but rather accommodate the lattice mismatch by a completely different mechanism. As shown in the high resolution transmission electron microscopy (HRTEM) image in Figs. 1.21(a,b) [105], bright and dark stripes that run perpendicular to the substrate interface with two different interplane spacings are observed in LSCO($x = 0.5$) films on STO(001) substrates, which presents a 1.8 % tensile lattice mismatch. The bright and dark stripes correspond to oxygen sufficient and deficient planes, respectively, as shown in Fig. 1.21(c). These alternating planes are a hallmark of the so-called brownmillerite crystal structure ($ABO_{2.5}$, shown in Fig. 1.22), which is derived from the perovskite structure, with *ordered* V_O formation in alternating (001) CoO_2 planes of the LSCO lattice, along staggered <110> lines, resulting in alternating planes of tetrahedrally- and octahedrally-coordinated Co ions. The oxygen-

deficient planes with tetrahedrally-coordinated Co in the brownmillerite structure have a larger interplanar spacing compared to the oxygen-sufficient planes with octahedrally-coordinated Co [107].

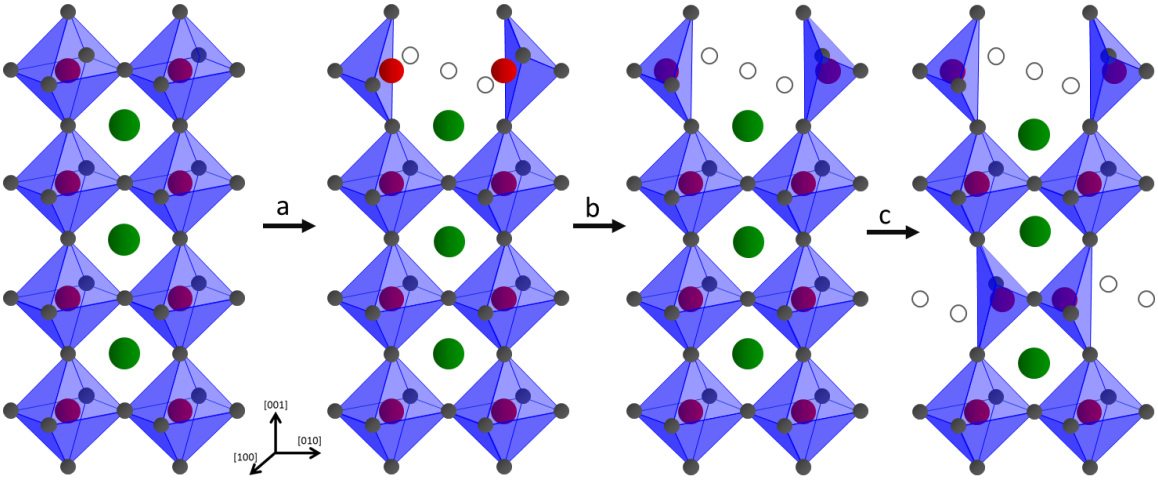

Fig. 1.22. Deriving brownmillerite (far right) from the perovskite (far left) crystal structure, where A/B cations are green/red, oxygens are gray, and oxygen vacancies (V_Os) are white. In step "a" the first line of V_Os are removed along the [110] direction. In step "b" the nearby B ions shift into their tetrahedral coordination. In step "c" the process is repeated two unit cells down, but with an offset in the [010] direction and the A-site cations sift toward the octahedrally coordinated BO_2 plane.

The LSCO films, therefore, form these oxygen-deficient planes to expand until the sum of the two interplanar spacings matches twice the STO lattice parameter. Obviously, V_Os are required to form this oxygen vacancy ordered (OVO) structure, and electron energy loss spectroscopy (EELS) measurements shown in Fig. 1.23(a) confirm that they accumulate near the LSCO/STO interface [107]. The V_O density decreases further from the interface as the LSCO film relaxes to its bulk structure, though it does so by forming OVO domains with a different orientation, rather than forming misfit dislocations [107]. A final, important, note is that the oxygen deficiency in these films does not reach the full brownmillerite $\delta = 0.5$ value for $x = 0.5$ LSCO films, but rather is around $\delta \sim 0.13$ near the substrate interface for films on STO(001) [107]. The brownmillerite structure is observed in $SrCoO_{2.5}$ films, however, where reversible switching between this brownmillerite phase and the cubic $SrCoO_{3-\delta}$ phase have been demonstrated using annealing treatments [108]. The general observation of mismatch accommodation *via* OVO in LSCO provides an excellent demonstration of its disposition towards V_O formation.

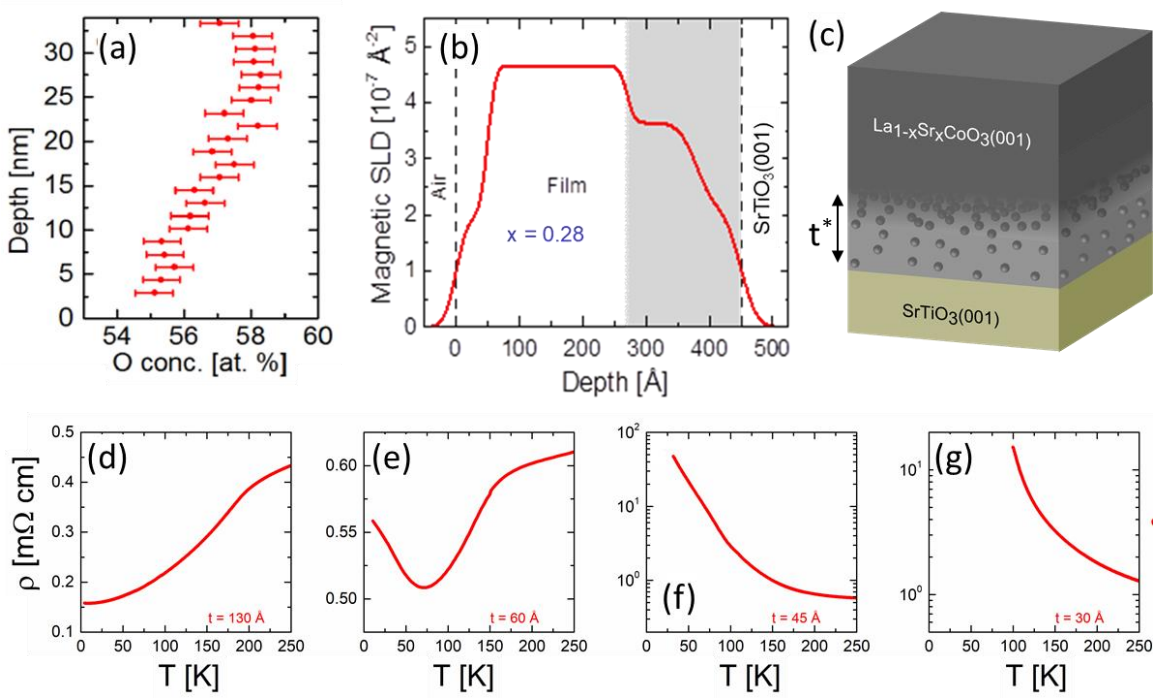

Fig. 1.23. (a) Laterally averaged depth profile (depth = 0 Å is the substrate/film interface) of the oxygen concentration, as determined from the integrated intensity of the O K-edge in electron energy loss spectroscopy measurements on an x = 0.5 $La_{1-x}Sr_xCoO_{3-\delta}$ (LSCO) film grown on $SrTiO_3$(001) [107]. (b) Depth profile (depth = 450 Å is the substrate/film interface) of the magnetic scattering length density (SLD) of an x = 0.28 LSCO film on $SrTiO_3$(001) [10]. (c) Schematic of the magnetoelectronic phase separation observed near the substrate interface in LSCO films, where the dark color represents ferromagnetic metallic regions and the lighter color represents insulating non-ferromagnetic regions. t^* indicates the x-dependent "dead layer" thickness (t^* ~ 60 Å for x = 0.5, and ~180 Å for x = 0.28). (d-g) Temperature (T) dependence of the resistivity (ρ) for x = 0.5 LSCO films of thickness 130 Å, 60 Å, 45 Å, and 30 Å, respectively [10].

The V_O accumulation near the LSCO/STO interface required to form the lattice-mismatch-accommodating OVO structure, as well as the OVO structure itself, impacts electronic and magnetic properties of these films. Thick (130 Å) LSCO (x = 0.5) films exhibit the expected FMM, metallic ρ(T) behavior with bulk-like T_C, as shown in Fig. 1.23(d) [10]. As the film thickness is reduced, however, the FMM behavior gives way to insulating, non-FM behavior (Figs. 1.23(d-g)) [10]. The onset of this insulating non-FM behavior is attributed to lowered x_{eff} near the substrate interface, a consequence of the increased V_O concentration in this region. In fact, IGMR transport signatures similar to bulk LSCO with x < 0.18 are observed in these ultrathin LSCO films, suggesting the presence of MEPS [95]. Direct evidence of MEPS near the substrate, even in thick LSCO films, was demonstrated using both small angle neutron scattering (SANS) [107] and polarized neutron reflectometry (PNR) measurements (Fig. 1.23(b)) [10]. Therefore, a

MEPS "dead layer" roughly 60 Å thick with suppressed magnetization and metallicity, shown schematically in Fig. 1.23(c), results as a consequence of the V_O accumulation near the LSCO/STO interface in these films.

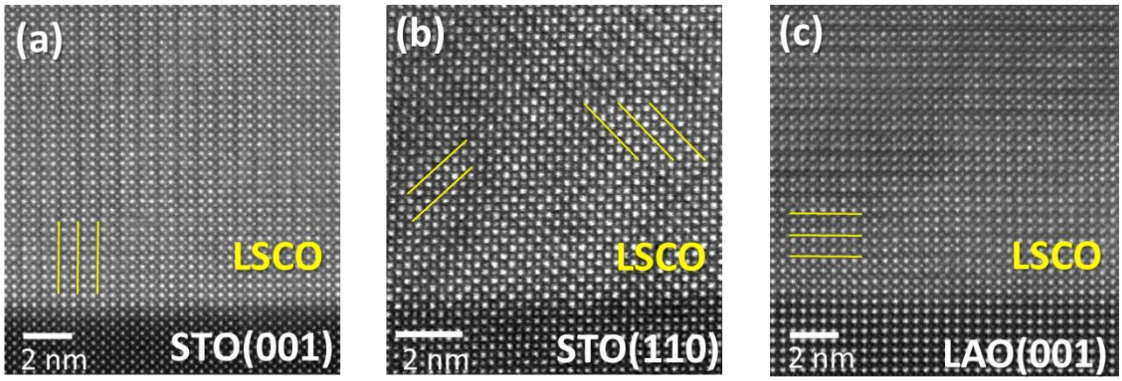

Fig. 1.24. [109] High resolution Z-contrast scanning transmission electron microscopy images of the interface regions of $x = 0.5$ $La_{1-x}Sr_xCoO_{3-\delta}$ films grown on (a) $SrTiO_3$(001), (b) $SrTiO_3$(110), and (c) $LaAlO_3$(001). Yellow lines mark the O deficient Co-O planes.

Importantly, all of these effects on the electronic and magnetic properties of LSCO films grown on STO fundamentally originate from the formation of the OVO structure as a lattice mismatch accommodation mechanism. It has been demonstrated that this lattice mismatch accommodation can be used to manipulate the OVO structure, and subsequently the electronic and magnetic properties, of LSCO films. This engineering of OVO is demonstrated in Fig. 1.24 [109]. The same OVO structure discussed on $x = 0.5$ LSCO films grown under 1.8% tensile mismatch with STO(001) is observed in the HRTEM image in Fig. 1.24(a), with OVO planes running perpendicular to the substrate interface. When LSCO is grown with the same lattice mismatch but different crystallographic orientation on STO(110) substrates, the OVO planes run at 45° angles with respect to the substrate interface (Fig. 1.24(b)). This 45° angle is driven by the fact that the OVO planes in the brownmillerite structure lie in the (001) Co-O planes. When LSCO is presented with a compressive mismatch (-1.2 %) by the substrate LAO(001), the OVO planes are found to run parallel to the substrate interface (Fig. 1.24(c)). These parallel planes result due to simple Poisson ratio arguments; in order to compress in the plane, the LSCO needs to expand in the out-of-plane direction, thus requiring the oxygen-deficient planes to run parallel to the interface.

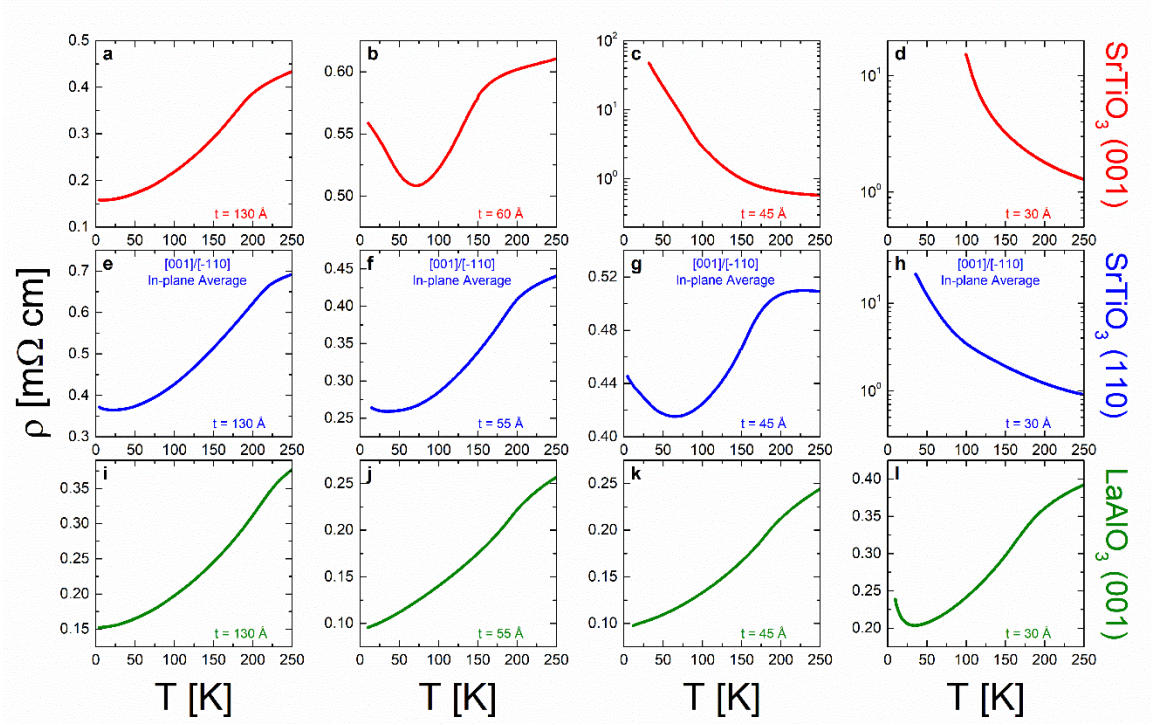

Fig. 1.25. [10] Temperature (T) dependence of the resistivity (ρ) for x = 0.5 LSCO films grown on (a-d) $SrTiO_3$(001), (e-h) $SrTiO_3$(110), and (i-l) $LaAlO_3$(001) with thickness labeled in each panel.

These controlled OVO orientations result in different electronic and magnetic properties of these films. For example, Fig. 1.25 shows how the thickness evolution of ρ(T) changes between these substrates [10]. While strongly insulating behavior is observed in x = 0.5 LSCO films on STO(001) at a thickness of 45 Å, films on STO(110) and LAO(001) remain metallic (Figs. 1.25(c,g,k)). In fact, metallic behavior is retained in LSCO films on LAO(001) down to 30 Å (8 unit cells). These data suggest the dead layers of films grown on STO(110) and LAO(001) are much thinner, which is supported by PNR measurements [10]. The reason for this suppressed dead layer thickness is actually different for these two substrates. In the case of films on STO(110), the 45° OVO plane orientations leads to faster strain relaxation compared to the STO(001) case because the OVO modulation vector (q), defined as the direction normal to the O vacancy planes, has a finite dot product with the growth direction [109] (where the vertical OVO planes on STO(001) do not). This faster strain relaxation leads to faster decrease in V_O concentration *vs*. distance from the substrate, thus reaching the x_{eff} required for FMM behavior at lower film thicknesses. The key feature for reduced dead layer thickness for films on LAO(001) is suspected to be a result of the smaller magnitude in mismatch, leading to lower overall V_O

densities and stronger FMM behavior at ultralow thicknesses. Importantly, this demonstrates that lattice mismatch and crystallographic orientation can be used as routes to engineer/tune the electronic and magnetic properties of these LSCO films. In fact, in Chapter 7, I will use these lattice mismatch and OVO-engineering strategies to control giant changes in the magnetic anisotropy and AMR in LSCO films.

1.3.3 *Goals for electrolyte gating studies*

In this section I will discuss the advantages of using LSCO EDLTs to address the three open questions in the area of electrolyte gating highlighted in Section 1.2.2.

1. Poorly understood electrostatic *vs.* electrochemical gating mechanisms, particularly with respect to oxygen vacancy formation in oxide EDLTs.

LSCO EDLTs have the potential to be profoundly useful in addressing the electrostatic *vs*. electrochemical gating mechanism in electrolyte-gated oxides. While V_O formation energies in many oxides are low, LSCO films at high *x* provide an interesting extreme where V_O formation energy is essentially zero. If the large electric fields in LSCO EDLTs cannot form V_Os, it would be reasonable to suspect gate-induced V_O formation is negligible in other oxides as well. If V_O formation indeed occurs, it may be possible to use these LSCO EDLTs as a benchmark for the upper limit of the extent of V_O formation in electrolyte gating, both in V_O density and the length scales involved (as the diffusion length of V_Os is also high in LSCO). Further, all of the previously published work on the prospect of V_O formation in oxide EDLTs has been done on *n*-type oxides, and only at positive biases where V_O doping and electrostatic electron accumulation are difficult to differentiate. Investigating the gating mechanism in *p*-type films such as LSCO could be an important step, where hole depletion may be easier to separate from V_O formation than electron accumulation and the importance of bias polarity can be better investigated.

2. A general lack of *in operando* probes.

While the list of potentially useful and exciting *in operando* characterization techniques is quite long, a logical place to start is with those that can help address the differentiation of electrostatic *vs*. electrochemical gating mechanisms in oxide EDLTs. The real

shortcoming there is the inability to distinguish electrochemical from electrostatic doping in transport measurements, where only changes in carrier density can be determined and not the origin of these carriers. Spectroscopic and scattering probes, however, could provide the tools to differentiate such mechanisms. Important capabilities in this regard will be the ability to overcome the small sample volumes buried under thick ILs/gels to detect V_O formation in quantitative fashion with spatial resolution. LSCO EDLTs provide a great starting point, as they may be the most prone to significant changes in electrochemical composition, perhaps providing the largest response in a variety of different signals.

3. The universality of the approach with respect to control of magnetic material properties.

Voltage control of the magnetic properties of LSCO is an exciting prospect, primarily due to the percolative transition it undergoes. The basic concept here is similar to that of the Mott transistor, where a small amount of electrostatically induced charge leads to dramatic electronic phase changes in the channel material. Here, it may be possible to drive a thin film of LSCO through a percolation transition from an insulating non-FM state to a FMM state by accumulating a small number of holes on its surface with electrolyte gating. If such a gate-induced FMM state were achieved, one may expect drastic changes in the LSCO films properties, such as conductivity, magnetization, T_C, *etc*. Further, if understanding of the *optimization* of such gate-induced percolation transitions was established, it may be applicable to other percolative materials (such as the manganites [5] and cuprates [110]) and even electric-field control strategies other than electrolyte gating, such as ferroelectric gating.

Chapter 2: Experimental methods

2.1 Growth of epitaxial $La_{1-x}Sr_xCoO_{3-\delta}$ films *via* high-pressure oxygen sputtering

As discussed in Section 1.3.3, EDLTs based on LSCO films could be particularly useful in addressing open issues involving electrolyte gating; therefore, high quality LSCO films are needed. Epitaxial growth of phase pure and stoichiometric LSCO films has been demonstrated with multiple growth techniques, including reactive sputtering [95,111], pulsed laser deposition [112], sol-gel synthesis [113], and metal-organic chemical vapor deposition [114]. All of these techniques require careful optimization with respect to deposition temperature, pressure, growth-gas composition, and cooling protocol, largely due to the propensity of LSCO to form V_Os. One synthesis strategy to overcome high V_O densities is a unique form of reactive sputtering, called "high-pressure oxygen sputtering." Conventional reactive sputtering methods typically use an Ar/O_2 gas mixture with total pressures in the 10-200 mTorr range [95], which has some distinct disadvantages when trying to grow V_O-prone LSCO films. Oxygen-ion-induced re-sputtering is known to be significant, due to the large mean free path of energetic oxygen ions in this pressure range (~530 μm at 100 mTorr), leading to severe film inhomogeneity, roughness, cation non-stoichiometry, and low net deposition rate [115]. Off-axis sputtering has been demonstrated to reduce re-sputtering, but makes deposition rates even slower [115]. While reducing the O_2 partial pressure has also been shown to mitigate this re-sputtering effect, it has typically been accompanied by low oxygen content, thus forcing post-growth annealing procedures to be used [95]. High-pressure oxygen sputtering circumvents this problem by growing in much higher pressures (~1-2 Torr) of *pure* O_2. The mean free path of oxygen ions is significantly suppressed at these pressures (~36 μm at 1.5 Torr), which means the reactive oxygen ions become thermalized before reaching the substrate, hence simultaneously mitigating re-sputtering and encouraging full oxygenation. This deposition technique is thus ideal for the growth of V_O-prone materials such as LSCO. In fact, high-pressure oxygen sputtering was first developed for the epitaxial growth of the high temperature superconducting material $YBa_2Cu_3O_7$ [116,117], which is similarly V_O-prone.

2.1.1 *$La_{1-x}Sr_xCoO_3$ target preparation*

LSCO sputtering targets were synthesized using standard ceramic processing methods [10]. Stoichiometric quantities of La_2O_3 (Alfa Aesar, 99.9 %) (which was dried in air at 1000 °C for 24 hours and then massed while hot due to its hygroscopic nature), Co_3O_4 (Alfa Aesar, 99.7 %), and $SrCO_3$ (Sigma-Aldrich, 99.9 %) were thoroughly ground together and calcined in an alumina crucible and air at 1000 °C for 7 days, with two intermediate grindings at even time intervals during those 7 days. A liquid binder (350 ml H_2O, 100 ml glycerine, 10 g polyvinyl alcohol) was added to these reacted powders and then they were subsequently cold pressed into 2"-diameter disks of ~3 mm thickness at 13,000 psi. These pressed disks were then sintered in air at 1200 °C for 24 hours, using warming and cooling ramp rates of 0.5 °C/min to minimize thermal stresses and maximize oxygen content. Powder X-ray diffraction and magnetometry were used to verify the phase purity and ferromagnetic T_C of the resultant sintered disks. The sintered disks were then sanded down to ~1.5" diameter and bonded to a copper backing plate with indium for mounting in the sputtering gun. Indium was first soldered meticulously to the back of the LSCO disk, then indium was used to coat the copper backing plate by heating on a hot plate at ~200 °C, then the disk was placed on the hot, indium covered copper plate. Extra weight (typically other blank copper plates) was then added on top of the bonded assembly, followed by natural cooling to room temperature. Extra indium was then sanded off and the assembly mounted on the sputtering gun, with machined alumina and Macor® washers covering the exposed copper portions of the assembly.

2.1.2 *High-pressure oxygen sputtering process*

The substrates used in this work were all bought commercially, either from MTI Corporation (Richmond, CA) or Crystec (Berlin, Germany). These include $SrTiO_3$ (STO), $LaAlO_3$ (LAO), $La_{0.18}Sr_{0.82}Al_{0.59}Ta_{0.41}O_3$ (LSAT), and $SrLaAlO_4$ (SLAO), all in the (001) orientation and with various sizes, though most were 5×5×0.5 mm^3. In terms of substrate cleaning, only dry nitrogen blowing was used to rid macroscopic dust particles, as solvent cleaning was found to leave unwanted residue. Further, substrates were annealed at 900 °C in 1 Torr of flowing O_2 for 15 min immediately prior to growth to remove organic surface contaminants [118]. LSCO targets, also prior to growth, were conditioned by slowly

ramping the DC sputter current and O_2 pressure (P_O). For a brand-new target, this conditioning would typically involve ~8 hours of pre-sputtering at 50 mA in P_O = 0.75 Torr, followed by stepwise increases in current (~25 mA) and P_O (~0.2 Torr) with ~ 1 hour of pre-sputtering at each step, up to the final growth current (200 mA) and P_O (~1.5 Torr). For a previously conditioned target, the pre-sputtering process typically involved a slow ramp up to the growth current and P_O over ~ 30 min, followed by a ~1 hour pre-sputter at growth conditions. The four primary process variables used to optimize LSCO film growth were substrate temperature (T_{sub}), P_O, DC sputter current, and target to substrate distance. The majority of this thesis focuses on x = 0.5 LSCO films, where these process variables have been particularly well optimized [10]. These optimal values are: T_{sub} of 600 °C, DC sputter current of 200 mA, target to substrate distance of 19 mm, and P_O that varies for each growth, between values of 1.3 and 1.6 Torr, in order to make the DC sputter voltage ~331 V. Films at other x values were similarly grown at T_{sub} = 600 °C and DC sputter current = 200 mA, however, the target to substrate distance was varied in the 16 - 21 mm range and the optimal DC sputter voltage (and thus the P_O values) varied between 320 and 335 V. These process variables were arrived at based on the optimization of these key film properties: phase purity, high oxygen content (lowest δ achievable), minimized ρ, maximized T_C, and lowest surface roughness. Section 2.2 includes details on the characterization techniques used for growth optimization.

2.2 $La_{1-x}Sr_xCoO_{3-\delta}$ film characterization

In this section I will introduce the basic characterization techniques performed on LSCO films prior to EDLT device fabrication. In addition to covering the basic principles and capabilities of each characterization technique, I will provide examples specific to LSCO film growth optimization to illustrate the features of most interest to this work.

2.2.1 *High-resolution X-ray diffraction*

High resolution X-ray diffraction (HRXRD) was performed on a PANalytical X'pert Pro diffractometer. A four-bounce Ge(220) monochromating crystal was used in tandem with a Cu X-ray tube source to provide highly monochromated Cu $K_{\alpha,1}$ radiation (λ = 1.54056 Å). Divergence slits of ½° were used on both the source and scattered beams. The

resulting angular resolution (combining the angular and spectral divergence) was ~ 0.004°. Samples were mounted on the sample holder using double-sided tape. Alignment was achieved by optimizing substrate peak intensities. Two primary scan geometries were utilized, including specular wide-angle XRD (WAXRD) with rocking curve (RC) analysis, and reciprocal space mapping (RSM).

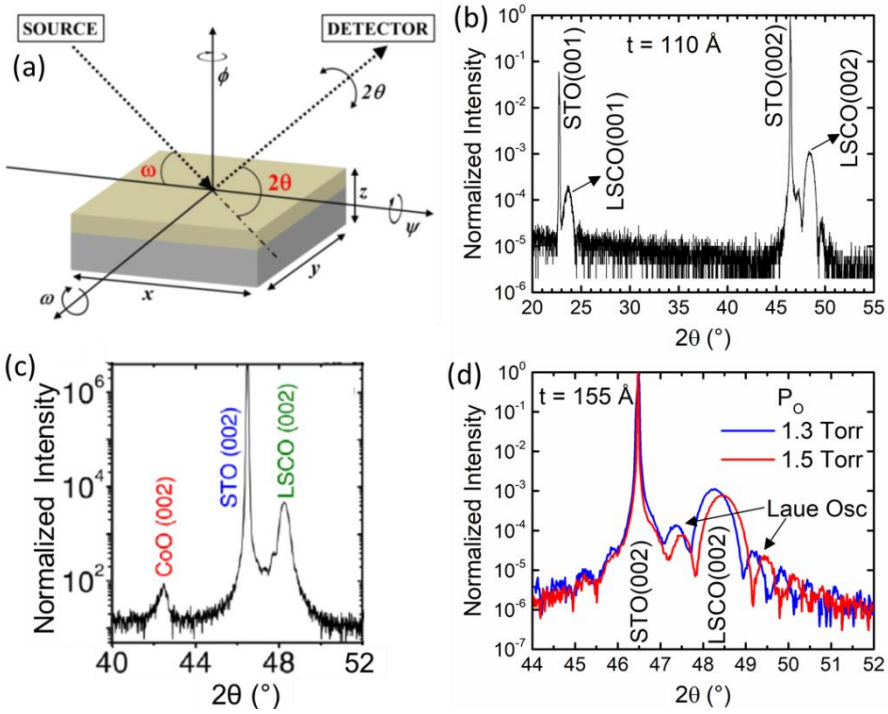

Fig. 2.1. (a) Schematic [10] depicting the angles and degrees of freedom in wide angle X-ray diffraction (WAXRD) measurements, with red labels used for the measured angles and italicized labels used for axes of motion. (b) A WAXRD scan of scattered X-ray intensity *vs*. scattering angle (2θ) for a 110 Å thick $x = 0.5$ $La_{1-x}Sr_xCoO_3$ (LSCO) film grown with high-pressure oxygen reactive sputtering on $SrTiO_3$(001) (STO(001)) at 600 °C and optimized process variables. The substrate and film peaks are labeled. (c) A WAXRD scan from a 250 Å thick $x = 0.5$ LSCO film grown on STO(001) at 700 °C using conventional reactive sputtering with argon and oxygen partial pressures of 50 and 20 mTorr, respectively [119]. (d) A WAXRD scan from 155 Å thick $x = 0.5$ LSCO films grown on STO(001) at 600 °C in oxygen pressure (P_O) of 1.3 (blue) and 1.5 (red) Torr.

The specular WAXRD geometry rotates the sample and detector with respect to the incident X-ray beam (ω and 2θ, respectively) in coupled fashion, setting ω = ½(2θ) as shown in Fig. 2.1(a) [10]. This orients the scattering vector (***Q***) perpendicular to the plane of the sample, thus probing the crystal planes that lie parallel to the film plane. This scan geometry provides a wealth of information, the first of which is phase purity. A typical WAXRD scan of scattering intensity *vs*. 2θ for a $x = 0.5$ LSCO film grown on STO(001) is shown in Fig. 2.1(b). Only (00L) STO substrate and LSCO film peaks are observed,

indicating phase purity to the detection limit (~5 %) and (00L) texturing of the LSCO film. An example of a non-phase pure LSCO film (grown by reactive sputtering in an Ar/O_2 gas mixture [119]) is shown in Fig. 2.1(c), where a peak was observed at 42.5° corresponding to CoO. The LSCO(002) film peak position ($2\theta_{002}$) was used to determine the LSCO out-of-plane lattice parameter, $c_{op} = \lambda/\sin\theta_{002}$. The value of c_{op} for optimized $x = 0.5$ LSCO films in the thickness range of 100 – 180 Å on STO(001) was 3.758 ± 0.005 Å. As expected for a film under biaxial in-plane tensile strain, this value is smaller than the bulk value 3.833 Å (*i.e.*, compressed by a value of 1.9 %). For example, films grown at lower P_O exhibit film peaks shifted to lower 2θ (as shown in Fig. 2.1(d)), yielding a slightly expanded c_{op} = 3.770 Å. This increased c_{op} was accompanied by an increase in electrical resistivity (discussed in more detail in Section 2.2.5), which is suspected to be a consequence of higher V_O concentration. The (002) film peak width can be used to calculate a Scherrer length, t_S, assuming all of the peak broadening comes from the finite thickness of the film (*i.e.*, assuming there is no relaxation or microstrain present, which is justified below) using the expression

$$t_S = \frac{0.9\lambda}{\Delta(2\theta_{002})\cos\theta_{002}} \qquad 2.1,$$

where $\Delta(2\theta)$ is the full width at half maximum of the (002) film peak and 0.9 is the shape factor assumed for these thin films. This value is typically within 10 Å of the thickness determined by grazing incidence X-ray reflectometry (reviewed in Section 2.2.2), suggesting little microstrain (and thus little strain relaxation) in these films. The Laue oscillations surrounding the film peak (highlighted in Fig. 2.1(d)) indicate low film roughness on short lateral scales and can also be used to quantify the film thickness, t_f, using

$$\sin\theta_{nL} = \frac{\lambda}{2t_f}\, n_L \qquad 2.2,$$

where θ_{nL} is the n_Lth order Laue oscillation. Linear fits to $\sin(\theta_n)$ *vs.* n_L were used to extract t_f, which is typically within 10% of the thickness determined by grazing incidence X-ray reflectometry. Finally, the mosaic spread of the LSCO film can be quantified using RC scans (data not shown), in which the sample is tilted such that $\omega \neq \frac{1}{2}(2\theta)$ near diffraction

peaks. Typical (002) RC peak widths for LSCO films (0.08°) were similar to that of (002) STO RC peak widths (0.05°), indicating the mosaic spreads of the LSCO films were quite small and simply matched that of the underlying substrate.

Finally, RSMs around the (013) substrate and film peaks were used to investigate the level of strain relaxation in LSCO films. In this measurement, initial alignment to the (013) substrate peak was followed by repeated rocking curves at different 2θ values in order to "map" the region of reciprocal space near the (013) substrate and film diffractions. The intensity is recorded for different ω and 2θ, then converted to a 2D intensity map as a function the in-plane ($Q_{//}$) and out-of-plane ($Q_{\perp}$) scattering vector components

$$Q_{//} = \frac{2\pi}{d_{010}} = \frac{2\pi}{\lambda}[\cos\omega - \cos(2\theta - \omega)] \quad 2.3 \text{ and}$$

$$Q_{\perp} = \frac{2\pi}{d_{001}} = \frac{2\pi}{\lambda}[\sin\omega + \sin(2\theta - \omega)] \quad 2.4,$$

where d_{010} and d_{001} are the (010) and (001) interplanar spacings, respectively. Fig. 2.2 shows an example RSM for a 380 Å thick x = 0.5 LSCO film grown on LAO(001). The film peak appears at a lower $3/d_{001}$ value, consistent with its larger c_{op} (3.890 Å) compared to the lattice parameter of LAO (3.789 Å), but appears at the same $1/d_{100}$ value, indicating it is epitaxially clamped with the same in-plane lattice parameter as LAO. For reference, the expected peak location for completely strained and relaxed LSCO is marked on the plot. Therefore, this LSCO film does not exhibit any strain relaxation, which was typical of all the LSCO films used in this work and is consistent with the absence of microstrain in the film peak width analysis mentioned above.

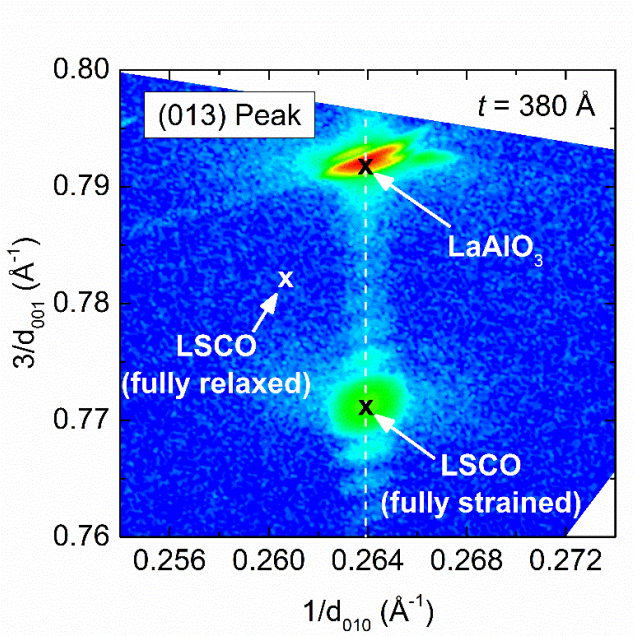

Fig. 2.2. Asymmetric reciprocal space maps around the (013) reflection of a 380 Å thick x = 0.5 LSCO film on $LaAlO_3$(001). The expected positions of the fully strained and fully relaxed LSCO reflections are marked and labeled. Clearly, the LSCO film peak lies at the fully strained position indicating no strain relaxation in films with thicknesses up to at least 380 Å.

2.2.2 *Grazing incidence X-ray reflectometry*

Grazing incidence X-ray reflectometry (GIXR) was performed on the same PANalytical X'pert Pro diffractometer discussed in Section 2.2.1, but with different optics. No monochromator was used in order to increase the incident beam intensity, resulting in the inclusion of both Cu $K_{\alpha,1}$ and $K_{\alpha,2}$ radiation with an average effective wavelength of 1.5419 Å. A 1/32° divergence slit and focusing mirror for collimation were used on the incident beam and a 0.1° parallel plate collimator was used on the reflected beam. The resulting angular resolution in this configuration was 0.04°. This specular geometry was used in a coupled scanning mode (*i.e.*, $\omega = \frac{1}{2}(2\theta)$).

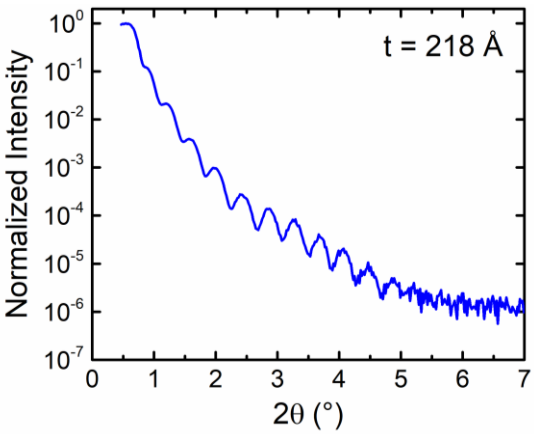

Fig. 2.3. Grazing incidence X-ray reflectivity from a 218 Å thick x = 0.5 $La_{1-x}Sr_xCoO_3$ film on $SrTiO_3$(001).

A typical reflectivity *vs.* 2θ for an x = 0.5 LSCO film grown on STO(001) is shown in Fig. 2.3. The overall falloff follows the laws of Fresnel reflectivity, which is proportional to θ^{-4}, and the different X-ray scattering length density (SLD, ρ_{xray}) between the substrate and film results in the observed Kiessig fringes. The SLD of a material is related to its mass density (ρ_m) through

$$\rho_{xray} = \frac{\rho_m N_a \sum_i b_i}{\sum_i m_i} \quad \text{and} \quad b_i = r_{el} f_i \qquad 2.5,$$

where the sums are over every atom in a material's unit cell, N_a is Avogadro's number, m_i is the atomic mass of the ith atom, b_i is the scattering length contribution from the ith atom, r_{el} is the classical electron radius ($e^2/(4\pi\varepsilon_0 m_0 c^2)$ = 2.82 × 10^{-15} m), and f_i is the real part of the atomic scattering factor for the ith atom. The Kiessig fringes observed can be used to extract the critical angle (θ_c) and the thickness (t) of the LSCO film using

$$n_K \lambda = 2t\sqrt{\sin^2\theta_{nK} - \sin^2\theta_c} \qquad 2.6,$$

where n_K is the Kiessig fringe order integer, θ_{nK} is the n_Kth order Kiessig fringe maxima, and λ is the X-ray wavelength (1.5419 Å in this case). Maximizing the correlation function from a linear fit of $\sin^2\theta_{nK}$ *vs.* n_K^2 by varying n_K of the first fringe observed (may not be n_K = 1), while constraining the intercept to be larger than zero, provides the film t (from the slope) and θ_c (from the intercept). The intercept must be larger than zero because θ_c is related to the film's electron density, $\rho_{el} = \pi\theta_c^2\lambda^{-2}r_{el}^{-1}$. Such GIXR data were typically used with Eq. 2.6 to extract film thicknesses for growth rate calibrations. Further information, however, such as roughness at the film/substrate interface and the film surface, as well as

non-uniform SLD depth profiles of the film, can be extracted using fitting software (*e.g.*, PANalytical X'pert Reflectivity or Refl1D). Importantly, in cases where such advanced fitting was performed, proper background subtraction was carried out. The non-specular background was subtracted by repeating reflectivity *vs.* 2θ scans with both positive and negative ω offsets, and subtracting their average from the zero offset scan (an example is shown in Fig. 2.4(a)). The ω offset was chosen such that it was large enough to be off the specular reflection peak, but not so large that it wasn't representative of the actual background signal, as shown in Fig. 2.4(b). While such background subtraction was necessary to extract accurate film properties in fitting, such as roughness, it was not crucial for quick thickness calculations because it does not change the Keissig fringe analysis (Eq. 2.6).

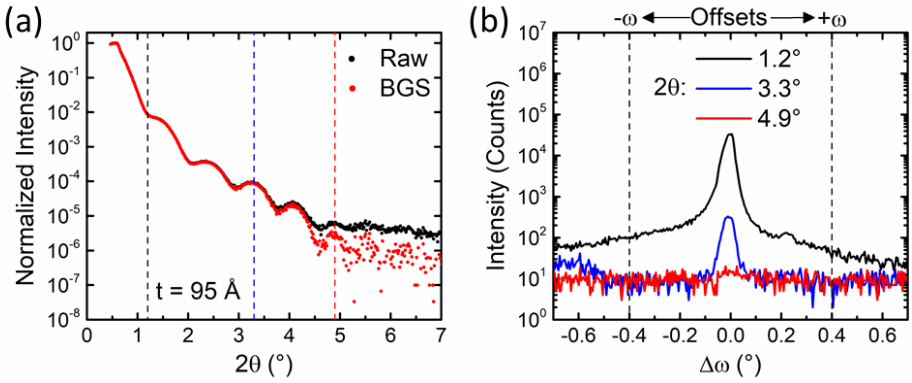

Fig. 2.4. (a) Grazing incidence X-ray reflectivity from a 95 Å thick x = 0.5 $La_{1-x}Sr_xCoO_3$ film on $SrTiO_3$(001) without non-specular subtraction ("Raw", black points) and with background subtraction ("BGS", red points). (b) Three characteristic 2θ locations (marked by dotted lines in (a)) where omega (ω) scans were performed to determine the ±ω offset of 0.4° used in the BGS scan.

2.2.3 *Atomic force microscopy*

Contact-mode atomic force microscopy (AFM) measurements were performed on a Bruker Nanoscope V Multimode 8 system to investigate the film surface topography. Cantilevers with 8 nm radius tips and force constants ranging between 0.6 and 2 N/m were used. Double-sided tape was used to affix the samples to the AFM sample holder. AFM height images of two 155 Å thick x = 0.5 LSCO films on LAO(001) are shown in Fig. 2.5, with each grown at a different target-to-substrate distance (Z). The surface morphology at Z = 19 mm (Fig. 2.5(a)) is clearly smoother than the result at 16 mm (Fig. 2.5(b)). This was

quantified by root mean square (RMS) surface roughness analysis, resulting in values of 0.25 and 0.54 nm at Z = 19 and 16 mm, respectively. While subtle changes in oxygen content (observed by lattice parameter and resistivity changes in the film) were occasionally observed in target-to-substrate distance studies, minimization of the film roughness was typically the driving factor in target-to-substrate distance optimization. Therefore, these AFM height images played a key role in optimization of LSCO film growths.

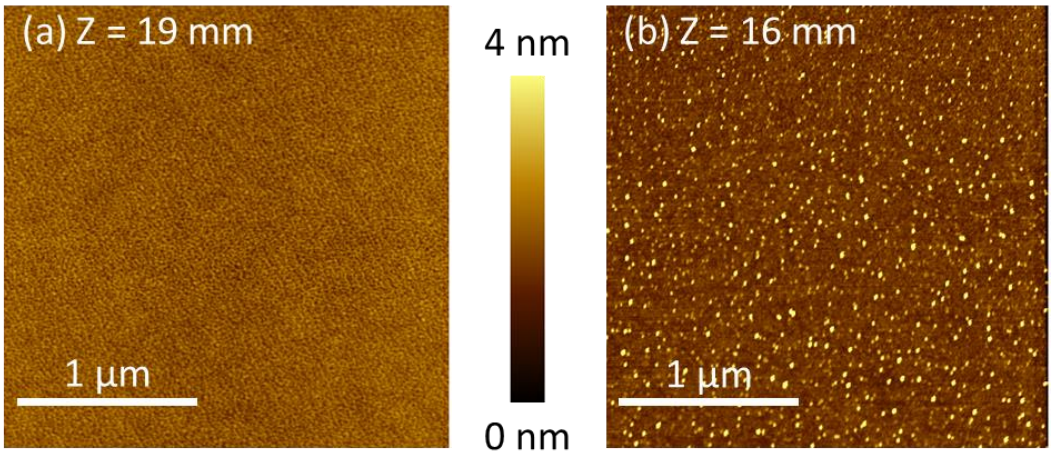

Fig. 2.5. Contact-mode atomic force microscopy height images (2.5 × 2.5 µm^2) of 155 Å thick x = 0.5 $La_{1-x}Sr_xCoO_3$ films on $LaAlO_3$(001) substrates grown at target-to-substrate distances (Z) of (a) 19 mm and (b) 16 mm. The height scale (center) is the same for both images.

2.2.4 *Magnetometry*

The magnetic behavior of LSCO films was investigated using a superconducting quantum interference device (SQUID) magnetometer inside a Quantum Design Magnetic Property Measuring System (MPMS) XL. Measurements were performed using the reciprocating sample oscillation head option, which has a magnetic moment sensitivity of 10^{-8} emu. The MPMS system has a He flow cryostat with sample temperature capabilities of 1.8 - 600 K (though the DC sample head and heater probe must be used for T > 300 K) and is equipped with a superconducting magnet capable of applying magnetic fields up to 7 T. Samples were mounted in plastic drinking straws for both in- and out-of-plane sample geometries, as shown in Fig. 2.6. The in-plane mounting consisted of placing the sample in a straw that was sliced along its length with a Teflon knife, then placing this assembly

into an un-sliced straw. The sliced straw reduces its diameter, thus squeezing the sample to hold it in place as shown in Fig. 2.6(b). The diameter reduction of one sliced straw was typically enough to hold a 5×5×0.5 mm^2 sample, but sometimes two sliced straws were required. The out-of-plane mounting required 2 slits to be cut into opposite sides of a straw and perpendicular to its long axis, allowing a 5×5×0.5 mm^2 sample to be slid in as shown in Fig. 2.6(b). Kapton tape was then used to keep the sample from sliding out of these slits, and long pieces were used to keep the flux from this tape constant in the extraction scans performed in the SQUID. Finally, Kapton tape was used to attach the straws to the MPMS probe adapter and seal the bottom of the straw (to catch the sample if it fell) for both mounting geometries. Note that care was taken to avoid magnetic tools and other contamination sources, as they are known to contribute magnetic moments comparable or even larger than those of the LSCO films studied here [120].

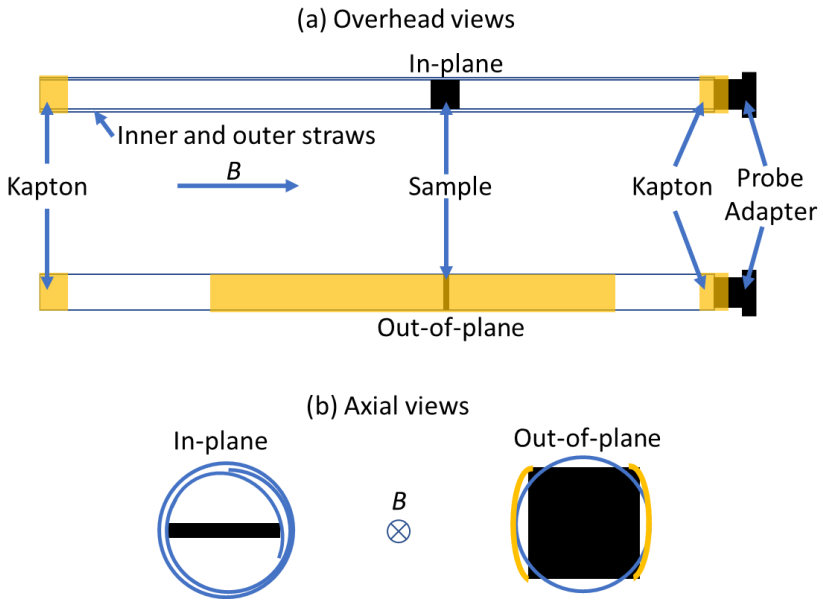

Fig. 2.6. (a) Overhead and (b) axial views of the in-plane and out-of-plane mounting system used in the MPMS.

Despite being careful to avoid magnetic contamination sources, some levels were unavoidable, particularly with respect to the background signals provided by substrates. Fig. 2.7(a) shows the magnetic moment *vs*. magnetic flux density (B) hysteresis loop for a 135 Å thick x = 0.5 LSCO film on LAO(001). Using linear fits at high B, the diamagnetic contribution of the LAO substrate can be subtracted, as shown in blue in Fig. 2.7(b). The magnetization (M), however, was found to have a higher saturation value (M_s) than bulk

(1.92 μ_B/Co) and two apparent coercive fields (B_c) indicated by the "double-loop" shape. Subtraction of the hysteresis loop performed at 300 K (well above the LSCO $T_C \approx 220$ K) removes these effects (Fig. 2.7(b), red points) however, suggesting the extra magnetic signal is coming from magnetic contaminants with T_C well above 300 K. While some of this magnetic contamination could be coming from dust particles, it is suspected the film growth process introduces most of these magnetic impurities in the substrate (as it is heated to 900 °C on a steel heater). This 300-K-backgound-subtraction technique was therefore used for most samples to obtain more reliable *M* calculations. This background subtraction technique, unfortunately, does not take into account any temperature dependence of the magnetic contamination signal. On other substrates, such as SLAO, this temperature dependence is significant, resulting in severe overestimation of *M*. Other strategies to subtract backgrounds in such systems included repeating scans after etching the film away with HCl, or simply measuring a blank substrate that went through the growth process minus the actual LSCO growth step. All of these background subtraction methods have their shortcomings and are continually being improved.

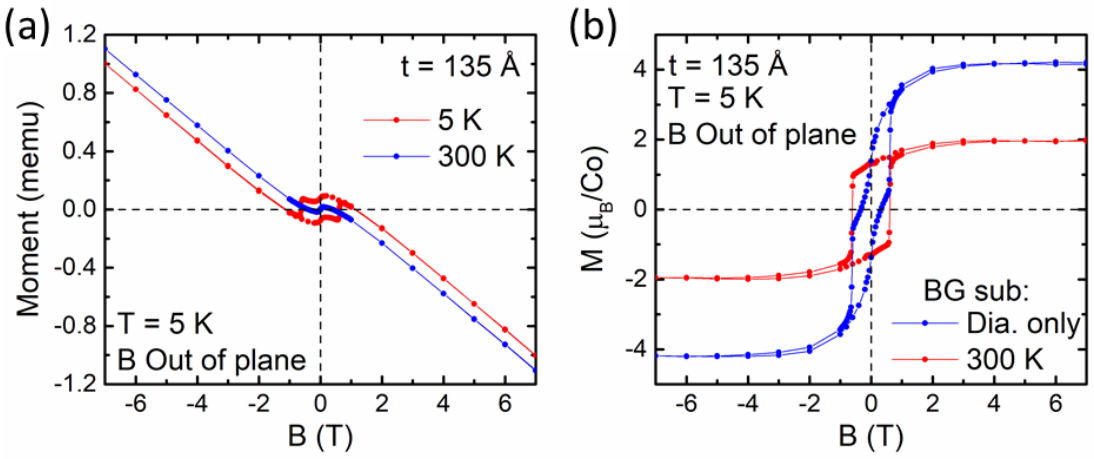

Fig. 2.7. (a) Magnetic moment *vs*. magnetic flux density (*B*) for a 135 Å thick $x = 0.5$ $La_{1-x}Sr_xCoO_3$ film on $LaAlO_3$(001) mounted in the out-of-plane geometry at 5 and 300 K in red and blue, respectively. (b) The resultant 5 K film magnetization (*M*) *vs*. *B* calculated after only subtracting the diamagnetic background of the substrate (blue) and after subtracting the 300 K scan (red).

2.2.5 *Electrical transport*

Electrical resistivity (ρ) of LSCO films was measured using the four wire van der Pauw technique [121], which utilizes two pairs of leads (source and sense) to eliminate line and contact resistances from ρ measurements. The four stipulations of the van der Pauw method are (i) contacts must be placed along the edge of a lamellar sample, (ii) the total contact area is kept to a minimum (< 10 % of the sample area), (iii) no holes or cracks are present in the sample, and (iv) the sample thickness is uniform [121]. For bare LSCO films, soldered In or sputtered Mg(5nm)/Au(50nm) contacts were placed on the corners as shown in Fig. 2.8. The two resistance configurations (R_1 and R_2) were used to calculate the LSCO film ρ using

$$\rho = \frac{\pi t}{\ln 2}\frac{R_1 + R_2}{2} f \qquad 2.9 \text{ and}$$

$$\cosh\left(\frac{\frac{R_1}{R_2} - 1}{\frac{R_1}{R_2} + 1}\frac{\ln 2}{f}\right) = \frac{1}{2}\exp\left(\frac{\ln 2}{f}\right) \qquad 2.10,$$

where t is the film thickness and f is the anisotropy factor, which was calculated by numerically solving Eq. 2.10. These resistances were measured with either AC or DC, depending on the magnitude of the resistance. AC electronics included a Lakeshore 370 AC resistance bridge and a Linear Research LR700 resistance bridge, both of which were operated at 13.7 Hz. DC electronics included Keithley 2400 and 2612B source-measure-units, as well as a Keithley 220 precision current source in combination with a Keithley 2000 or 2002 multimeter. Attention was paid to ensure the contact behavior was Ohmic and free of self-heating in all cases. Such measurements were performed in a variety of cryostats, with temperature capabilities between 1.5 and 300 K, that were equipped with either an electromagnet (B up to 2 T) or a superconducting magnet (B up to 9 T). In all cases the sample was mounted to the cryostat-specific sample holder using GE varnish, with In-soldered gold wires electrically connecting the sample to cryostat wires.

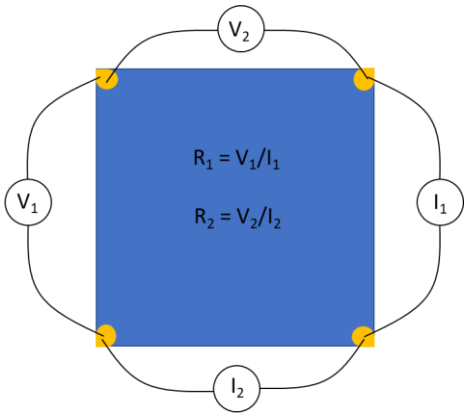

Fig. 2.8. Schematic of wiring in a van der Pauw geometry for resistivity measurements.

As mentioned in Section 2.1.2, LSCO film growth optimization often included ρ considerations. In the $x = 0.5$ case, optimized film growth resulted in a minimized ρ, which was accompanied by a maximization of T_C, and minimization of both c_{op} and surface roughness. Using the 155 Å thick, $x = 0.5$ LSCO films grown on STO(001) at different P_O that were shown in Fig. 2.1(d), for example, the 300 K ρ was lower and residual resistivity ratio (RRR = ρ(300 K)/ρ(5 K)) was higher for the film grown at higher P_O (with the smaller c_{op}), as summarized in Table 2.1.

Table 2.1. Oxygen growth pressure (P_O) dependence of the out-of-plane lattice parameter (c_{op}), 300 K resistivity (ρ), and residual resistivity ratio (RRR) for 155 Å thick, $x = 0.5$ $La_{1-x}Sr_xCoO_3$ films grown on $SrTiO_3$(001).

P_O [Torr]	c_{op} [Å]	ρ(300 K) [mΩcm]	RRR
1.3	3.770	0.38	1.7
1.5	3.758	0.29	2.5

2.3 $La_{1-x}Sr_xCoO_{3-\delta}$ device fabrication

The fabrication process for creating an LSCO EDLT is shown schematically in Fig. 2.9. Ar ion milling was first used in conjunction with a steel mask to define the LSCO channel, which in most cases was 1×1 mm^2 on a 5×5 mm^2 substrate (other geometries for each specific *in operando* characterization technique are discussed in their respective sections below). Milling was performed with a beam voltage of 200 V, current of 70 mA, an accelerating voltage of 24 V, and a substrate temperature of 6 °C, where the estimated mill rate was ~10 Å/min. Note that this milling process is known to make STO substrates conductive by forming V_Os [122], thus ruling this them out for LSCO EDLT studies. This

effect was not observed on LAO, SLAO, and LSAT substrates. Sputter deposition of Mg(5 nm)/Pt(50 nm) through a second steel mask then formed the channel and gate electrodes. Often, high resistance electrical shorts between the channel and gate electrodes were observed, arising from deposition of Mg/Pt on the side of the sample during electrode deposition. Sanding the sample sides prior to gel application eliminated such shorts. "Cut and stick" ion gels were made [55] by spin-coating on glass wafers from a 1:4:7 (by weight) solution of polymer:ionic liquid:solvent, with the polymer being P(VDF-HFP), the ionic liquid EMI:TFSI, and the solvent acetone. After spin-coating, the gels were treated in a vacuum oven at 70 °C for ~12 hours to remove residual solvent. The gels were then transferred to the fabricated LSCO devices by cutting sections from the glass wafers with a blade and placing them on the patterned devices using tweezers. Following gel application, the samples were quickly cooled below ~275 K to avoid electrochemical degradation. Four-terminal resistance measurements on the LSCO channel were made in similar manner to those of bare films discussed in Section 2.2.5, and an additional Keithley 2400 source-measure-unit was used to apply gate voltages and measure displacement currents.

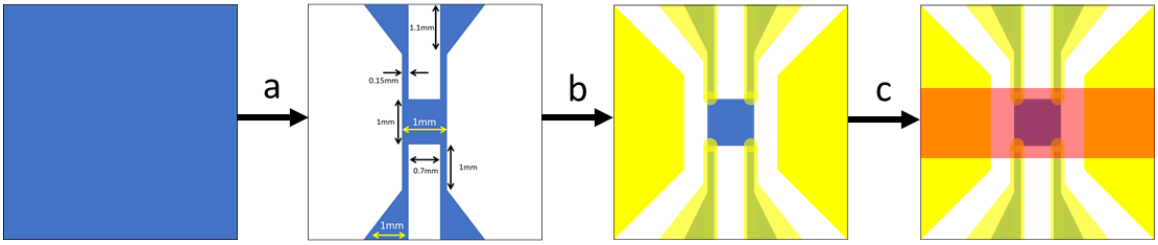

Fig. 2.9. Device fabrication schematic for a 1×1 mm^2 channel on a 5×5 mm^2 substrate. Steps a-c are Ar ion milling, electrode deposition, and ion gel application, respectively. The $La_{1-x}Sr_xCoO_3$ film, exposed substrate, electrodes, and ion gel are represented by the colors blue, white, yellow, and red, respectively.

2.4 In operando synchrotron X-ray diffraction

In operando synchrotron X-ray diffraction (SXRD) measurements were performed at the 33-ID beamline at the Advanced Photon Source. Similar WAXRD scans to those discussed in Section 2.2.1 were taken, one advantage of SXRD simply being its much larger X-ray beam intensity. The X-ray beam brilliance (*i.e.*, the number of photons of a given wavelength and direction illuminating a given area per unit time) typically achievable with 3rd generation synchrotrons is larger than 10^{18} photons $s^{-1}mm^{-2}mrad^{-2}$

(0.1% BW)$^{-1}$, where 0.1% BW denotes a bandwidth of 0.001ν centered around the frequency ν, which is more than 10^5 times larger than a typical laboratory X-ray tube source. This large intensity proved crucial, as significant signals could be observed through the thick overlying ion gels on LSCO EDLTs. A six-circle Kappa-type goniometer with a Pilatus II 100 K area detector was used with an incident X-ray energy = 20 keV (λ = 0.62 Å), and a ~100 μm beam diameter. For these measurements, 3×3 mm^2 LSCO channels were used on 10×10 mm^2 substrates, as shown in Fig. 2.10(a). These larger channels were used so that sequential measurements could be performed on different channel areas, as repeated scanning caused beam damage (which is discussed in more detail in Chapter 4). Also note that the channel electrode geometry in this case consisted of electrodes angled toward the corner of the substrate. These electrodes were designed this way to maximize the available incident and diffracted beam paths, as the soldered connections could have created significant impediments. The sample was mounted to the cold-finger cryostat using silver paint (being careful not to create electrical shorts) and the four cryostat wires were In-soldered directly to the sample, as shown in Fig. 2.10(b). Note that the cryostat only had four wires, making four-terminal channel resistance measurements impossible (at least one wire is needed for the gate). Instead, a simple two terminal measurement was performed as shown in Fig. 2.10(a). This *in situ* monitoring of the LSCO channel was used to ensure the expected gating effects occurred. Prior to applying the gel, the sample was aligned in the X-ray beam in air. For all measurements the sample was in a vacuum (< 10^{-5} Torr) environment and all gate V_gs were applied at temperatures between 280 and 290 K for 30 min. The measuring temperature for SXRD was 150 K in order to mitigate beam damage of the sample, which is discussed in more detail in Chapter 4.

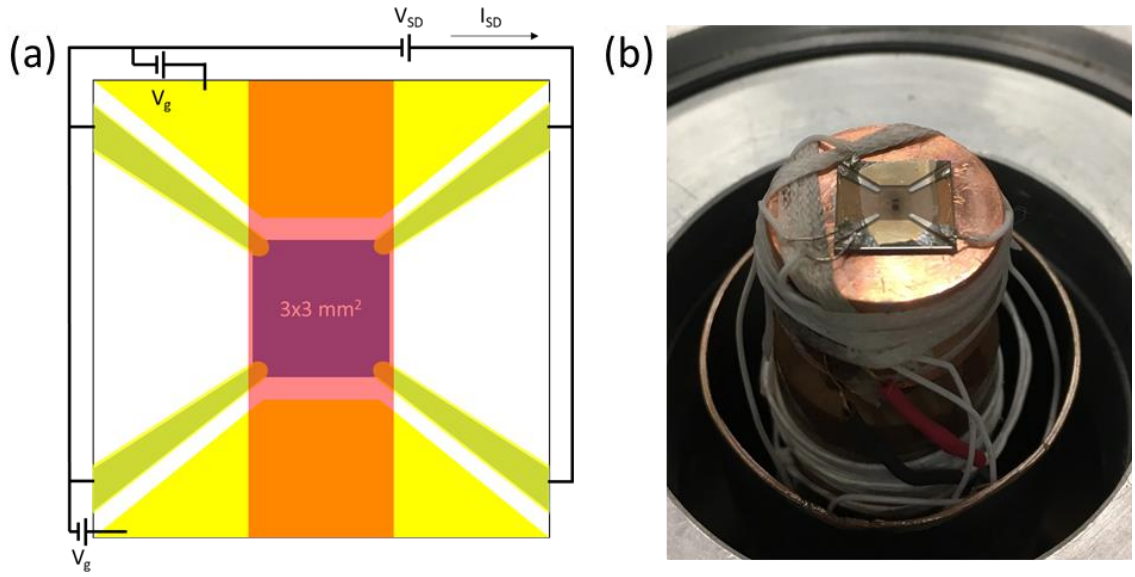

Fig. 2.10. (a) Device schematic for a 3×3 mm^2 channel on a 10×10 mm^2 substrate. The $La_{1-x}Sr_xCoO_3$ film, exposed substrate, electrodes, and ion gel are represented by the colors blue, white, yellow, and red, respectively. The source drain bias (V_{SD}) and current (I_{SD}) were used to calculate the two-terminal resistance across the channel (V_{SD}/I_{SD}) and the gate bias (V_g) was applied to both gate pads. (b) Photograph of a device mounted on the 33-ID beamline at the Advanced Photon Source.

2.5 In operando polarized neutron reflectometry

In operando polarized neutron reflectometry (PNR) measurements were performed on the Polarized Beam Reflectometer at the NIST Center for Neutron Research (Chapter 4) and the Magnetism Reflectometer at the Spallation Neutron Source at Oak Ridge National Laboratory (Chapter 6). Neutron reflectometry principles are very similar to the GIXR principles discussed in Section 2.2.1, but with ρ_{xray} and b_i in Eq. 2.5 replaced by the nuclear SLD (ρ_n) and the *neutron* scattering length contribution from each atom, respectively. The scattering of neutrons is fundamentally different than X-rays, however, with their chargeless and massive nature resulting in scattering from nuclei as opposed to electrons. Neutrons thus have much higher penetrating power compared to X-rays and a much weaker atomic number dependence of b_i, leading to higher sensitivity to some lighter elements. In fact, unlike the X-ray case where b_i can be predicted quantitatively (Eq. 2.5), atomic neutron scattering lengths are more difficult to theoretically predict, but can be looked up in data tables [123]. The penetrating nature of neutrons proved critical for *in operando* characterization of LSCO EDLTs, as they were able to penetrate the thick overlying ion

gels. Further, neutrons possess a magnetic moment, thus making neutron reflectometry sensitive to *M* depth profiles. The magnetic SLD (ρ_m) is given by

$$\rho_m = CM \quad 2.11,$$

where *C* (2.853×10^{-9} $Å^{-2}cm^3/emu$) is a dimensional physical constant that converts magnetization to a magnetic scattering length. The manner in which ρ_m adds to the ρ_n depends on the relative orientation of the film's magnetization and the spin axis of polarization of the incident neutron beam, as well as whether the neutron spin direction is preserved (non-spin-flip) or reversed (spin-flip) in the scattering event. For non-spin-flip interactions with the neutron polarization in the film plane, ρ_m is simply additive to the nuclear SLD and sensitive to the sample magnetization component parallel ($M_{//}$) to the neutron polarization axis. For spin-flip interactions with the neutron polarization in the film plane, ρ_m is adds to the nuclear SLD in complex fashion and is sensitive to the sample magnetization component perpendicular ($M_{\perp}$) to the neutron polarization axis Note that none of the four reflectivity channels are sensitive to any component of *M* perpendicular to the film plane (*i.e.*, parallel to ***Q***). The four possible reflectivity channels are, therefore, two non-spin-flip channels (R^{++} and R^{--}) and two spin-flip channels (R^{+-} and R^{-+}), where (+) and (-) indicate the incident (left) and reflected (right) neutron beam polarization. Their respective SLDs are given by

$$\rho^{++} = \rho_n + \rho_m \quad 2.12,$$

$$\rho^{+-} = \rho_n - i\rho_m \quad 2.13,$$

$$\rho^{-+} = \rho_n + i\rho_m \quad 2.14, \text{ and}$$

$$\rho^{--} = \rho_n - \rho_m \quad 2.15.$$

In practice, the (+) neutron polarization direction is set parallel to the applied *B*. Furthermore, if measurements are performed in a saturating *B*, the non-spin-flip components vanish ($M_{\perp} = 0$). Therefore, by measuring R^{++} and R^{--} in saturating in-plane *B* and simultaneously fitting both of these channels using software such as Refl1D, the depth profiles of ρ_n and ρ_m can be extracted.

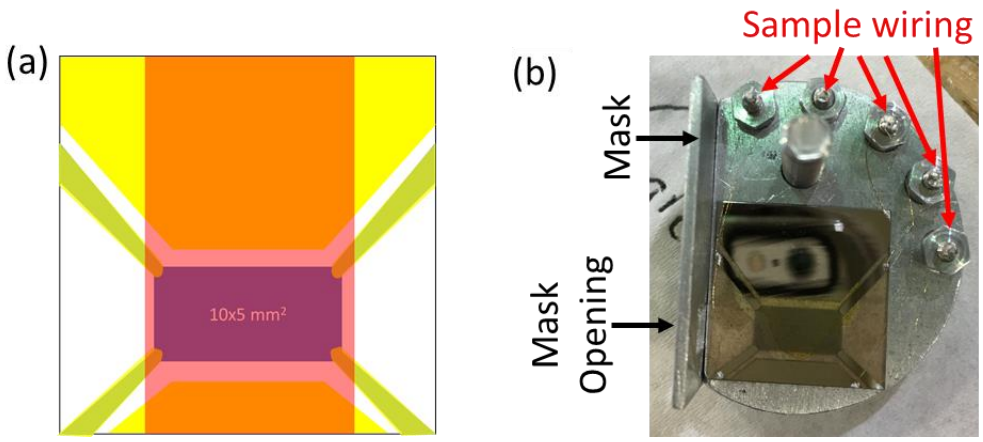

Fig. 2.11. (a) Device schematic for a 10×5 mm^2 channel on a 20×20 mm^2 substrate. The $La_{1-x}Sr_xCoO_3$ film, exposed substrate, electrodes, and ion gel are represented by the colors blue, white, yellow, and red, respectively. (b) Photograph of a device mounted on the sample holder for the Polarized Beam Reflectometer at the NIST Center for Neutron Research.

For the *in operando* PNR measurements performed on the Polarized Beam Reflectometer at the NIST Center for Neutron Research (Chapter 4), 10×5 mm^2 LSCO channels on 20 × 20 mm^2 LAO substrates were used, as shown in Fig. 2.11(a). The LSCO channel was offset from the substrate center because the 3 T magnet on the beamline causes depolarization of the neutron beam, which is minimized when offset from the center of the beam path. The sample was mounted on a borated-aluminum sample holder with silver paint, and rigged with the beam mask shown in Fig. 2.11(b). This beam mask was used to mask the gate and channel electrodes from the neutron beam. Two 5×5 mm^2 exposed LAO substrate regions remained in the beam path, however, and had to be included in the reflectivity fitting (discussed in Chapter 4). Both non-spin-flip channels were measured in specular geometry (with non-specular reflectivity subtracted) using a monochromated (4.75 Å) neutron beam at 30 K (well below $T_C \approx 220$ K) in a 3 T in-plane B. The sample was in a vacuum (< 10^{-5} Torr) environment and all V_gs were applied at temperatures between 280 and 290 K for 30 min. An Fe/Si supermirror and an Al-coil spin flipper were used to select the spin state of the incident neutron beam either parallel (+) or antiparallel (-) to the magnetic field. A second supermirror and flipper assembly were used to select the spin state of the scattered neutron beam. The non-spin flip cross sections, (+ +) and (- -) are sensitive to the depth profiles of the nuclear scattering length density and the projection of the magnetization parallel to the applied field.

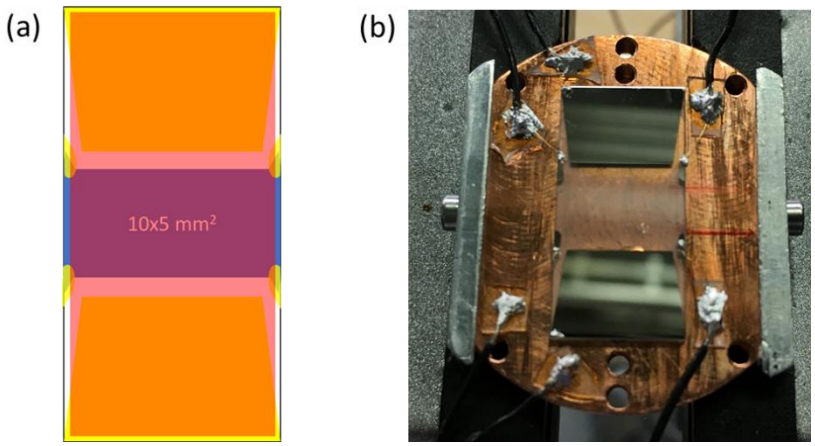

Fig. 2.12. (a) Device schematic for a 10×5 mm^2 channel on a 10×20 mm^2 substrate. The $La_{1-x}Sr_xCoO_3$ film, exposed substrate, electrodes, and ion gel are represented by the colors blue, white, yellow, and red, respectively. (b) Photograph of a device mounted on the sample holder for the Magnetism Reflectometer at the Spallation Neutron Source at Oak Ridge National Laboratory.

For the *in operando* PNR measurements performed on the Magnetism Reflectometer at the Spallation Neutron Source at Oak Ridge National Laboratory (Chapter 6), 5×10 mm^2 LSCO channels on 10×20 mm^2 SLAO substrates were used, as shown in Fig. 2.12(a). Note that this sample geometry eliminates the exposed substrate regions. The sample was mounted on a copper sample holder with GE varnish. In this case, slits on the beamline were used to mask the gate and channel electrodes from the neutron beam. Measurements were performed at 30 K in a 1 T in-plane *B*. The sample was in a vacuum (< 10^{-5} Torr) environment and all gate V_gs were applied at temperatures between 280 and 290 K for 30 min. Both non-spin-flip channels were measured in specular geometry (with non-specular reflectivity subtracted). The spallation source produces neutron pulses as opposed to the continuous neutron beam produced by the reactor source and the NCNR. Instead of determining the neutron wavelength using monochromation, the time at which the neutrons arrive at the detector is used to determine that specific neutron's wavelength (those arriving first are traveling faster and have a smaller wavelength). In this case, 30 Hz neutron beams were used. With a range of neutron wavelengths arriving with each pulse, only a small subset of 2θ values are required to cover the desired *Q* range. A typical set of 2θ values, wavelength ranges (chosen with choppers on the beamline), and counting times is shown in Table 2.2. The corresponding R^{++} (R^{--} was left off this plot for clarity) *vs*. *Q* subsets that were stitched together and the final re-binning of the data are shown in Fig. 2.13.

Table 2.2. Scan parameters used on the Magnetism Reflectometer at the Spallation Neutron Source at Oak Ridge National Laboratory (Chapter 6), where 2θ was the detector angle, λ was the center wavelength (the typical range was λ ± 2 Å), and c_t is the estimated counting time (note that some of the large 2θ scans were stopped short of the full c_t).

2θ (°)	0.55	0.55	0.78	1.09	1.52	2.13	2.56	2.98	3.58	4.17	5.02	5.84
λ (Å)	8.2	5.7	5.7	5.7	5.7	5.7	5.7	5.7	5.7	5.7	5.7	5.7
c_t (min)	20	20	40	60	90	150	210	240	300	360	480	600

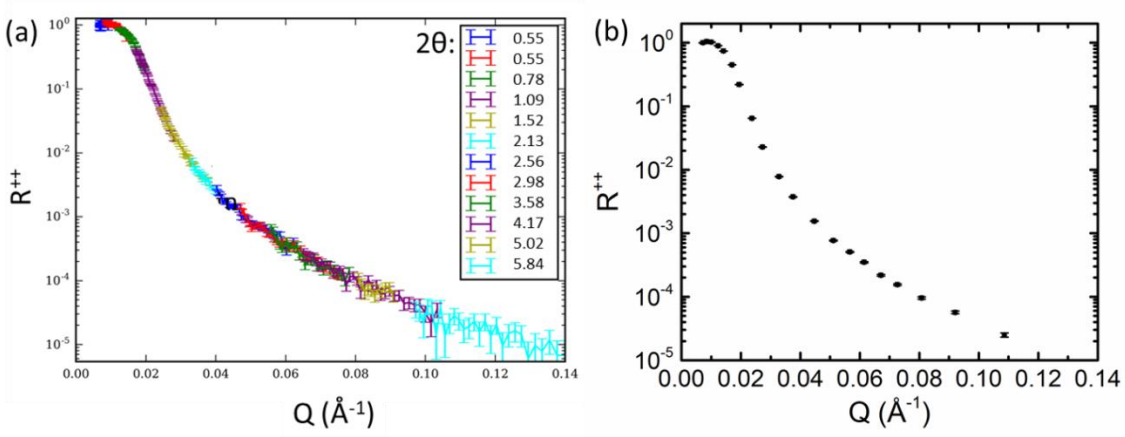

Fig. 2.13. The ++ channels of reflectivity (R^{++}) *vs*. scattering vector magnitude (Q) from a 6 unit cell thick x = 0.5 $La_{1-x}Sr_xCoO_{3-\delta}$ device at gate bias of -3 V, magnetic field of 1 T, and temperature of 30 K (the same data shown in Chapter 6), including the individual subsets at different detector angles (2θ) corresponding to the values in Table 2.2 in (a) and the final re-binning of the data in (b).

Chapter 3: Electrostatic *vs*. electrochemical doping and control of ferromagnetism in ion-gel-gated ultrathin $La_{0.5}Sr_{0.5}CoO_{3-\delta}$

This chapter is mainly based on the publication "*Electrostatic vs. electrochemical doping and control of ferromagnetism in ion-gel-gated ultrathin* $La_{0.5}Sr_{0.5}CoO_{3-\delta}$" in ACS Nano (2016) by Jeff Walter, Helin Wang, Bing Luo, C. Daniel Frisbie, and Chris Leighton, adapted with permission from Ref. [124], copyright (2016) American Chemical Society. In this chapter, we address the first and third open issues in electrolyte gating discussed in Section 1.2.2 (*i.e.*, the poorly understood electrostatic *vs*. electrochemical gating mechanisms in oxide EDLTs and application of electrolyte gating to controlling magnetic material properties). Electrolyte gating is applied to ultrathin epitaxial films of $La_{0.5}Sr_{0.5}CoO_{3-\delta}$. While this material is heavily hole-doped, and is therefore expected to exhibit modest gate-induced changes even in EDLTs, the detailed knowledge of the *x*-dependent electronic properties in LSCO (including in ultrathin films) provides an excellent platform for an improved understanding of the mechanisms of gating. Careful transport studies reveal that the application of negative gate bias leads to a reversible resistance decrease, at least to some threshold voltage, consistent with reversible hole accumulation, *i.e*., predominantly electrostatic operation. Application of positive bias, on the other hand, immediately leads to large irreversible resistance increases, which experiments in inert and O_2 atmospheres (supported by atomic force microscopy and X-ray photoelectron spectroscopy) show unequivocally to be due to V_O formation. It is argued that this asymmetry in electrostatic *vs*. electrochemical response can be understood based on the known redox instability of this hole-doped oxide, with important general implications for *p*- and *n*-type oxides. Voltage control of electronic/magnetic properties is then demonstrated under hole accumulation, including resistivity, magnetoresistance, and Curie temperature, T_C. The large anomalous Hall coefficient and perpendicular magnetic anisotropy in these LSCO films (which arises due to the use of LAO(001) substrates that apply compressive stress) are shown to provide a particularly powerful probe of magnetism, enabling direct extraction of the voltage-dependent order parameter and T_C shift. The latter is found to be 12 K (7 %), which we argue should grow considerably at lower *x*.

3.1 Temperature and gate bias windows

A schematic of the device used in this study is shown in Fig. 3.1(a). Details on LSCO growth and device fabrication are included in Section 2.3 but, briefly, 8-unit-cell-thick epitaxial films of x = 0.5 LSCO were deposited on LAO(001) substrates *via* high pressure oxygen reactive sputter deposition. At these high x values bulk LSCO is a heavily hole-doped ferromagnetic metal with $T_C \approx 250$ K and low temperature (T) single crystal resistivity, $\rho \approx 75$ μΩcm [9,88,89,94]. The 8-unit-cell films used here also exhibit ferromagnetic metallic behavior, but with $T_C \approx 170$ K and low temperature $\rho \approx 175$ μΩcm. The suppressed T_C and increased ρ occur due to the dead-layer effects that suppress ferromagnetic/metallic behavior in ultrathin film perovskites. In LSCO we have shown that this is due to strain-induced V_O ordering, which increases the V_O density, thus depleting holes [95,107,109]. The small compressive lattice mismatch on LAO(001) (1.2 %) minimizes this V_O formation/hole depletion (compared to tensile strain on STO(001) for example), and these ultrathin film properties thus compare favorably to those on most other substrates. Note that ultrathin films are employed here to maximize the effects of surface charge density modulation by gating, and minimize current shunting from the sub-surface region. In this context, simple estimates of the Thomas-Fermi screening length yield values of just 1-3 unit cells in LSCO50, highlighting the near-surface nature of the induced changes in EDLTs.

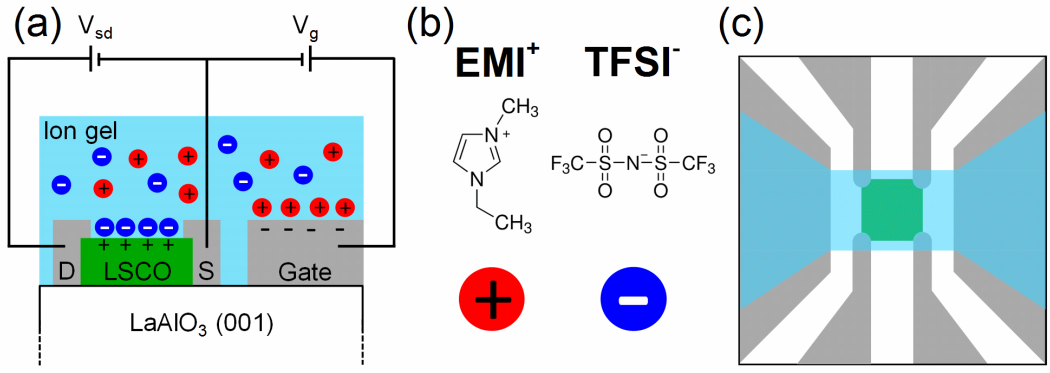

Fig. 3.1. (a) Side view schematic of the ion-gel-gated electric double layer transistors. "LSCO" designates $La_{0.5}Sr_{0.5}CoO_{3-\delta}$, S/D/Gate are the metallic source/drain/gate electrodes, and V_{sd}/V_g are the source-drain/gate voltages, respectively. The red/blue charges are the cations/anions of the ion gel, and the +/– indicate holes/electrons. (b) Molecular structures of the cations and anions in the ion gel (EMI:TFSI). (c) Top view device schematic; the $LaAlO_3$(001) substrate measures 5 × 5 mm^2, the LSCO channel 1 × 1 mm^2. The color scheme is identical to (a), *i.e.* blue ion gel, gray electrodes, green LSCO, and white $LaAlO_3$ substrate.

To form EDLTs, LSCO channels were patterned to 1×1 mm^2 using Ar ion milling, followed by DC magnetron sputtering of Mg(5 nm)/Pt(50 nm) channel and gate electrodes. Mg was chosen for its known Ohmic contact properties with LSCO [95] and Pt was selected for the gate due to its large work function, which enhances hole accumulation at negative V_g. Immediately prior to loading such channels for measurement, a "cut and stick" ion gel [55] consisting of the ionic liquid EMI:TFSI (Fig. 3.1(b)) and the polymer P(VDF-HFP) was applied to the surface, straddling the channel and gate electrodes (see Fig. 3.1(c)). These ion gels are a relatively recent advance, providing the benefits of solid-state materials while maintaining very high capacitance [55,59,61]. In this case the addition of only 20 wt. % P(VDF-HFP) to EMI:TFSI results in a rubbery solid that is easy to handle and amenable to a side-gated device architecture (Fig. 3.1(a) and (c)), while maintaining ~ 90 % of the specific capacitance of the pure ionic liquid. We note that we employ here a side-gate geometry (see Fig. 3.1(a) and (c)), which results in relatively slow gating dynamics, as returned to below.

The first set of transport measurements performed (Fig. 3.2) aimed to establish the T window over which gating is effective. In ionic-liquid- or ion-gel-based EDLTs a lower limit for gating exists due to the ionic mobility diminishing on cooling, bounded in pure ionic liquids by the freezing point. Below this the electric field in the EDL is frozen-in and cannot typically be dynamically tuned; rewarming above the freezing point is required to change the V_g-controlled surface carrier density. Particularly in oxide devices, literature observations suggest that operation at too *large* a T is also problematic, due to deleterious electrochemical reactions [37]. To probe this possibility in our case, the time (τ) dependence of the LSCO channel resistance drift ($\Delta R/R_0$) at $V_g = 0$ was measured between 200 and 300 K, the inset to Fig. 3.2(a) showing an example at 298 K. Even without application of bias the channel resistance drifts upwards linearly with t (the solid line is a fit to $\Delta R/R_0 = A(T)*\tau$), which is taken as an indication of continuous degradation of the LSCO. The T dependence of the drift rate A is plotted in the main panel to Fig. 3.2(a), showing that this degradation is slowed dramatically by cooling. It should be noted here that even at $V_g = 0$ the band alignment in these Pt/ion gel/LSCO devices may result in a built-in electric field at the ion gel/LSCO interface, potentially accelerating electrochemical reactions. Further insight into this electrochemical degradation is provided

below, although we note immediately that reduction of the LSCO would be qualitatively consistent with the positive drift in $\Delta R/R_0$. In any event, Fig 3.2(a) demonstrates that this degradation can be effectively mitigated by cooling, $\Delta R/R_0$ falling to < 0.5 %/hr at 275 K. All data in this paper were thus taken after rapid cooling to 275 K or below.

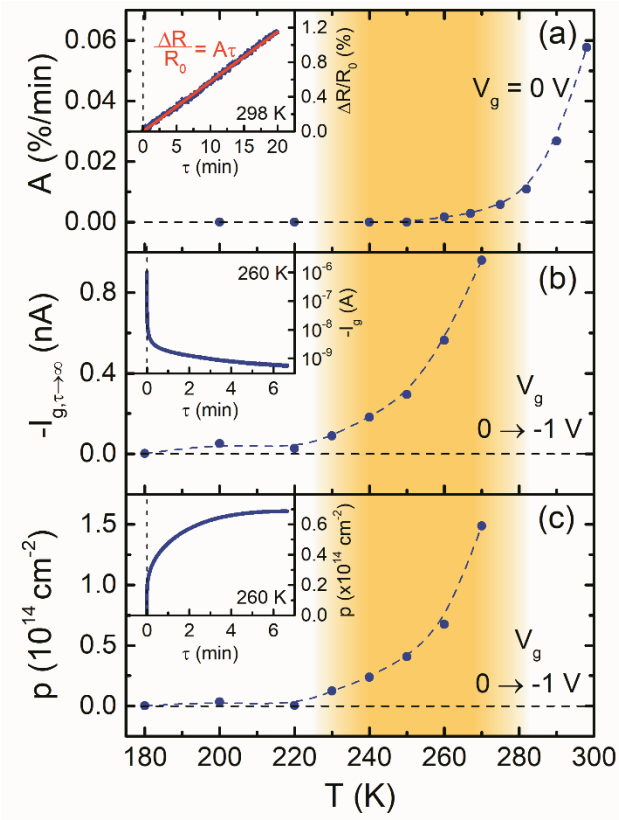

Fig. 3.2. Temperature (T) dependence of (a) the zero bias resistance creep coefficient, A, (b) the long time (τ) gate leakage current ($I_{g,\tau\to\infty}$) at V_g = -1 V, and (c) the deduced injected hole density, p, at V_g = -1 V. The parameter A is defined in the inset to (a), which shows the time dependence of the relative resistance change $\Delta R/R_0$ at 298 K. The insets to (b) and (c) show the time dependence of I_g and p, respectively, due to a V_g step from 0 to -1 V at 260 K. The shaded yellow region marks the optimal temperature window for gating.

In order to establish the *lower* bound for the effective T window for gating, a simple probe of ion mobility was performed. This was achieved by abruptly stepping V_g from 0 to -1 V at a given T then measuring the subsequent time evolution of the gate current, I_g. An example is shown in the inset to Fig. 3.2(b) at T = 260 K, the initial current (essentially the gate displacement current) gradually falling off to a constant in the long time limit ($I_{g,\tau\to\infty}$). As shown in the main panel of Fig. 3.2(b), $I_{g,\tau\to\infty}$ is strongly T-dependent, rising above ~ 230 K, but remaining below 1 nA even at 275 K. We associate this current with the onset of ionic mobility near 230 K. That this mobility is sufficient to enable accumulation of

large charge densities at the LSCO surface in reasonable times (< 10 min) is confirmed in Fig. 3.2(c), which plots the transferred charge normalized by the channel area (A_c), which we denote by

$$p = -\frac{1}{eA_c}\int_0^{10\ \mathrm{min}} I_g d\tau \qquad 3.1.$$

An example is shown in the inset to Fig. 3.2(c) at 260 K, where p saturates at ~ 0.7×10^{14} cm^{-2} after application of -1 V. The main panel to Fig. 3.2(c) reveals that p indeed turns on quickly above ~ 230 K, consistent with Fig. 3.2(b), establishing the lower T bound for effective gating. As indicated by the shaded yellow region in Fig. 3.2, the effective T window for electrolyte gating in these LSCO/EMI:TFSI devices is thus between ~ 230 and 275 K. Use of larger magnitudes of negative gate biases than -1 V does not effect this window.

With the T window established, attention was turned to the response to V_g, the goal being to understand the limits for electrostatic *vs*. electrochemical operation. One simple approach is to probe the reversible and irreversible responses of the channel resistance, R, to application and removal of various magnitudes and polarities of V_g. This was initially done in vacuum (< 10^{-4} Torr), the concept being that any V_g application resulting in V_O formation in LSCO (an obvious possibility given prior work) is likely to create an irreversible R change in such a low O_2 pressure environment. $V_g(\tau)$ profiles designed to probe this are shown in Fig. 3.3(a), where V_g is stepped from 0 to -1 V (red curve), 0 to -3.5 V (blue curve), and 0 to +0.5 V (green curve) for 30 mins, before returning to 0 V. The corresponding changes in LSCO channel resistance (ΔR) at T = 260 K are shown in Fig. 3.3(b). R indeed decreases upon application of V_g < 0 (*i.e.*, ΔR is negative), with the magnitude of ΔR increasing from -1 to -3.5 V, consistent with accumulation of additional holes at the LSCO surface. At this temperature, ΔR reaches -16.6 % at V_g = -3.5 V after 30 mins. In terms of dynamics, the responses seen here are relatively slow, consistent with other ionic liquid/gel studies employing low temperatures to minimize degradation [37], likely exacerbated in our case by the side-gate geometry. While for V_g = -1 V (red curve) the resistance change is completely reversible (*i.e.*, ΔR quickly returns to zero after V_g removal), after the application of -3.5 V (blue curve) the resistance recoils to a positive ΔR

when V_g is removed, *i.e.*, the channel resistance is irreversibly *increased* by application and removal of V_g. We thus parameterize the channel response to V_g in terms of a gate-induced resistance change, ΔR_{gate}, and an irreversible resistance change *after removal of the bias*, ΔR_{irrev}, as illustrated in Fig. 3.3(b). For the V_g = + 0.5 V case, *i.e.*, positive bias, the resistance increases on gate application, as expected, but again does not return to the starting value after bias removal; ΔR_{irrev} is again present and is positive.

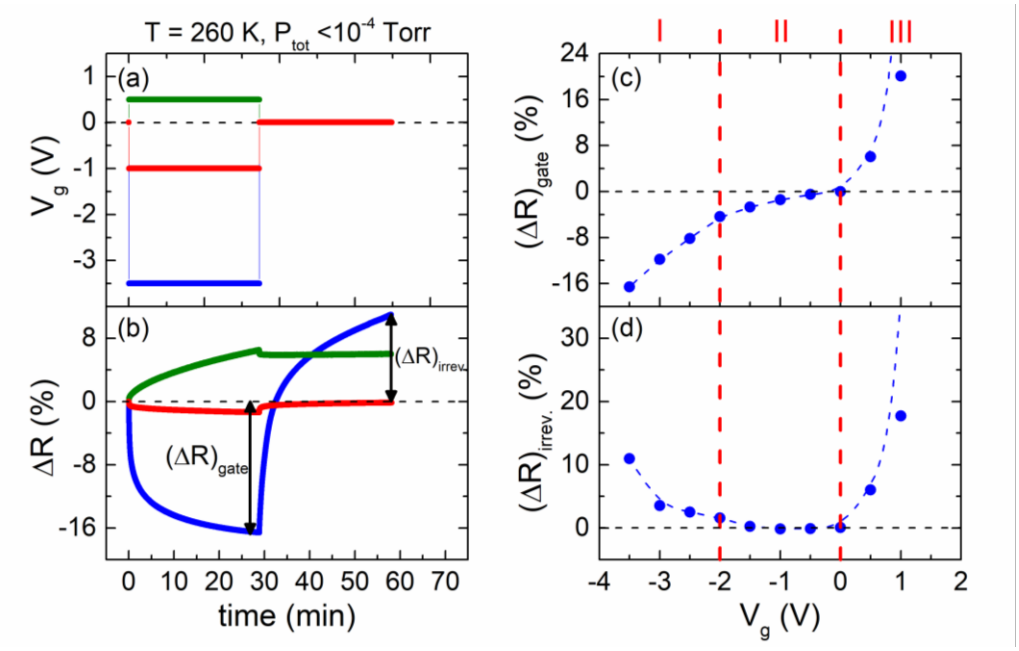

Fig. 3.3. Time dependence of (a) gate voltage (V_g) and (b) the resistance change, ΔR, due to gate bias steps from 0 to -1 to 0 V (red), 0 to -3.5 to 0 V (blue), and 0 to +0.5 to 0 V (green). V_g dependence of (c) the reversible gate-induced resistance change, $(\Delta R)_{gate}$, and (d) the irreversible resistance change, $(\Delta R)_{irrev}$; blue dashed lines are guides to the eye. Definitions of $(\Delta R)_{gate}$ and $(\Delta R)_{irrev}$ are illustrated in (b) for the V_g = -3.5 V curve (blue). All data were taken at 260 K and P_{tot} < 10^{-4} Torr. The dashed vertical lines in (c) and (d) separate Regimes I, II and III.

The V_g dependences of ΔR_{gate} and ΔR_{irrev} are shown at 260 K in Fig. 3.3(c) and (d), for both bias polarities. It should be noted here that, generally, channel resistance lowering for V_g < 0 could be interpreted electrostatically, in terms of hole accumulation, or electrochemically, in terms of oxidation (*e.g.*, annihilation of V_O's, or even formation of O interstitials [125]). Conversely, resistance increases at V_g > 0 could be interpreted electrostatically, in terms of hole depletion (electron accumulation), or electrochemically, in terms of reduction (*i.e.*, V_O creation). What is actually observed in Fig. 3.3(c) and (d) is three distinct regimes of operation, and a strong asymmetry between positive and negative V_g. The simplest regime occurs at small negative gate bias, -2 V < V_g < 0 V, which we label

Regime II. In this regime ΔR_{gate} increases in magnitude with increasingly negative V_g, with negligible ΔR_{irrev} in these *in vacuo* experiments. Given the relatively rapid and largely reversible response, we associate this regime simply with hole accumulation, *i.e.*, predominantly electrostatic operation. Further evidence of electrochemical inactivity in this regime is provided below. Larger negative biases (V_g < -2 V) induce entry into Regime I, which is characterized by significantly larger magnitudes of ΔR_{gate}, but also non-negligible ΔR_{irrev}. At -3.5 V for instance, an R change of -16.6 % is achieved, but with an irreversible increase of 11 % after removal of V_g. This irreversibility at sufficiently negative V_g is of course suggestive of electrochemical effects, for which we present further evidence below. We note for now, however, that in terms of LSCO redox reactions, enhanced negative ΔR_{gate} would require gate-induced oxidation beyond the initial formal Co valence of 3.5+. Given the instability of Co^{4+} in the octahedral environment in perovskites, which is responsible for facile V_O formation in LSCO at x > 0.5 [98,99,126], this is indeed likely to result in electrochemical instability after removal of V_g, consistent with the positive ΔR_{irrev}. Unlike the transition between Regimes I and II, the transition to Regime III (V_g > 0) is abrupt. Specifically, essentially *any* V_g > 0 induces a regime in which essentially all of the gating effect is irreversible, *i.e.*, $\Delta R_{gate} \approx \Delta R_{irrev}$. R does increase with V_g, as expected for hole depletion, but the strong irreversibility clearly suggests the formation of V_Os, further supported by measurements presented below.

3.2 Gas environment dependence

Summarizing Fig. 3.3(c) and (d), three regimes exist. In Regime I (V_g < -2 V) a significant gating effect is found, of the expected polarity, but with substantial irreversibility after V_g removal *in vacuo*, suspected to be due to electrochemistry. In Regime II (-2 V < V_g < 0 V), completely reversible gate effects are observed, in accord with simple electrostatic operation. Finally, in Regime III (V_g > 0 V) highly irreversible gate-induced increases in R are found, likely due to V_O creation. In order to confirm the suspected roles of V_g-induced redox electrochemistry, measurements were performed in other environments. Specifically, Fig. 3.4 shows transport data (*i.e.*, $\Delta R_{gate}(V_g)$ and $\Delta R_{irrev}(V_g)$) taken in both inert (Ar and He) and O_2-rich environments, a temperature of 275 K being selected to enhance effects due to electrochemical reactions. In each case the total

pressure was 1 atm, pure in the cases of Ar and He, and 50 % O_2 / 50 % He for the O_2-rich case. The first noteworthy point is that the responses seen in Ar and He are not only similar to one another, but also similar to vacuum. The same three V_g regimes are in fact present: Small negative V_g induces a small negative R change with negligible irreversibility after V_g removal, larger negative V_g induces larger R decreases but with significant irreversible R increase after V_g removal, and essentially any positive V_g induces large, predominantly irreversible R increases. While some quantitative differences between Ar and He are apparent, particularly at positive bias, these are within sample-to-sample variations at 275 K, where the V_g-induced electrochemical effects are strong. We view it as unsurprising that some level of variance in results is obtained in positive bias, under reducing conditions, at elevated temperatures.

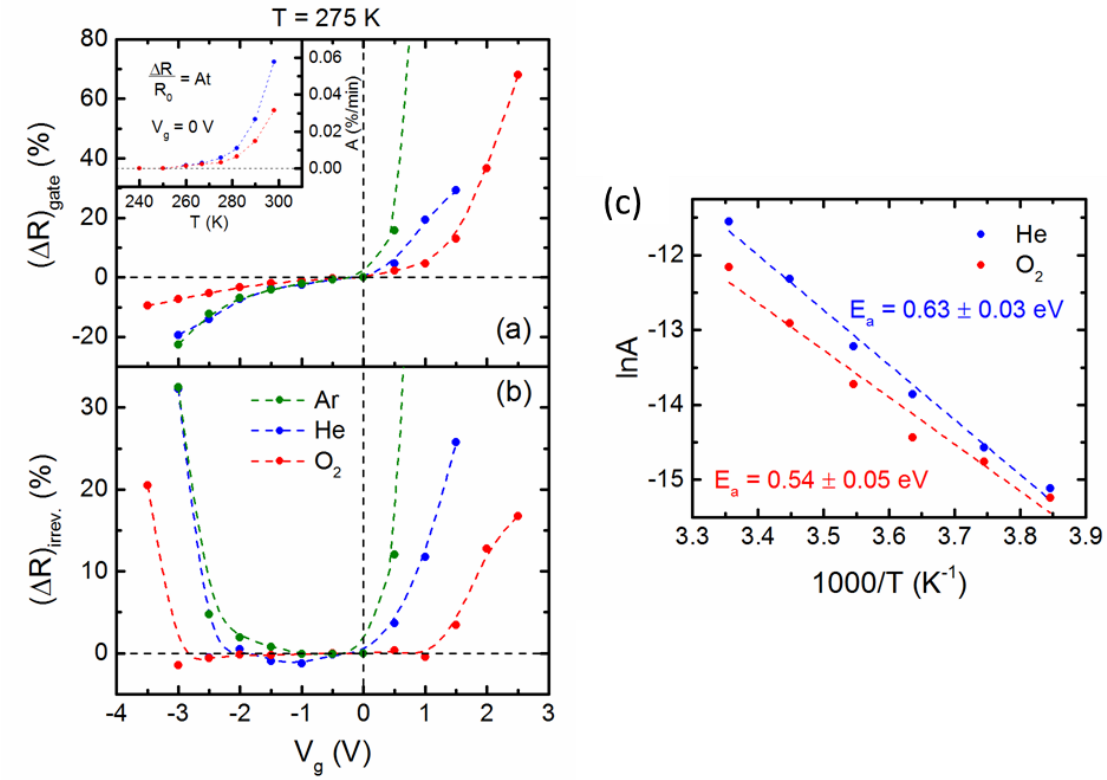

Fig. 3.4. 275 K gate voltage dependence of (a) $(\Delta R)_{gate}$, and (b) $(\Delta R)_{irrev}$, in Ar, He, and O_2 (green, blue, and red, respectively) atmospheres. The total pressure for all cases was 1 atm; pure in the cases of Ar and He, whereas the O_2 case was 0.5 atm of O_2 and 0.5 atm of He. The inset shows the T dependence of the coefficient A in He and O_2. (c) Arrhenius plot of the temperature dependence of the zero gate bias resistance drift ($A(T)$ in $\Delta R/R_0 = A(T)*time$) in both He and O_2 atmospheres, from the inset of panel (a). The corresponding activation energies, E_a, in each case (0.63 ± 0.03 eV and 0.54 ± 0.05 eV for He and O_2 respectively) are labelled on the plot.

Significant differences are observed in an O_2-rich environment, however. Specifically, the high V_g response in ΔR_{gate} is suppressed for both polarities, accompanied by a substantial widening of the V_g window over which ΔR_{irrev} is negligible. This window in fact widens to -3 V < V_g < +1 V (from -2 V < V_g < 0 V in vacuum), strong evidence that O_2 suppresses the relevant electrochemical reactions. Specifically, we propose that under large negative V_g the availability of oxygen suppresses V_O formation *after* removal of the gate bias, while for positive V_g the presence of oxygen suppresses V_O formation *during* application of the bias. As in prior work [50–52], these mechanisms rely on oxygen diffusion through the ionic liquid/gel. As a final piece of evidence for the role of redox electrochemistry, in the inset to Fig. 3.4(a) we show the equivalent of Fig. 3.2(a) (*i.e.*, V_g = 0 channel resistance drift data), taken in both He (blue) and O_2-rich (red) environments. The presence of O_2 suppresses the zero bias R drift by a factor of ~2, strong evidence that the degradation in channel resistance at elevated T is indeed due to V_O formation. Although the T range probed is modest, the drift rate (A) follows Arrhenius behavior, as shown in Fig. 3.4(c); the activation energy shifts from 0.63 ± 0.03 eV in He to 0.54 ± 0.05 eV in O_2.

3.3 *Ex situ* characterization

With the division between electrochemical and electrostatic gate response better understood, the impact on LSCO surface morphology was probed *via* contact-mode atomic force microscopy (AFM), performed before and after V_g application (Fig. 3.5). Fig. 3.5(a) first shows the as-grown LSCO surface before application of an ion gel, which presents unit-cell-high step edges separating ~150-nm-wide atomically-smooth terraces. Fig. 3.5(b) shows the morphology after application of the gel, maintaining V_g = 0 at 260 K, then subsequently removing the gel with tweezers and sequential sonication in acetone and methanol. Aside from minor degradation, minimal changes in morphology are observed. After the application of V_g = -3.5 V and subsequent gel removal, however, a distinct morphology change is observed, particles of diameter ~100 nm forming on an otherwise unperturbed LSCO surface. As supported by spectroscopic results below, we believe this debris to be remnant ion gel; that there is higher surface coverage of this residual gel in Fig. 3.5(c) compared to (b) suggests stronger interaction between the gel and LSCO film under larger negative V_g.

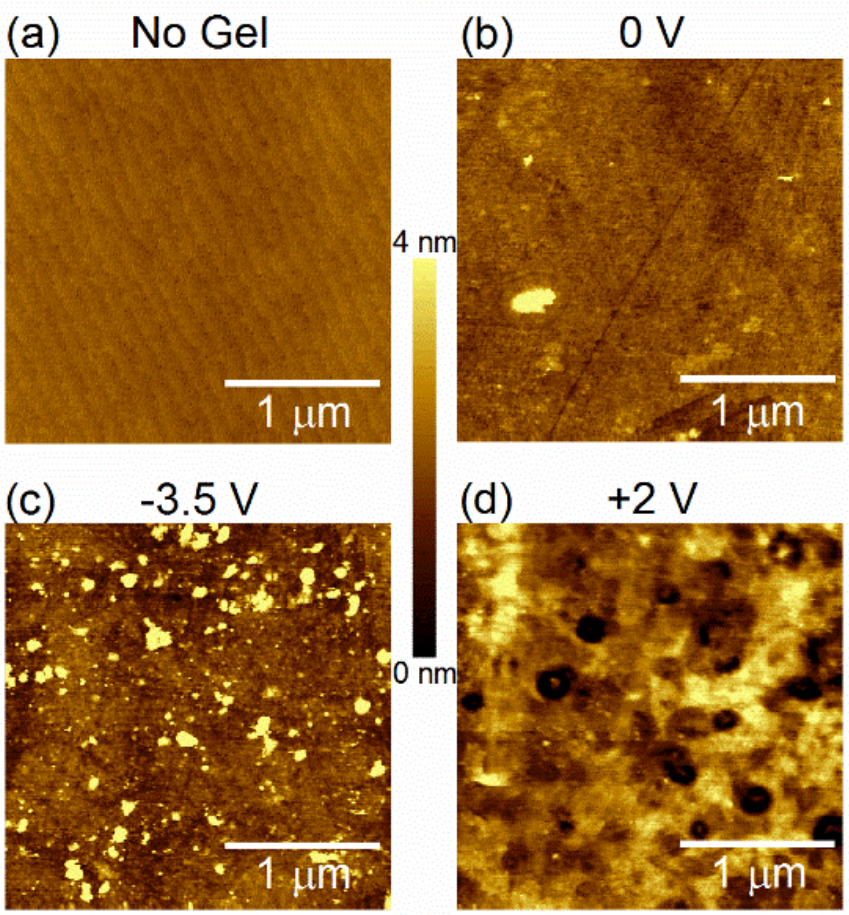

Fig. 3.5. Contact mode atomic force microscopy (AFM) height images (2.5 × 2.5 μm^2) of the surfaces of an LSCO channel (a) before application of the ion gel, (b) after applying the gel but maintaining V_g = 0, (c) after applying V_g = -3.5 V, and (d) after applying V_g = +2 V. The height scale (center) is the same for all images. All gate voltages mentioned were applied at 260 K.

Consistent with the data of Fig. 3.3 and 3.4, it is application of positive bias (V_g = +2 V, Fig. 3.5(d)) that induces the most dramatic changes. In this case conspicuous differences in morphology occur after gating, the LSCO developing an inhomogeneous porous structure, with pits of diameter 50-200 nm. While an accurate determination of the average depth of these is difficult with contact-mode AFM, our best estimate lies at 3.1 nm, indistinguishable from the film thickness (8 unit cells, 3 nm), suggesting that the pits penetrate the entire film. Given the conclusions above regarding large irreversible R increases and V_O formation at positive V_g, we associate these pits with local regions that have undergone particularly strong reduction, eventually leading to etching. The areal density of the pits from AFM is ~10^8 cm^{-2} which we note is (*a*) similar to typical dislocation densities in complex oxide substrates [127], and (*b*) similar to the etch pit density, and thus

inferred threading dislocation density, found from experiments on the specific substrates used here. The latter employed a 3 M nitric acid solution, generating an etch pit density of ~10^8 cm^{-2} after 1 hour at 95°C. It is thus plausible that the pits in Fig. 3.5(d) are associated with enhanced electrochemical etching at dislocations. While electrochemical etching with ionic liquids has recently been reported to modify the superconducting transition temperature *via* thickness reduction in FeSe films [128], little appears to be known about etching mechanisms, lateral uniformity, *etc*. Further work in this area would be beneficial.

Continuing with structural and chemical characterization before and after V_g application, Fig. 3.6 shows X-ray photoelectron spectroscopy (XPS) data from the same devices highlighted in Fig. 3.5. Wide binding energy (BE) range scans of each film (*i.e*., no gel applied; gel applied, V_g = 0; V_g = -3.5 V; V_g = +2.0 V) were first recorded, and are shown in Fig. 3.6(a-d). Peaks from LSCO are labeled in red, the gray labels corresponding to contaminants, specifically Pt, In, C, and F. While Pt, In, and C are attributable to the contact pads, residual In solder from those pads, and atmospheric exposure, respectively, the F 1s peak at 684 eV is of higher interest. This peak appears only after gel application and removal (compare Fig. 3.6(a) with 3.6(b-d)). Given that both the TFSI anion and P(VDF-HFP) polymer in the ion gels used here contain F, we ascribe this to the residual ion gel suggested from the AFM images in Fig. 3.5(b) and (c).

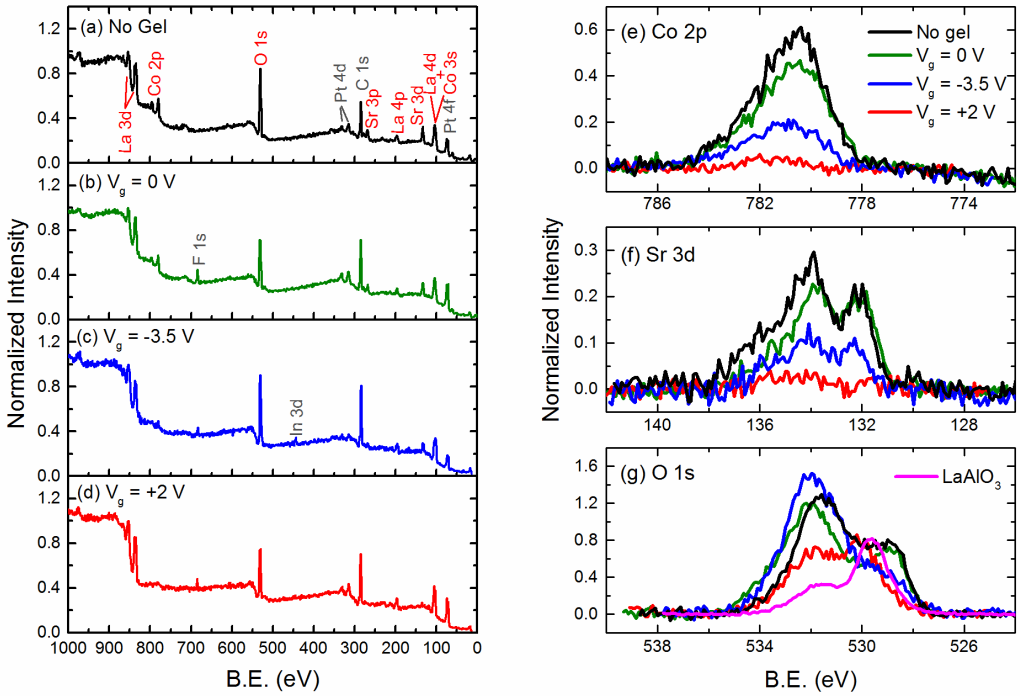

Fig. 3.6. X-ray photoelectron spectroscopy (XPS) survey scans of an LSCO channel (a) before application of the ion gel (black), (b) after applying the gel but maintaining $V_g = 0$ (green), (c) after applying V_g = -3.5 V (blue), and (d) after applying V_g = +2 V (red). All gate voltages mentioned were applied at 260 K. Peaks due to atomic constituents in the film are labelled in red and those from contact electrodes or contamination are labelled in gray. High resolution XPS scans of the Co 2*p*, Sr 3*d*, and O 1*s* peaks are shown in panels (e), (f), and (g), respectively, with the same color scheme as panels (a)-(d). Panel (g) includes an XPS spectrum on the O1*s* edge of a $LaAlO_3$(001) substrate in magenta for reference.

Moving on to the peaks from LSCO, Fig. 3.6(e-g) show higher resolution scans around the Co 2*p*, Sr 3*d*, and O 1*s* peaks, respectively, with the intensities normalized to La 3*d*. In all cases only minor differences are observed between films with no gel applied (black curves) and films exposed to a gel at $V_g = 0$ V (green curves). This is unsurprising given the above transport and AFM. Also consistent with the above findings, the situation changes markedly after application of V_g = +2 V (red curves). In this case Fig. 3.6(e) and (f) show large reductions in the Co 2*p* and Sr 3*d* intensities (again, relative to La 3*d*), which we attribute to electrochemical etching of significant fractions of the LSCO, thus exposing the LAO substrate. This is consistent with the porous morphology shown in Fig. 3.5(d), although we note that such strong Co and Sr signal reductions indicate some etching over the whole area of the film, in addition to the pits. The O 1*s* spectrum in the V_g = +2 V case (Fig. 3.6(g)) is also consistent with these arguments, particularly in that the spectrum becomes similar to that of LAO, which is shown in Fig. 3.6(g) for comparison. Considering

next V_g = -3.5 V (blue curves in Fig. 3.6(e-g)), we find that the Co 2*p* and Sr 3*d* signals are again diminished with respect to as-grown LSCO (albeit less so than at + 2V), potentially due to the La_2O_3 surface segregation observed by Lang *et al.* after application of $V_g < 0$ in $La_{1/3}Sr_{2/3}FeO_3$ films [67]. In terms of the response of the O 1*s* signal to V_g = -3.5 V (Fig. 3.6(g)), the primary observation is the enhancement of the 532 eV peak at the expense of the 529 eV intensity. We note that the peak at 532 eV is generally assigned to surface-bonded O species (*e.g.*, hydroxides, carbonates, *etc*.), whereas the peak at 529 eV is typically assigned to O in a solid-state crystalline environment [129–131]. Within this interpretation the increased intensity of the 532 eV peak after application of V_g = -3.5 V could be linked to the increased density of surface particles seen in Fig. 3.5(c). These may also contain LSCO decomposition products generated in the electrochemical degradation that occurs after removal of the negative V_g. As a final comment on XPS, we note that the observed changes in O 1*s* spectra, both the increased intensity of surface-bonded O from ion gel/LSCO decomposition products after negative biasing and the substrate exposure after positive biasing, are consistent with the findings of Bubel *et al*. in ionic liquid gating of $NdNiO_3$ [49].

3.4 Implications of bias-polarity-dependent gating mechanism

Before moving on to V_g control of transport and magnetism in LSCO, it is worthwhile to consider the general implications of the above findings, particularly the asymmetry in electrostatic *vs*. electrochemical response with respect to V_g polarity (Fig. 3.3 and 3.4). LSCO at x = 0.5 is interesting in this regard as it is a heavily hole-doped oxide on the verge of redox instability. This is because as x is increased in LSCO the substitution of Sr^{2+} for La^{3+} leads to progressive oxidation of Co from 3+ towards 4+ formal valence. Co^{4+} is unstable in the octahedral environment in perovskites, however, as evidenced by the fact that $SrCoO_3$ can only be stabilized under high O pressure or by electrochemical means [99,126]. At some threshold average valence (at a fixed temperature and O_2 pressure), V_O formation thus becomes facile, with small formation enthalpy [98]. We believe that this instability towards V_O formation, which is particularly strong in high x LSCO, but common to some extent in many oxides, is responsible for the asymmetry in electrostatic *vs*. electrochemical response seen in Fig. 3.3 - 3.6. Specifically, under positive

V_g the redox instability renders V_O formation strongly favored over hole depletion, whereas under small negative V_g hole accumulation is favored over V_O annihilation. At larger negative V_g the increase in Co formal valence pushes the system beyond electrochemical stability, and V_O formation thus occurs after V_g removal, leading to the observed irreversibility. We note for completeness that the true situation in LSCO may involve O 2*p* holes in addition to/rather than Co^{4+} (a negative charge transfer gap has been suggested, and Co-O hybridization is significant) [97], but this does not substantially alter the above arguments.

Interesting in terms of prior work is to project this understanding onto other systems, particularly undoped perovskites such as STO. In that case V_O formation energies are also low, the difference being that while *n*-doping is facile (the mobility of electrons in the t_{2g}-derived conduction band is high, particularly at low *T*), *p*-doping is not [132]. Gating can therefore only be achieved under electron doping (positive V_g), where the system is most prone to electrochemistry (V_O formation). It is thus possible that oxides that can be hole doped are intrinsically simpler to work with in EDLTs (in terms of electrostatic operation) than those that typically only support *n*-type conduction, *e.g.*, STO, TiO_2, and VO_2 [32,38,42,50–52]. Further experiments along these lines would clearly be worthwhile. Low *x* LSCO is one prospect for such, as the V_O formation energy can be controllably increased.

3.5. Electrostatic control of ferromagnetism in initially ferromagnetic films

We now progress to the electrolyte gate control of the electronic and magnetic properties of these LSCO films, which, given the above, we confine to $V_g < 0$. Between $V_g = 0$ and -2 V this gating is expected to be electrostatic and reversible. While larger negative V_g will induce irreversibility after removal of the voltage, these larger negative biases can still be used to probe the extent of modulation of electronic/magnetic properties, provided that $|V_g|$ is incrementally increased without returning to 0 V. The data shown in Fig. 3.7 were acquired in this mode. Specifically, $V_g = 0$ was first applied at 260 K then the system was cooled to 5 K before acquiring data on warming. After returning to 260 K the gate bias was then stepped to -1 V, followed by cooling and acquiring data, then rewarming to 260 K and increasing $|V_g|$, eventually reaching -4 V.

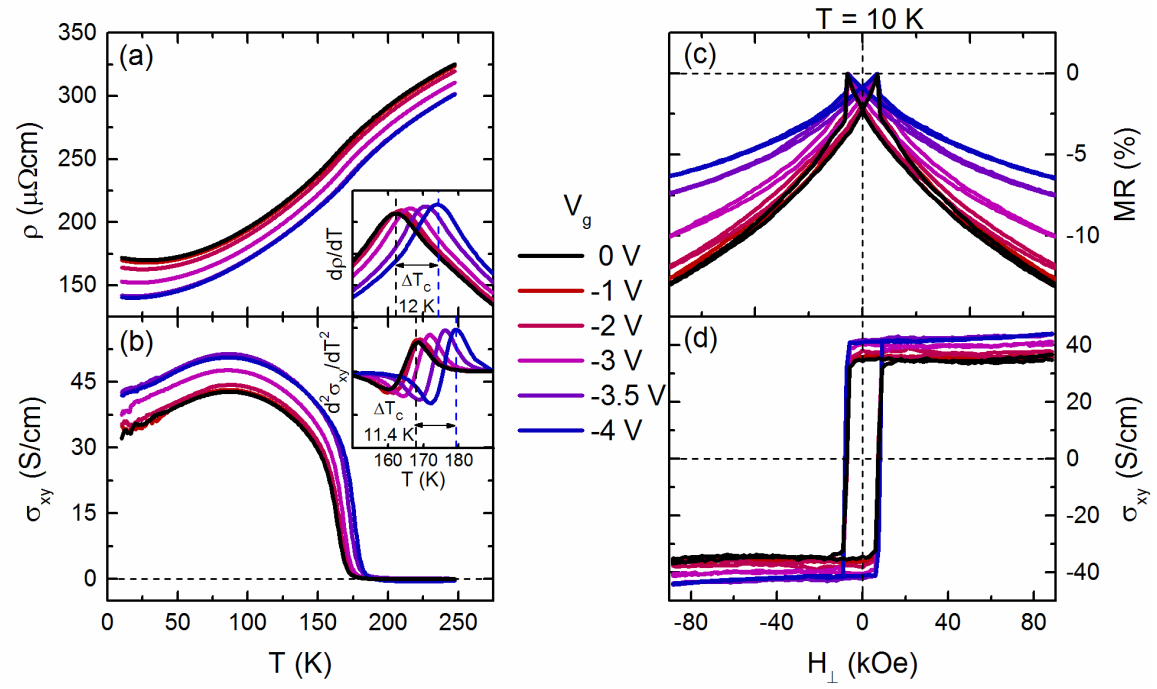

Fig. 3.7. Temperature dependence of (a) the zero field channel resisitivity, ρ, and (b) the low field (remanent) transverse conductivity, σ_{xy}, at V_g = 0, -1, -2, -3, -3.5 and -4 V (*i.e.*, six curves). More detail on the measurement in (b) is provided in Fig. 3.9. The insets to (a) and (b) show $d\rho/dT$ and $d^2\sigma_{xy}/dT^2$, respectively. Also shown are the 10 K out-of-plane magnetic field ($H_\perp$) dependence of (c) the magnetoresistance, *MR*, and (d) σ_{xy}, at V_g = 0, -1, -2, -3, -3.5 and -4 V, (*i.e.*, six curves).

Considering first the T dependence of the channel resistivity, the zero gate bias $\rho(T)$ shown in Fig. 3.7(a) is consistent with prior measurements of 8 unit-cell-thick films on LAO(001). Metallic behavior is observed, with positive temperature coefficient of resistance (*i.e.*, $d\rho/dT > 0$), a residual resistivity ratio near 2, ρ(10 K) ≈ 175 μΩcm, and an inflection in $\rho(T)$ near T_C (~170 K). With application of V_g the channel resistance is lowered due to hole accumulation, the magnitude of the gate-induced change being relatively weakly T dependent. (Note that Fig. 3.7(a) actually plots the resistivity, $\rho(T)$, determined from $R(T)$ using the film thickness. The gate-induced changes likely do not extend over the entire thickness, but relative comparisons of $\rho(T)$ among various V_g's remain valid). Between 0 and -4 V the channel resistivity change amounts to -7.3 % at 250 K, increasing to -18.2 % at 5 K. Detailed analysis of the V_g-induced difference in ρ (Fig. 3.8) does reveal some distinct features in the T dependence, the magnitude of resistivity modulation reaching maxima at $T = T_C$ and as $T \rightarrow 0$. As discussed in the caption of Fig. 3.8, we associate this with enhanced ρ in these regions due to spin disorder; the V_g-induced resistivity difference and magnetic field (H) induced resistivity difference (*i.e.*, the

magnetoresistance, MR) are thus correlated. In terms of the overall magnitude of the V_g-induced ρ change (-18.2 % at 5 K under V_g = -4 V), we note that this is modest, consistent with the high hole density metallic starting point.

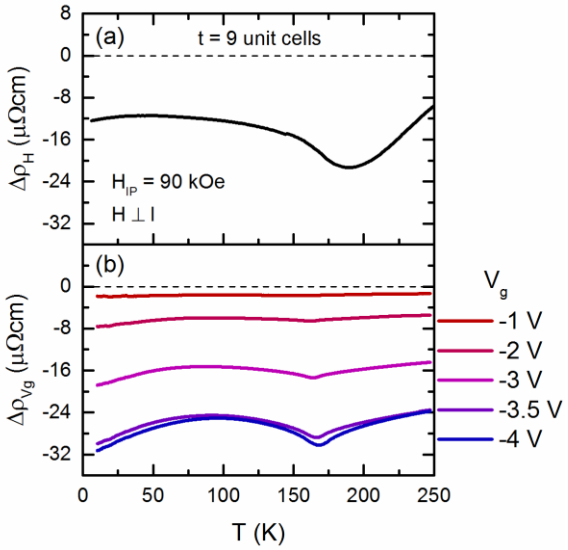

Fig. 3.8. Temperature dependence of the change in resistivity, $\Delta\rho_H$, for a 9-unit-cell-thick LSCO film grown on a $LaAlO_3$(001) substrate upon applying a 90 kOe in-plane magnetic field, H_{IP}, with the current flowing perpendicular to H_{IP}. The strongest effects occur around T_C (due to spin disorder) and as $T \rightarrow 0$ (due to the inter-cluster magnetoresistance discussed in the paper (also a form of spin disorder)). **(b)** Temperature dependence of the change in resistivity, $\Delta\rho_{Vg}$, for the 8 unit cell thick LSCO film (Fig. 3.7(a)) upon application of V_g = -1, -2, -3, -3.5 and -4 V. $\Delta\rho_{Vg}$ is relatively temperature independent except near T_C and at low T. A very similar shape is found in (a), indicating that the field-induced and voltage-induced changes are correlated. In essence the largest doping response occurs in the T regions with strongest spin-dependent resistivity. Note that because the film in (a) is slightly thicker, its T_C is slightly higher than in (b), thus causing the peak in $\Delta\rho_H$ to shift to a slightly higher T.

The inflection in $\rho(T)$ in LSCO is known to occur close to, but just below T_C, and is thus a good indirect indicator of any shift in the magnetic ordering temperature [94]. This is probed in detail in the inset to Fig. 3.7(a), which shows the V_g dependence of $d\rho/dT$ from 150 to 190 K. The spin disorder scattering peak is seen to shift upwards by 12 K from V_g = 0 to -4 V, suggesting a gate-induced T_C increase of 12 K, further confirmed below *via* anomalous Hall effect. Continuing with resistivity analysis, another indication of V_g-induced modification of electronic properties is provided by $\rho(H)$, *i.e.*, the MR. As shown in Fig. 3.7(c), at V_g = 0 these ultrathin LSCO films exhibit a strong hysteretic negative MR in fields perpendicular to the plane ($H_\perp$), related to dead layer effects. Specifically, and as discussed in prior work on STO(001)/LSCO [95,107], the strain-induced V_O

ordering [109] in this system leads to V_O accumulation near the substrate interface, reducing the effective doping, x_{eff}. At some thickness this is reduced to the point that it falls below the $x_{eff} = 0.22$ critical level [88] for the loss of phase-pure ferromagnetism in LSCO, leading to the nanoscale magneto-electronic phase separation that characterizes the low doping regime of this material [9,88,89,94,95,107]. This phase separation is interface-induced in this case, the dead layers being composed of nanometric ferromagnetic metallic clusters in a non-ferromagnetic semiconducting matrix [95,107]. Transport between such clusters is strongly *H*-dependent, leading to a hysteretic negative MR characteristic of the magnetically phase-separated state [95,107]. Of highest interest here, we find that this inter-cluster MR is significantly suppressed (by about a factor of 2) by application of V_g = -4 V (Fig.3.7(c)). This indicates suppression in the dead layer (*i.e.*, non-ferromagnetic) thickness in response to gate-induced holes, consistent with the strengthening of the ferromagnetic state seen from the T_C increase (Fig. 3.7(a)).

One potential route to more direct information on the V_g response of the magnetism in these ultrathin films is the use of the anomalous Hall effect (AHE). This is particularly attractive in LSCO due to the large anomalous Hall conductivity ($\sigma_{AH} \approx 40$ S/cm) [133], and perpendicular magnetic anisotropy, which generate a large low field AHE signal, easily separable from the ordinary Hall effect. In this case the transverse (Hall) resistivity, ρ_{yx}, can be written [96]

$$\rho_{yx} = R_O \mu_0 H_\perp + R_{AH} \mu_0 M \qquad 3.2,$$

where μ_0 is the permeability of free space, R_O is the ordinary Hall coefficient, R_{AH} is the anomalous Hall coefficient, and M is the magnetization. Due to the large hole density and R_{AH} in LSCO, Eq. 3.2 reduces to $\rho_{yx} \approx R_{AH}\mu_0 M$ at the fields of interest here. Using the definition of transverse conductivity, σ_{xy}, and that $R_{AH} \propto \sigma_{AH}$, we then obtain

$$\sigma_{xy} = \rho_{yx}/\rho_{xx,0}^2 \propto \sigma_{AH} M \qquad 3.3,$$

where $\rho_{xx,0}$ is the zero field resistivity. At fixed T and V_g, σ_{AH} is constant, and we can thus use σ_{xy} as a direct probe of M. This is illustrated in Fig. 3.7(d), where $\sigma_{xy}(H)$ at 10 K is shown as a function of V_g, revealing clear, square, hysteresis loops. Consistent with the

MR in Fig. 3.7(c), the coercivity is found to be 7 kOe, independent of V_g. This indicates that the coercivity of the conductive region probed in transport (*i.e.*, the film surface region) is doping independent, consistent with the coercivity of bulk LSCO at doping levels above percolation ($x_{eff} > 0.18$) [94].

While the coercivity from Fig. 3.7(d) is independent of V_g, the magnitude of σ_{xy} is not, the zero field σ_{xy} increasing from 35 to 44 S/cm from $V_g = 0$ to -4 V. While it is tempting to interpret this as a V_g-induced increase in saturation magnetization, this is complicated by the V_g-induced decrease of $\rho_{xx,0}$, which also increases σ_{xy}. The V_g control over T_C can nevertheless be directly verified using the AHE, as shown in Fig. 3.7(b). In this figure we isolate the zero H (*i.e.*, remanent) $\sigma_{xy}(T)$ by cooling in +90 kOe, reducing the field to a small nominal value (+50 Oe, maintained to avoid remnant field effects), measuring $\rho_{yx}(T)$ on warming, and then repeating for negative cooling and measuring fields. We then plot the remanent $\sigma_{xy} = [\rho_{yx}(T, +50\text{ Oe}) - \rho_{yx}(T, -50\text{ Oe})]/2[\rho_{xx}(T, 0)]^2$, generating the curves shown in Fig. 3.7(b) as a function of V_g. (More details are provided in Fig. 3.9 and its caption). A downturn in σ_{xy} is observed at low T, perhaps reflecting a competition between in-plane and perpendicular magnetic anisotropies, but, most importantly, $\sigma_{xy}(T)$ indeed reveals a ferromagnetic order parameter shape as $T \rightarrow T_c^-$, demonstrating the power of this type of AHE measurement. The deduced increase in T_C under $V_g = -4$ V is thus directly verified, most clearly in the inset, where $d^2\sigma_{xy}/dT^2$ at various V_g is shown from 150 to 190 K. The observed 11.4 K shift in T_C is in good agreement with the inset to Fig. 3.7(a), albeit with the spin disorder peak in $d\rho/dT$ systematically down-shifted from the more accurate measure of T_C provided by the AHE.

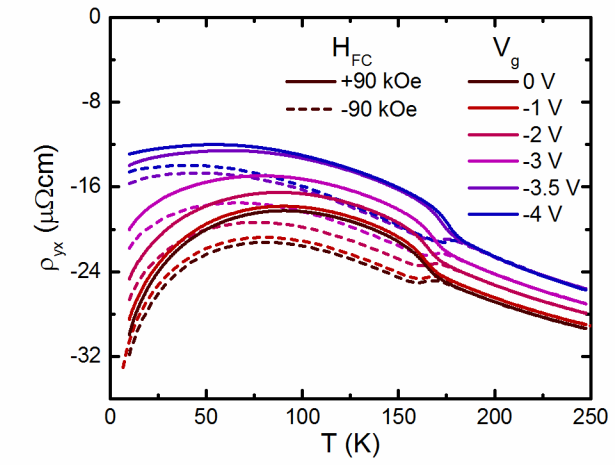

Fig. 3.9. Temperature dependence of the low field ρ_{yx} (no background subtraction) after cooling in positive and negative magnetic fields (H_{FC} = ±90 kOe), as used to calculate $\sigma_{xy}(T)$ in Fig. 3.7(b). Data are shown for V_g = 0, -1, -2, -3, -3.5 and -4 V. For H_{FC} = +90 kOe the magnetic field was reduced to +50 Oe while measuring ρ_{yx} on warming, whereas for H_{FC} = -90 kOe the magnetic field was reduced to -50 Oe for the measurement. The small measuring fields of ±50 Oe were favored over the zero field (remanent) case to avoid the experimental problem of unknown remanent magnetic fields in the superconducting magnet after reducing the magnet current to zero.

It is worthwhile to place the T_C shift observed (12 K, or 7 %) in the context of prior work on perovskite ferromagnets. In this regard the most comparable results we are aware of are the 10 K shift in electrolyte-gated $La_{0.8}Ca_{0.2}MnO_3$ [33], and the 40 K shift in ferroelectric-gated $La_{0.8}Sr_{0.2}MnO_3$ [134]. In these cases, however, the ρ values were ~50 mΩcm, over two orders of magnitude higher than the LSCO studied here. A 12 K Curie temperature shift can thus be viewed quite positively given the expectation of strengthening gate effects with increasing ρ. An important element in further quantification is an estimate of the actual induced surface hole density. Previous ion gel gating studies on other materials achieved this *via* integration of I_g, extending the data of Fig. 3.2(c) to all V_g's [53]. Attempts to do this in the current devices generated unphysically large areal hole densities at high V_g, however, likely due to parasitic capacitance in the side-gated geometry. Top-gate devices are thus desirable, but formation of the gate electrode on the ion gel is not conducive to the rapid cooling to 275 K required to mitigate LSCO degradation. Determination of the induced hole density from Hall effect is another option, but is complicated in this case by the need to measure at $T >> T_C$, or in large H, to isolate the ordinary component from the AHE. Moreover, the relationship between ordinary Hall coefficient and x is non-trivial in LSCO [93]. Inverting the problem, one simple estimate

that can be made is of the hole density required to induce a 12 K T_C shift. Based purely on $T_C(x)$ from bulk crystals this yields Δx_{eff} of 0.03 between 0 and -4 V (from 0.19 to 0.22 in x_{eff}). This amounts to only 0.2×10^{14} cm^{-2}, far below expectations, likely underscoring the unreasonableness of quantitatively comparing bulk chemical doping with surface electrostatic doping of ultrathin films. In any case it is clear that much larger V_g-induced modulation in properties is anticipated in lower x, higher resistivity LSCO films. One intriguing possibility is to use compositions around $x = 0.15$, *i.e.*, just sub-percolation, seeking to gate from a phase-separated semiconducting state to a long-range ferromagnetic metal. This is the doping level at which the rate of change of the magnetic ordering temperature with doping is also maximized. The current work lays the foundation for this, demonstrating (*a*) that the transition should be traversed under hole accumulation (*i.e.*, from the insulating side) to ensure reversible electrostatic response, and (b) that the AHE will serve as an excellent probe of V_g-dependent magnetic response.

3.6 Conclusions

In summary, we have used ultrathin films of a ferromagnetic metallic oxide of high interest, LSCO, to address two main open questions with electrolytic gating. The first is the issue of electrostatic *vs*. electrochemical operation of electrolyte-based transistors, particularly with respect to the role for oxygen vacancies. The primary finding, arrived at from (atmosphere-dependent) transport experiments and surface structural/chemical probes, is a remarkably strong asymmetry in response with respect to gate bias polarity. Simple electrostatic hole accumulation is observed for $V_g < 0$ up to some threshold, whereas the application of essentially *any* $V_g > 0$ is found to cause irreversible electrochemistry *via* bias-induced V_O formation. These observations have been rationalized in terms of the known redox stability of LSCO, implications for the field in general being discussed in detail, particularly with respect to the controversial results in *n*-type systems such as VO_2. The second open issue addressed is the potential of electrolyte gating for voltage control of magnetic order and properties. Despite the use of a heavily hole-doped system, optimized for straightforward interpretation of the results rather than large V_g-induced changes, clear reversible electrostatic tuning of resistivity, magnetoresistance, and T_C have been obtained at $V_g < 0$. The combination of a large anomalous Hall effect and strong

perpendicular magnetic anisotropy in ultrathin $LaAlO_3$(001)/LSCO films has been shown to provide a powerful *in situ* probe of gate-controlled magnetism, directly demonstrating a 12 K (7%) T_C shift, comparable to the state-of-the-art. Lower x films are expected to reveal more dramatic property modulation, including the possibility of a gate-induced percolation transition from a cluster phase to a long-range-ordered ferromagnet.

Chapter 4: Ion-gel-gating-induced oxygen vacancy formation in epitaxial $La_{0.5}Sr_{0.5}CoO_{3-\delta}$ films from *in operando* X-ray and neutron scattering

This chapter is mainly based on the publication "*Ion-gel-gating-induced oxygen vacancy formation in epitaxial $La_{0.5}Sr_{0.5}CoO_{3-\delta}$ films from in operando X-ray and neutron scattering*" in Physical Review Materials (2017) by Jeff Walter, Guichuan Yu, Biqiong Yu, Alexander Grutter, Brian Kirby, Julie Borchers, Zhan Zhang, Hua Zhou, Turan Birol, Martin Greven, and Chris Leighton, adapted with permission from Ref. [135], copyright (2017) American Physical Society. In this work we address the first and second open issues in electrolyte gating discussed in Section 1.2.2 (*i.e.*, the poorly understood electrostatic *vs.* electrochemical gating mechanisms in oxide EDLTs and the general lack of *in operando* probes). We demonstrate application of both synchrotron X-ray diffraction (SXRD) and polarized neutron reflectometry (PNR) as *in operando* probes of epitaxial LSCO EDLTs, utilizing the penetration of hard X-rays and neutrons. SXRD reveals only a small (<0.1 %) decrease in the out-of-plane lattice parameter under negative V_g, compared to a large increase at positive V_g (up to 1 % at +2 V). Complementary bulk powder XRD (PXRD) and thermo-gravimetric analysis (TGA) confirm that such lattice expansion is consistent with V_O formation, reproduced by density functional theory (DFT). The cell volume dependence on oxygen deficiency is then used to "calibrate" *in operando* SXRD, enabling *quantification* of the V_g-dependent V_O density, which reaches $\delta = 0.16$ at +2 V. Importantly, SXRD indicates that these V_Os proliferate through the entire thickness of ~30-unit-cell-thick films. This is confirmed by V_g-dependent PNR, the suppressed magnetization extending through the whole film, in *quantitative* agreement with the determined O deficiency. These results not only advance our understanding of gating mechanisms in oxide EDLTs, but demonstrate powerful new approaches to *in operando* structural and magnetic studies.

4.1 *In operando* synchrotron X-ray diffraction

Details on LSCO growth and device fabrication are included in Section 2.3 but, briefly, epitaxial LSCO was deposited on LAO(001) using high-pressure oxygen sputtering and then thoroughly characterized [95,107,109,136]. Bulk-like metallic ferromagnetism with Curie temperature, $T_C \approx 220$ K was obtained above 7 unit cell thicknesses. EDLTs employing ~10-μm-thick "cut and stick" ion gels [55] (see Fig. 4.1(a)) were then fabricated from these films. *In operando* SXRD (Fig. 4.1(a)) was performed on the 33-ID beamline of the Advanced Photon Source, with 20 keV (λ = 0.62 Å) radiation. Fig. 4.1(b) and (c) display specular 00*L* scans around the 002 LAO substrate reflection, examining the effects of X-ray beam damage.

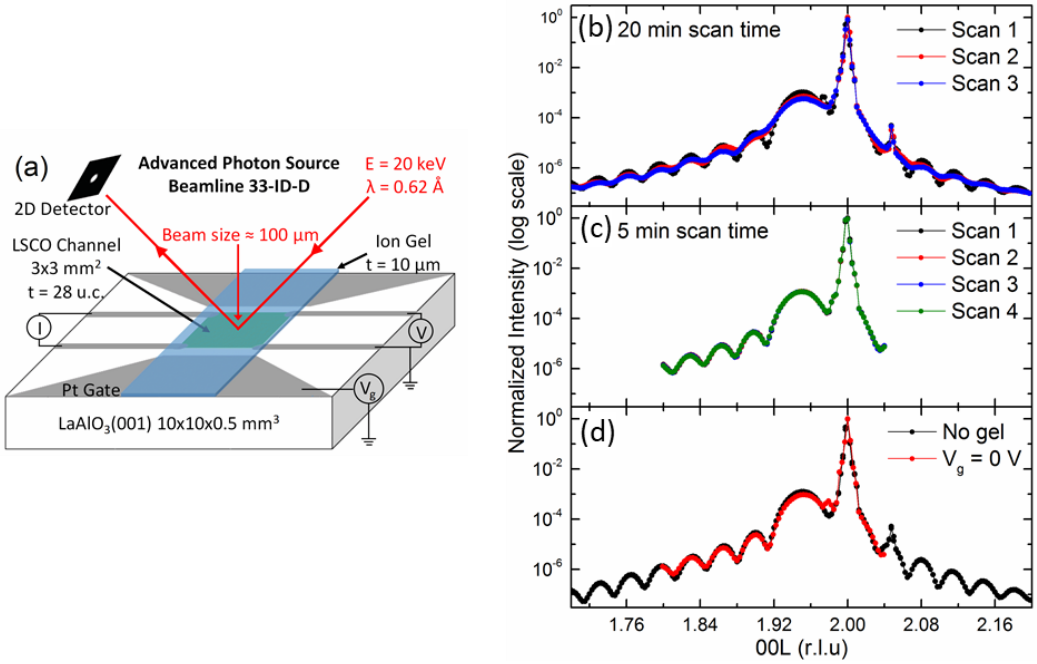

Fig. 4.1. (a) Device and experimental setup schematic for synchrotron X-ray diffraction on epitaxial $La_{0.5}Sr_{0.5}CoO_{3-\delta}$ films. Specular synchrotron X-ray diffraction (SXRD) scans near the 002 reflection of the $LaAlO_3$(001) (LAO) substrate, where *L* is in reciprocal lattice units (r.l.u.) of the LAO substrate, examining (b-c) X-ray beam damage, and (d) ion-gel-induced sample changes.

Fig. 4.1(b) shows three repeated scans with $V_g = 0$ V with beam exposure times of 20 minutes/scan. Significant changes from the first (black) to third (blue) scan are observed, including suppressed intensity of both the 002 LSCO film peak and its Laue oscillations. We attribute these changes to X-ray beam induced damage, as no other changes were made to the sample between scans. Note, however, that the signatures of beam damage do not

include significant changes in peak position in reciprocal lattice units (L). We were able to mitigate beam damage effects, as shown in Fig. 4.1(c), which shows four repeated scans with V_g = 0 V with beam exposure times of 5 minutes/scan. The scans in this case are indistinguishable, suggesting the shorter beam exposure time to have minimized beam damage to below detection limits. We also performed all measurements at 150 K, and measured on a new sample location for every warming and cooling cycle (*i.e.*, every new V_g), to further minimize beam damage effects. Fig. 4.1(d) compares the results from a sample prior to ion gel application (black) to post-ion gel application (red) with a gate bias, V_g = 0 V maintained on cooling to the 150 K measuring temperature. No significant differences are observed, suggesting the application of the ion gel alone did not cause any significant structural changes in the LSCO channel.

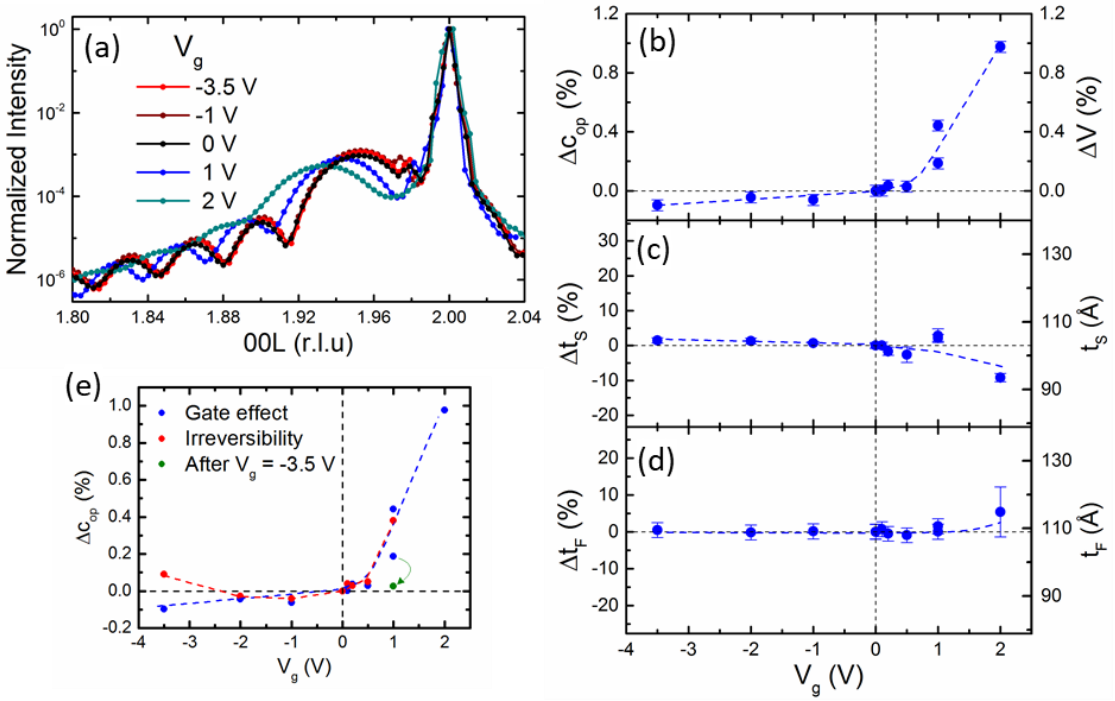

Fig. 4.2. (a) Gate-bias-(V_g)-dependent specular diffraction (00L) scans, where L is in reciprocal lattice units (r.l.u.) of the LAO substrate. (b) Change in c-axis lattice parameter (Δc_{op}, left axis) and cell volume (ΔV, right axis) with V_g. (c) Change in Scherrer thickness (Δt_s, left axis), and t_s itself (right axis), *vs*. V_g. (d) Change in film thickness from Laue fringes (Δt_f), and t_f itself (right axis), *vs*. V_g. (e) Gate effect and irreversibility (defined in the text) in c_{op} as a function of V_g. Dotted lines are guides to the eye.

Having established the ion gels did not damage the film immediately upon application and having developed scan parameters that minimize beam damage effects, we can now proceed to study the effects of bias application. Fig. 4.2(a) displays specular 00L scans

around the 002 LAO substrate reflection, at V_g = -3.5, -1, 0, 1 and 2 V. The V_g = 0 scan is typical of LAO(001)/LSCO [109,137]: a well-defined LSCO peak occurs at L = 1.95, corresponding to out-of-plane lattice parameter c_{op} = 3.89 Å, surrounded by Laue oscillations. As expected for a fully-strained film with negligible microstrain (Fig. 2.2), the Scherrer length from the film peak width (t_S = 103 ± 6 Å) and the thickness from the oscillation spacing (t_f = 109 ± 7 Å) are in agreement with the thickness from X-ray reflectometry prior to gel application (t = 110 ± 5 Å, *i.e.*, 28 unit cells). When gating is performed, negative V_g (*e.g.*, -1 or -3.5 V in Fig. 4.2(a)) results in only small changes in the 002 LSCO peak. For positive V_g, however, the situation is different: the LSCO reflection rapidly shifts to lower L, and the Laue oscillations become less prominent, indicating increased roughness/structural disorder. These changes are summarized in Fig. 4.2(b-d), which shows the V_g dependence of the c-axis lattice parameter shift (Δc_{op}), Scherrer length shift (Δt_S), and fringe spacing thickness shift (Δt_f). The right axes show the cell volume change (ΔV) and absolute t_S and t_f, respectively. From Fig. 4.2(b), the asymmetry with respect to V_g polarity is striking. Negative V_g up to -3.5 V results in a c_{op} decrease of < 0.1% (roughly linear in V_g), whereas V_g = +2 V induces a large (non-linear) 1% lattice expansion. As shown in Figs. 4.2(c,d), this shift in c_{op} is accompanied by barely any variation in t_S and t_f, the only evidence of a statistically significant change occurring in t_S at + 2 V. This indicates, as can be seen from Fig. 4.2(a), that the LSCO film peak and Laue oscillations are uniformly shifted to lower L at positive V_g, with no significant broadening or peak splitting. This suggests that the positive-bias-induced lattice expansion occurs through the entire thickness of these 28-unit-cell films.

In these measurements, which were performed in vacuum, the increase in c_{op} at positive V_g is irreversible, as shown in Fig. 4.2(e). This reversibility experiment shown in Fig. 4.2(e) proceeded in the following steps: (1) the sample was cooled to 150 K with V_g = 0 V; (2) a SXRD scan was performed to calculate the initial c_{op} ($c_{op,i}$); (3) the sample was warmed to ~285 K and a V_g was applied; (4) the sample was cooled to 150 K and c_{op} was measured at V_g ($c_{op,Vg}$); (5) the sample was warmed to ~285 K and V_g = 0 V was applied; (6) the sample was cooled to 150 K and c_{op} was measured at V_g = 0 V ($c_{op,f}$); (7) steps 3 – 6 were then repeated for different V_gs. The gate effect (blue) is given by Δc_{op} = (100 %)×($c_{op,Vg}$ –

$c_{op,i})/c_{op,i}$, and the irreversibility (red) is given by $\Delta c_{op} = (100\ \%)\times(c_{op,f} - c_{op,i})/c_{op,i}$. Note that the irreversibility matches well with our previously reported resistance irreversibility [124] (discussed in Section 3.1, Fig. 3.3). Specifically, reversible behavior is observed for -2 V < V_g < 0 V. Irreversibility eventually appears at V_g < -2 V, with completely irreversible behavior being observed at positive V_g. In the case of the green data point, after applying V_g = 1 V and measuring a gate effect of Δc_{op} = 0.2 %, instead of applying V_g = 0 V we applied V_g = -3.5 V and measured $c_{op,f}$ at V_g = -3.5 V. Even after applying V_g = -3.5 V, $c_{op,i}$ is not completely recovered (*i.e.*, $c_{op,f} > c_{op,i}$) and is not close to the gate effect observed at V_g = -3.5 V. Also note that these lattice parameter changes cannot be explained by X-ray beam damage, as that was not observed to change the film peak position (Fig. 4.1(b)).

4.2 Quantification of oxygen vacancy density by comparing to bulk

As discussed above, earlier transport studies on LSCO revealed similarly asymmetric V_g response, ascribed to V_O formation at positive bias, and electrostatic hole accumulation at negative bias [124] (discussed in Section 3.1, Fig. 3.3). V_O formation is thus an obvious possibility for the positive-bias-induced lattice expansion in Fig. 4.2(b). To investigate the cell volume - V_O density relationship in LSCO, *bulk* samples (polycrystalline powders synthesized in the same manner as LSCO sputtering targets, described in Section 2.1.1) were systematically reduced in a thermo-gravimetric analysis (TGA) apparatus. As previously reported [9], LSCO powders synthesized under these conditions have relatively low oxygen deficiency (*i.e.*, $\delta \approx 0$) as deduced from magnetization, Curie temperature, resistivity, and iodometric titration. TGA was performed on ~100 mg samples of LSCO powder using a TA Instruments Q500 in an atmosphere of N_2 flowing at 60 mL/min. Each sample was ramped to a maximum temperature at a ramp rate of 10 °C/min, held at that maximum temperature for 5 min, and cooled to room temperature at 10 °C/min. The maximum temperature was varied from 340 – 1000 °C. Powder XRD (PXRD) on LSCO powders pre- and post-TGA was performed on a Rigaku MiniFlex 600 equipped with a Cu source and graphite diffracted beam monochromator, allowing Cu $K_{\alpha,1}$ and $K_{\alpha,2}$ pass-through. The PXRD pattern of the initial LSCO (bottom of Fig. 4.3(a)) is consistent with expectations for $Pm\bar{3}m$ LSCO (Fig. 4.3(b)). Note here that a crossover from $R\bar{3}c$ to $Pm\bar{3}m$

occurs around x = 0 in LSCO. While minor deviations from cubic are thus possible, we simply analyze all the data here in terms of the cubic structure. As justified by the synthesis conditions and measured magnetic properties, we label this sample "δ = 0" in Fig. 4.3(a), *i.e.*, we assume an initial state with negligible V_O density. The progressive reduction cycles shown in Fig. 4.3(c), to maximum temperatures from 340 - 1000 °C, result in mass loss that can be directly converted to δ. The PXRD patterns in Fig. 4.3(a) are thereby labeled with a deduced δ, increasing towards the top. The cubic perovskite structure is retained up to δ = 0.202, above which secondary phases form, being LSCO reduction products (brownmillerite, binary oxides, *etc*.).

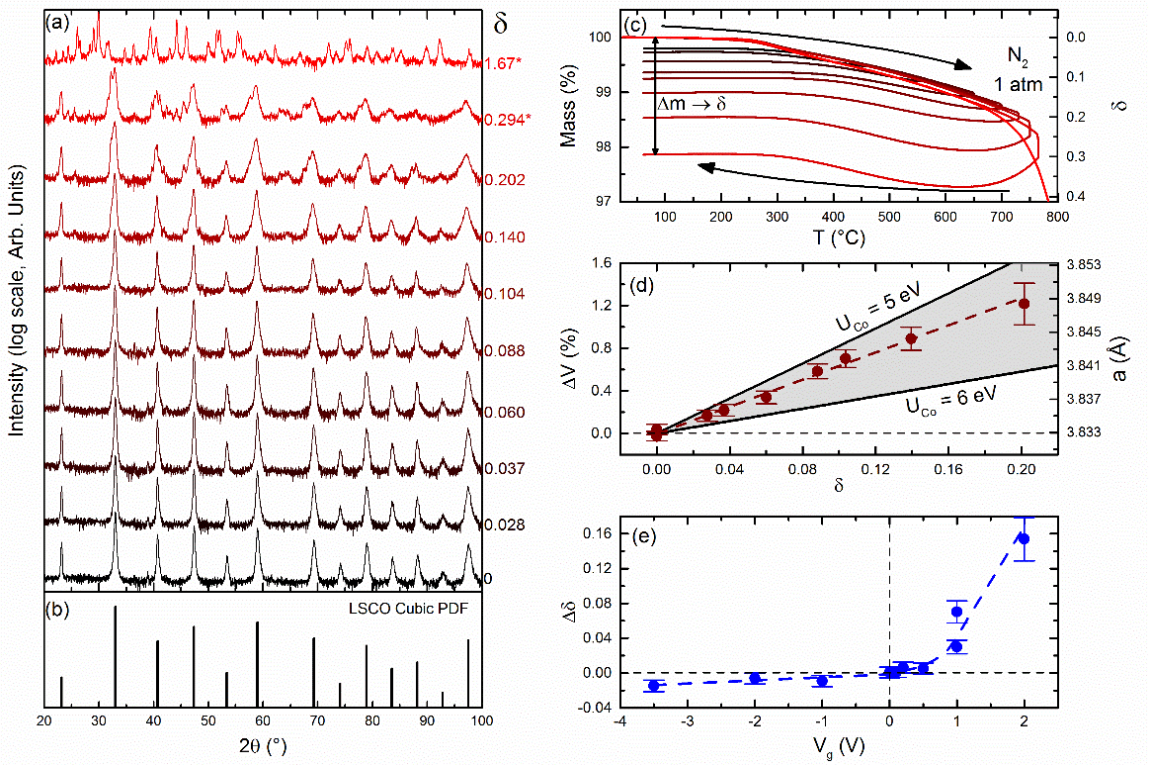

Fig. 4.3. (a) Powder X-ray diffraction patterns of *bulk* $La_{0.5}Sr_{0.5}CoO_{3-\delta}$ before and after the thermogravimetric analysis (TGA) scans shown in (b), which induce progressive reduction. The δ values from TGA are labeled on the right side of (a), and the curves are color-coordinated with (b). * denotes samples no longer in the perovskite structure, which are omitted from further analysis. (b) Reference powder diffraction pattern for cubic $La_{0.5}Sr_{0.5}CoO_3$. (c) *Bulk* TGA scans, *i.e*., sample mass change (left axis) and conversion to δ (right axis) *vs.* temperature, for reduction in flowing N_2. (d) Change in *bulk* cell volume (ΔV) and *bulk* lattice parameter (a) as a function of δ. The maroon dotted line is a straight line fit and the solid black lines are the theoretical ΔV due to formation of oxygen vacancies (U_{Co} = 5 and 6 eV). (e) Change in δ (Δδ) with V_g in *epitaxial films*, obtained by combining Figs. 4.2(b) and 4.3(d). The blue dashed line is a guide to the eye.

As shown in Fig. 4.3(d), which plots the cubic lattice parameter (a) and cell volume expansion (ΔV) *vs*. δ, the reduction of bulk LSCO is indeed accompanied by lattice expansion, qualitatively consistent with prior work [138–140]. ΔV increases linearly with V_O concentration, at a rate that can be reproduced by DFT. First principles DFT calculations were performed using the Projector Augmented Wave scheme [141,142] implemented in the Vienna *ab initio* Simulation Package [143,144]. The exchange correlation energy was calculated using the PBEsol functional [145], and the rotationally invariant DFT+U scheme was employed [146]. An 8×8×8 Monkhorst-Pack grid was used for the primitive perovskite cell [147]. The plane wave energy cut-off was set at 500 eV. Calculations for the effects of O vacancies were performed in 80 atom supercells with one or two O vacancies. The relative positions of the oxygen vacancies (shown in Fig. 4.4) give rise to different supercell volumes, and we have taken into account only the lowest energy vacancy configuration to calculate these. Incorporation of V_Os in DFT supercells at various concentrations results in the solid lines shown in Fig. 4.3(d) for Co U values (U_{Co}) of 5 and 6 eV. A U_{Co} between these values, which is reasonable for Co perovskites [148], thus quantitatively reproduces the experimental $\Delta V(\delta)$. Table 4.1 shows the DFT results used to create the solid lines shown in Fig. 4.3(d), as well as results for U_{Co} between 5 and 6 eV.

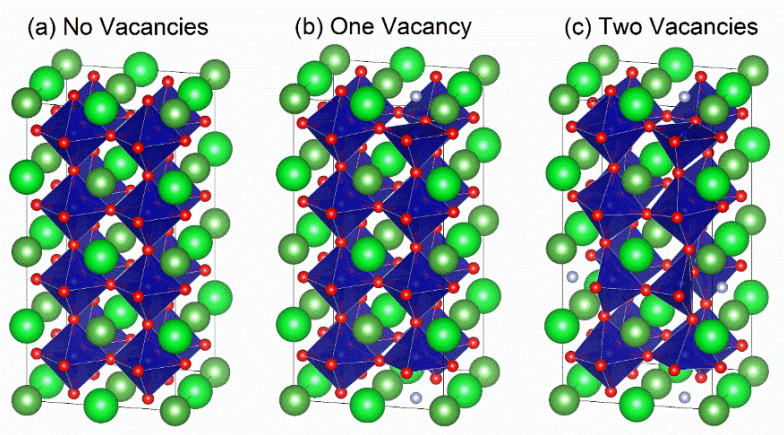

Fig. 4.4. (a) The 2×2×4 LSCO perovskite supercell with 80 atoms used for the DFT calculations. Sr and La ions are shown in green, Co ions are shown in blue, and O anions are shown in red. (b) The lowest energy configuration for a single vacancy in the supercell where the O vacancy site is shown in gray. The only other symmetry equivalent configuration for a single vacancy is slightly higher in energy (by a few meV per formula unit), but leads to no significant volume difference than the lowest energy one. (c) The lowest energy configuration for two vacancies in the supercell that we used. Other configurations, where the two oxygen vacancies are further from each other, are tens of meV per formula unit higher in energy and are not taken into account. Table 4.1 below summarizes the results on volume expansion in these supercells.

Table 4.1. The lattice constant and expansion parameters for $La_{0.5}Sr_{0.5}CoO_{3-\delta}$, where $a(\delta) = a_0 + a_1\delta$. The DFT calculations were performed without spin polarization, and a Hubbard U only on the Co ion. $J = 0.7$ eV was kept constant in all calculations. As discussed above, a 2×2×4 supercell was used, in which different locations of 1 or 2 oxygen vacancies were considered. (For the final results listed in this table, only the 3 lowest energy vacancy configurations were used, one with a single and two with double O vacancies in the supercell.) The experimental values of a_0 and a_1 (determined from the linear fit in Fig. 4.3(d)) are shown in the bottom row.

U_{Co} (eV)	a_0 (Å)	a_1 (Å/vacancy)
5.0	3.758	0.1025
5.2	3.760	0.0876
5.4	3.763	0.0738
5.6	3.765	0.0591
5.8	3.768	0.0465
6.0	3.771	0.0364
Experiment	3.833	0.0795

Taken with the earlier indirect conclusion of V_O formation from transport, and the observation of irreversibility in vacuum that is suppressed in O_2, we take these results as strong evidence for V_O formation as the source of lattice expansion at positive V_g in Fig. 4.2(b). Importantly, this $\Delta V(\delta)$ relationship for bulk LSCO can then be used in conjunction with the $\Delta V(V_g)$ relationship for gated films to quantitatively estimate the change in δ induced by V_g. This essentially uses the bulk data of Fig. 4.3(d) as a calibration to quantify $\delta(V_g)$ from Fig. 4.2(b), assuming the cell expansion with δ to be similar in films and bulk. The straight line fit in Fig. 4.3(d) was used for this purpose, resulting in Fig. 4.3(e). Here, we simply plot Δδ, the V_g-induced change in δ with respect to zero bias, as the initial δ in these films is not accurately known, though it we have estimated $\delta \approx 0.09$ in prior work [137]. The resulting induced δ's at positive V_g are large but reasonable, reaching 0.16 at 2 V. Note here that: (*a*) $\delta < 0.5$ even at the largest positive V_g is consistent with the absence of brownmillerite in SXRD, and (b) strong arguments can be made against a H incorporation mechanism. Recent work has pointed to the possibility of electrochemical incorporation of H in ion liquid/gel gated complex oxides, such as $SrCoO_{2.5}$ [63] and WO_3 [66]. In our case, at a nominal starting Co valence of 3.5, positive gate bias does not lead to reduction to the $(La,Sr)CoO_{2.5}$ brownmillerite phase. It is after induction of this brownmillerite phase that H incorporation is observed in $SrCoO_{2.5}$, however, and we thus

believe it is unlikely that H incorporation plays a dominant role here. Additionally, note that in our experiments, measurements of gate current as a function of gate voltage reveals no evidence for distinct features at the potential differences expected to result in hydrolysis of any remnant H_2O in our ion gels [63]. This would be the simplest mechanism for availability of H species.

In the analysis above we directly compared unit cell volume expansion of the bulk, $\Delta V(\delta)$ in Fig. 4.3(d), to convert $\Delta V(V_g)$ for our films shown in Fig. 4.2(b) to the $\Delta\delta(V_g)$ shown in Fig. 4.3(e). While this is a reasonable approach (confirmed by comparison to the results from PNR data below), we show below an alternative approach. This alternative uses the Poisson ratio to account for the difference in strain states in the bulk (unstrained) and in films (biaxially strained). We begin with the linear elasticity relationship $\sigma_{ij} = C_{ijkl}\varepsilon_{kl}$, where σ_{ij}, C_{ijkl}, and ε_{kl} are the stress, stiffness, and strain tensors. Assuming a homogeneous, isotropic medium, the linear elasticity relationship simplifies to the following

$$\sigma_{xx} + \sigma_{yy} + \sigma_{zz} = \frac{E}{1-2\nu}\left(\varepsilon_{xx} + \varepsilon_{yy} + \varepsilon_{zz}\right) \quad 4.1,$$

$$\sigma_{xx} = \frac{E}{1+\nu}\varepsilon_{xx} + \frac{\nu E}{(1+\nu)(1-2\nu)}\left(\varepsilon_{xx} + \varepsilon_{yy} + \varepsilon_{zz}\right) \quad 4.2, \text{ and}$$

$$\sigma_{zz} = \frac{E}{1+\nu}\varepsilon_{zz} + \frac{\nu E}{(1+\nu)(1-2\nu)}\left(\varepsilon_{xx} + \varepsilon_{yy} + \varepsilon_{zz}\right) \quad 4.3,$$

where E is the Young's modulus and ν is the Poisson ratio. Assigning the *xy*-plane as the film plane, we can set $\sigma_{zz} = 0$ (*i.e.*, no out-of-plane stress), $\varepsilon_{xx} = \varepsilon_{yy} = (a_s\text{-}a)/a$, and $\varepsilon_{zz} = (c_{op}\text{-}a)/a$, where a_s, a, and c_{op} are the substrate, bulk, and out-of-plane film lattice parameters, respectively. Using these definitions and Eqs. 4.1 - 4.3 we come to the following relationship

$$a = \frac{c_{op}(1-\nu)+2\nu a_s}{1+\nu} \quad 4.4.$$

Here, if we insert the $a(\delta)$ from Fig. 4.3(d) and assume a ν value we can calculate $\delta(V_g)$ by inserting the $c_{op}(V_g)$ results from Fig. 4.2(b). The results of such a calculation are shown for different ν values in Fig. 4.5. Reasonable agreement with Fig. 4.3(e) can be achieved with $\nu \approx 1/3$, as expected. However, the exact results are quite sensitive to the assumed value of ν, as demonstrated by the significant spread in δ values (~0.1) upon varying ν by only 10 % (around the reasonable value of $\nu = 1/3$). Note also that the assumption that these LSCO films are isotropic is questionable in this case, particularly considering the oxygen

vacancy ordering present to some extent in these films. The sensitivity to the choice of ν and the questionable assumption of isotropic behavior are the main reasons we chose to use the simpler unit cell volume approach in Fig. 4.3(e).

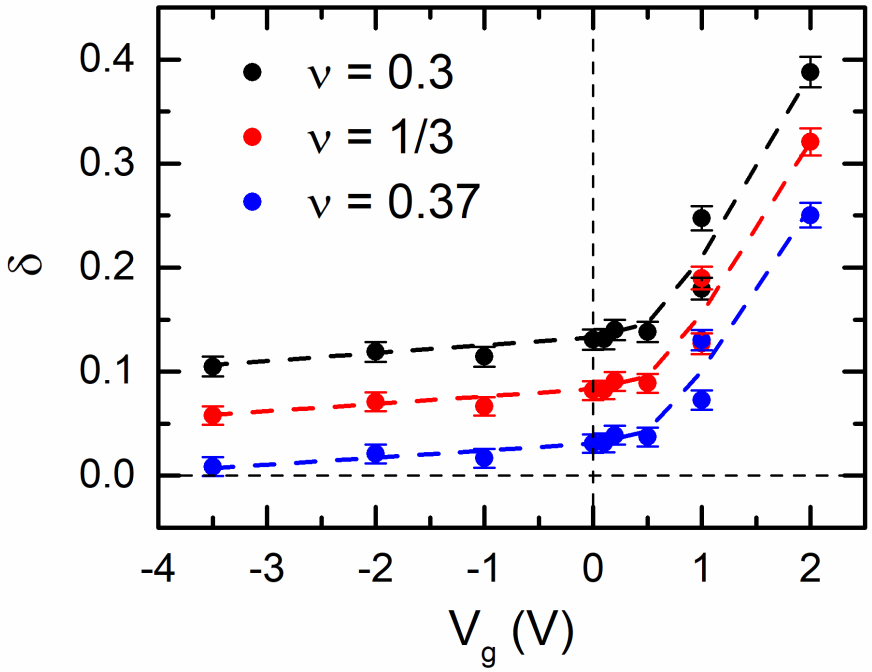

Figure 4.5. Calculation of oxygen vacancy density (δ in $La_{0.5}Sr_{0.5}CoO_{3-\delta}$) *vs.* gate bias ($V_g$) based on the linear elasticity considerations discussed above, with Poisson ratio (ν) of 0.3, 1/3, and 0.37 in black, red and blue, respectively. The dotted lines are simply guides to the eye.

While the interpretation of the large structural changes at $V_g > 0$ are thus clear, the small ones occurring at $V_g < 0$ could involve both electrochemistry and electrostatics. One possibility here is that the small lattice contraction seen in Fig. 4.2(b) truly corresponds to a minor amount of V_O annihilation, *i.e.*, a literal interpretation of Fig. 4.3(e) in terms of filling of V_O's. In experiments performed in vacuum the source of the required O for this process is not clear, however, although trapping of O species in the ion gel and hydrolysis of impurity H_2O are possible [63]. Another relevant point is that our prior transport studies demonstrated the response at negative V_g to be largely reversible, even *in vacuo*, suggesting simple electrostatic hole accumulation. Interestingly, DFT calculations indeed reproduce a lattice contraction with hole accumulation, as shown in Table 4.2 below. This electrostatic effect would be expected to be confined to the near-surface region, however, rather than throughout the film thickness. The small cell contraction found at negative V_g is thus not straightforward to interpret, requiring further investigation.

Table 4.2. The lattice constant and expansion parameters for $La_{0.5}Sr_{0.5}CoO_3$ with $2n$ extra electrons per formula unit, where $a(x) = a_0 + a_2 n$. The DFT calculations were performed without spin polarization, and a Hubbard U only on the Co ion. $J = 0.7$ eV was kept constant in all calculations. As discussed above, a 2×2×4 supercell was used, with 1, 2, 3 or 4 extra electrons. There are no oxygen ions removed, so this is a calculation of the effect of changing the electron density only.

U_{Co} (eV)	a_0 (Å)	a_2 (Å/electron)
5.0	3.758	0.4179
5.2	3.760	0.4194
5.4	3.763	0.4206
5.6	3.767	0.4072
5.8	3.769	0.3906
6.0	3.773	0.3692

4.3 *In operando* polarized neutron reflectometry

Clearly, a key conclusion from the above is that bias-induced V_O's appear to penetrate the entire film thickness. To verify this, a depth-sensitive technique, neutron reflectometry, was applied. Although V_O formation at the densities in Fig. 4.3(e) results in nuclear scattering length density changes that are difficult to discern (Table 4.3), the subsequent impact on magnetization is substantial.

Table 4.3. Calculated neutron scattering length densities (SLDs) for the sample components in this work [123]. The comparison between $La_{0.5}Sr_{0.5}CoO_3$ and $La_{0.5}Sr_{0.5}CoO_{2.84}$ demonstrates that neutron reflectometry may not be sensitive enough to directly observe the changes (~3%) in SLD upon inducing $\delta = 0.16$ (estimated from SXRD and bulk powder analysis).

Material	Mass density (g/cm^3)	Neutron SLD (10^{-6} Å^{-2})
$LaAlO_3$	6.52	5.33
$La_{0.5}Sr_{0.5}CoO_3$	6.45	4.86
$La_{0.5}Sr_{0.5}CoO_{2.84}$	6.40	4.71
Ion Gel (80% Ionic Liquid, 20% Polymer)	~1.5	2.63
Ionic Liquid: $C_8H_{11}F_6N_3O_4S_2$	1.5	2.38
Polymer: $C_5H_2F_7$	1.8	3.63

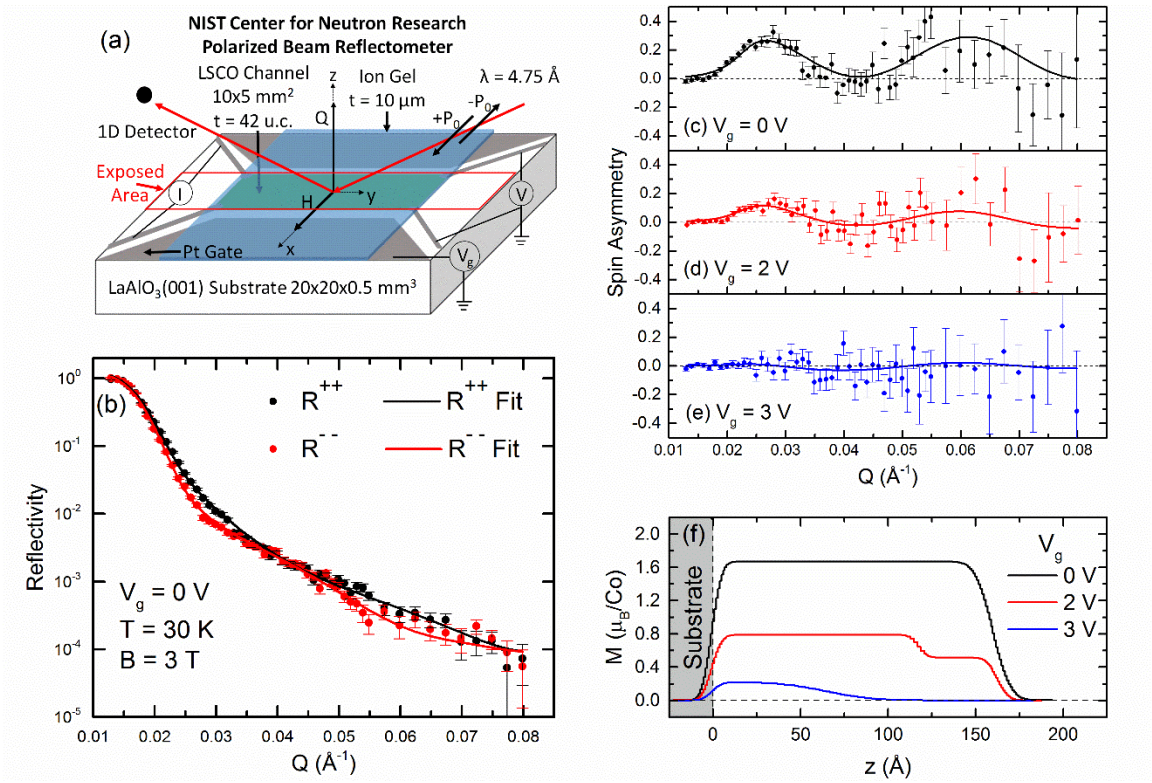

Fig. 4.6. (a) Device and experimental setup schematic for polarized neutron reflectometry on epitaxial $La_{0.5}Sr_{0.5}CoO_{3-\delta}$ films. (b) Reflectivity (R) *vs*. scattering vector magnitude, Q, from a 165 Å film at zero gate bias (V_g), 30 K, and 3 T. Black and red denote the non-spin-flip "R^{++}" and "R^{--} " channels, respectively, for both data (points) and the fits to the model discussed in the text (lines). (c-e) Spin asymmetry at 30 K in 3T for V_g = 0, 2, and 3 V, respectively. Solid lines are fits to the model discussed in the text. (f) Extracted magnetization (M) depth profile at 30 K in 3 T for V_g = 0, 2, and 3 V; z = 0 is the substrate/film interface.

Magnetization depth profiling *via* PNR was thus performed on the Polarized Beam Reflectometer at the NIST Center for Neutron Research (Section 2.5), using devices scaled to 10 × 5 mm^2 LSCO channels (Fig. 4.6(a)). Fig. 4.6(b) shows the scattering vector (Q) dependence of the specular neutron reflectivity for 42-unit-cell-thick LSCO, at 30 K in a 3 T in-plane field [] at V_g = 0. The non-spin-flip reflectivities ("R^{++}" and "R^{--}") are shown, where "+" and "–" indicate the polarization of the incoming and outgoing beams (Fig. 4.6(a)). As expected, well below T_C in a large in-plane field, R^{++} and R^{--} are clearly split. Fig. 4.6(c) plots the spin asymmetry, SA = $(\frac{R^{++}-R^{--}}{R^{++}+R^{--}})$, which, in the absence of large V_g-dependent chemical changes, highlights the magnetic scattering. This SA is positive, with two oscillations visible to the maximum Q. Most significantly, Fig. 4.6(d,e) shows that the SA responds dramatically to V_g. The SA is reduced substantially at 2 V, but with a similar oscillation period, while at 3 V the SA appears completely suppressed. Even prior to

quantitative analysis, this SA reduction with V_g indicates strong suppression of the magnetization, the similarity of the period in Figs. 4.6(c,d) indicating little change in magnetic thickness, *i.e.*, relatively uniform suppression.

Quantitative refinement was performed using Refl1D to substantiate these conclusions, resulting in the solid line fits in Fig. 4.6(b,c,d,e). As shown in Table 4.4, these fits are based on a model including the LAO substrate, LSCO film, and ion gel. The refined nuclear scattering length densitiy for LSCO is as expected, and independent of V_g (along with the chemical thickness). Note here that varying δ between $La_{0.5}Sr_{0.5}CoO_3$ and $La_{0.5}Sr_{0.5}CoO_{2.84}$ (as in Fig. 4.3(e)) results in nuclear scattering length density changes of only 3 %, confirming little sensitivity to this effect. The depth-dependent magnetization ($M(z)$), however, is highly sensitive to V_O density. The refined $M(z)$ from Fig. 4.6(b-e) is plotted in Fig. 4.6(f). At $V_g = 0$ a single ferromagnetic LSCO layer with $M = 1.68$ μ_B/Co describes the data (Fig. 4.6(b,c)), with roughnesses of 4 Å and 8 Å at the LAO/LSCO and LSCO/ion gel interfaces, respectively. 1.68 μ_B/Co is slightly lower than the bulk saturation magnetization (1.9 μ_B/Co), but is consistent with magnetometry on these films. While a reasonable description of the 2 and 3 V data was also possible with a single ferromagnetic LSCO layer with progressively suppressed M, statistically significant fit improvements were obtained by introducing a second layer. This captures the weak dip to negative SA around 0.045 $Å^{-1}$ in Fig. 4.6(d). The resulting $M(z)$ in Fig. 4.6(f) reveals strong suppression of M with increasing V_g. At 2 V, M is roughly cut in half, the region closest to the ion gel interface having a slightly stronger reduction than the bulk of the film. At 3 V, M then becomes very small, a weakly magnetized bottom section of the LSCO providing the fit in Fig. 4.6(e). These results not only confirm near-uniform magnetization suppression, but are also *quantitatively* consistent with the δs from SXRD. Explicitly, taking the depth-averaged $M(V_g)$ from Fig. 4.6(f), and using bulk data for the x dependence of saturation magnetization in $La_{1-x}Sr_xCoO_3$ [9], an effective doping level (x_{eff}) can be extracted at each V_g. Using the fact that Sr hole doping is compensated by V_Os according to $x_{eff} = x - 2\delta$ (assuming doubly ionized V_O donors), the curves in Fig. 4.6(f) can then be associated with an induced δ. These values are 0.11 and 0.18 for $V_g = 2$ and 3 V, which, considering the approximations, are in reasonable agreement with Fig. 4.3(e). While this analysis ignores

other factors in the relationship between M and δ, making it only approximate, such an approach has been employed before and independently verified [107].

Table 4.4. Parameters used to fit the PNR data described in the main text. The top value is the nuclear SLD, t is the layer thickness, σ is the layer roughness (Gaussian width), and M is the magnetization of each layer. All scans were performed at 30 K in an in-plane magnetic field of 3 T. Note that for all biases an incoherent addition of a simple $LaAlO_3$/vacuum interface was required. Specifically, the $LaAlO_3$/vacuum sample composed 50 % of the total signal, consistent with the exposure of equal areas of $LaAlO_3$/vacuum and $LaAlO_3$/LSCO/ion gel portions sample in the beam path (see Fig. 4.6(a)). The same SLD was used for $LaAlO_3$ as that shown below, with a σ = 2 Å; zero SLD for vacuum was used. Note that the nuclear SLDs of $LaAlO_3$ and LSCO match the calculated values in Table 4.3 quite well. The SLD of the ion gel, however, is a factor of ~3 lower than the calculated value in Table 4.3. We cannot directly identify the source of this discrepancy, though it could come from an overestimation of the ion gel mass density (1.5 g/cm^3), lower density in as-processed films, development of voids or cracks, *etc*.

V_g (V)	$LaAlO_3$	Bottom LSCO	Top LSCO	Ion gel
0	5.29×10^{-6} Å^{-2} $t = \infty$ σ = 4.4 Å M = 0	4.91×10^{-6} Å^{-2} t = 160.5 Å σ = 7.9 Å M = 1.68 μ_B/Co	-	0.81×10^{-6} Å^{-2} $t = \infty$ σ = NA M = 0
2	5.29×10^{-6} Å^{-2} $t = \infty$ σ = 4.4 Å M = 0	4.91×10^{-6} Å^{-2} t = 118 Å σ = 3.9 Å M = 0.79 μ_B/Co	4.91×10^{-6} Å^{-2} t = 45 Å σ = 5.0 Å M = 0.51 μ_B/Co	0.81×10^{-6} Å^{-2} $t = \infty$ σ = NA M = 0
3	5.29×10^{-6} Å^{-2} $t = \infty$ σ = 4.4 Å M = 0	4.91×10^{-6} Å^{-2} t = 65 Å σ = 20.8 Å M = 0.22 μ_B/Co	4.91×10^{-6} Å^{-2} t = 100 Å σ = 1.0 Å M = 0 μ_B/Co	0.81×10^{-6} Å^{-2} $t = \infty$ σ = NA M = 0

Given that the electric field in EDLTs based on metallic perovskites should be screened over quite short scales (the Thomas-Fermi screening length is a few unit cells) the observation of gate-induced V_O formation through 40-unit-cell films warrants discussion. One interpretation is that V_O creation is first achieved by the EDL electric field at the extreme surface of LSCO. While the details remain to be understood, this would then generate an O chemical potential gradient, driving further out-migration of O from the bulk, potentially assisted by the electric field [149]. Importantly, the V_O diffusivity in LSCO [150] is large enough to support this interpretation, translating to a V_O diffusion length of 35 nm at 300 K on the time scales used here, well in excess of the 17 nm film

thickness. The enthalpy of formation of V_Os is also low in LSCO (as utilized in recent Gd gettering studies [151,152]) due to the instability of Co^{4+} formal valence. This results in extraordinary redox activity at x = 1, consistent with recent demonstrations of thermal [108] and electrolyte-assisted [63] switching between $SrCoO_{3-\delta}$ and brownmillerite $SrCoO_{2.5}$. The extent to which EDLT response in a given system involves redox is thus heavily influenced by the enthalpy of formation of V_Os, their diffusivity, and the V_g polarity.

4.4 Conclusions

In summary, we report the use of SXRD and PNR as *in operando* probes of gating mechanisms in ion-gel-based LSCO EDLTs. Large positive-bias-induced lattice expansion is observed, providing direct evidence of V_O formation. Complementary bulk measurements using TGA and PXRD, supported by DFT, are then used to quantify the V_g-dependent V_O density, which reaches δ = 0.16 at +2 V. This electrochemical reduction penetrates the entire thickness of ~30-unit-cell-thick films, confirmed by uniform suppression of the magnetization depth profile from PNR, quantitatively consistent with the deduced V_O density. The results thus establish SXRD and PNR as powerful *in operando* probes of electrolyte-gated materials, significantly advancing our understanding of gating mechanisms in oxide EDLTs.

Chapter 5: Percolation *via* combined electrostatic and chemical doping in complex oxides

This chapter is mainly based on the publication "*Percolation via combined electrostatic and chemical doping in complex oxide films*" in Physical Review Letters (2017) by Peter P. Orth, Rafael M. Fernandes, Jeff Walter, Chris Leighton, and Boris I. Shklovskii, adapted with permission from Ref. [153], copyright (2017) American Physical Society. In this work we address the third open issue in electrolyte gating discussed in Section 1.2.2 (*i.e.*, the application of electrolyte gating to control of magnetic material properties). Specifically, we address the fact that, despite the capability of EDLTs to reach surface charge densities $> 10^{14}$ cm^{-2}, often they fall short of inducing phase transitions of interest due to the need for 10^{15} cm^{-2}. In such cases one obvious strategy is to employ a combination of chemical and electrostatic doping, bringing the material close to some electronic and/or magnetic phase boundary by chemical substitution, then using surface electrostatic tuning of the carrier density to reversibly traverse the critical point. The work presented here focuses on such combined electrostatic surface and bulk chemical doping and resulting electronic and/or magnetic *percolation* transitions. This is an important situation in complex oxide materials due to the widespread observation of electronic and magnetic inhomogeneity (as in manganites [5], cuprates [110], and cobaltites [9,88,89], for example), where many transitions, such as from insulator to metal or from short to long-range magnetism, are percolative in nature. We approach this problem using classical percolation theory [154,155]. While our analysis and results are general, and could apply to percolation transitions in various materials, in this Letter we are motivated by physics of the perovskite oxide cobaltite, LSCO, which undergoes a percolation transition from insulator to metal at $x_{c,LSCO} \approx 0.18$ [9,94]. In this work we identify two different percolation phenomena: bulk-assisted surface percolation and surface-assisted bulk percolation. The first case applies to a system that is initially far away from the (thickness-dependent) bulk percolation threshold $x_c(t)$. In addition to the trivial effect that bulk doping ($x > 0$) increases the surface doping level (s), percolation on the surface is further facilitated by diluted bulk dopants providing bridges that connect disjunct finite surface clusters. In the second case, where the bulk chemical doping level is close to the percolation threshold, $x_c(t) - x << 1$, we find that

small electrostatic gating of a fraction of the surface lattice sites (Δs) helps to reach bulk percolation by connecting large finite bulk clusters on the surface. We show that the amount of surface charge that must be induced electrostatically to reach percolation (Δs_c) grows moderately with ($x_c - x$) for thin films, but increases sharply for thicker films.

5.1 Numerical modeling of percolation

The theoretical study of percolation phenomena in correlated systems has a long history [154–160]. The combination of bulk chemical and surface electrostatic doping, however, defines an unusual percolation problem that is thus far largely unexplored theoretically. The schematic setup is shown in Fig. 5.1, where the total (top) surface carrier density is given by:

$$s = x + \Delta s \qquad 5.1.$$

It arises from doping by both chemical substitution of a fraction of lattice sites x and electrostatic gating of a fraction of surface lattice sites Δs, and implies $s \leq 1$.

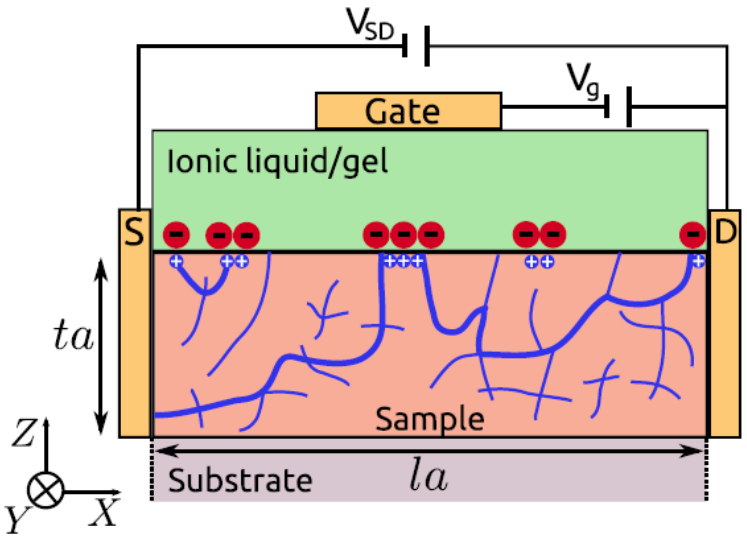

Fig. 5.1. Schematic setup showing a thin-film sample (red) of thickness ta and area $la \times la$, where a is the lattice constant, with large finite clusters (blue) due to bulk doping. The ionic liquid or gel (light green) on top of the sample induces a number of holes (blue spheres) at the top surface—proportional to the applied gate voltage V_g. Red spheres denote anions in the ionic liquid or gel that move towards the surface due to the applied voltage. For bulk doping close to percolation $x_c - x << 1$ (surface-assisted bulk percolation), electrostatically induced holes connect finite bulk clusters at the surface resulting in a conducting path (highlighted) between source (S) and drain (D) electrodes. The highlighted upper left-hand cluster shows bulk bridges connecting two surface clusters, which is the dominant effect of bulk dopants for $x << x_c$ (bulk-assisted surface percolation).

To derive our results, we consider the site percolation problem on the cubic lattice of size $la \times la \times ta$ along the X, Y, and Z axes defined in Fig. 5.1, where a is the lattice constant and l, t are integers ($t \leq l$). This geometry describes films of thickness ta and surface area $(la)^2$. We note that the new scaling laws in Eqs. 5.2, 5.3, 5.4, and 5.6 that we derive below are universal and therefore independent of microscopic details such as lattice symmetry or local connectivity. They thus apply to LSCO and other experimental systems even though the percolation thresholds, which are not universal quantities, may differ from that of a cubic lattice $x_{c,3D} = 0.31$ [161]. The thin-film percolation problem is solved using the numerical algorithm described in Refs. [162,163]. Starting from an empty lattice, a fraction x of sites is first randomly filled in the whole lattice to simulate bulk chemical doping. We verify that the bulk doping percolation threshold on the isotropic cubic lattice ($l = t$) lies at $x_{c,3D} = 0.31$, and increases for $t < l$; *i.e.*, $x_c(t) > x_c(l) \equiv x_{c,3D}$ [154]. To study the role of surface doping, we stop at a bulk doping level $x < x_c(t)$ and subsequently add a fraction Δs of sites exclusively on the top surface layer to simulate electrostatic gating. The total surface density of sites at the top surface is then given by Eq. 5.1. While electrostatically doping the system, we continuously monitor whether a percolating path exists between the two side surfaces at $X = 0$ and $X = la$. We define the critical total density of sites at the top surface that is required for percolation between the side surfaces as s_c. The amount of charge density that must be transferred *via* electrostatic doping is then denoted Δs_c.

In Fig. 5.2(a), we show numerical results for Δs_c as a function of the starting bulk chemical doping level x. Figure 5.2(b) shows s_c as a function of x. For pure surface doping, $x = 0$, we find the percolation threshold of the 2D square lattice, $\Delta s_c(0) = 0.59$ [155]. For small $x << x_c(t)$, the behavior of $\Delta s_c(x)$ depends only weakly on the film thickness t. In contrast, for $x_c(t) - x << 1$ the function $\Delta s_c(x)$ depends strongly on the thickness t, displaying a sharp enhancement as x decreases for thick films but a much more gradual one for thin films.

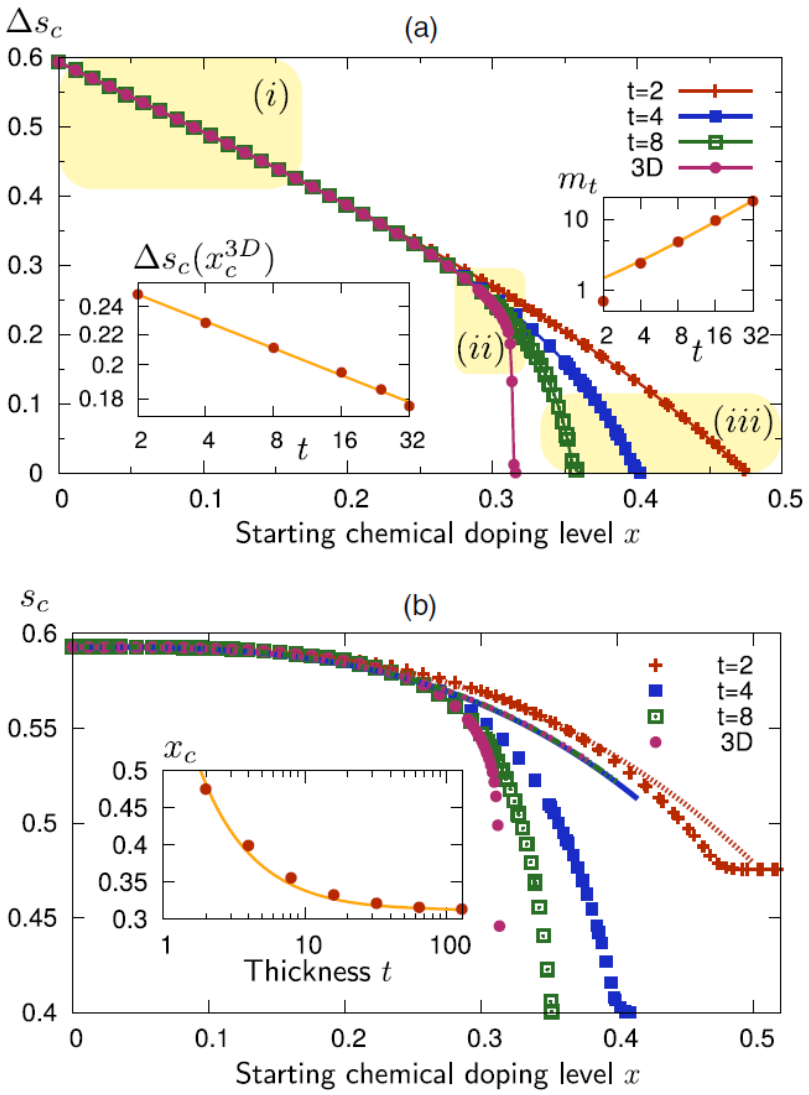

Fig. 5.2. (a) Surface charge density Δs_c that must be electrostatically induced to reach percolation, as a function of starting bulk chemical doping level x. Different curves correspond to different thicknesses t and are obtained from extrapolating results for system sizes $l \times l \times t$ with l = 32, 64, 128 to $l^{-1} \to 0$ and are averaged over at least 4.1×10^5 disorder realizations. The curve labeled "3D" is for $t = l$. The left inset shows that Δs_c at the bulk percolation threshold $x_{c,3D} = 0.31$ obeys Eq. 5.4 (yellow line) with $c_2 = 0.27$ and $\nu_{fit} = 0.89 \pm 0.01$. The right inset shows the slope of $s_c - x_c = m_t(x_c - x)$ close to $x_c(t) - x << 1$, verifying Eq. 5.6, with $c_5 = 0.56$. Yellow rectangles mark the three regimes labeled (i)– (iii), addressed by our analytical theory. (b) Total surface charge at percolation s_c as a function of x. The lines are fits of the numerical results according to Eq. 5.2 with $b = 0.91$ for $t = 2$ and $b = 1.12$ for $t = 4$, 8, l. The inset shows the thickness-dependent bulk percolation threshold $x_c(t)$ for purely chemical doping. The yellow line obeys Eq. 5.5 with $x_{c,3D} = 0.312$, $\nu = 0.88$ [161], and $c_3 = 1.21$.

5.2 Analytical theory

To develop an analytical scaling theory [154], we focus on three limits: (i) $x << x_c(t)$, (ii) $x_{c,3D} - x << 1$, and (iii) $x_c(t) - x << 1$, which are indicated by yellow rectangles in Fig. 5.2(a). The first case can be described as bulk-assisted surface percolation and the other two by surface-assisted bulk percolation.

(i) For $x << x_c(t)$, we have $s_c(0) - s_c(x) << 1$: the system is close to the 2D percolation threshold on the surface, but far from percolation in the bulk. As a result, the typical size of bulk clusters is rather small. These small bulk clusters (away from the surface) can still assist percolation at the surface by providing short bridges across missing links between disconnected finite large surface clusters, as shown in Fig. 5.1. Since the smallest possible bulk bridge consists of three sites below the surface, at $x << 1$ the main contribution of the bulk doping arises from such bridges, yielding:

$$s_c(x) = s_c(0) - bx^3 \qquad 5.2.$$

As shown in Fig. 5.2(b), this equation, with weakly t-dependent coefficient b, describes the numerical results well for $s_c(0) - s_c(x) << 1$; for $t = 2$ it is even applicable over almost the full range of doping levels up to x_c.

(ii) In the regime of small $x_c^{3D} - x << 1$, the 3D bulk is close to the percolation threshold, but the surface concentration is far from the surface percolation threshold. Thus, while large critical finite clusters exist in the bulk, with a typical size of $\xi(x) \approx a(x_{c,3D} - x)^{-\nu}$ and correlation length exponent $\nu = 0.88$ [155,161], the largest surface clusters remain small.

Let us first discuss the case of an infinite isotropic 3D system. If sites were randomly added in the bulk, an infinite cluster connecting $X = 0$ and $X = la$, which looks like a network of links and nodes with typical separation $\xi(x)$, would occur after adding $N = N_0(x_{c,3D} - x)l^3$ sites, with $N_0 \approx 2$. Because this infinite cluster provides percolation inside a layer of height $\xi(x)$ below the surface, the number of sites $\Delta N = N_0(x_{c,3D} - x)l^2\xi(x)/a$ we have added to this layer is sufficient to induce percolation along the layer. We assume that addition of sites to any of the ξ/a planes parallel to the surface within this layer equally contributes to the probability to connect critical clusters. Then, instead of homogeneously

doping the layer of volume $(la)^2\xi(x)$, we can reach percolation by adding all these sites to the surface plane only. This yields a critical surface density of:

$$s_c(x) = x_{c,3D} + \Delta N/l^2 = x_{c,3D} + c_1(x_{c,3D} - x)^{1-\nu} \quad 5.3,$$

with a nonuniversal constant c_1. We see that since $\nu < 1$, connecting bulk clusters on the surface can be done by very small surface addition Δs at $x_{c,3D} - x << 1$. Scaling in Eq. 5.3 only holds for $(x_{c,3D} - x)^{1-\nu} << 1$. Since $1 - \nu = 0.12 << 1$ [155,161], the validity of Eq. 5.3 is thus limited to a tiny region of x close to $x_{c,3D}$, which explains the sharp rise of $\Delta s_c(x)$ for $t = l$ (3D) in Fig. 5.2.

A finite thickness t of the film introduces another length scale, which cuts off the scaling behavior of Eq. 5.3 as soon as $\xi(x) > ta$, and Eq. 5.3 is replaced by:

$$s_c(x) = x_{c,3D} + c_2 t^{1-1/\nu} \quad 5.4,$$

with non-universal constant c_2. We numerically verify this scaling behavior at $x = x_{c,3D}$, as shown in the (left) inset of Fig. 5.2(a). A fit to our data yields $\nu_{fit} = 0.89 \pm 0.01$, confirming the expected scaling with $\nu = 0.88$ [155,161]. To derive Eq. 5.4, we first notice that the bulk percolation threshold $x_c(t)$ of a film of thickness t is reached when an infinite bulk cluster with correlation length $\xi[x_c(t)] \leq ta$ appears. From this, it follows that [154]:

$$x_c(t) = x_{c,3D} + c_3 t^{-1/\nu} \quad 5.5,$$

with non-universal constant $c_3 = 1.21$, which is in agreement with our numerical results shown in the inset of Fig. 5.2(b). Therefore, to achieve percolation at $x = x_{c,3D}$, a film with width t must acquire $\Delta N = c_4(x_c(t) - x_{c,3D})tl^2 = c_2 l^2 t^{1-1/\nu}$ filled sites, where c_4 is a non-universal constant. As above, we assume that we can reach the percolation threshold by bringing all these sites into the surface plane by electrostatic gating, yielding Eq. 5.4. Note that Eq. 5.4 crosses over to Eq. 5.3 at $\xi(x) = ta$.

(iii) We now investigate s_c for $x_c(t) - x << 1$. In this regime, it holds that $\xi(x) > ta$, since the correlation length at $x_c(t)$ fulfills $\xi[x_c(t)] = ta$. We find that $\Delta N = N_0[x_c(t) - x]l^2 t$ sites should be added to the system in order to reach percolation, such that the critical surface percolation threshold obeys:

$$s_c(x) = x_c(t) + c_5 t[x_c(t) - x] \quad 5.6,$$

with non-universal constant c_5. We demonstrate in the (right) inset of Fig. 5.2(a) that our numerical results follow this scaling relation of the slope $m_t = c_5 t$, with $c_5 = 0.56$. Note that the scaling breaks down for the thinnest system, $t = 2$, which is instead described by Eq. 5.2 over the full range of bulk doping levels x [see Fig. 5.2(b)].

The key insight from our results is that bulk chemical doping largely reduces the amount of electrostatic surface charge Δs_c required to reach percolation (compared to the 2D value) in a region of initial chemical doping levels $x_{c,3D} < x < x_c(t)$. In this regime, the critical surface charge s_c scales with the thickness according to Eq. 5.6 and therefore grows quickly for thicker films. The underlying physical phenomenon is that less surface charge must be transferred by electrostatic gating if percolation is induced by connecting finite large bulk clusters on the surface rather than creating a percolating path that is confined to the surface alone. The width of this region $x_c - x_{c,3D} \propto t^{-1/\nu}$ rapidly narrows for thicker films. For smaller x, the dominant effect of the bulk dopants is to act as short bridges between disconnected surface clusters. This reduces the number of surface sites that must be filled to reach percolation only slightly compared to the 2D case (see Eq. 5.2).

5.3 Enhanced surface magnetization

If the percolation transition is associated with ferromagnetic ordering, as for LSCO, the extension of the percolating cluster from the surface into the bulk leads to a dramatic volume enhancement of the surface saturation magnetization M_s in the case of surface-assisted bulk percolation [cases (ii) and (iii)]. To capture this equilibrium phenomenon, in Fig. 5.3 we show the size (i.e., number of sites) of the largest cluster N_c (per surface area l^2) as a function of electrostatic doping Δs. Beyond the percolation threshold $\Delta s > \Delta s_c(x)$, this cluster percolates and its size, *i.e.*, number of sites with ferromagnetically polarized Co spins, is proportional to the surface saturation magnetization $M_s \propto N_c/l^2$. For small doping levels, we observe regular surface percolation at $\Delta s_c \approx 0.59$. The percolated path is almost entirely confined to the top surface layer and the magnetization enhancement is absent: $N_c/l^2 \lesssim 1$. However, if the system is initially doped closer to the (bulk) percolation threshold x_c, the percolating cluster extends significantly into the bulk and we observe N_c/l^2

> 1. As the (fractal) dimension of this cluster exceeds $d = 2$, we find that N_c/l^2 becomes as large as 4 for a film of thickness $t = 16$ (a fully magnetized film corresponds to $N_c/l^2 = t$). This shows that bulk doping ultimately generates a much larger saturation magnetization, because of the inclusion of preformed clusters of spin polarized sites. We further predict an unusual depth profile of magnetization $M_s(z)$ as a function of distance z from the surface, which can be directly experimentally measured using polarized neutron reflectometry or indirectly inferred using X-ray magnetic circular dichroism (XMCD) or the magneto-optical Kerr effect (MOKE).

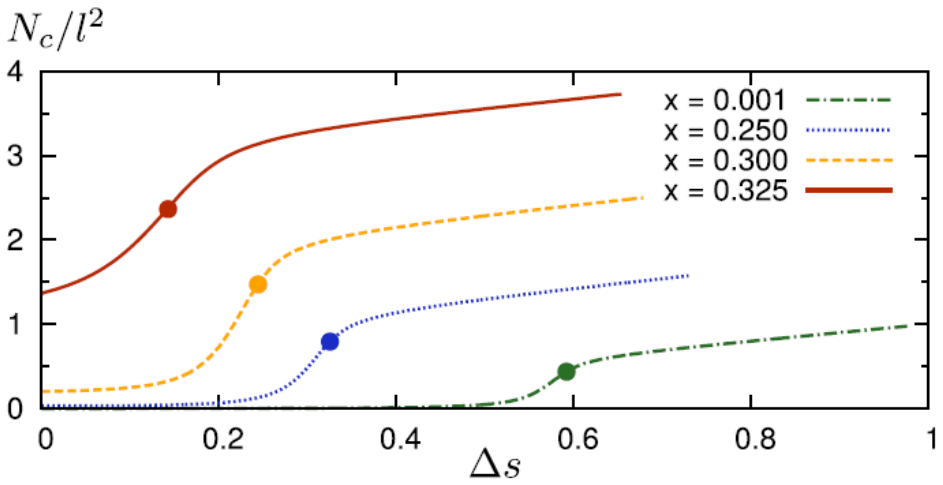

Fig. 5.3. Surface density of the largest cluster in the system $N_c = l^2$ as a function of electrostatic doping Δs in a film of thickness $t = 16$. Dots indicate percolation thresholds $\Delta s_c(x)$. For $\Delta s > \Delta s_c$, N_c/l^2 is proportional to the surface saturation magnetization M_s. The plot shows the large enhancement of M_s due to the extension of the infinite cluster deep into the bulk.

5.4 Conclusions

Motivated by existing and ongoing experiments on complex oxide thin films, we have studied a new percolation problem, where bulk chemical doping is combined with electrostatic doping of the surface. We have derived new analytical formulas describing universal scaling behavior of the electrostatic percolation threshold and explored the full crossover from bulk to surface percolation numerically. Experimental predictions that follow from our analysis are the following. (i) The critical surface charge density at percolation s_c depends only weakly on the starting bulk doping level x, except in proximity to the bulk percolation transition $x_{c,3D} < x < x_c(t)$. The crossover from surface-assisted to

bulk-assisted percolation occurs more abruptly for thicker films. Given limitations of ionic liquid, gel or ferroelectric gating, experimental validations of gate-induced percolation may thus rely in most cases on chemically doping close to the percolation threshold. (ii) Once percolation is reached, the saturation magnetization M_s is largely enhanced due to the presence of critical clusters extending deep into the bulk. (iii) The existence of ferromagnetic bulk clusters will also be reflected in the dependence of the magnetization $M_s(z)$ on the distance z from the surface. Our work thus shows that "bulk" magnetic properties can be controlled using "surface" electrostatic gating. In our approach, the transition to long-range ferromagnetic order in LSCO is driven solely by percolation, and not by order parameter fluctuations. While at low enough temperatures thermal fluctuations are indeed weak, quantum fluctuations remain present. However, previous studies of diluted quantum magnetic systems found that the percolation threshold and certain percolation critical exponents (such as β and ν) are unaffected by quantum fluctuations [164,165], even in the presence of dissipation [166,167], which is expected to occur on the metallic side of the transition. Finally, while we have focused on electrostatic gating, our conclusions also apply to electrochemical doping describing, for example, the transfer of oxygen vacancies into the surface of a sample.

Chapter 6: Giant electrostatic modification of magnetism *via* electrolyte-gate-induced cluster percolation in $La_{1-x}Sr_xCoO_{3-\delta}$

This chapter is mainly based on the manuscript "*Giant electrostatic modification of magnetism via electrolyte-gate-induced cluster percolation in* $La_{1-x}Sr_xCoO_{3-\delta}$" by Jeff Walter, Timothy Charlton, Haile Ambaye, Michael Fitzsimmons, Peter P. Orth, Rafael M. Fernandes, Boris Shklovskii, and Chris Leighton, which was submitted for review to Physical Review Letters in May 2018. In this work we address the third open issue in electrolyte gating discussed in Section 1.2.2 (*i.e.*, the application of electrolyte gating to control of magnetic material properties). We first briefly summarize what has been achieved in electrolyte-gate-control of magnetism and discuss the specifics of applying the theory laid out in Chapter 5. We then validate the theoretical predictions discussed in Chapter 5 (*i.e.*, thickness tuning to the brink of percolation in highly doped LSCO films, rather than tuning the doping level in thick films, followed by electrolyte gating is a promising means to optimize electrostatic control of magnetism) through transport studies of LSCO EDLTs *vs*. x_{eff} and thickness (t_{exp}). Thickness tuning is indeed established as an ideal means to tune to the brink of a percolation insulator-metal transition (IMT), 6 u.c. proving optimal. Ion gel gating of 6 u.c. films of $x = 0.5$ LSCO is then shown to enable *electrostatic* tuning from a short-range-ordered insulator to a long-range FM metal, spanning a 150 K T_C range with only -4 V. The induced FM is robust, with 1 T coercivity, high remanance, and perpendicular anisotropy. *In operando* PNR not only confirms FM, but establishes deeper penetration of induced magnetization than naively expected, in further agreement with the theoretical predictions discussed in Section 5.3.

6.1 Current status of voltage-controlled magnetism with electrolyte gating

Despite obvious potential, less progress has been made with using EDLTs to control magnetism [33,38] compared to superconducting transitions [32,35–37,39] and IMTs [34,42,49,50]. This is a long-standing challenge in physics and technology, voltage-control of magnetic order and properties potentially providing many opportunities in data storage and processing [3,22,23,151]. Studies of electrolyte-gate-control of magnetism are thus rapidly expanding, a logical first step being control of T_C in FM conductors. In the last

decade, the electrically-induced T_C shift in EDLTs has risen from 30 K in $La_{0.8}Ca_{0.2}MnO_3$ [33] and $SrRuO_3$ [44], to 66 K in $La_{0.6}Sr_{0.4}MnO_3$ [70], 90 K in $La_{0.6}Sr_{0.4}MnO_3/SrCoO_{3-\delta}$ [168], 110 K in Co [169], 130 K in $Pr_{0.55}(Ca_{0.7}Sr_{0.3})_{0.45}MnO_3$ [170], and, recently, 220-225 K in $La_{0.5}Sr_{0.5}CoO_{3-\delta}$ [135] and $(H)SrCoO_{3-\delta}$ [63]. While this is impressive, it is important to distinguish *electrostatic* control from *electrochemical* [44,49,168,50,51,63–66,124,135]. Both approaches are of high interest, but the additional ionic motion in electrochemical control could lead to slower, less reversible operation. In oxide EDLTs, for example, field-induced V_O creation and diffusion is established [44,49–51,63–65,124,135,168], along with H injection and extraction [63,66], and it is exactly such "magneto-ionic" mechanisms that are implicated in these large T_C shifts [33,44,63,70,135,168–170]. Our work on $La_{0.5}Sr_{0.5}CoO_{3-\delta}$ EDLTs provided an illustrative example by distinguishing electrochemistry at positive V_g from predominantly electrostatic response at negative V_g (Chapters 3 and 4) [124,135]. In essence, positive V_g results in electric fields oriented for field-assisted V_O creation and diffusion, favored by low formation enthalpy. At negative V_g, however, annihilation of V_O is thermodynamically disfavored, electrostatic hole accumulation dominating. Electrostatic *vs*. electrochemical response is therefore understood based on V_g polarity and the formation enthalpy and diffusivity of V_O (Chapters 3 and 4) [124,135]. Critically, *electrochemical* control at $V_g > 0$ resulted in $La_{0.5}Sr_{0.5}CoO_3$ T_C shifts of ~220 K (Chapter 4) [135], while *electrostatic* operation at $V_g < 0$ resulted in a T_C shift of only 12 K in -4 V (Chapter 3) [124].

6.2 Theory guided optimization of electrolyte-gated $La_{1-x}Sr_xCoO_{3-\delta}$ films

A natural question is thus how electrostatic control of magnetic order in such materials can be optimized. Given the common tendency to evolve from inhomogeneous phases to uniform FMs with doping (LSCO [9,89,94], LSMO [5], *etc*.), one attractive concept (Fig. 1(a)) is to chemically dope to the brink of a percolation IMT (note the preformed filaments in Fig. 6.1(a)) and then gate across the transition, potentially generating anomalously large increases in T_C, magnetization, conductivity, *etc*. This situation was considered in our recent site percolation theory [153] (Chapter 5), resulting in Fig. 6.1(b), which is a recreation of Fig. 5.2(a) with the axes re-scaled (discussed below). The solid lines here show the predicted 2D surface electrostatic doping densities required to achieve percolation

($\Delta s_{c,th}$, per formula unit) *vs*. the starting effective chemical doping (x_{eff}), for multiple thicknesses (t_{th}). We use x_{eff} here due to finite V_O density in LSCO, which compensates nominal doping, x. In the thick (3D) limit, $\Delta s_{c,th}$ at $x_{eff} = 0$ is 0.5 (the 2D homogeneous value), decreasing with x_{eff} before vanishing at the LSCO 3D percolation threshold (x_{eff} = 0.18 [94]). The x_{eff} axis was scaled by a factor of $x_{c,LSCO}/x_{c,3D}$ (*i.e.*, 0.18/0.312) in order to apply Fig. 5.2(a) to the specific case of LSCO. The value of $x_{c,LSCO} = 0.18$ is actually consistent with the 3D homogeneous percolation threshold, thus we also decided to re-scale the $\Delta s_{c,th}$ axis such that the homogeneous 2D threshold (0.5) was achieved at $x_{eff} = 0$, as opposed to the site percolation threshold (0.59) shown in Fig. 5.2(a). Such rescaling is possible because of the universality of the theoretical approach, as discussed in Section 5.1. Considering that an experimentally achievable Δs in a perovskite EDLT is ~0.1 (shaded region in Fig. 1(b)), the steepness of $\Delta s_{c,th}$ near percolation means that tuning x_{eff} to the brink of percolation in thick films would require unreasonable compositional control. Also shown in Fig. 1(b), however, is $\Delta s_{c,th}(x_{eff})$ at 8, 4, and 2 u.c. thickness, showing shallower approach to percolation. At 2 u.c., for example, an achievable Δs of ~0.1 enables percolation at $0.23 < x_{eff} < 0.27$, a *400 times* wider window than 3D. Thickness tuning to the brink of percolation thus predicted as a promising means to optimize electrostatic control of magnetism.

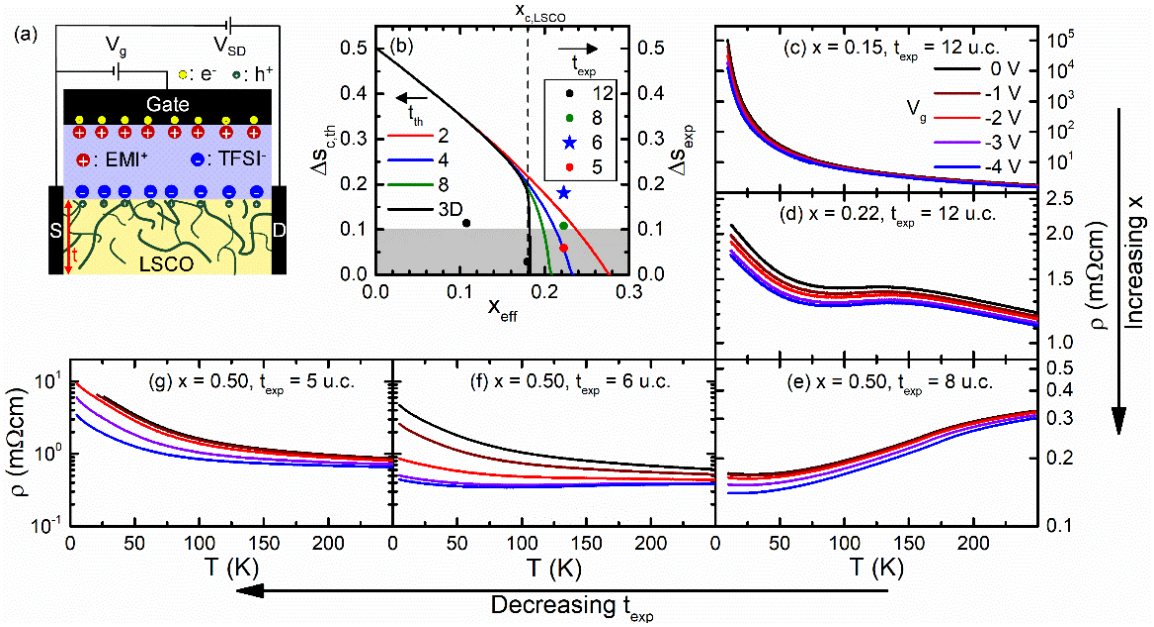

Fig. 6.1. (a) $La_{1-x}Sr_xCoO_{3-\delta}$ (LSCO) EDLT schematic. S/D represents source/drain, V_g/V_{SD} the gate/source-drain voltages, red/blue charges the ion gel cations/anions, and yellow/gray charges electrons/holes, respectively. The LSCO film has thickness t and sub-percolative clusters are shown. (b) Solid curves (color coded for different theoretical thickness, t_{th}) show the theoretical surface charge density required to induce percolation, $\Delta s_{c,th}$ (left axis), *vs.* bulk chemical doping, x_{eff}. These are obtained from Fig. 5.2(a), by rescaling to the LSCO experimental percolation threshold, $x_{c,LSCO}$, as discussed in the main text. Data points (right axis, color coded to the experimental thickness, t_{exp}) show the maximum experimental surface charge density achieved, Δs_{exp}. (c-g) Temperature, T, dependence of resistivity, ρ (log scales), for LSCO films with nominal x = 0.15, 0.22, 0.5, 0.5, and 0.5 at t_{exp} = 12, 12, 8, 6, and 5 unit cells, respectively, at gate bias, V_g = 0 to -4 V.

Epitaxial LSCO EDLTs utilizing solid-state ion gel electrolytes based on the IL EMI:TFSI were prepared and characterized [124,135], as detailed in Section 2.3. *Throughout this paper, only negative V_gs are applied, working exclusively in electrostatic mode*. PNR measurement details are provided in Section 2.5. Note that both LAO(001) and SLAO(001) substrates were used. The ρ(T, V_g) for 8 u.c. thick x = 0.5 films grown on LAO and SLAO are shown in Figs. 6.2(a,b), respectively. Note that these films begin at similar ρ values and the gate-induced decrease in ρ at negative V_g is also similar, demonstrating that both the starting films and the gating effects observed on these two substrates are similar. We thus treat the two substrates as interchangeable. Note that we chose SLAO for PNR measurements as it does not exhibit multiple reflections due to twinning as LAO does, therefore making the data reduction more straightforward.

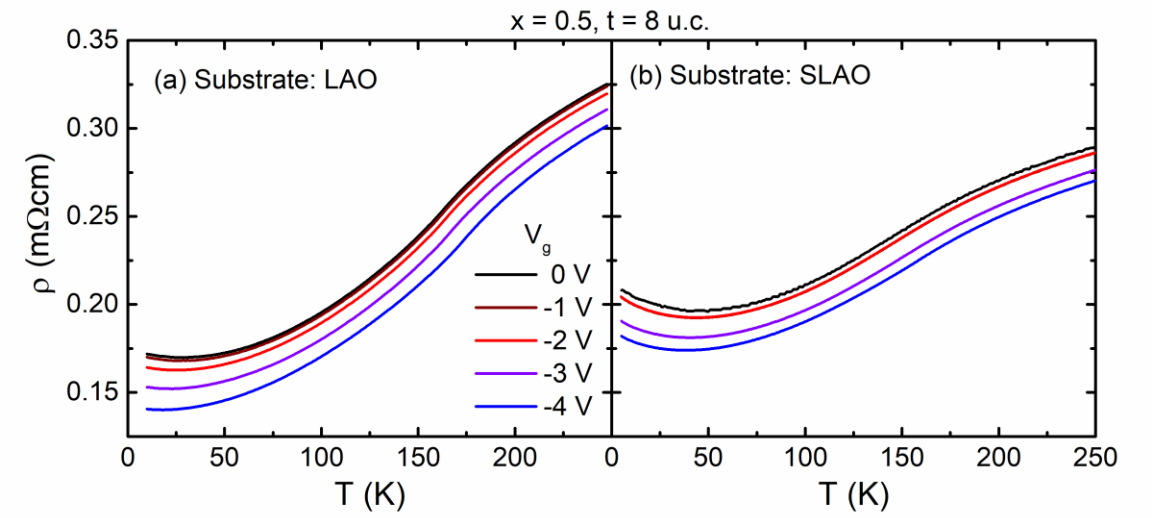

Fig. 6.2. Temperature (T) and gate bias (V_g) dependence of resistivity (ρ) for 8 u.c. thick $La_{0.5}Sr_{0.5}CoO_{3-\delta}$ films grown on (001)-oriented (a) $LaAlO_3$ (LAO) and (b) $SrLaAlO_4$ (SLAO).

We now move back to Fig. 6.1 to test the theoretical predictions with transport studies of LSCO EDLTs *vs.* x_{eff} and t_{exp}. Fig. 6.1(c-e) first shows the effect of varying x_{eff} while keeping t_{exp} approximately constant at 8-12 u.c., *i.e.*, the thick-film-limit in this system, where dead layer effects are weak. Starting at $x = 0.50$ (Fig. 6.1(e)), as in Chapter 3 [], the ρ(T) displays clearly metallic behavior, well beyond the percolation IMT. Applying V_g = -4 V decreases the low T resistivity by ~18% *via* electrostatic hole doping, the inflection point between 162 and 174 K evidencing the previously reported 12 K T_C shift, confirmed by anomalous Hall effect (AHE) [124] (Chapter 3). The impact of decreasing chemical doping is shown in Figs. 6.1(d,c), for $x = 0.22$ and 0.15. Progressively insulating behavior is observed, as expected, but *without* a V_g-induced IMT. At $x = 0.15$, for example, insulating ρ(T) occurs, but application of -4 V, while generating a ten-fold low T resistivity decrease, is incapable of inducing percolation. As illustrated in Fig. 6.1(e,f,g), fixing $x = 0.50$ and progressively reducing t_{exp} (from 8 to 5 u.c.) is more effective, as predicted. In particular, at 6 u.c., initially insulating ρ(T) occurs, but with application of -4 V driving a ten-fold decrease in low T resistivity, to a state with positive $d\rho/dT$. A gate-induced percolative IMT is thus realized in LSCO EDLTs, *via* thickness tuning.

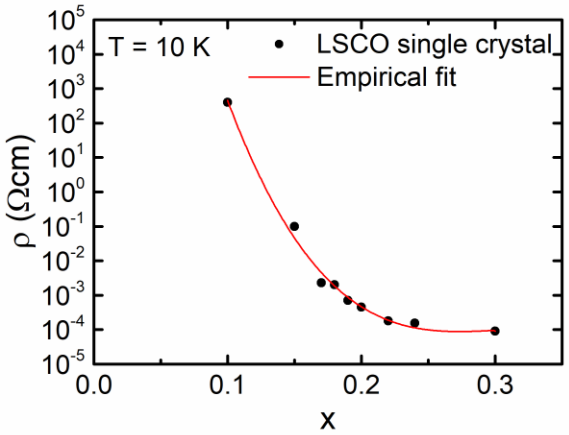

Fig. 6.3. 10 K resistivity (ρ) for $La_{1-x}Sr_xCoO_3$ single crystals *vs*. *x* []. The black points are from individual crystals and the red line is the empirical fit used to extract the effective doping level (x_{eff}) and the achieved electrostatic doping (Δs_{exp}) as discussed in the main text.

That these results are at least qualitatively consistent with our prior percolation theory is shown in Fig. 6.1(b). The colored points here (right axis) show the *achieved* electrostatic doping (Δs_{exp}) as a function of x_{eff}, for various thicknesses, t_{exp}. Estimates of x_{eff} were attained by comparing the 10 K resistivity (ρ) of each sample at V_g = 0 V to ρ(10 K, *x*) for LSCO single crystals [93], which is shown in Fig. 6.3 (the empirical fit in red was used to smooth the *x* dependence and interpolate between *x* values). Estimates of Δs_{exp} assumed the gate-induced change in ρ happened uniformly throughout the entire film thickness. The ρ(10 K) at V_g = - 4 V was again compared to Fig. 6.3, extracting a new x_{eff}(-4 V) and thus the change $\Delta x_{eff} = x_{eff}(-4\text{ V}) - x_{eff}(0\text{ V})$. The value for Δs_{exp} was then calculated by projecting Δx_{eff} to the surface using $\Delta s_{exp} = t_{exp} \times \Delta x_{eff}$. While the assumption that the gate-induced changes are uniform throughout the entire film thickness is probably a poor one (*i.e.*, the *t* in which Δx_{eff} actually occurs is probably smaller than t_{exp}), considering the 1-3 u.c. screening lengths in LSCO, this estimation provides a useful upper limit of the Δs_{exp}. With estimates of x_{eff} and Δs_{exp} for each of the samples in Figs. 6.1(c-g), we can now compare to the theoretical predictions in Fig. 6.1(b). The *x* = 0.15 film in Fig. 1(c), for example, has x_{eff} = 0.11 (black point, Fig. 6.1(b)), the achieved Δs_{exp} = 0.11 falling well below the $\Delta s_{c,th}$ = 0.33 required to reach percolation, consistent with the V_g dependence in Fig. 6.1(c). The situation is very different at *x* = 0.50, however. The thick-film-limit x_{eff} determined there is 0.22, consistent with the metallic ρ(*T*) (Fig. 6.1(e)). Although quantitative comparisons between theoretical and experimental thickness dependences are complicated by several

issues (as discussed below), decreasing t_{exp} from 8 to 6 u.c. does significantly increase Δs_{exp} (to 0.18), realizing a situation where $\Delta s_{exp} > \Delta s_{c,th}$, even when comparing to the extreme thin-film-limit (t_{th} = 2 u.c., red line, Fig. 6.1(b)). Thickness-tuning of "overdoped" LSCO films thus results in EDLTs that can be electrostatically gated through the percolation IMT.

As mentioned above, quantitative comparisons between theoretical and experimental thickness in Fig. 6.1(b) are complicated by several issues. Fig. 6.4 reproduces the thickness-dependent bulk percolation threshold, $x_c(t)$ (scaled such that $x_{c,3D} = x_{c,LSCO} = 0.18$ in a similar manner to what was done for x_{eff} in Fig. 6.1(b)), from inset of Fig. 5.2(b) . As discussed above, the effective chemical doping level of the x = 0.5 films was determined to be x_{eff} = 0.22. Using Fig. 6.4, the t at which films of this doping level are expected to cross the percolation transition is 4.4 u.c., below this value the films are expected to be un-percolated. In contrast, however, we observe this crossover experimentally to be somewhere between t_{exp} = 6 and 7 u.c. Esssentially, this suggests the films used here contain ~2 u.c. worth of "dead layers." These dead layers could arise from non-uniform oxygen vacancy depth profiles, as similar films grown on $SrTiO_3$(001) have been shown to accumulate oxygen vacancies near the substrate/film interface and at the film surface []. The 1-2 u.c. roughnesses typically observed could also be contributing to this discrepancy. Considering the ~2 u.c. difference between the theoretical and experimental critical thicknesses for percolation, we have chosen to compare the t_{exp} = 6 and 5 u.c. films (Figs. 6.1(f,g)) to t_{th} = 4 and 2, respectively, hence the use of similar colors for those thicknesses in Fig. 6.1(b).

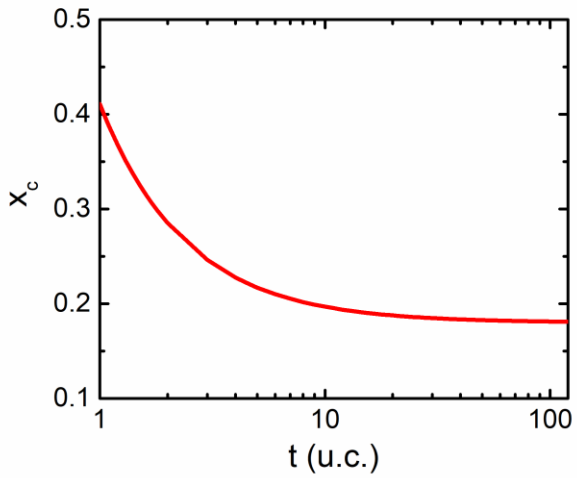

Fig. 6.4. Thickness (t) dependence of the bulk percolation threshold (x_c) for purely chemical doping, re-scaled by a factor of $x_{c,LSCO}/x_{c,3D}$ = 0.18/0.31 from Ref. [153].

Further, a second method of estimating a lower limit for Δs_{exp} was performed, with the results shown in Fig. 6.5. This alternative method assumes the gate-induced changes only occur in the top unit cell, thus exploring the opposite limit compared to the prior assumption of uniform changes. In this case, the sheet resistance (R_s) at 10 K and V_g = -4 V for each sample was modeled as two parallel resistors; one of the resistors (R_g) being the gated layer at the top of the film the other (R_{ug}) the ungated portion at the bottom of the film. R_s is given by

$$R_s^{-1} = R_{ug}^{-1} + R_g^{-1} \quad 6.1,$$

$$R_{ug} = (t_{exp} - 1 \text{ u.c.}) \times \rho_{ug} \quad 6.2, \text{ and}$$

$$R_g = (1 \text{ u.c.}) \times \rho_g \quad 6.3,$$

where ρ_{ug} is the ungated layer resistivity (which is the same as the V_g = 0 V resistivity) and ρ_g is the gated layer resistivity. Using Eqs. 6.1 - 6.3, ρ_g was extracted for each sample and compared to the single crystal values in Fig. 6.3 to get a new x_{eff} for the gated layer, again allowing for calculation of $\Delta s_{exp} = (1 \text{ u.c.}) \times \Delta x_{eff}$. The resulting estimations of Δs_{exp} using the second method are shown in Fig. 6.5. All of the values are about a factor of two smaller than the Δs_{exp} estimated with the first method (shown in Fig. 6.1(b)), again providing a lower limit of Δs_{exp}. Note that the conclusions do not change when comparing these two methods, as the t_{exp} = 6 u.c. film is still consistent with gate-induced percolation ($\Delta s_{exp} > \Delta s_{c,th}$).

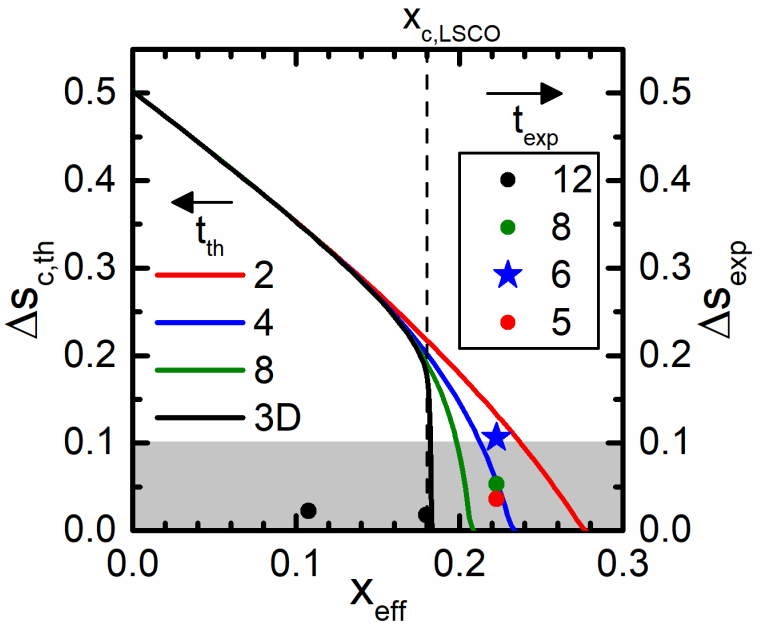

Fig. 6.5. Solid curves (color coded for different theoretical thickness, t_{th}) show the theoretical surface charge density required to induce percolation, $\Delta s_{c,th}$ (left axis), *vs.* bulk chemical doping, x_{eff}. These are obtained from Fig. 5.2(a), by rescaling to the LSCO experimental percolation threshold, $x_{c,LSCO}$ [94]. Data points (right axis, color coded to the experimental thickness, t_{exp}) show the maximum experimental surface charge density achieved, Δs_{exp}, calculated using the parallel resistor model discussed above.

6.3 Gate-induced ferromagnetism achieved by cluster percolation

Fig. 6.6 demonstrates that the gate-induced IMT in these 6 u.c. LSCO films also drives a transition from a magnetically-clustered state to a long-range FM metal. Initial evidence comes from Fig. 6.6(a), where positive $d\rho/dT$ emerges at $V_g \leq$ -3 V, accompanied by inflection near 150 K; in LSCO, such inflection points strongly suggest FM order []. More direct evidence comes from the AHE, as in Fig. 6.6(f). Shown here is the 5 K B dependence of the transverse conductivity ($\sigma_{xy} = \rho_{xy}/\rho_{xx}^2$, where ρ_{xy} is transverse resistivity and ρ_{xx} is the $B = 0$ longitudinal ρ), revealing a remarkable evolution with V_g. At $V_g = 0$ and -1 V no trace of AHE is detected, but at V_g = -2 V weak AHE emerges, growing into a large, hysteretic effect by -3, -4 V. This is strong evidence for long-range FM, electrostatically-induced from a non-FM starting point. Notably, the gate-induced FM is robust, exhibiting 1 T coercivity, remanence of 61 % of saturation, and strong perpendicular magnetic anisotropy (PMA). The latter is a feature of LSCO under compressive strain [] (as is the case here), the large anomalous Hall conductivity leading to $\sigma_{xy}(B)$ dominated by

magnetism [124]. Setting a small out-of-plane B = 0.02 T and measuring $\sigma_{xy}(T)$ then enables an order parameter measurement. As shown in Fig. 2(c), $\sigma_{xy}(T)$ reveals negligible FM at 0 and -1 V, a minor increase at the lowest T at -2 V, but strong FM order at -3, -4 V. The low T downturn in $\sigma_{xy}(T)$ may reflect the upturn in $\rho(T)$ (Fig. 6.6(a)), or T-dependent competition between in-plane and perpendicular anisotropy [124], the main point, however, being the order-parameter behavior at high T, directly demonstrating T_C up to 150 K at -4 V. The electrostatically-induced T_C shift by thickness-tuning to the brink of percolation in LSCO is thus 150 K, over an order of magnitude higher than the previous 12 K [124].

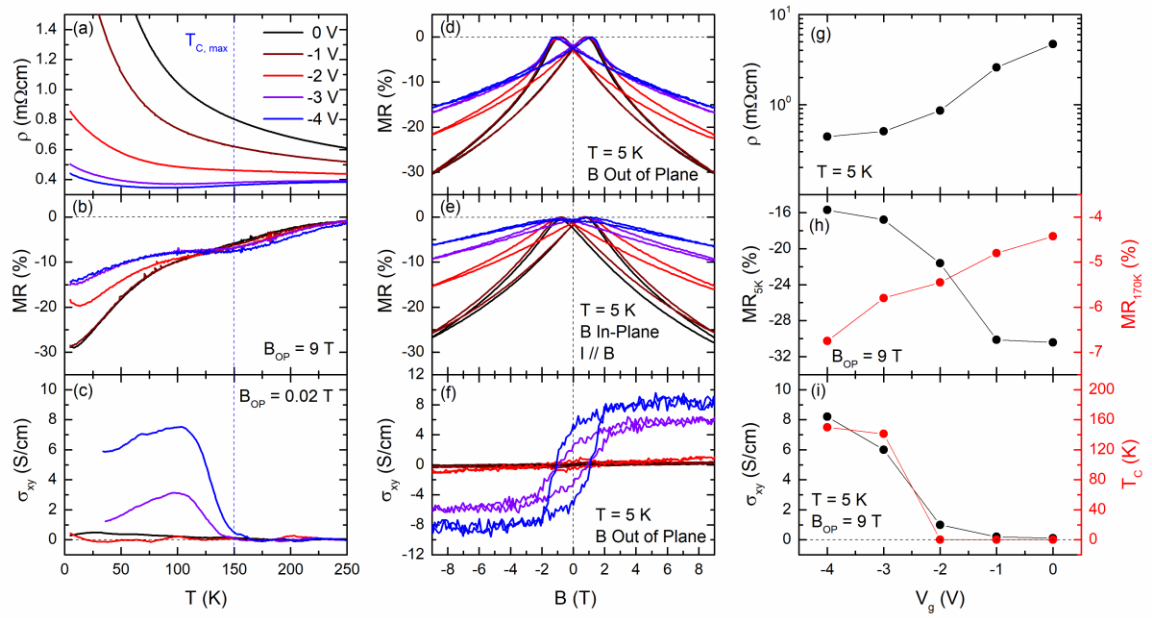

Fig. 6.6. (a,b,c) Temperature, T, dependence of (a) zero magnetic field resistivity, ρ, (b) 9 T out-of-plane magnetoresistance, MR, and (c) low field (out-of-plane field, B_{OP} = 0.02 T) transverse conductivity, σ_{xy}, at gate bias, V_g = 0 to -4 V. (d,e,f) 5 K B dependence of (d) out-of-plane MR, (e) in-plane MR (with current, $I \parallel B$), and (f) σ_{xy}, at V_g = 0 to -4 V. (g,h,i) V_g dependence of (g) ρ at 5 K, (h) out-of-plane MR at 5 K (left axis) and 170 K (right axis), and (i) σ_{xy} at 5 K and B_{OP} = 9 T (left axis), and the Curie temperature, T_C (right axis). All data are from the x = 0.5, t_{exp} = 6 unit cell $La_{1-x}Sr_xCoO_{3-\delta}$ film in Fig. 6.1(f).

Magnetoresistance (MR) measurements support these conclusions. Shown in Fig. 6.6(b) is the T dependence of MR = $[\rho(T,B)-\rho(T,B_c)]/\rho(T,B_c)$, where B_c is the coercive field, and B is fixed, out-of-plane, at 9 T. At V_g = 0, $MR(T)$ simply increases monotonically on cooling, reaching -30% at low T. As shown in Fig. 6.6(d,e), this is due to an essentially isotropic, negative, hysteretic MR, with peaks in ρ at $\pm B_c$. This is a well-known

phenomenon in LSCO, arising due to spin-dependent inter-cluster transport on the insulating side of the IMT, *i.e.*, an intergranular giant-magnetoresistance-type effect [89]. This MR is thus exactly as expected in a sub-percolative starting film. As the magnitude of V_g is increased, however, this low T isotropic MR is weakened, while a high T MR turns on, around the induced T_C (Fig. 6.6(b)). This is again as expected, arising due to the spin-disorder MR known to exist around T_C in the FM metallic phase of LSCO [89,94]. As shown in Fig. 6.6(d,e), the low T MR in the gate-induced FM metallic state additionally becomes more anisotropic than at low V_g (by a factor of ~3), due to the onset of anisotropic magnetoresistance (AMR) [95]. The V_g dependence of MR(B,T) is therefore in excellent agreement with a gate-induced transition from a magnetically-clustered insulator to a long-range FM metal.

A succinct summary of the evolution with V_g is provided in Fig. 6.6(g,h,i). As V_g decreases from 0 to -4 V the low T resistivity falls by over an order of magnitude, driven by electrostatic hole accumulation (Fig. 6.6(g)). T-dependent measurements confirm this to be due to a percolation IMT. Accompanying the IMT, the MR evolves from a state dominated by isotropic inter-cluster MR (Fig. 6.6(h), left axis), to a state with substantial MR near T_C due to field-induced suppression of spin-disorder (Fig. 6.6(h), right axis axis), also exhibiting low T AMR (Fig. 6.6(d,e)). Finally, and most directly, as V_g is decreased below -2 V a strong AHE turns on (Fig. 6.6(i), left axis), the FM T_C increasing from 0 to 150 K.

6.4 *In operando* polarized neutron reflectometry

While the transport-based evidence for gate-induced percolation to an FM state is strong, *in operando* PNR measurements were also performed, seeking confirmation of long-range FM, as well as the depth-profile of induced magnetization, M. The latter is important, as our recent theory predicts anomalously deep penetration of M, deeper than induced holes, due to surface-gating-mediated connection of existing clusters (Section 5.3, Fig. 5.3). Fig. 6.7(a) shows the specular neutron reflectivity, R, *vs*. scattering wavevector (Q), for a 6 u.c. x = 0.5 LSCO film at V_g = -3 V, T = 30 K, and B = 1 T (in-plane). Shown are the non-spin-flip reflectivities (R^{++} and R^{--}), where the "+" and "-" indicate the relative polarization of the incoming and outgoing neutrons. While weak, splitting is indeed

observed between R^{++} and R^{--}, consistent with long-range ordered FM at -3 V. This is shown more clearly in Fig. 6.7(b), which plots the Q dependence of the spin asymmetry, $SA = [(R^{++} - R^{--})/(R^{++} + R^{--})]$, at V_g = 0 and -3 V. The SA is statistically insignificant at V_g = 0, but becomes finite at -3 V, growing monotonically to SA = 0.1 at Q = 0.09 Å^{-1}. Note here that the absence of oscillations in $R(Q)$ and $SA(Q)$ in this Q range is expected, due to the ultralow (6 u.c.) thickness.

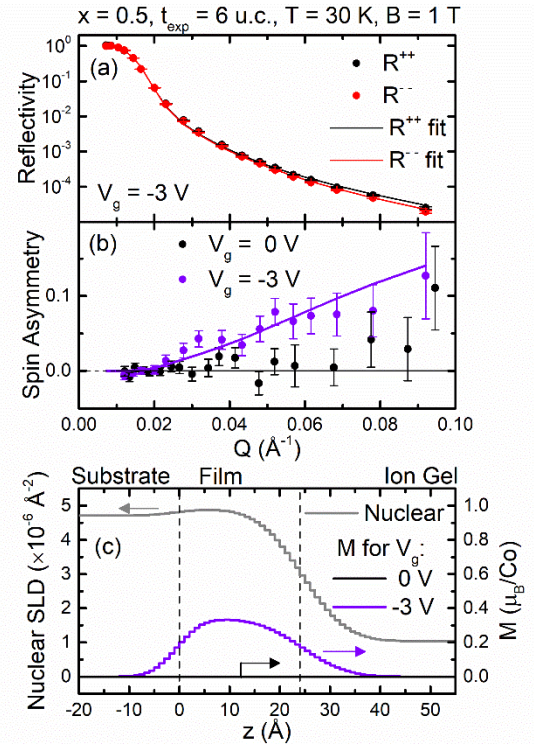

Fig. 6.7. (a) Neutron reflectivity, R, *vs*. scattering wavevector magnitude, Q, from an x = 0.5, t_{exp} = 6 unit cell $La_{1-x}Sr_xCoO_{3-\delta}$ film at gate bias, V_g = -3 V, 30 K, and 1 T (in-plane). Black and red denote non-spin-flip "$R^{+\,+}$" and "$R^{-\,-}$" channels, for both data (points) and fits (solid lines). (b) Spin asymmetry *vs.* Q for V_g = 0, -3 V. Lines are fits with the depth profiles in (c). (c) Depth profiles of the nuclear scattering length density, SLD, (left axis) and magnetization, M, (right axis) for V_g = 0, -3 V; the film/substrate interface is at z = 0.

While the above confirms gate-induced long-range FM, quantitative refinement provides additional insight. The solid line fits in Fig. 6.7(a,b) are based on simple depth (z) profiles for the nuclear and magnetic SLD, as shown in Fig. 6.7(c). Table 6.1 shows the neutron SLDs calculated from the material stoichiometry and mass density using Ref. [123]. Table 6.2 shows the refined parameters used to generate the nuclear and $M(z)$ depth profiles in Fig. 6.7(c). The refined *magnetic* SLD at V_g = 0 is indeed zero at all z, confirming that long-range FM is absent. At V_g = -3 V, however, good fits can only be

achieved with finite magnetic SLD, the best-fit $M(z)$ being shown in Fig. 6.7(c) (right axis). Remarkably, M is quite uniform with depth, the maximum value being 0.34 μ_B/Co, and the magnetic and nuclear roughnesses being identical. To put this in context, at $T_C \approx 150$ K, bulk LSCO saturates at $M \approx 0.8$ μ_B/Co [9]. This LSCO film has PMA, however, which is not overcome by the experimentally available in-plane $B = 1$ T, and we would thus expect $M < 0.8$ μ_B/Co, consistent with our result.

Table 6.1. Calculated neutron scattering length densities (SLDs) for the sample components [123].

Material	Mass density (g/cm^3)	Neutron SLD (10^{-6} Å^{-2})
$SrLaAlO_4$	5.92	4.71
$La_{0.5}Sr_{0.5}CoO_3$	6.45	4.86
Ion Gel (80% Ionic Liquid, 20% Polymer)	~1.5	2.63
Ionic Liquid: $C_8H_{11}F_6N_3O_4S_2$	1.5	2.38
Polymer: $C_5H_2F_7$	1.8	3.63

Table 6.2. Parameters used to fit the PNR data in Fig. 6.7(a). The top value is the nuclear SLD, t is the layer thickness, σ is the layer roughness (Gaussian width), and M is the magnetization of each layer. Note that the nuclear SLDs of $SrLaAlO_4$ and LSCO match the calculated values in Table 6.1 quite well. The SLD of the ion gel, however, is a factor of ~3 lower than the calculated value in Table 6.1. A similar discrepancy was previously observed in Chapter 4.

V_g (V)	SrLaAlO4	LSCO	Ion gel
0	4.71×10^{-6} Å^{-2} $t = \infty$ σ = 4.0 Å $M = 0$	4.90×10^{-6} Å^{-2} $t = 25$ Å σ = 7.0 Å $M = 0$ μ_B/Co	1.04×10^{-6} Å^{-2} $t = \infty$ σ = NA $M = 0$
-3	4.71×10^{-6} Å^{-2} $t = \infty$ σ = 4.0 Å $M = 0$	4.90×10^{-6} Å^{-2} $t = 25$ Å σ = 7.0 Å $M = 0.34$ μ_B/Co	1.04×10^{-6} Å^{-2} $t = \infty$ σ = NA $M = 0$

Importantly, alternative, non-uniform $M(z)$ profiles weighted to the LSCO top surface can be safely excluded. In fact, the determined $M(z)$ extends significantly deeper than the induced carrier profile based on simple Thomas-Fermi screening calculations, which

indicate 90 % carrier confinement in the top 2.5 u.c. Thomas-Fermi screening length (l_{TF}) calculations were made using

$$l_{TF} = \frac{1}{2}\left(\frac{a_0^3}{n}\right)^{1/6} \quad 6.4 \text{ and}$$

$$a_0 = (0.53\ \text{Å})k/m \quad 6.5,$$

where a_0 is the Bohr radius, n the carrier density, k the relative dielectric constant, and m the relative effective mass. To calculate an upper limit of l_{TF} = 4.2 Å (~1.1 u.c.), a high estimate of k = 100 and low estimates of $n = 7 \times 10^{21}$ cm^{-3} and m = 4 were used [93]. The $M(z)$ profile shown in Fig. 6.8 is based on this calculation, with 90 % of the induced M in the top 9.6 Å (2.5 u.c.). This result again validates our recent percolation theory predictions, occurring due to gate-mediated connection of existing sub-percolative clusters that penetrate the entire film thickness.

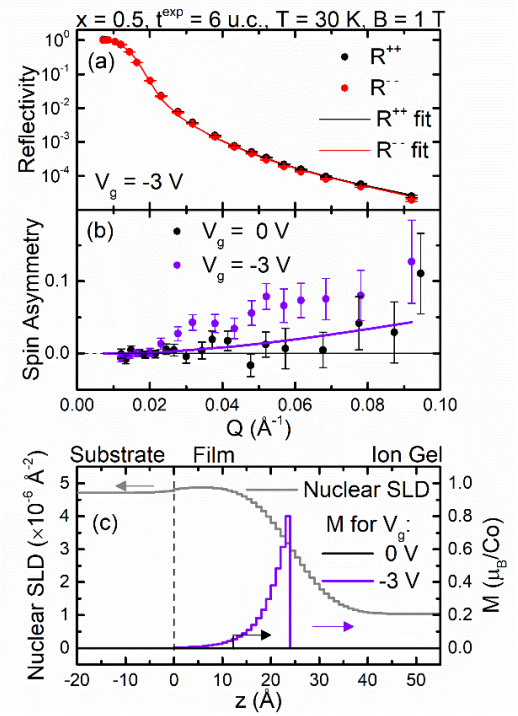

Fig. 6.8. (a) Neutron reflectivity, R, *vs*. scattering wavevector magnitude, Q, from an x = 0.5, t_{exp} = 6 unit cell $La_{1-x}Sr_xCoO_{3-\delta}$ film at gate bias, V_g = -3 V, 30 K, and 1 T (in-plane). Black and red denote non-spin-flip "$R^{+\,+}$" and "$R^{-\,-}$" channels, for both data (points) and fits (solid lines). (b) Spin asymmetry *vs.* Q for V_g = 0, -3 V. Lines are fits with the depth profiles in (c). (c) Depth profiles of the nuclear scattering length density, SLD, (left axis) and magnetization, M, (right axis) for V_g = 0, -3 V; the film/substrate interface is at z = 0. The $M(z)$ profile for V_g = -3 V (purple) was calculated using Thomas-Fermi screening calculations discussed in the main text, resulting in simulated *SA* well below the experimental values in panel (b).

6.5 Conclusions

In summary, using ion-gel-based epitaxial LSCO EDLTs, thorough verification of a recent prediction of the efficacy of thickness tuning to approach the verge of a percolation IMT has been demonstrated. At an optimal thickness of 6 u.c., a gate-induced transition from an insulating magnetically-clustered state to a long-range FM metal is demonstrated by transport and PNR. This enables giant *electrostatic* T_C modulation of 150 K, dramatically increased over the prior 12 K. This 150 K shift is, to our knowledge, the largest *electrostatic* value in any electrolyte-gated material. The only comparable electrostatic value by any method in a complex oxide FM from ferroelectric gating [27,28,134] of $La_{0.8}Sr_{0.2}MnO_3$; optimal results being obtained in ultrathin films [27], including a gate-induced $T_{C,max} \approx 190$ K, though lacking low-T data prevent calculation of ΔT_C. This work thus brings electrostatically-induced T_C shifts into the same realm as electrochemical T_C shifts, but with significant potential advantages in switching speed and reversibility. Future efforts with higher T_C materials could potentially realize such T_C shifts even around room temperature, creating FMs with tunable thermal stability.

Chapter 7: Giant perpendicular magnetic anisotropy and anisotropic magnetoresistance in lattice-mismatch-engineered oxygen-vacancy-ordered $La_{1-x}Sr_xCoO_{3-\delta}$ films

In this chapter I will switch to controlling the electronic and magnetic properties of LSCO films with lattice mismatch engineering, as opposed to electrolyte gating. *None of the results presented in this chapter involve electrolyte gating*. First, I will demonstrate that $x = 0.5$ LSCO films presented with tensile and compressive lattice mismatch have in-plane and perpendicular magnetic anisotropy (PMA), respectively. Estimations of the anisotropy energy density (K) yield values as high as 6×10^6 erg/cm^3, which is three times larger than bulk LSCO and an of magnitude higher than typical manganite films. Further, the large PMA observed on compressive substrates is found to be thickness independent in these fully strained LSCO films, suggesting the underlying cause is not driven by a film/substrate interface effect. At lower x, the PMA observed on compressive LAO substrates is found to diminish. Scanning transmission electron microscopy measurements also show the density of oxygen vacancy ordered (OVO) planes is diminished at lower x values. Two possible causes of the giant magnetic anisotropy in LSCO films are currently being considered, though neither has been established as more likely to-date. The first possible cause is that the OVO planes create giant magnetocrystalline uniaxial anisotropy, with the OVO plane modulation vector determining the magnetic easy axis. The second possible cause uses simple strain arguments based on the deformation of the CoO_6 octahedra and concomitant changes to the crystal field environment. Finally, giant anisotropic magnetoresistance (AMR) is observed in these LSCO films. In fact, $x = 0.5$ LSCO films on LAO exhibit AMR values as high as 40 % at low temperature, which is more than an order of magnitude larger than bulk LSCO and the largest *conventional* AMR, to our knowledge, reported from all ferromagnetic materials. Again, the underlying cause for this giant AMR has remained elusive, with the OVO structure and strain effects both being considered.

7.1 Lattice mismatch engineering of magnetic anisotropy

7.1.1 Structural characterization

Details on LSCO growth are included in Section 2.1 but, briefly, epitaxial films of LSCO were deposited *via* high pressure oxygen reactive sputter deposition on $SrTiO_3$ (STO), $LaAlO_3$ (LAO), $La_{0.18}Sr_{0.82}Al_{0.59}Ta_{0.41}O_3$ (LSAT), and $SrLaAlO_4$ (SLAO) substrates, all in the (001) orientation. The crystal structure, lattice parameters, and resultant lattice mismatch (ε_{xx}) with $x = 0.5$ LSCO for each substrate is shown in Table 7.1.

Table 7.1. Structural parameters of bulk $x = 0.5$ LSCO and the substrates used in this study. The pseudocubic lattice parameter (a_c) was calculated for LAO using $a = a_c\sqrt{2}$. For SLAO $a = a_c$ because films were grown on (001) oriented SLAO substrates. The lattice mismatch ε_{xx} was calculated using $\varepsilon_{xx} = (a_c - a_{LSCO})/a_{LSCO}$, where a_{LSCO} is the cubic lattice parameter for bulk $x = 0.5$ LSCO (3.833 Å).

	Structure	a (Å)	c (Å)	a_c (Å)	ε_{xx} (%)
LSCO ($x = 0.5$)	Cubic	3.833	-	-	-
STO	Cubic	3.905	-	-	+1.8
LSAT	Cubic	3.868	-	-	+0.8
LAO	Rhombohedral ($\alpha_R = 60.5°$)	5.365	13.11	3.789	-1.2
SLAO	Tetragonal	3.754	12.63	3.754	-2.1

Figs. 7.1(a-d) show representative WAXRD scans in the vicinity of the (002) LSCO film peak for 90-Å-thick, $x = 0.5$ films grown on STO, LSAT, LAO, and SLAO, respectively. Qualitatively, all scans show well-defined (002) film peaks and Kiessig fringes, demonstrating the LSCO films are epitaxial with low roughness. The LSCO film out-of-plane lattice parameters (c_{op}) were calculated based on the (002) film peak position and used to calculate the out-of-plane strain, $\varepsilon_{zz} = (c_{op} - a_{LSCO})/a_{LSCO}$, where a_{LSCO} is the cubic lattice parameter for bulk $x = 0.5$ LSCO (3.833 Å). As shown in Fig. 7.1(e), a linear dependence of ε_{zz} *vs.* ε_{xx} is observed with a slope of -1. This is the expected behavior for a material under biaxial strain with a Poisson ratio (ν) of 1/3, as shown by the red dotted line in Fig. 7.1(e). The value of $\nu = 1/3$ is observed in other oxides [135], suggesting the results here are reasonable. A reciprocal space map around the (013) LAO and LSCO peaks for a

380-Å-thick film is shown in Fig. 7.1(f). The film peak appears at a lower $3/d_{001}$ value, consistent with its larger c_{op} (3.890 Å) compared to the lattice parameter of LAO (3.789 Å), but appears at the same $1/d_{010}$ value, suggesting it is epitaxially clamped to the LAO substrate with the same in-plane lattice parameter. For reference, the expected peak location for completely strained and relaxed LSCO are shown on the plot. Therefore, these LSCO films are pseudomorphic with the underlying substrate and do not exhibit any strain relaxation up to thicknesses of 380 Å (at least on LAO). Finally, as discussed in Section 1.3.2, it has been well established that x = 0.5 LSCO films exhibit OVO with an in-plane modulation vector (*i.e.*, V_O stripes normal to the film/substrate interface, see Fig. 1.24(a)) when grown under tensile lattice mismatch on STO and an out-of-plane modulation vector (*i.e.*, V_O stripes parallel to the film/substrate interface, see Fig. 1.24(c)) when grown under compressive mismatch on LAO. While scanning transmission electron microscopy has not been performed on films grown on LSAT and SLAO, the fact that the OVO structure is the mismatch accommodation mechanism leads us to believe films on LSAT and SLAO will exhibit OVO with in-plane and out-of-plane modulation vectors, respectively.

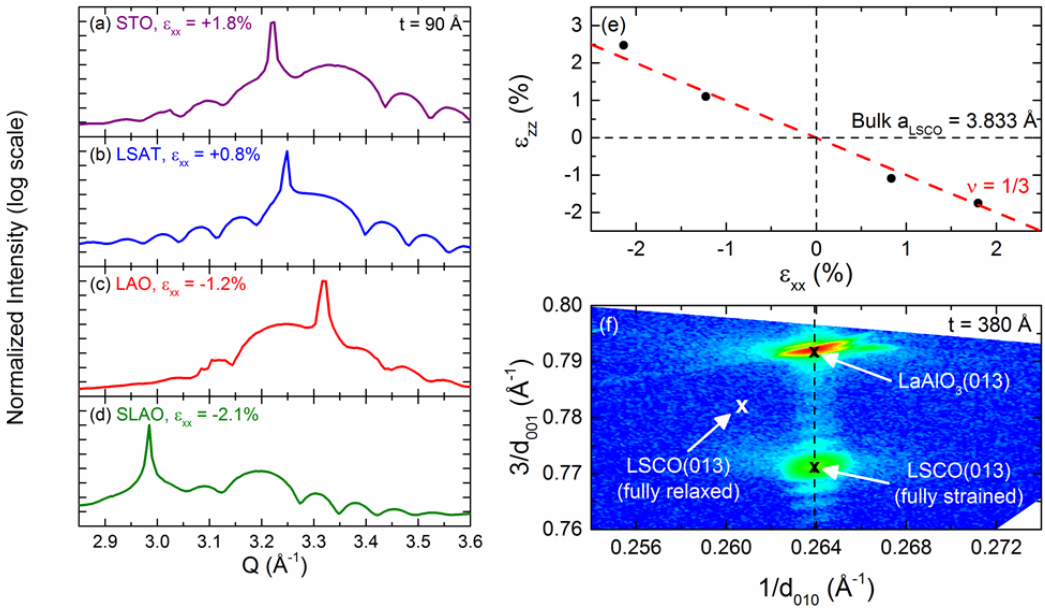

Fig. 7.1. (a-d) Specular WAXRD scans of diffracted beam intensity *vs*. out-of-plane scattering vector magnitude (Q) for 90-Å-thick x = 0.5 LSCO films grown on (001) oriented STO, LSAT, LAO, and SLAO, respectively. (e) Out-of-plane strain (ε_{zz}) *vs*. in-plane lattice mismatch (ε_{xx}) calculated as discussed in the main text for the films shown in (a-d) using the bulk x = 0.5 lattice parameter (a_{LSCO} = 3.833 Å). The red dotted line shows the expected result for biaxially strained films with Poisson ratio, ν = 1/3. (f) Asymmetric reciprocal space map around the 013 reflection of a 380 Å thick x = 0.5 LSCO film on LAO. The expected positions of the LAO substrate and fully strained and fully relaxed LSCO reflections are marked and labeled.

7.1.2 *Lattice mismatch dependence of magnetic anisotropy at x = 0.5*

The temperature (T) dependence of M is shown in Fig. 7.2(a-d) for 90-Å-thick x = 0.5 LSCO films on STO, LSAT, LAO, and SLAO, respectively. The two curves for each sample are for out-of-plane ("OoP", solid) and in-plane ("IP", dashed) orientations. In all cases the applied magnetic field (H) while cooling and measuring was 1 kOe. Starting with the IP orientation on STO, which presents a 1.8 % tensile mismatch (Fig. 7.2(a)), ferromagnetic (FM) behavior is observed with a T_C of ~215 K, which is consistent with prior reports [95,107]. In the OoP orientation, however, M is significantly suppressed while measuring in H = 1 kOe, indicating a preferred IP orientation of M. Similar behavior is observed on LSAT (Fig. 7.2(b)), which presents a tensile mismatch of 0.8 %.

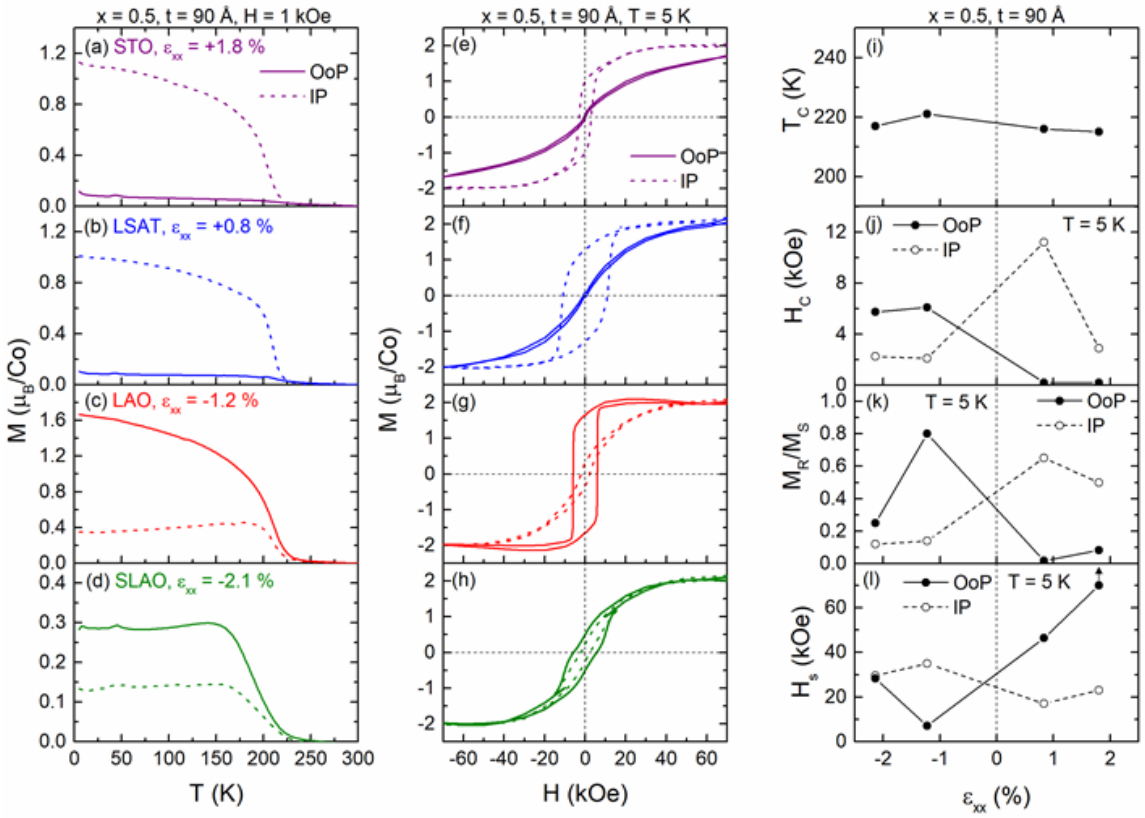

Fig. 7.2. Magnetometry on 90-Å-thick x = 0.5 LSCO films grown on (001)-oriented STO (purple), LSAT (blue), LAO (red), and SLAO (green). (a-d) Temperature (T) dependence of the magnetization (M) for out-of-plane (OoP, solid) and in-plane (IP, dashed) orientations, in cooling and measuring magnetic fields (H) of 1 kOe. (e-h) M *vs.* H hysteresis loops at T = 5 K for OoP (solid) and IP (dashed) orientations. Lattice mismatch (ε_{xx}) dependence of (i) Curie temperature (T_C) determined from the preferred M axis, (j) 5 K coercivity (H_c), (k) 5 K remnant magnetization normalized by the saturation magnetization (M_R/M_s), and (l) the saturation field (H_s) at 5 K as defined in the main text. Results for both OoP (filled points, solid line) and IP (open points, dashed line) orientations are shown in (j-l), where the lines simply connect points.

This behavior inverts on LAO, which presents a 1.2 % compressive mismatch. As shown in Fig. 7.2(c), FM behavior is observed with a similar T_C of 221 K, but the larger M in the OoP orientation indicates the preferred orientation on LAO is OoP; *i.e.*, the sample exhibits perpendicular magnetic anisotropy (PMA). PMA is also observed in the similarly compressive (2.1 %) case of SLAO, as shown in Fig. 7.2(d), with larger M in the OoP orientation.

The H dependence of M at T = 5 K for the same four samples is shown in Fig. 7.2(e-h). Again, starting with STO (Fig. 7.2(e)), FM hysteresis is observed in the IP orientation with saturation magnetization (M_s) of ~2 μ_B/Co and coercivity (H_c) of 2.9 kOe, both of which are consistent with prior reports of x = 0.5 LSCO films on STO [95], as well as consistent with the bulk LSCO M_s of 1.92 μ_B/Co [9,94,95]. Further characterizing the shape of the IP hysteresis loop on STO, the remnant magnetization (M_R) is 1 μ_B/Co and the saturation field (H_s, in this case I have defined this as the field at which M reaches 0.9M_s) is ~23 kOe. In comparison, the OoP loop shows significantly suppressed H_c and M_R, as well as much larger H_s, clearly indicating the IP direction is the preferred axis of M, which is consistent with the $M(T)$ data in Fig. 7.2(a). Similar results are found on LSAT, as shown in Fig. 7.2(f), with larger H_c and M_R, as well as smaller H_s, being observed in the IP orientation compared to the OoP orientation. Again, large differences are observed on the compressive LAO and SLAO substrates (Fig. 7.2(g) and (h), respectively), with larger H_c, larger M_R, and smaller H_s being observed in the OoP orientation compared to the IP orientation. These characteristic features are summarized as a function of ε_{xx} in Fig. 7.2(i-l), including T_C, H_c, M_R/M_s, and H_s, respectively. While $T_C \approx 220$ K is essentially independent of ε_{xx}, there is a clear polarity dependence of the other three parameters. Under tensile mismatch ($\varepsilon_{xx} > 0$), H_c and M_R/M_s are larger, and H_s smaller, for the IP orientation compared to the OoP orientation. This indicates that the preferred axis of M is in-plane. Exactly the opposite is observed under compressive mismatch ($\varepsilon_{xx} < 0$), with larger H_c, larger M_R/M_s, and smaller H_s observed for the OoP orientation, indicating compressive mismatch leads to PMA.

To put this lattice mismatch control of magnetic anisotropy into context, it will be useful to briefly review the magnetic anisotropy observed in bulk LSCO. Fig. 7.3 shows

$M(H)$ curves of x = 0.3 [171] and x = 1 [99] LSCO single crystals. In the low field regime for both doping levels, $M_{111} > M_{110} > M_{100}$, indicating in x = 0.3 and x = 1 LSCO single crystals that the easy magnetization axis is <111> and the hard axis is <100>. A <111> easy axis is also supported by domain formation studies using small angle neutron scattering on x = 0.2 LSCO single crystals [171]. Note that this situation with easy, medium, and hard magnetization axes along <111>, <110>, and <100> is similar to that of face-centered-cubic (FCC) Ni [96]. The extremely large field (~60 kOe) required to fully saturate the x = 0.3 LSCO single crystal along the <100> direction has been attributed to isolated non-FM phases existing in the system (*i.e.*, magnetic inhomogeneities) [171]. Another explanation put forth to describe similarly large saturation fields [172] and huge anisotropic magnetostriction [173] in polycrystalline x = 0.3 LSCO powder is a field induced orbital instability, which leads to a spin-state change in Co^{3+} ions from LS to IS with strong intra-atomic spin orbit coupling [172,173].

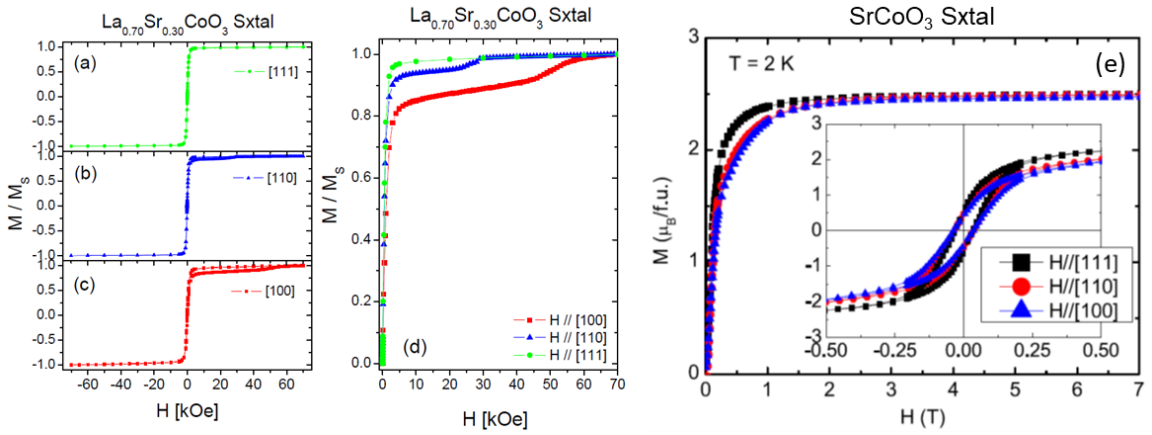

Fig. 7.3. Normalized magnetization (M/M_s) hysteresis loops of a $La_{0.7}Sr_{0.3}CoO_3$ single crystal (Sxtal) at 10 K for an applied magnetic field (H) along the (a) [111], (b) [110], and (c) [100] orientations and (d) normalized virgin curves from Ref. [171]. (e) 2 K hysteresis loop for a $SrCoO_3$ Sxtal along the same orientations, with the low field details shown in the inset, from Ref. [99].

In order to compare the magnitude of the bulk magnetic anisotropy observed in these crystals to that observed in the epitaxial films above, we will need estimates of the magnetic anisotropy energy (K). For a cubic material [96]

$$K = K_0 + K_1(\alpha_1^2\alpha_2^2 + \alpha_2^2\alpha_3^2 + \alpha_3^2\alpha_1^2) + K_2(\alpha_1^2\alpha_2^2\alpha_3^2) \qquad 7.1,$$

where K_0, K_1, and K_2 are magnetocrystalline anisotropy constants, usually expressed in erg/cm^3, and α_1, α_2, and α_3 are the cosines of the angles between the magnetization and the three principal axes in the cubic system. Higher order terms can be used in Eqn. 7.1, but are generally not needed [96]. In order to observe easy, medium, and hard axes along <111>, <110>, and <100>, respectively, as is observed in LSCO single crystals and FCC Ni, K_1 must be negative and $-\infty < K_2 < 9|K_1|/4$. The values for FCC Ni at room temperature, for example, are $K_1 = -4.5 \times 10^4$ erg/cm^3 and $K_2 = -2.3 \times 10^4$ erg/cm^3 [96]. In order to compute K_1 and K_2 for LSCO single crystals, more thorough magnetometry would be required. Simple estimates of the magnitude of K can be calculated, however, using the energy density required to saturate a material in the hard direction, which is given to first order by [96]

$$K = \frac{M_s H_a}{2} \qquad 7.2,$$

where H_a is the anisotropy field, or the field needed to saturate the magnetization. Here, I will use $H_a \approx H_s$ (as defined above). To get an idea of how well this approximation works for a material with cubic anisotropy, the calculation for FCC Ni yields K = (500 emu/cm^3)*(175 Oe)/2 = 4.4×10^4 erg/cm^3 [96], which is clearly comparable to the K_1 and K_2 reported above.

Using Eqn. 7.2 with the data shown in Fig. 7.3(e) for the x = 1 LSCO single crystal (*i.e.*, $SrCoO_3$), which has M_s = 2.5 μ_B/Co (which converts to 413 emu/cm^3 using a = 3.829 Å) and H_s = 9 kOe along the <100> direction [99], $K = 1.9 \times 10^6$ erg/cm^3, which agrees well with prior reports in polycrystalline LSCO [172]. A similar value is calculated for the x = 0.3 LSCO single crystal if the high-field feature in Fig. 7.3(d) is ignored. Note that values for bulk ferromagnetic manganites lie about an order of magnitude below this, falling around $1 - 4 \times 10^5$ erg/cm^3 [172]. Using Eqn. 7.2 with the data shown in Fig. 7.2(g) for the x = 0.5 LSCO film grown on LAO, which exhibits PMA with M_s = 2 μ_B/Co (which converts to 332 emu/cm^3 using the structural parameters shown in Fig. 7.1(e)) and H_s = 36 kOe, $K = 6.0 \times 10^6$ erg/cm^3. Therefore, not only is the direction of the magnetic anisotropy controlled by lattice mismatch in x = 0.5 LSCO films, but the magnitude of K in these films is also around three times larger than bulk LSCO.

7.1.3 *Possible underlying causes for perpendicular magnetic anisotropy*

Clearly, the next step is to understand the underlying cause for the enhanced magnetic anisotropy in these epitaxial $x = 0.5$ LSCO films compared to bulk, and why it lies in- and out-of-plane for tensile and compressive lattice mismatches, respectively. In this regard, a simple place to start is to analyze three key differences between these films and bulk LSCO; (1) the presence of strain, *i.e.*, the crystal structure of the films is not cubic (*c.f.*, $SrCoO_3$) or rhombohedral (*c.f.*, $x = 0.3$ LSCO), (2) the presence of a substrate/film interface, and (3) the presence of OVO. Beginning with the presence of strain, a comparison to the magnetic anisotropy of epitaxial $La_{1-x}Sr_xMnO_3$ (LSMO) films near $x = 1/3$ will be useful. PMA anisotropy in LSMO films grown under compressive lattice mismatch on LAO (-1.2 %) and in-plane magnetic anisotropy in LSMO films grown under tensile lattice mismatch on STO (1.8 %) have been reported in magnetometry [174,175] and magnetic force microscopy [176] studies. This mismatch dependence of the magnetic anisotropy direction is the same as we observe in LSCO films, but, importantly, these LSMO films do not exhibit OVO. This suggests it may not be required to include OVO, and strain alone may describe the directional dependence of the magnetic anisotropy. The K value estimated using Eqn. 7.2 for a fully-strained, 250-Å-thick LSMO films grown on LAO with PMA [175] is 9×10^5 erg/cm^3, which is between 2 and 9 times larger than the value for bulk LSMO [172] and comparable to the three-fold increase observed in our LSCO films. Further, for partially strain-relaxed LSMO films on LAO (1100-Å-thick) $K \approx 2.2 \times 10^5$ erg/cm^3 [174], which is comparable to bulk LSMO. The fact that similar K enhancement and directionalities are observed in LSMO and LSCO films under strain, and that the enhancement is diminished in partially strain-relaxed LSMO films, suggests strain alone could be the underlying cause for the magnetic anisotropy characteristics of these films. To our knowledge, unfortunately, no descriptions of *how* strain could lead to such dramatic magnetic anisotropy changes have been put forth. Modifications to the crystal field environment are the obvious place to start investigating, as altered occupancy of *d* orbitals with different angular momentum quantum numbers could significantly influence the spin-orbit-coupling, which is at the root of all magnetic anisotropy. Further theoretical work is clearly needed and is currently being pursued.

The second difference between LSCO films and bulk is the presence of the substrate/film interface, which could give rise to an interfacial magnetic anisotropy that leads to the PMA observed in LSCO films on LAO and SLAO. Interfacial magnetic anisotropy is the driving force for the PMA observed in: (1) ultrathin films or multilayers combining a ferromagnetic metal (Fe, Co, and/or Ni) with a metal that has a large spin-orbit interaction (*e.g.*, Pt or Pd), and (2) ferromagnetic metal/oxide interfaces [177]. The latter case is particularly relevant, as quite large interfacial anisotropies have been observed (~1 erg/cm^2 [177]) despite the fact that these ferromagnetic metal/oxide interfaces typically lack high-atomic-number elements that are generally required to achieve large spin-orbit coupling [177], which is also the case with LSCO films here. Interestingly, electronic hybridization between the oxygen and transition metal orbitals are thought to be the root cause of the PMA observed in such structures. Similar mechanisms could also be active in the PMA observed in the LSCO films discussed here. Thickness dependence of the magnetic anisotropy has been well-established for proving the PMA in such systems is driven by interface effects. At low thicknesses, the interfacial magnetic anisotropy dominates the shape and magnetocrystalline anisotropies, thus leading to PMA. As the thickness increases above a few nanometers, however, the shape and magnetocrystalline anisotropies overtake the interfacial anisotropy, leading to in-plane magnetic anisotropy []. Thickness dependence measurements of T_C, H_c, and M_R/M_s for x = 0.5 LSCO films grown on LAO are shown in Fig. 7.4. Weak thickness dependence is observed in all of these parameters, with larger H_c and M_R/M_s observed in the OoP orientation compared to the IP orientation. Clearly, these results indicate PMA is preserved to at least t = 400 Å in LSCO films on LAO and that the PMA is not driven by a film/substrate interface effect.

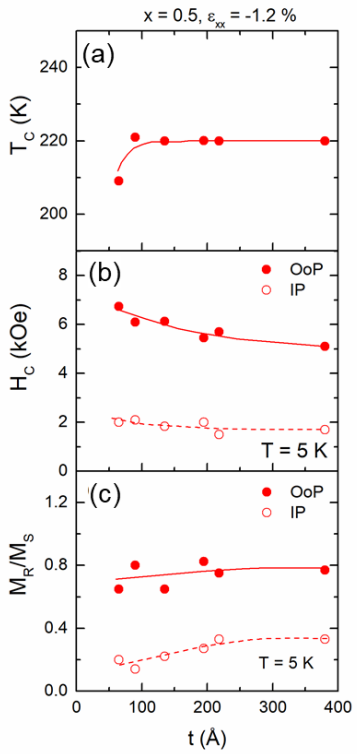

Fig. 7.4. Thickness (t) dependence of (a) Curie temperature (T_C), (b) 5 K coercivity (H_c), and (c) 5 K remnant magnization, normalized by the saturation magnetization (M_R/M_s), for x = 0.5 LSCO films grown on LAO(001). Results for both OoP (filled points, solid line) and IP (open points, dashed line) orientations are shown; lines are guides to the eye.

Finally, the OVO present in these films will be entertained as the underlying cause for the change in magnetic easy axis compared to the bulk. Recall that the OVO planes lie parallel to the film/substrate interface on LAO(001) and perpendicular to the interface on STO(001), as shown in Fig. 1.24. The PMA observed on LAO and the in-plane anisotropy observed on STO could be consequences of the OVO if the brownmillerite-like structure (Fig. 1.22) leads to a magnetocrystalline anisotropy perpendicular to the OVO planes (*i.e.*, parallel to the OVO modulation vector). One way to test this idea would be to see if the PMA remains after removal of OVO from these films. We cannot do this at x = 0.5 alone, because the OVO is fixed by the lattice mismatch, x-dependence provides interesting results. Fig. 7.5 shows magnetometry and high resolution transmission electron microscopy (HRTEM) images (taken by our collaborators Mariona Cabero Piris and Maria Varela) of ~90-Å-thick LSCO films on LAO at x = 0.05, 0.15, 0.28, and 0.5. The same $M(H)$ shown in Fig. 7.2(g) is reproduced in Fig. 7.5(a), showing the large PMA at x = 0.5, along with the clear OVO structure (highlighted by the red arrows) in Fig. 7.5(e). At x =

0.28, the IP and OoP loops are quite similar, as shown in Fig. 7.5(b), indicating a suppression of the PMA. While in-plane OVO is still observed at x = 0.28 (Fig. 7.5(f)), the oxygen deficient planes are more sporadic compared to the x = 0.5 sample. For the x = 0.15 and 0.05 samples, which are insulating and do not exhibit long-range FM order, PMA is no longer observed and OVO is further suppressed in x = 0.15 and completely absent in x = 0.05. The fact that PMA and OVO are both diminished at lower x values could support the idea that the OVO structure is the underlying cause for the magnetic anisotropy in LSCO films. This x dependence, however, is also convoluted with loss of ferromagnetism and other x dependent factors so it is not definitive evidence.

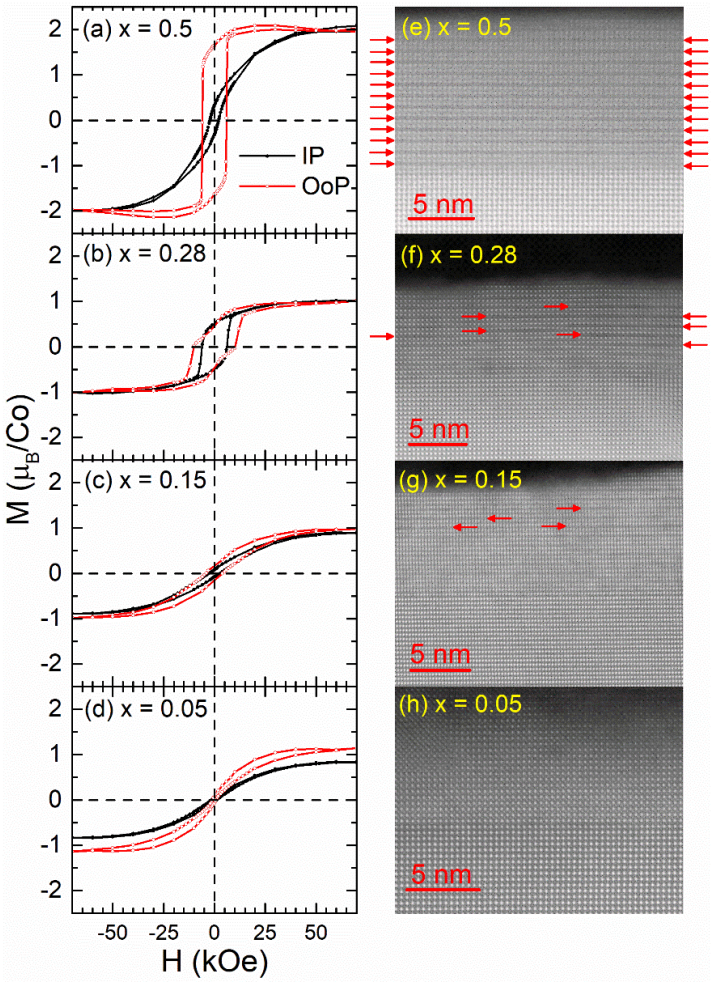

Fig. 7.5. Magnetization (M) *vs.* magnetic field (H) hysteresis loops at T = 5 K for out-of-plane (OoP, red) and in-plane (IP, black) orientations of LSCO films grown on LAO(001) with x values of (a) 0.5, (b) 0.28, (c) 0.15, and (d) 0.05. High resolution Z-contrast scanning transmission electron microscopy images of the interface regions of LSCO films grown on LAO(001) with x values of (e) 0.5, (f) 0.28, (g) 0.15, and (h) 0.05. The red arrows mark oxygen deficient planes.

Interestingly, another way to view the possibility of a "bulk" magnetocrystalline anisotropy in the OVO brownmillerite structure would be to treat the alternating oxygen sufficient and deficient planes as a superlattice with individual layer thicknesses of one unit cell. Thinking about the magnetic anisotropy like this re-introduces the interfacial magnetic anisotropy concepts discussed above, but here, the interface would be between octahedrally-coordinated-Co (oxygen sufficient) and tetrahedrally-coordinated-Co (oxygen deficient) planes. The thickness-dependent study shown in Fig. 7.4 does not apply in this case, because the OVO structure (and the superlattice period of two unit cells) persists throughout the entire film at all thicknesses. An interesting case for comparison lies in the large magnetic anisotropy observed in Ruddlesden-Popper (n = 1) Sr_2CoO_4 films [178]. In these films, CoO_2 planes with octahedrally-coordinated Co^{4+} are separated by two SrO planes (as shown in Fig. 7.6(a)), such that they can be thought of as superlattices similar to the OVO structure in LSCO films, but with no tetrahedral $CoO_{2-\delta}$ planes. In the case where the CoO_2 planes are perpendicular to the substrate (SLAO(100), note the different orientation compared to the (001) orientation used throughout this work) interface, the films exhibit large magnetic anisotropy perpendicular to these planes (along the *c*-axis), as shown in Fig. 7.6(b). We are not aware, however, of any studies on such films with the CoO_2 planes running parallel to the substrate interface, where we would expect PMA to occur. Finally, the magnetic anisotropy of brownmillerite $SrCoO_{2.5}$ could be informative. Unfortunately, brownmillerite $SrCoO_{2.5}$ is antiferromagnetic, thus the magnetic structure studies that have been performed on $SrCoO_{2.5}$ may not be applicable. Regardless, it is generally accepted that the magnetic structure of $SrCoO_{2.5}$ is G-type with moments lying in the OVO planes, thus directly contradicting the results in our LSCO films where the easy axis lies perpendicular to the OVO planes.

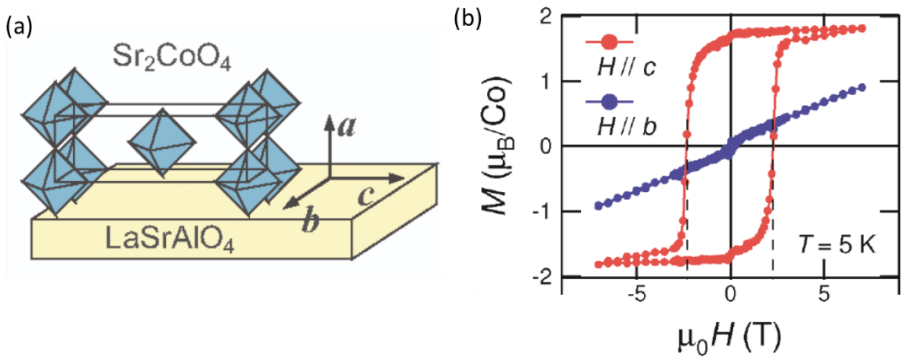

Fig. 7.6. From Ref. [178]. (a) Schematic of growth of Sr_2CoO_4(100) film on $LaSrAlO_4$(100) substrate and definition of the principal axes. (b) Magnetic field (H) dependence of the magnetization (M) for the Sr_2CoO_4(100) film at 5 K along the c (red) and b (blue) axes as defined in panel (a).

7.2 Giant anisotropic magnetoresistance and anomalous Hall effect

In addition to the large and lattice-mismatch-dependent magnetic anisotropy in these epitaxial LSCO films, interesting magnetotransport properties are also observed. Beginning with a simple comparison of LSCO films and bulk, ρ(T) for a 195-Å-thick x = 0.5 LSCO film grown on LAO(001), where ε_{xx} = -1.2 %, and an x = 0.3 LSCO single crystal [94] are shown in Fig. 7.7. As expected for LSCO at this doping level, ferromagnetic and metallic behavior is observed, with the following features observed for the x = 0.5 LSCO film: ρ(5 K) = 60 μΩcm, *RRR* = 3.5, and an inflection in ρ(T) near T_C (220 K). While the *RRR* and T_C are slightly smaller than that of an x = 0.3 LSCO single, the ρ of the film is even lower than that of the crystal, indicating excellent film quality.

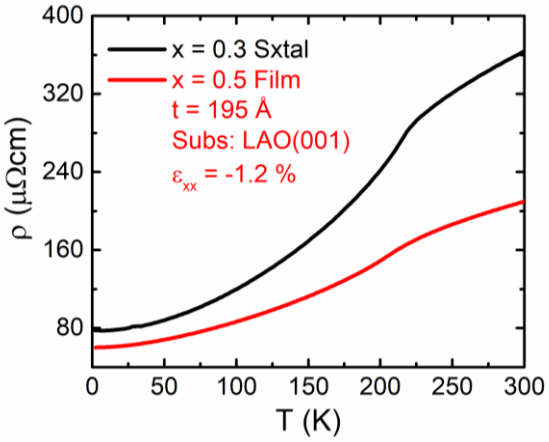

Fig. 7.7. Temperature (T) dependence of resistivity (ρ) for a x = 0.3 LSCO single crystal (Sxtal) (black) [] and a 195-Å-thick x = 0.5 LSCO film grown on LAO(001), where the lattice mismatch (ε_{xx}) is -1.2 % (red).

Magnetotransport measurements on the same 195-Å-thick x = 0.5 LSCO film grown on LAO(001) are shown in Fig. 7.8. Magnetoresistance (*MR*) measurements were first performed with H applied in the film plane, but at different angles (θ) with respect to the applied current (I), as shown in Fig. 7.8(a). The definition of *MR* used here is

$$MR = \frac{R - R_c}{R_c} \times 100\ \% \qquad 7.3,$$

where R is the resistance measured at a given H, T, and θ, and R_c is the resistance at the coercive field for that given T and θ. The $MR(H)$ at 5 K is positive for θ = 0° (*i.e.*, I parallel to H, $MR_{//}$) and negative for θ = 90° (*i.e.*, I perpendicular to H, $MR_{\perp}$), as shown in Fig. 7.8(b). The anisotropy of the *MR* observed is not a surprise, as the film is ferromagnetic at this temperature and the well-known phenomena of anisotropic magnetoresistance (AMR) is typically observed in ferromagnetic materials. What is a surprise, however, is the magnitude of the anisotropy, quantified by $AMR = MR_{//} - MR_{\perp}$, which reaches 40 % at H = 90 kOe. As discussed in more detail below, this *AMR* is a factor of two larger than any value obtained with conventional transition metal alloys, and possibly the largest *conventional* AMR ever observed. Therefore, the temperature and angle dependence of the observed *AMR* were used to investigate whether the observed magnitude could really be due to the conventional AMR effect alone. As shown in Fig. 7.8(c), the 90 kOe *AMR* value decreases monotonically with increasing temperature, as expected for conventional AMR, which scales with the square of the magnetization (M^2) [96]. The *AMR* value does remain finite above T_C = 220 K, however, but can be simply explained by the large field (90 kOe) smearing out T_C. The angular dependence of conventional AMR is [96]

$$R(\theta) = \Delta R \cos^2\theta + R_{\perp} \qquad 7.4,$$

where ΔR is the difference between the resistance with the I parallel to H ($R_{//}$) and the resistance with I perpendicular to H ($R_{\perp}$). Fig. 7.8(d) shows R(θ) in H = 90 kOe for temperatures between 2 K and 300 K (points), as well as fits to Eqn. 7.4 (lines). The angular dependence is well described by Eqn. 7.4 at all temperatures, which provides strong evidence that the giant *AMR* observed in this LSCO film is solely a consequence of the conventional AMR effect.

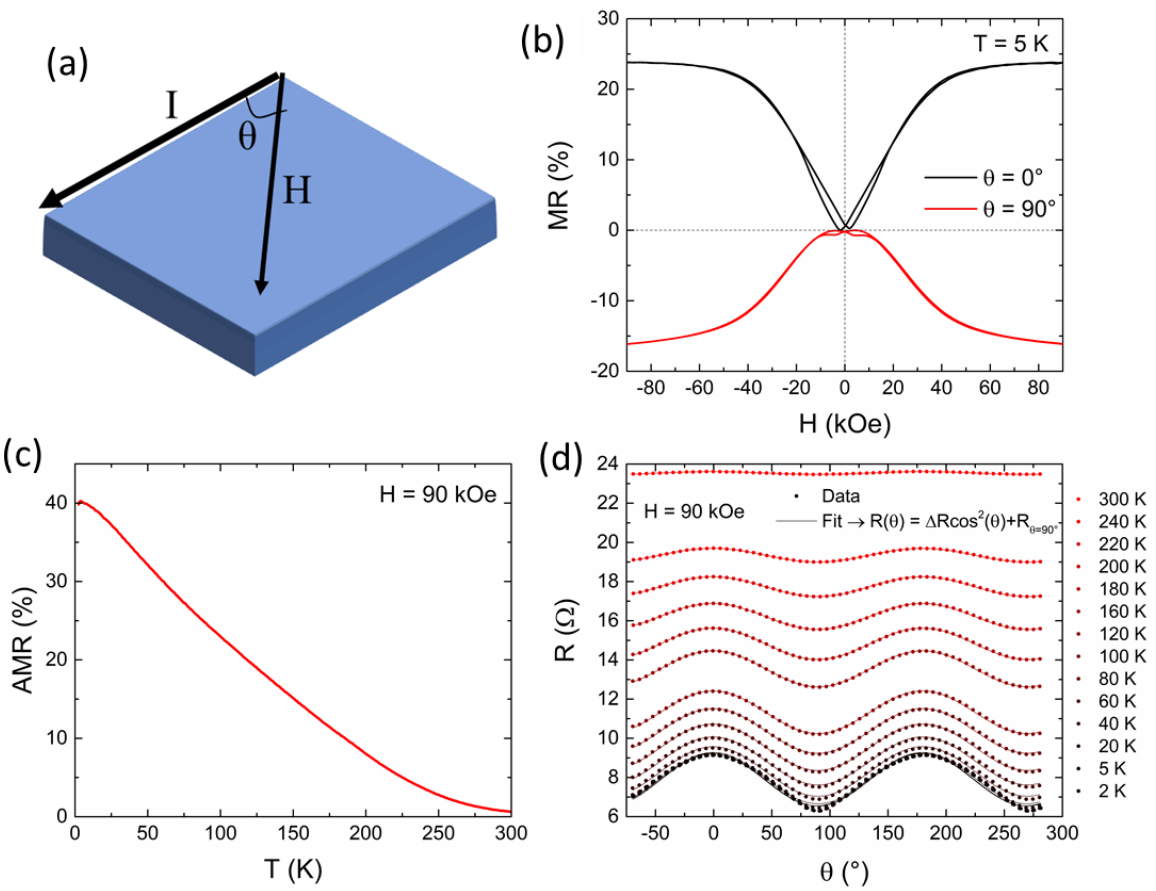

Fig. 7.8. (a) Schematic showing the orientation of the bias current (*I*), magnetic field (*H*), and the angle between them (θ). (b) The 5 K magnetoresistance (*MR*) *vs.* *H* measured with *I* // *H* (θ = 0°, black line) and *I* ⊥ *H* (θ = 90°, red line). (c) The anisotropic magnetoresistance (*AMR*, defined in the main text) *vs*. temperature (*T*) with *H* = 90 kOe. (d) The θ dependence of the film resistance (*R*) in *H* = 90 kOe at the temperatures shown on the right. The points represent the experimental data and the lines represent fits to Eqn. 7.4.

In addition to large *AMR*, these films also exhibit a large anomalous Hall effect, as discussed in Section 3.5. The *H*-dependence of the transverse conductivity (σ_{xy}), with *H* applied normal to the film surface, is shown in Fig. 7.9(a). Clearly, the hysteresis loop observed is consistent with the large PMA observed in LSCO films grown on LAO(001), with large H_c and significant remanence indicating robust ferromagnetism. Using extrapolation from the high-field results to *H* = 0 yields a value for the anomalous Hall conductivity (σ_{AHE}) of 84 S/cm. This value is consistent with the universal scaling of σ_{AHE} with the longitudinal conductivity (σ_{xx} = 1.7 × 10^4 S/cm for this film), which lies at the cusp between the "dirty" regime (σ_{xx} < 10^4 S/cm) where $\sigma_{AHE} \propto \sigma_{xx}^{1.6}$ and the "intermediate" regime (10^4 S/cm < σ_{xx} < 10^6 S/cm) where $\sigma_{AHE} \approx 1000$ S/cm (*i.e.*, constant

with respect to σ_{xx}) [133]. The high field slope in Fig. 7.9(a) can be used to estimate a hole density, assuming it arises from the ordinary Hall effect, yielding a value of 8.1×10^{22} cm^{-3}. Prior reports of hole densities in x = 0.3 LSCO single crystals determined from the ordinary Hall effect at 300 K are quite varied, ranging from 0.5 - 14.3 $\times 10^{22}$ cm^{-3} [93,133], thus making the estimate here reasonable. Fig. 7.9(b) shows $\sigma_{xy}(T)$ measured in remanence (H = 50 Oe), which follows a ferromagnetic order parameter shape and is consistent with the T_C measured in magnetometry (Fig. 7.4(a)).

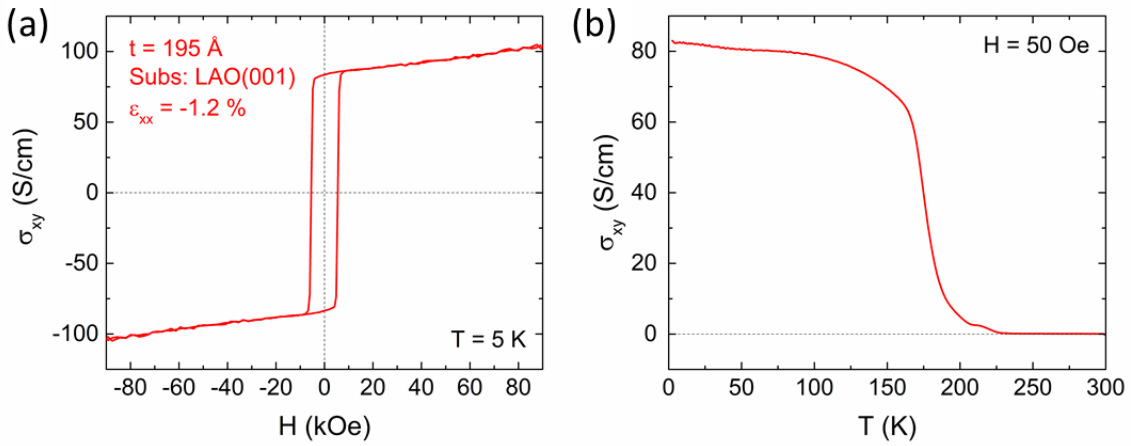

Fig. 7.9. (a) Transverse conductivity (σ_{xy}) *vs*. magnetic field (H) at 5 K for a 195-Å-thick, x = 0.5 LSCO film grown on LAO(001), where the lattice mismatch (ε_{xx}) is -1.2 %, with H applied perpendicular to the film plane. (b) Temperature (T) dependence of σ_{xy}, measured in H = 50 Oe, with σ_{xy} calculated in the same manner as Section 3.5.

The t-dependence of the *RRR* and the 5 K value of ρ, *AMR*, and σ_{AHE} for x = 0.5 films grown on LAO(001) are shown in Fig. 7.10(a-d). The small increase in ρ and decreases in *RRR*, *AMR*, and σ_{AHE} at low t can all be ascribed to approaching the dead layer t of ~7 unit cells (~28 Å) observed for x = 0.5 films grown on LAO(001) (Chapter 7). Otherwise, all of these parameters are essentially t-independent, suggesting the large *AMR* and σ_{AHE} values observed are intrinsic to these LSCO films, similar to the large PMA, and not an interface induced effect. The ε_{xx}-dependence of the same parameters is shown in Fig. 7.10(e-h) for 195-Å-thick films on the same substrates used for the magnetic anisotropy study above. Also shown are the values from an x = 0.3 LSCO single crystal [], which is used as the ε_{xx} = 0 point of reference (except for the *AMR* value, for which no data was available at x = 0.3; here, the value from a $SrCoO_3$ crystal is used). The 5 K ρ has a weak

ε_{xx} dependence, as shown in Fig. 7.10(e), with a minimum observed on LAO. The *RRR* also has a weak ε_{xx} dependence in the films (Fig. 7.10(f)), with a maximum observed on LAO. All of the films have a much smaller *RRR* compared to the bulk sample, which is probably a consequence of increased surface scattering in the thin films. The $\sigma_{AHE}(\varepsilon_{xx})$ shown in Fig. 7.10(g) is largest for the $x = 0.3$ single crystal. Note that the extremely small value for the film on STO could be a consequence of the large in-plane magnetic anisotropy (see Fig. 7.1(e)), which makes it difficult to saturate the out-of-plane *M* orientation and perform the high-field-extrapolation to $H = 0$ to calculate σ_{AHE}. Finally, the ε_{xx}-dependence of the *AMR* in Fig. 7.10(h) demonstrates the significant enhancement of *AMR* observed in these LSCO films compared to a bulk $SrCoO_3$ single crystal, where *AMR* = 1.8 % [99]. While the *AMR* peaks for films on LAO, the *AMR* on all of the substrates are more than an order of magnitude larger than the bulk value.

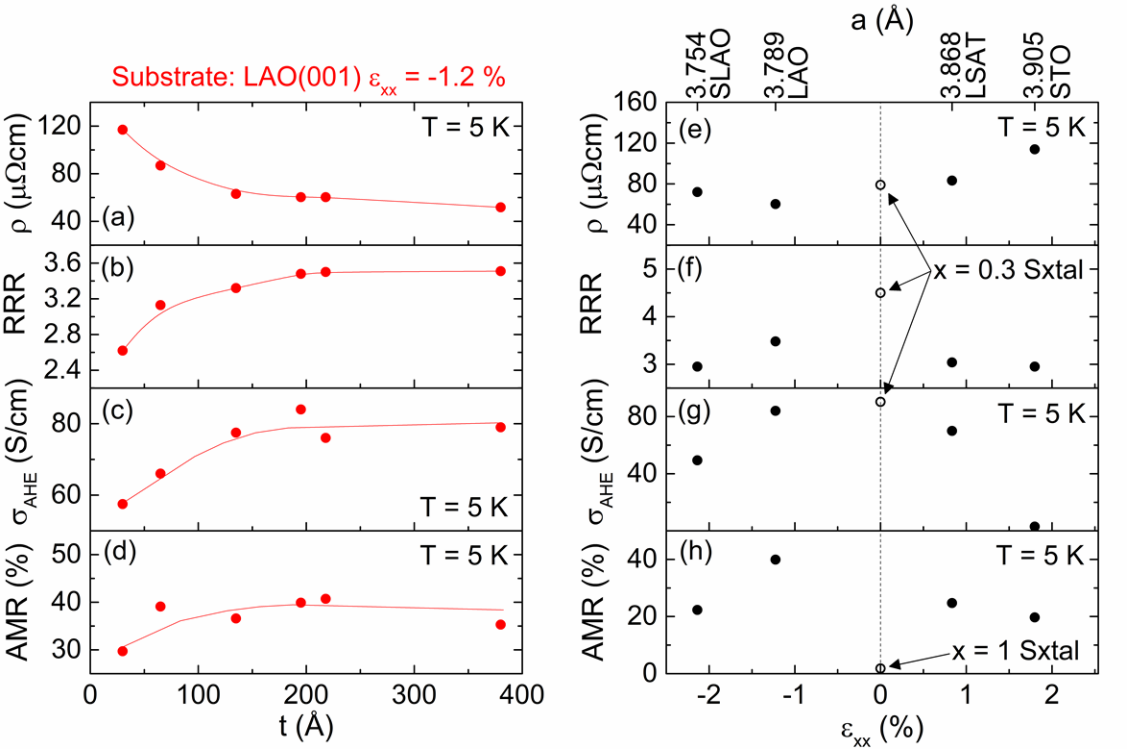

Fig. 7.10. Thickness (*t*) dependence of $x = 0.5$ LSCO films grown on LAO(001) (where the lattice mismatch (ε_{xx}) is -1.2 %), of (a) the 5 K resistivity (ρ), (b) the residual resistivity ratio (*RRR*), (c) the 5 K anomalous Hall conductivity (σ_{AHE}), and (d) the 5 K anisotropic magnetoresistance (*AMR*), all of which are defined in the main text. The solid lines are guides to the eye. The same four parameters are shown as a function of ε_{xx} in (e-f), respectively, for 195-Å-thick, $x = 0.5$ films grown on different substrates. Also shown in (e-f) are LSCO single crystal values, represented by open points, for the *x* values labeled.

To put the *AMR* values observed here in context, the 40 % value on LAO is the largest conventional *AMR* we are aware of. In ferromagnetic transition metal alloys, the *AMR* peaks at 20 % (at low *T*) for alloys with average Bohr magneton number of ~0.9 [179]. While much larger anisotropies can be observed in different magnetoresistance mechanisms (such as anisotropic CMR where anisotropies as large as 100 % have been observed [180]), the largest *conventional AMR* we are aware of is 32 %, which was measured in holmium single crystals [179]. The fact that both the magnetic anisotropy and *AMR* are enhanced in these LSCO films compared to bulk LSCO is interesting, as both of these phenomena fundamentally originate from spin-orbit interactions. Again, we cannot resolve whether strain or OVO structures are the source of the enhanced spin-orbit coupling in these films. Further theoretical work in this regard is clearly warranted.

7.3 Conclusions

In summary, enhanced magnetic anisotropy is observed in epitaxial LSCO films, with PMA and in-plane anisotropy observed under compressive and tensile lattice mismatch, respectively. Giant anisotropic magnetoresistance and anomalous Hall effect are also observed; we have, in fact, observed the largest conventional AMR in any material, that we are aware of. Thickness dependent measurements rule out the possibility that these enhancements are driven by a substrate/film interface effect. Further work is needed to elucidate the underlying cause for these effects, however, with leading ideas based on strain- or OVO-induced enhancement of the spin-orbit coupling with respect to bulk LSCO.

Chapter 8: Summary and outlook

The key contributions of this work to the scientific community lie in addressing three open issues in electrolyte gating, an exciting new platform for materials research. Using ion gel transistors based on epitaxial LSCO films, we first addressed the poorly understood electrostatic *vs.* electrochemical gating mechanisms, particularly with respect to oxygen vacancy formation in oxide EDLTs. In essence we found a dramatic asymmetry in response with respect to bias polarity, with oxygen vacancy formation at positive bias and electrostatic hole accumulation at negative bias. We arrived at this conclusion based on transport measurements performed in inert and O_2-rich atmospheres, as well as *in operando* SXRD and PNR measurements. This was interpreted in a simple picture where electrostatic *vs*. electrochemical response is dictated by enthalpy of formation of V_Os, bias polarity, and carrier type. Critically, the *in operando* probes also allowed for quantification and depth-profiling of the positive-bias-induced V_O densities, which were large ($\delta \approx 0.16$) and penetrated deep (> 16 nm) in these films. These results are thus of general interest to the community applying electrolyte gating to oxides; both in demonstrating the potential power of *in operando* probes and in exploring gating mechanisms in LSCO, which provides an interesting limit of low enthalpy of formation and high diffusivity of V_Os.

Electrical control of magnetism, a long-standing goal in physics and technology, was then demonstrated in both electrochemical and electrostatic modes. Electrochemical control is possible even in thick films, due to the low formation enthalpy and high diffusivity of V_Os in LSCO. Further, working at negative bias in electrostatic mode, and guided by theory, we then demonstrated reversible electrical control of T_C over a 150 K window. This electrostatic T_C modulation is the largest achieved by electrolyte gating to date, and comparable to state-of-the-art techniques such as ferroelectric gating. Such impressive T_C control was achieved *via* gate-induced cluster percolation, leading to optimized control of ferromagnetism, directly verified by magnetoresistance, anomalous Hall effect, and PNR measurements.

While the work above has led to significantly improved understanding of electrolyte gating, it has also unveiled some new questions to answer. The first is whether the irreversibility associated with V_O formation can be mitigated. The field of electrolyte

gating of oxides in general, partially impacted by the results reported here, has come to the realization that some of these electrochemical mechanisms (V_O formation, H^+ intercalation, *etc.*) can be extremely useful in materials studies. For instance, if we were able to return oxygen ions back to the lattice after V_O formation at positive bias, we could then traverse the phase space of LSCO with V_O-doping and perhaps not be charge-screening-limited as we are in electrostatic mode. More thorough transport dynamics in O_2-rich environments could be important to developing new strategies in this regard. Other options could include dissolution of O-containing molecules or ions in the IL during gating, particularly those that may be amenable to dissociating O atoms/ions (*e.g.*, OH^- in H_2O), hopefully intensifying the role O_2 plays. Further, how the bias polarity and reversibility evolve at lower x is interesting, as x provides a way to tune the V_O formation energy and diffusivity in LSCO (at lower x there is less Co in the nominal 4+ valence state, thus leading to lower formation enthalpy of V_O).

Another way to improve reversibility would be to develop strategies to prevent V_O formation, such as including a diffusion barrier between the IL and the film. The ideal diffusion barrier would be ultrathin, such that the capacitance of the EDL remained high, and would have to be insulating. Promising diffusion barrier candidates include atomically-thin 2D boron-nitride and self-assembled monolayers of organic molecules. Self-assembled monolayers are particularly interesting, as they provide a way to tune the diffusion barrier thickness using organic molecule size, essentially by changing the length of alkyl chains. Preventing V_O in LSCO EDLTs would be a great way to test such diffusion barriers, as we now know V_O formation is facile in LSCO EDLTs.

Another obvious place for further investigation lies in testing the universality of the strategies to achieve gate-induced percolation in other materials. Exciting in this regard would be moving to a similarly percolative system with higher typical values of T_C, such as the manganites. In such systems it may be possible to achieve giant modification of room temperature ferromagnetism. Further, developing ideas for the optimization of electrolyte-gate-control of magnetism, or other properties, in non-percolative materials could prove just as fruitful as the studies presented here.

References

[1] A. Jun, J. Kim, J. Shin, and G. Kim, ChemElectroChem **3**, 511 (2016).

[2] G. H. Haertling, J. Am. Ceram. Soc. **82**, 797 (1999).

[3] R. Ramesh and N. A. Spaldin, Nat. Mater. **6**, 21 (2007).

[4] E. Dagotto, Rev. Mod. Phys. **66**, 763 (1994).

[5] E. Dagotto, T. Hotta, and A. Moreo, Phys. Rep. **344**, 1 (2001).

[6] R. E. Cohen, Nature **358**, 136 (1992).

[7] V. . Kharton, A. . Viskup, E. . Naumovich, and N. . Lapchuk, Solid State Ionics **104**, 67 (1997).

[8] Y. Tokura and N. Nagaosa, Science **288**, 462 (2000).

[9] J. Wu and C. Leighton, Phys. Rev. B **67**, 174408 (2003).

[10] S. Bose, Complexity at Cobaltite Interfaces: The Interplay between Strain, Stoichiometry, Magnetism and Transport, 2014.

[11] F. Hellman, A. Hoffmann, Y. Tserkovnyak, G. S. D. Beach, E. E. Fullerton, C. Leighton, A. H. MacDonald, D. C. Ralph, D. A. Arena, H. A. Dürr, P. Fischer, J. Grollier, J. P. Heremans, T. Jungwirth, A. V Kimel, B. Koopmans, I. N. Krivorotov, S. J. May, A. K. Petford-Long, J. M. Rondinelli, N. Samarth, I. K. Schuller, A. N. Slavin, M. D. Stiles, O. Tchernyshyov, A. Thiaville, and B. L. Zink, Rev. Mod. Phys. **89**, 025006 (2017).

[12] P. W. Anderson, Phys. Rev. **79**, 350 (1950).

[13] J. B. Goodenough, Phys. Rev. **100**, 564 (1955).

[14] J. Kanamori, J. Phys. Chem. Solids **10**, 87 (1959).

[15] P. W. Anderson and H. Hasegawa, Phys. Rev. **100**, 675 (1955).

[16] J. H. Haeni, P. Irvin, W. Chang, R. Uecker, P. Reiche, Y. L. Li, S. Choudhury, W. Tian, M. E. Hawley, B. Craigo, A. K. Tagantsev, X. Q. Pan, S. K. Streiffer, L. Q. Chen, S. W. Kirchoefer, J. Levy, and D. G. Schlom, Nature **430**, 758 (2004).

[17] F. M. Granozio, G. Koster, and G. Rijnders, MRS Bull. **38**, 1017 (2013).

[18] A. Ohtomo and H. Y. Hwang, Nature **427**, 423 (2004).

[19] J. A. Bert, B. Kalisky, C. Bell, M. Kim, Y. Hikita, H. Y. Hwang, and K. A. Moler, Nat. Phys. **7**, 767 (2011).

[20] G. H. Jonker and J. H. Van Santen, Physica **16**, 337 (1950).

[21] M. Fath, S. Freisem, A. A. Menovsky, Y. Tomioka, J. Aarts, and J. A. Mydosh, Science **285**, 1540 (1999).

[22] W.-G. Wang, M. Li, S. Hageman, and C. L. Chien, Nat. Mater. **11**, 64 (2011).

[23] U. Bauer, L. Yao, A. J. Tan, P. Agrawal, S. Emori, H. L. Tuller, S. van Dijken, and G. S. D. Beach, Nat. Mater. **14**, 174 (2015).

[24] S. M. Wu, S. A. Cybart, D. Yi, J. M. Parker, R. Ramesh, and R. C. Dynes, Phys. Rev. Lett. **110**, 067202 (2013).

[25] D. Pantel, S. Goetze, D. Hesse, and M. Alexe, Nat. Mater. **11**, 289 (2012).

[26] C. H. Ahn, J.-M. Triscone, and J. Mannhart, Nature **424**, 1015 (2003).

[27] X. Hong, A. Posadas, and C. H. Ahn, Appl. Phys. Lett. **86**, 142501 (2005).

[28] H. J. A. Molegraaf, J. Hoffman, C. A. F. Vaz, S. Gariglio, D. van der Marel, C. H. Ahn, and J.-M. Triscone, Adv. Mater. **21**, 3470 (2009).

[29] C. H. Ahn, A. Bhattacharya, M. Di Ventra, J. N. Eckstein, C. D. Frisbie, M. E. Gershenson, A. M. Goldman, I. H. Inoue, J. Mannhart, A. J. Millis, A. F. Morpurgo, D. Natelson, and J.-M. Triscone, Rev. Mod. Phys. **78**, 1185 (2006).

[30] J. H. Ngai, F. J. Walker, and C. H. Ahn, Annu. Rev. Mater. Res. **44**, 1 (2014).

[31] H. Shimotani, H. Asanuma, A. Tsukazaki, A. Ohtomo, M. Kawasaki, and Y. Iwasa, Appl. Phys. Lett. **91**, 082106 (2007).

[32] K. Ueno, S. Nakamura, H. Shimotani, A. Ohtomo, N. Kimura, T. Nojima, H. Aoki, Y. Iwasa, and M. Kawasaki, Nat. Mater. **7**, 855 (2008).

[33] A. S. Dhoot, C. Israel, X. Moya, N. D. Mathur, and R. H. Friend, Phys. Rev. Lett. **102**, 136402 (2009).

[34] R. Scherwitzl, P. Zubko, I. G. Lezama, S. Ono, A. F. Morpurgo, G. Catalan, and J. M. Triscone, Adv. Mater. **22**, 5517 (2010).

[35] A. T. Bollinger, G. Dubuis, J. Yoon, D. Pavuna, J. Misewich, and I. Božović, Nature **472**, 458 (2011).

[36] K. Ueno, S. Nakamura, H. Shimotani, H. T. Yuan, N. Kimura, T. Nojima, H. Aoki,

Y. Iwasa, and M. Kawasaki, Nat. Nanotechnol. **6**, 408 (2011).

[37] X. Leng, J. Garcia-Barriocanal, S. Bose, Y. Lee, and A. M. Goldman, Phys. Rev. Lett. **107**, 027001 (2011).

[38] Y. Yamada, K. Ueno, T. Fukumura, H. T. Yuan, H. Shimotani, Y. Iwasa, L. Gu, S. Tsukimoto, Y. Ikuhara, and M. Kawasaki, Science **332**, 1065 (2011).

[39] J. Ye, Y. Zhang, R. Akashi, and M. Bahramy, Science **338**, 1193 (2012).

[40] D. Braga, I. G. Lezama, H. Berger, and A. F. Morpurgo, Nano Lett. **12**, 5218 (2012).

[41] H. Ji, J. Wei, and D. Natelson, Nano Lett. **12**, 2988 (2012).

[42] M. Nakano, K. Shibuya, D. Okuyama, T. Hatano, S. Ono, M. Kawasaki, Y. Iwasa, and Y. Tokura, Nature **487**, 459 (2012).

[43] S. H. Kim, K. Hong, W. Xie, K. H. Lee, S. Zhang, T. P. Lodge, and C. D. Frisbie, Adv. Mater. **25**, 1822 (2013).

[44] H. T. Yi, B. Gao, W. Xie, S.-W. Cheong, and V. Podzorov, Sci. Rep. **4**, 6604 (2014).

[45] Y. Saito and Y. Iwasa, ACS Nano **9**, 3192 (2015).

[46] W. Xie and C. D. Frisbie, J. Phys. Chem. C **115**, 14360 (2011).

[47] W. Xie, S. Wang, X. Zhang, C. Leighton, and C. D. Frisbie, Phys. Rev. Lett. **113**, 1 (2014).

[48] H. Yuan, H. Shimotani, J. Ye, S. Yoon, H. Aliah, A. Tsukazaki, M. Kawasaki, and Y. Iwasa, J. Am. Chem. Soc. **132**, 18402 (2010).

[49] S. Bubel, A. J. Hauser, A. M. Glaudell, T. E. Mates, S. Stemmer, and M. L. Chabinyc, Appl. Phys. Lett. **106**, 122102 (2015).

[50] J. Jeong, N. Aetukuri, T. Graf, T. D. Schladt, M. G. Samant, and S. S. P. Parkin, Science **339**, 1402 (2013).

[51] M. Li, W. Han, X. Jiang, J. Jeong, M. G. Samant, and S. S. P. Parkin, Nano Lett. **13**, 4675 (2013).

[52] T. D. Schladt, T. Graf, N. B. Aetukuri, M. Li, A. Fantini, X. Jiang, M. G. Samant, and S. S. P. Parkin, ACS Nano **7**, 8074 (2013).

[53] S. Wang, M. Ha, M. Manno, C. D. Frisbie, and C. Leighton, Nat. Commun. **3**,

1210 (2012).

[54] W. Xie, X. Zhang, C. Leighton, and C. D. Frisbie, Adv. Electron. Mater. **3**, 1600369 (2017).

[55] K. H. Lee, M. S. Kang, S. Zhang, Y. Gu, T. P. Lodge, and C. D. Frisbie, Adv. Mater. **24**, 4457 (2012).

[56] H. Yuan, H. Shimotani, A. Tsukazaki, A. Ohtomo, M. Kawasaki, and Y. Iwasa, Adv. Funct. Mater. **19**, 1046 (2009).

[57] M. Galiński, A. Lewandowski, and I. Stepniak, Electrochim. Acta **51**, 5567 (2006).

[58] M. Armand, F. Endres, D. R. MacFarlane, H. Ohno, and B. Scrosati, Nat. Mater. **8**, 621 (2009).

[59] T. P. Lodge, Science **321**, 50 (2008).

[60] S. Ono, S. Seki, R. Hirahara, Y. Tominari, and J. Takeya, Appl. Phys. Lett. **92**, 1 (2008).

[61] J. H. Cho, J. Lee, Y. Xia, B. Kim, Y. He, M. J. Renn, T. P. Lodge, and C. D. Frisbie, Nat. Mater. **7**, 900 (2008).

[62] J. Lee, M. J. Panzer, Y. He, T. P. Lodge, and C. D. Frisbie, J. Am. Chem. Soc. **129**, 4532 (2007).

[63] N. Lu, P. Zhang, Q. Zhang, R. Qiao, Q. He, H.-B. Li, Y. Wang, J. Guo, D. Zhang, Z. Duan, Z. Li, M. Wang, S. Yang, M. Yan, E. Arenholz, S. Zhou, W. Yang, L. Gu, C.-W. Nan, J. Wu, Y. Tokura, and P. Yu, Nature **546**, 124 (2017).

[64] Y. Dong, H. Xu, Z. Luo, H. Zhou, D. D. Fong, W. Wu, and C. Gao, APL Mater. **5**, 051101 (2017).

[65] A. M. Perez-Muñoz, P. Schio, R. Poloni, A. Fernandez-Martinez, A. Rivera-Calzada, J. C. Cezar, E. Salas-Colera, G. R. Castro, J. Kinney, C. Leon, J. Santamaria, J. Garcia-Barriocanal, and A. M. Goldman, Proc. Natl. Acad. Sci. **114**, 215 (2017).

[66] X. Leng, J. Pereiro, J. Strle, G. Dubuis, A. T. Bollinger, A. Gozar, J. Wu, N. Litombe, C. Panagopoulos, D. Pavuna, and I. Božović, Quantum Mater. **2**, 35 (2017).

[67] A. C. Lang, J. D. Sloppy, H. Ghassemi, R. C. Devlin, R. J. Sichel-Tissot, J. C. Idrobo, S. J. May, and M. L. Taheri, ACS Appl. Mater. Interfaces **6**, 17018 (2014).

[68] D. Okuyama, M. Nakano, S. Takeshita, H. Ohsumi, S. Tardif, K. Shibuya, T. Hatano, H. Yumoto, T. Koyama, H. Ohashi, M. Takata, M. Kawasaki, T. Arima, Y. Tokura, and Y. Iwasa, Appl. Phys. Lett. **104**, 023507 (2014).

[69] G. Dubuis, Y. Yacoby, H. Zhou, X. He, A. T. Bollinger, D. Pavuna, R. Pindak, and I. Božović, Sci. Rep. **6**, 32378 (2016).

[70] B. Cui, C. Song, G. Wang, Y. Yan, J. Peng, J. Miao, H. Mao, F. Li, C. Chen, F. Zeng, and F. Pan, Adv. Funct. Mater. **24**, 7233 (2014).

[71] P. M. Raccah and J. B. Goodenough, Phys. Rev. **155**, 932 (1967).

[72] S. Yamaguchi, Y. Okimoto, H. Taniguchi, and Y. Tokura, Phys. Rev. B **53**, R2926 (1996).

[73] S. R. English, J. Wu, and C. Leighton, Phys. Rev. B **65**, 220407 (2002).

[74] A. Doi, J. Fujioka, T. Fukuda, S. Tsutsui, D. Okuyama, Y. Taguchi, T. Arima, A. Q. R. Baron, and Y. Tokura, Phys. Rev. B **90**, 2 (2014).

[75] M. A. Korotin, S. Y. Ezhov, I. V. Solovyev, V. I. Anisimov, D. I. Khomskii, and G. A. Sawatzky, Phys. Rev. B **54**, 5309 (1996).

[76] R. F. Klie, J. C. Zheng, Y. Zhu, M. Varela, J. Wu, and C. Leighton, Phys. Rev. Lett. **99**, 1 (2007).

[77] S. Yamaguchi, Y. Okimoto, and Y. Tokura, Phys. Rev. B **55**, R8666 (1997).

[78] C. Zobel, M. Kriener, D. Bruns, J. Baier, M. Grüninger, T. Lorenz, P. Reutler, and A. Revcolevschi, Phys. Rev. B **66**, 020402 (2002).

[79] M. W. Haverkort, Z. Hu, J. C. Cezar, T. Burnus, H. Hartmann, M. Reuther, C. Zobel, T. Lorenz, A. Tanaka, N. B. Brookes, H. H. Hsieh, H.-J. Lin, C. T. Chen, and L. H. Tjeng, Phys. Rev. Lett. **97**, 38 (2006).

[80] A. Podlesnyak, S. Streule, J. Mesot, M. Medarde, E. Pomjakushina, K. Conder, A. Tanaka, M. W. Haverkort, and D. I. Khomskii, Phys. Rev. Lett. **97**, 1 (2006).

[81] S. Noguchi, S. Kawamata, K. Okuda, H. Nojiri, and M. Motokawa, Phys. Rev. B **66**, 944041 (2002).

[82] A. Mineshige, M. Inaba, T. Yao, Z. Ogumi, K. Kikuchi, and M. Kawase, J. Solid State Chem. **121**, 423 (1996).

[83] D. Louca and J. L. Sarrao, Phys. Rev. Lett. **91**, 22 (2003).

[84] D. Phelan, D. Louca, K. Kamazawa, S. H. Lee, S. N. Ancona, S. Rosenkranz, Y. Motome, M. F. Hundley, J. F. Mitchell, and Y. Moritomo, Phys. Rev. Lett. **97**, 1 (2006).

[85] A. Podlesnyak, M. Russina, A. Furrer, A. Alfonsov, E. Vavilova, V. Kataev, B. Büchner, T. Strässle, E. Pomjakushina, K. Conder, and D. I. Khomskii, Phys. Rev. Lett. **101**, 1 (2008).

[86] A. Podlesnyak, G. Ehlers, M. Frontzek, A. S. Sefat, A. Furrer, T. Strässle, E. Pomjakushina, K. Conder, F. Demmel, and D. I. Khomskii, Phys. Rev. B **83**, 1 (2011).

[87] P. P. Orth, D. Phelan, C. Leighton, and R. M. Fernandes, Under review.

[88] C. He, S. El-Khatib, J. Wu, J. W. Lynn, H. Zheng, J. F. Mitchell, and C. Leighton, Europhys. Lett. **87**, 27006 (2009).

[89] J. Wu, J. W. Lynn, C. J. Glinka, J. Burley, H. Zheng, J. F. Mitchell, and C. Leighton, Phys. Rev. Lett. **94**, 037201 (2005).

[90] P. L. Kuhns, M. J. R. Hoch, W. G. Moulton, A. P. Reyes, J. Wu, and C. Leighton, Phys. Rev. Lett. **91**, 127202 (2003).

[91] M. J. R. Hoch, P. L. Kuhns, W. G. Moulton, A. P. Reyes, J. Lu, J. Wu, and C. Leighton, Phys. Rev. B **70**, 1 (2004).

[92] D. Phelan, D. Louca, S. Rosenkranz, S. H. Lee, Y. Qiu, P. J. Chupas, R. Osborn, H. Zheng, J. F. Mitchell, J. R. D. Copley, J. L. Sarrao, and Y. Moritomo, Phys. Rev. Lett. **96**, 6 (2006).

[93] C. He, S. Eisenberg, C. Jan, H. Zheng, J. F. Mitchell, and C. Leighton, Phys. Rev. B **80**, 214411 (2009).

[94] H. M. Aarbogh, J. Wu, L. Wang, H. Zheng, J. F. Mitchell, and C. Leighton, Phys. Rev. B **74**, 134408 (2006).

[95] M. A. Torija, M. Sharma, M. R. Fitzsimmons, M. Varela, and C. Leighton, J. Appl. Phys. **104**, (2008).

[96] R. C. O'Handley, *Modern Magnetic Materials - Principles and Applications*; Wiley & Sons: New York, (2000).

[97] S. Medling, Y. Lee, H. Zheng, J. F. Mitchell, J. W. Freeland, B. N. Harmon, and F. Bridges, Phys. Rev. Lett. **109**, 1 (2012).

[98] G. H. Jonker and J. H. Van Santen, Physica **19**, 120 (1953).

[99] Y. Long, Y. Kaneko, S. Ishiwata, Y. Taguchi, and Y. Tokura, J. Phys. Condens. Matter **23**, 245601 (2011).

[100] J. W. Freeland, J. X. Ma, and J. Shi, Appl. Phys. Lett. **93**, 212501 (2008).

[101] V. V. Mehta, M. Liberati, F. J. Wong, R. V. Chopdekar, E. Arenholz, and Y. Suzuki, J. Appl. Phys. **105**, 5 (2009).

[102] N. Biškup, J. Salafranca, V. Mehta, M. P. Oxley, Y. Suzuki, S. J. Pennycook, S. T. Pantelides, and M. Varela, Phys. Rev. Lett. **112**, 1 (2014).

[103] V. V. Mehta, N. Biskup, C. Jenkins, E. Arenholz, M. Varela, and Y. Suzuki, Phys. Rev. B **91**, 1 (2015).

[104] H. Hsu, P. Blaha, and R. M. Wentzcovitch, Phys. Rev. B **85**, 1 (2012).

[105] J. Gazquez, W. Luo, M. P. Oxley, M. Prange, M. a Torija, M. Sharma, C. Leighton, S. T. Pantelides, S. J. Pennycook, and M. Varela, Nano Lett. **11**, 973 (2011).

[106] J. W. Matthews and A. E. Blakeslee, J. Cryst. Growth **27**, 118 (1974).

[107] M. A. Torija, M. Sharma, J. Gazquez, M. Varela, C. He, J. Schmitt, J. A. Borchers, M. Laver, S. El-Khatib, and C. Leighton, Adv. Mater. **23**, 2711 (2011).

[108] H. Jeen, W. S. Choi, M. D. Biegalski, C. M. Folkman, I.-C. Tung, D. D. Fong, J. W. Freeland, D. Shin, H. Ohta, M. F. Chisholm, and H. N. Lee, Nat. Mater. **12**, 1057 (2013).

[109] J. Gazquez, S. Bose, M. Sharma, M. A. Torija, S. J. Pennycook, C. Leighton, and M. Varela, APL Mater. **1**, 012105 (2013).

[110] A. N. Pasupathy, A. Pushp, K. K. Gomes, C. V Parker, J. Wen, Z. Xu, G. Gu, S. Ono, Y. Ando, and A. Yazdani, Science **320**, 196 (2008).

[111] D. O. Klenov, W. Donner, L. Chen, A. J. Jacobson, and S. Stemmer, J. Mater. Res. **18**, 188 (2003).

[112] J. T. Cheung, P. E. D. Morgan, D. H. Lowndes, X.-Y. Zheng, and J. Breen, Appl. Phys. Lett. **62**, 2045 (1993).

[113] K. Hwang, H. Lee, S. Min, and B. Kang, J. Sol-Gel Sci. Technol. **3**, 175 (2000).

[114] Z. L. Wang and J. S. Yin, Philos. Mag. B **77**, 49 (1998).

[115] A. C. Westerheim, L. S. Yu-Jahnes, and A. C. Anderson, IEEE Trans. Magn. **27**,

1001 (1991).

[116] U. Poppe, J. Schubert, R. R. Arons, W. Evers, C. H. Freiburg, W. Reichert, K. Schmidt, W. Sybertz, and K. Urban, Solid State Commun. **66**, 661 (1988).

[117] U. Poppe, N. Klein, U. Dähne, H. Soltner, C. L. Jia, B. Kabius, K. Urban, A. Lubig, K. Schmidt, S. Hensen, S. Orbach, G. Müller, and H. Piel, J. Appl. Phys. **71**, 5572 (1992).

[118] P. Ambwani, P. Xu, G. Haugstad, J. S. Jeong, R. Deng, K. A. Mkhoyan, B. Jalan, and C. Leighton, J. Appl. Phys. **120**, 055704 (2016).

[119] M. Sharma, J. Gazquez, M. Varela, J. Schmitt, and C. Leighton, J. Vac. Sci. Technol. A **29**, 051511 (2011).

[120] M. A. Garcia, E. Fernandez Pinel, J. De La Venta, A. Quesada, V. Bouzas, J. F. Fernández, J. J. Romero, M. S. Martín González, and J. L. Costa-Krämer, J. Appl. Phys. **105**, (2009).

[121] L. J. van der Pauw, Philips Tech. Rev. **20**, 220 (1958).

[122] T. Sato, K. Shibuya, T. Ohnishi, K. Nishio, and M. Lippmaa, Jpn. J. Appl. Phys. **46**, L515 (2007).

[123] Neutron SLD calculations were performed using the NIST Neutron activation and scattering calculator at https://www.ncnr.nist.gov/resources/activation/

[124] J. Walter, H. Wang, B. Luo, C. D. Frisbie, and C. Leighton, ACS Nano **10**, 7799 (2016).

[125] Note that the TFSI- anion contains oxygen, which could be electrochemically transferred to the LSCO channel.

[126] C. K. Xie, Y. F. Nie, B. O. Wells, J. I. Budnick, W. a. Hines, and B. Dabrowski, Appl. Phys. Lett. **99**, 052503 (2011).

[127] R. Wang, Y. Zhu, and S. Shapiro, Phys. Rev. Lett. **80**, 2370 (1998).

[128] J. Shiogai, Y. Ito, T. Mitsuhashi, T. Nojima, and A. Tsukazaki, Nat. Phys. **12**, 42 (2015).

[129] M. Imamura, N. Matsubayashi, and H. Shimada, J. Phys. Chem. B **104**, 7348 (2000).

[130] D. A. Kumar, S. Selvasekarapandian, H. Nithya, J. Leiro, Y. Masuda, S. D. Kim, and S. K. Woo, Powder Technol. **235**, 140 (2013).

[131] A. Machocki, T. Ioannides, B. Stasinska, W. Gac, G. Avgouropoulos, D. Delimaris, W. Grzegorczyk, and S. Pasieczna, J. Catal. **227**, 282 (2004).

[132] A. Spinelli, M. A. Torija, C. Liu, C. Jan, and C. Leighton, Phys. Rev. B **81**, 155110 (2010).

[133] T. Miyasato, N. Abe, T. Fujii, a. Asamitsu, S. Onoda, Y. Onose, N. Nagaosa, and Y. Tokura, Phys. Rev. Lett. **99**, 086602 (2007).

[134] X. Hong, A. Posadas, A. Lin, and C. H. Ahn, Phys. Rev. B **68**, 134415 (2003).

[135] J. Walter, G. Yu, B. Yu, A. Grutter, B. Kirby, J. Borchers, Z. Zhang, H. Zhou, T. Birol, M. Greven, and C. Leighton, Phys. Rev. Mater. **1**, 071403(R) (2017).

[136] S. Kelly, F. Galli, J. Aarts, S. Bose, M. Sharma, and C. Leighton, Appl. Phys. Lett. **105**, 2012 (2014).

[137] X. Wu, J. Walter, T. Feng, J. Zhu, H. Zheng, J. F. Mitchell, N. Biškup, M. Varela, X. Ruan, C. Leighton, and X. Wang, Adv. Funct. Mater. **27**, 1704233 (2017).

[138] R. P. Haggerty and R. Seshadri, J. Phys. Condens. Matter **16**, 6477 (2004).

[139] J. Mizusaki, Y. Mima, S. Yamauchi, and K. Fueki, J. Solid State Chem. **80**, 102 (1989).

[140] A. Ringuedé and J. Fouletier, Solid State Ionics **139**, 167 (2001).

[141] P. E. Blöchl, Phys. Rev. B **50**, 17953 (1994).

[142] G. Kresse and D. Joubert, Phys. Rev. B **59**, 1758 (1999).

[143] G. Kresse and J. Hafner, Phys. Rev. B **47**, 558 (1993).

[144] G. Kresse and J. Furthmüller, Phys. Rev. B **54**, 11169 (1996).

[145] J. P. Perdew, A. Ruzsinszky, G. I. Csonka, O. A. Vydrov, G. E. Scuseria, L. A. Constantin, X. Zhou, and K. Burke, Phys. Rev. Lett. **100**, 136406 (2008).

[146] A. I. Liechtenstein, V. I. Anisimov, and J. Zaanen, Phys. Rev. B **52**, R5467 (1995).

[147] H. J. Monkhorst and J. D. Pack, Phys. Rev. **13**, 5188 (1976).

[148] H. Hsu, P. Blaha, R. M. Wentzcovitch, and C. Leighton, Phys. Rev. B **82**, 100406 (2010).

[149] M. Youssef, K. J. Van Vliet, and B. Yildiz, Phys. Rev. Lett. **119**, 1 (2017).

[150] R. De Souza, Solid State Ionics **106**, 175 (1998).

[151] D. A. Gilbert, A. J. Grutter, E. Arenholz, K. Liu, B. J. Kirby, J. A. Borchers, and B. B. Maranville, Nat. Commun. **7**, 12264 (2016).

[152] D. A. Gilbert, A. J. Grutter, P. Murray, R. V. Chopdekar, A. M. Kane, A. L. Ionin, S. R. Spurgeon, B. J. Kirby, B. B. Maranville, A. T. N'Diaye, A. Mehta, E. Arenholz, K. Liu, Y. Takamura, and J. A. Borchers, Unpublished.

[153] P. P. Orth, R. M. Fernandes, J. Walter, C. Leighton, and B. I. Shklovskii, 2 (2016).

[154] B. I. Shklovskii and A. L. Efros, *Electronic Properties of Doped Semiconductors*, Springer Series in Solid-State Sciences Vol. 45 (Springer, Heidelberg, 1984).

[155] D. Stauffer and A. Aharony, *Introduction to Percolation Theory*, 2nd ed (Taylor & Francis, London, 1994).

[156] T. Vojta and J. Schmalian, Phys. Rev. Lett. **95**, 1 (2005).

[157] R. Yu, T. Roscilde, and S. Haas, Phys. Rev. Lett. **94**, 1 (2005).

[158] N. Bray-Ali, J. E. Moore, T. Senthil, and A. Vishwanath, Phys. Rev. B **73**, 1 (2006).

[159] L. Wang and A. W. Sandvik, Phys. Rev. Lett. **97**, 2 (2006).

[160] R. M. Fernandes and J. Schmalian, Phys. Rev. Lett. **106**, 1 (2011).

[161] J. Wang, Z. Zhou, W. Zhang, T. M. Garoni, and Y. Deng, Phys. Rev. E **87**, 1 (2013).

[162] M. E. J. Newman and R. M. Ziff, Phys. Rev. Lett. **85**, 4104 (2000).

[163] M. E. J. Newman and R. M. Ziff, Phys. Rev. E **64**, 16 (2001).

[164] T. Senthil and S. Sachdev, Phys. Rev. Lett. **77**, 5292 (1996).

[165] A. W. Sandvik, Phys. Rev. B **66**, 1 (2002).

[166] M. Al-Ali, J. A. Hoyos, and T. Vojta, Phys. Rev. B **86**, 1 (2012).

[167] J. A. Hoyos and T. Vojta, Phys. Rev. B **74**, 1 (2006).

[168] B. Cui, C. Song, F. Li, X. Y. Zhong, Z. C. Wang, P. Werner, Y. D. Gu, H. Q. Wu, M. S. Saleem, S. S. P. Parkin, and F. Pan, Phys. Rev. Appl. **8**, 1 (2017).

[169] K. Shimamura, D. Chiba, S. Ono, S. Fukami, N. Ishiwata, M. Kawaguchi, K.

Kobayashi, and T. Ono, Appl. Phys. Lett. **100**, 122402 (2012).

[170] T. Hatano, Z. Sheng, M. Nakamura, M. Nakano, M. Kawasaki, Y. Iwasa, and Y. Tokura, Adv. Mater. **26**, 2874 (2014).

[171] C. He, Magneto-Electronic Phase Separation in Doped Cobaltites, 2009.

[172] J. Mira, J. Rivas, M. Vázquez, M. R. Ibarra, R. Caciuffo, and M. A. Señarís Rodríguez, Europhys. Lett. **62**, (2003).

[173] M. R. Ibarra, R. Mahendiran, C. Marquina, B. García-Landa, and J. Blasco, Phys. Rev. B **57**, R3217 (1998).

[174] C. Kwon, M. C. Robson, K.-C. Kim, J. Y. Gu, S. E. Lofland, S. M. Bhagat, Z. Trajanovic, M. Rajeswari, T. Venkatesan, a. R. Kratz, R. D. Gomez, and R. Ramesh, J. Magn. Magn. Mater. **172**, 229 (1997).

[175] F. Tsui, M. C. Smoak, T. K. Nath, and C. B. Eom, Appl. Phys. Lett. **76**, 2421 (2000).

[176] R. Desfeux, S. Bailleul, A. Da Costa, W. Prellier, and A. M. Haghiri-Gosnet, Appl. Phys. Lett. **78**, 3681 (2001).

[177] B. Dieny and M. Chshiev, Rev. Mod. Phys. **89**, (2017).

[178] J. Matsuno, Y. Okimoto, Z. Fang, X. Z. Yu, Y. Matsui, N. Nagaosa, M. Kawasaki, and Y. Tokura, Phys. Rev. Lett. **93**, 1 (2004).

[179] T. R. Mcguire and R. I. Potter, IEEE Trans. Magn. **11**, 1018 (1975).

[180] J.-B. Yau, X. Hong, A. Posadas, C. H. Ahn, W. Gao, E. Altman, Y. Bason, L. Klein, M. Sidorov, and Z. Krivokapic, J. Appl. Phys. **102**, 103901 (2007).